

DTIC FILE COPY

4

~~GL-TR-89-0310~~

ANALYSIS OF REGIONAL PHASES USING THREE-COMPONENT DATA.

AD-A219 482

M. Nafi Toksöz
Ari Ben-Menahem
Anton M. Dainty
Batakrishna Mandal
Michael Prange
Arcangelo G. Sena

Earth Resources Laboratory
Department of Earth, Atmospheric, and
Planetary Sciences
Massachusetts Institute of Technology
Cambridge, Massachusetts 02139

20 November 1989

Final Report
19 August 1987—31 August 1989

DTIC
SELECTED
MARCH 12 1990
S E D

APPROVED FOR PUBLIC RELEASE; DISTRIBUTION UNLIMITED

Geophysics Laboratory
Air Force Systems Command
United States Air Force
Hanscom Air Force Base, Massachusetts 01731-5000

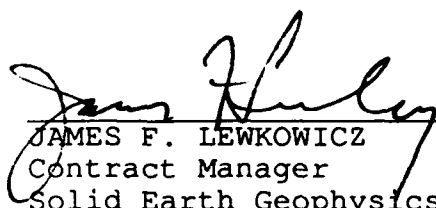
90 03 09 070

SPONSORED BY
Defense Advanced Research Projects Agency
Nuclear Monitoring Research Office
ARPA ORDER NO.5307

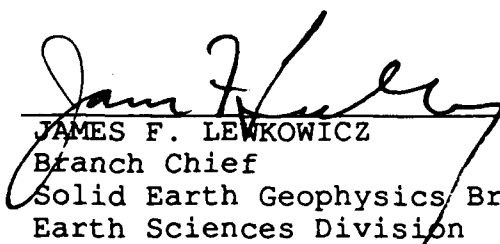
MONITORED BY
Geophysics Laboratory
F19628-87-K-0054

The views and conclusions contained in this document are those of the authors and should not be interpreted as representing the official policies, either expressed or implied, of the Defense Advanced Research Projects Agency or the U.S. Government.

This technical report has been reviewed and is approved for publication.

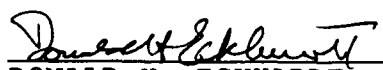


JAMES F. LEWKOWICZ
Contract Manager
Solid Earth Geophysics Branch
Earth Sciences Division



JAMES F. LEWKOWICZ
Branch Chief
Solid Earth Geophysics Branch
Earth Sciences Division

FOR THE COMMANDER



DONALD H. ECKHARDT, Director
Earth Sciences Division

This report has been reviewed by the ESD Public Affairs Office (PA) and is releasable to the National Technical Information Service (NTIS).

Qualified requestors may obtain additional copies from the Defense Technical Information Center. All others should apply to the National Technical Information Service.

If your address has changed, or if you wish to be removed from the mailing list, or if the addressee is no longer employed by your organization, please notify GL/IMA, Hanscom AFB, MA 01731-5000. This will assist us in maintaining a current mailing list.

Do not return copies of this report unless contractual obligations or notices on a specific document requires that it be returned.

Unclassified

SECURITY CLASSIFICATION OF THIS PAGE

REPORT DOCUMENTATION PAGE

1a. REPORT SECURITY CLASSIFICATION unclassified		1b. RESTRICTIVE MARKINGS										
2a. SECURITY CLASSIFICATION AUTHORITY		3. DISTRIBUTION/AVAILABILITY OF REPORT Approved for public release; distribution unlimited										
2b. DECLASSIFICATION/DOWNGRADING SCHEDULE												
4. PERFORMING ORGANIZATION REPORT NUMBER(S)		5. MONITORING ORGANIZATION REPORT NUMBER(S) GL-TR-89-0310										
6a. NAME OF PERFORMING ORGANIZATION Earth Resources Laboratory, Dept. of Earth, Atmospheric, and Planetary Sciences	6b. OFFICE SYMBOL (If applicable)	7a. NAME OF MONITORING ORGANIZATION Geophysics Laboratory										
6c. ADDRESS (City, State, and ZIP Code) • Massachusetts Institute of Technology Cambridge, MA 02139		7b. ADDRESS (City, State, and ZIP Code) Hanscom AFB, MA 01731-5000										
8a. NAME OF FUNDING/SPONSORING ORGANIZATION Defense Advanced Research Projects Agency	8b. OFFICE SYMBOL (If applicable) NMRO	9. PROCUREMENT INSTRUMENT IDENTIFICATION NUMBER F19628-87-K-0054										
8c. ADDRESS (City, State, and ZIP Code) 1400 Wilson Blvd. Arlington, VA 22209-2308		10. SOURCE OF FUNDING NUMBERS <table border="1"> <tr> <td>PROGRAM ELEMENT NO. 62714E</td> <td>PROJECT NO. 7A10</td> <td>TASK NO. DA</td> <td>WORK UNIT ACCESSION NO. CM</td> </tr> </table>		PROGRAM ELEMENT NO. 62714E	PROJECT NO. 7A10	TASK NO. DA	WORK UNIT ACCESSION NO. CM					
PROGRAM ELEMENT NO. 62714E	PROJECT NO. 7A10	TASK NO. DA	WORK UNIT ACCESSION NO. CM									
11. TITLE (Include Security Classification) Unclassified; Analysis of Regional Phases Using Three-Component Data												
12. PERSONAL AUTHOR(S) M.N. Toksoz, A. Ben-Menahem, A.M. Dainty, B. Mandal, M. Prange, A.G. Sena												
13a. TYPE OF REPORT Final	13b. TIME COVERED FROM 8/19/87 TO 8/31/89	14. DATE OF REPORT (Year, Month, Day) 89 / 11 / 20	15. PAGE COUNT 232									
16. SUPPLEMENTARY NOTATION												
17. COSATI CODES <table border="1"> <tr> <th>FIELD</th> <th>GROUP</th> <th>SUB-GROUP</th> </tr> <tr> <td></td> <td></td> <td></td> </tr> <tr> <td></td> <td></td> <td></td> </tr> </table>		FIELD	GROUP	SUB-GROUP							18. SUBJECT TERMS (Continue on reverse if necessary and identify by block number) rough interface scattering, sources in anisotropic media, crustal attenuation.	
FIELD	GROUP	SUB-GROUP										
19. ABSTRACT (Continue on reverse if necessary and identify by block number) The objective of this project was to conduct basic research on the propagation of seismic energy at regional (100–1000 km) distances for purposes of monitoring underground nuclear explosions. The problems studied were scattering of seismic body waves by rough interfaces, the effect of anisotropic media on the seismic radiation from sources embedded in them, and the attenuation of crustal phases. This Final Report consists of preprints of four papers on these subjects. The first concerns scattering of body waves by rough interfaces. A plane wave (P or S) incident on a rough interface is considered. If the interface were plane the solution would be given by the classical reflection and transmission coefficients from which the reflected and transmitted fields can be constructed. A perturbation solution is found for the additional scattered field under the approximations that the interface height perturbation is much smaller than a wavelength and the interface slope perturbations are much less than unity. The solution may be expressed as three-dimensional scattering kernels that allow reconstruction of the scattered reflected and transmitted fields.												
20. DISTRIBUTION/AVAILABILITY OF ABSTRACT <input checked="" type="checkbox"/> UNCLASSIFIED/UNLIMITED <input type="checkbox"/> SAME AS RPT <input type="checkbox"/> DTIC USERS		21. ABSTRACT SECURITY CLASSIFICATION Unclassified										
22a. NAME OF RESPONSIBLE INDIVIDUAL James F. Lewkowicz		22b. TELEPHONE (Include Area Code) 617/377-3028	22c. OFFICE SYMBOL GL/LWH									

Unclassified

BLOCK 19: Abstract

The second and third papers are on the subject of sources embedded in anisotropic media. In the second paper asymptotic far field expressions of the exact spectral elastodynamic Green's tensor are found; in the third paper this tensor is evaluated numerically by the discrete wavenumber method. These results are used to examine the radiation pattern of seismic waves from different types of sources. This is a crucial problem in monitoring underground nuclear tests because the radiation pattern is a potential discriminant between explosions and other types of source. Specifically, it is demonstrated that for specific values of the parameters of the anisotropic medium an explosion may show a radiation pattern similar to that of an earthquake in an isotropic medium. This is the first time the problem of a source embedded in an anisotropic medium has been solved; the effects discussed here are totally separate from the effects of plane wave propagation in anisotropic media discussed in the previous literature.

The final paper treats the problem of attenuation of shear wave energy in the crust. Models of crustal attenuation (Q) as a function of depth and frequency are found for two non-tectonic regions, the north-eastern U.S. and Fennoscandia, with crystalline basement rock extending to the surface. The method used is matching complete synthetic seismograms with observed seismograms. Our study differs from other studies, however, in that we are interested in finding a general model of crustal attenuation in terms of the operative processes. Such a model would in principle be applicable to any geologically similar region. We find that attenuation is high ($Q < 100$ at 1 Hz) in the upper crust and is probably controlled by fluid flow in fractures (frequency dependence of $Q f^{0.5}$). In the middle crust (depth 2–10 km) attenuation is moderate ($100 < Q < 500$ at 1 Hz) and may be due to scattering (frequency dependence of $Q f^1$). Attenuation is low and frequency-independent in the lower crust, indicating anelastic attenuation in an environment where microfractures have been annealed.

Table of Contents

Abstract	i
List of Contributing Scientists	iv
List of Previous Related Contracts	iv
Bibliography of Publications Sponsored by Contract	iv
“Perturbation Approximation of 3-D Seismic Scattering” by M. Prange and M.N. Toksöz	1
“Seismic Source Theory in Inhomogeneous Anisotropic Media” by A. Ben-Menahem and A.G. Sena	53
“Computation of Complete Waveforms in General Anisotropic Media-Results from an Explosion Source in Anisotropic Medium” by B. Mandal and M.N. Toksöz	151
“Frequency-dependent Attenuation in the Crust” by M.N. Toksöz, B. Mandal and A.M. Dainty	201

Accession For	NTIS	U.S.A.	DTIC	U.S.A.	Identif.
By	Dept. of Energy	Sci. & Tech. Services	Dist	Assist. Dir.	Ref. Ser.
A-1					



List of Contributing Scientists

M. Nafi Toksöz, Professor of Geophysics, Massachusetts Institute of Technology

Ari Ben-Menahem, Visiting Scientist, Massachusetts Institute of Technology ^a

Anton M. Dainty, Visiting Scientist, Massachusetts Institute of Technology

Batakrishna Mandal, Research Scientist, Massachusetts Institute of Technology

Michael Prange, Graduate Research Assistant, Massachusetts Institute of Technology

Arcangelo Sena, Graduate Research Assistant, Massachusetts Institute of Technology

^aAlso NRC Fellow, Earth Sciences Division, Geophysics Laboratory, Air Force Systems Command.

List of Previous and Related Contracts

DARPA/AFGL Contract F19628-86-K-0004 "Influence of Scattering on Seismic Waves", February 1985 to January 1988.

DARPA/AFGL Contract F19628-88-K-0036 "Seismic Wave Propagation, Attenuation and Scattering over Regional Distances", August 1988 to July 1989.

DARPA/AFGL Contract F19628-89-K-0020 "Regional Seismograms: Attenuation and Scattering", July 1989 to June 1991.

Bibliography of Publications Totally or Partially Sponsored by the Contract

Prange, M., and M.N. Toksöz (1988). Scattering of crustal phases at regional distances due to rough interfaces. *Papers Presented at 10th Ann. DARPA/AFGL Seismic Res. Symp.*, 31-37.

Toksöz, M.N., E. Reiter and B. Mandal (1988). Seismic attenuation in the crust. *Papers Presented at 10th Ann. DARPA/AFGL Seismic Res. Symp.*, 127-134.

Prange, M., and M.N. Toksöz (1988). *Analysis of Regional Phases Using Three-Component Data.*

Report AFGL-TR-88-0322, Air Force Geophysics Laboratory, Hanscom AFB, Massachusetts,
ADA205480.

Toksöz, M.N., B. Mandal, E.E. Charrette and E. Reiter (1988). Seismic attenuation in the crust.
EOS 69, 1319 (abs.).

Mandal, B., and M.N. Toksöz (1989). Synthetics seismograms and radiation patterns for an explosion
in anisotropic media. *Papers Presented at 11th Ann. DARPA/AFGL Seismic Res. Symp.*,
301-312.

Prange, M., and M.N. Toksöz (1989). Perturbation approximation of 3-D seismic scattering. *Submitted to Geophys. J.*

Ben-Menahem, A., and A.G. Sena (1989). Seismic source theory in inhomogeneous anisotropic
media. *Submitted to J. Geophys. Res.*

Mandal, B., and M.N. Toksöz (1989). Computation of complete waveforms in general anisotropic
media - results from an explosion source in anisotropic medium. *Submitted to Geophys. J.*

Toksöz, M.N., B. Mandal and A.M. Dainty (1989). Frequency-dependent attenuation in the crust.
In preparation for Geophys. Res. Lett.

PERTURBATION APPROXIMATION OF 3-D SEISMIC SCATTERING

M. Prange and M.N. Toksöz

Earth Resources Laboratory

Department of Earth, Atmospheric, and Planetary Sciences

Massachusetts Institute of Technology

ABSTRACT

A method is presented for computing three-dimensional seismic wave scattering from a rough interface. The matrix method used is appropriate for direct implementation in existing propagator matrix-based seismogram synthesis programs. It is derived using a perturbation approach which requires interface height perturbations to be small relative to the wavelengths of scattered waves, and interface slope perturbations to be much less than unity. These validity conditions are based on an order-of-error analysis of the truncation of the perturbation series. These conditions are numerically investigated by comparison of frequency-wavenumber domain and time domain perturbation results with those generated by a second-order finite difference method for several rough interface models with Gaussian auto-correlation functions. In the ω - k domain comparisons, the perturbation method is accurate for RMS interface height deviations of less than about 10 percent of the smallest wavelength in the scattered field. This result is independent of RMS interface slope in the tested range of 0.037 to 0.99. Comparisons of seismograms generated by the two methods show that error does increase with increasing RMS slope, but at half the rate of error growth with increasing height. Time domain error is acceptable for RMS height deviations of less than about 20 percent and RMS slopes of less than about 0.25. A three-dimensional scattering kernel is defined which facilitates analysis of two- and three-dimensional scattered field results.

INTRODUCTION

The presence of a rough interface can strongly affect seismic waves reflected from and transmitted through that interface, even when the scale of roughness is much less than a wavelength. These effects include changes in the amplitude, scattering angle, frequency content, and wave-type conversion of the scattered wave. Available exact solutions take the form of integral equations (DeSanto and Brown, 1986) or finite difference/finite element formulations (Levander and Hill, 1985) that are prohibitively expensive to solve in three dimensions. In this paper, we present a perturba-

tion approach to the solution of the three-dimensional elastic wave equation which satisfies welded boundary conditions at a rough interface. This solution is an extension of two-dimensional surface wave scattering formulations (Kennett, 1972; Gilbert and Knopoff, 1960). The method requires the height and slope of interface irregularities to be small with respect to the wavelengths of the elastic waves present. The accuracy of the perturbation method is then explored for two-dimensional models by comparing solutions for a series of rough interface models with those generated by a second-order finite difference method. The scattering results are first compared in the frequency-wavenumber domain in the form of scattering coefficients. The scattered wave fields computed with the perturbation and finite difference methods are separated into up- and down-going P and SV waves, and these scattering coefficients are individually compared. Comparisons are also made in the time-space domain by comparing seismograms. Finally, we discuss the features of the three-dimensional scattered field.

THREE-DIMENSIONAL SCATTERING FORMULATION

A fine-scale blow-up of a three-dimensional rough interface is shown in Figure 1. The irregular interface is described by $z = h(x, y)$, and has a downward normal $\underline{n}(x, y)$. It separates an upper medium, described by compressional and shear wave velocities α_1 and β_1 and density ρ_1 , from a lower medium, described by α_2 , β_2 , and ρ_2 . The essence of the formulation is to project displacements and stresses on the two sides of the rough interface onto a planar surface whose depth equals the mean depth of the rough interface. These projected fields are then expanded in a perturbation series in h about a background field consisting of the known planar interface solution. This procedure results in a formulation in which the rough interface scattering problem is replaced by a planar interface scattering problem with sources along the planar interface generating the rough interface component of the scattered field.

The general form of the elastic wave equation which is valid for small displacements in the absence of body forces is

$$-\rho\omega^2 u_i = \tau_{ji,j}, \quad i, j \in \{x, y, z\}, \quad (1)$$

where u_i is the i th component of the displacement vector, τ_{ji} is the i, j component of the Cauchy stress tensor, the comma denotes differentiation of τ_{ji} in the j -th coordinate direction, ω is the temporal frequency, and the Einstein summation convention applies. Throughout this paper, the Fourier transform in x , y , and t uses an implied phase factor of $\exp(ik_x x + ik_y y - i\omega t)$. For an

isotropic solid, stresses are related to displacements by the constitutive relation

$$\tau_{ij} = \lambda u_{k,k} \delta_{ij} + \mu(u_{i,j} + u_{j,i}), \quad (2)$$

where δ_{ij} is the Kronecker symbol, and λ and μ are the Lamé parameters. Equations (1) and (2) can be expressed as a 6×6 matrix wave equation in the form

$$\frac{d\underline{r}}{dz} = \underline{\underline{A}} \underline{r}, \quad (3)$$

where \underline{r} is the displacement-stress vector defined by $\underline{r} = [u_x, u_y, u_z, \tau_{xz}, \tau_{yz}, \tau_{zz}]^T$ and $\underline{\underline{A}}$ is defined by

$$\underline{\underline{A}} = \begin{bmatrix} 0 & 0 & -\partial_x & \frac{1}{\mu} & 0 & 0 \\ 0 & 0 & -\partial_y & 0 & \frac{1}{\mu} & 0 \\ \frac{-\lambda}{\lambda+2\mu} \partial_x & \frac{-\lambda}{\lambda+2\mu} \partial_y & 0 & 0 & 0 & \frac{1}{\lambda+2\mu} \\ -\rho\omega^2 & -\mu(1 + \frac{2\lambda}{\lambda+2\mu}) \partial_{xy} & 0 & 0 & 0 & \frac{-\lambda}{\lambda+2\mu} \partial_x \\ -\zeta \partial_{xx} - \mu \partial_{yy} & & & & & \\ -\mu(1 + \frac{2\lambda}{\lambda+2\mu}) \partial_{xy} & -\rho\omega^2 & 0 & 0 & 0 & \frac{-\lambda}{\lambda+2\mu} \partial_y \\ & -\mu \partial_{xx} - \zeta \partial_{yy} & & & & \\ 0 & 0 & -\rho\omega^2 & -\partial_x & -\partial_y & 0 \end{bmatrix} \quad (4)$$

with $\zeta = 4\mu(\lambda + \mu)/(\lambda + 2\mu)$.

Welded boundary conditions at the rough interface require continuity of displacement and traction at each point on the interface. These tractions are measured with respect to the local tangent plane at each point on the interface, and are given by $T_j = \sigma_{jk} n_k$, where the downward unit normal n_k is defined by

$$\begin{bmatrix} n_x \\ n_y \\ n_z \end{bmatrix} = \frac{1}{\sqrt{1 + h_{,x}^2 + h_{,y}^2}} \begin{bmatrix} -h_{,x} \\ -h_{,y} \\ 1 \end{bmatrix} \quad (5)$$

A new displacement-stress vector $\hat{\underline{r}}$ is defined using these tangent plane tractions so that $\hat{\underline{r}}$ is continuous at the rough interface. $\hat{\underline{r}}$ is defined as

$$\begin{bmatrix} u_x \\ u_y \\ u_z \\ T_x \sqrt{1 + h_{,x}^2 + h_{,y}^2} \\ T_y \sqrt{1 + h_{,x}^2 + h_{,y}^2} \\ T_z \sqrt{1 + h_{,x}^2 + h_{,y}^2} \end{bmatrix} = \begin{bmatrix} 1 & 0 & 0 & 0 & 0 & 0 \\ 0 & 1 & 0 & 0 & 0 & 0 \\ 0 & 0 & 1 & 0 & 0 & 0 \\ -h_{,x}\zeta\partial_x & ,x\frac{2\lambda\mu}{\lambda+2\mu}\partial_y & 0 & 1 & 0 & h_{,x}\frac{-\lambda}{\lambda+2\mu} \\ -h_{,y}\mu\partial_y & -h_{,y}\mu\partial_x & & & & \\ -h_{,x}\mu\partial_y & -h_{,x}\mu\partial_x & 0 & 0 & 1 & h_{,y}\frac{-\lambda}{\lambda+2\mu} \\ -h_{,y}\frac{2\lambda\mu}{\lambda+2\mu}\partial_x & -h_{,y}\zeta\partial_y & & & & \\ 0 & 0 & 0 & -h_{,x} & -h_{,y} & 1 \end{bmatrix} \begin{bmatrix} u_x \\ u_y \\ u_z \\ \tau_{xz} \\ \tau_{yz} \\ \tau_{zz} \end{bmatrix} \quad (6)$$

Writing (6) in a form which explicitly expresses the h dependence, this transformation takes the form

$$\hat{\underline{r}}(x, y; h) = (\underline{\underline{I}} + h_{,x}\underline{\underline{Q}}_x + h_{,y}\underline{\underline{Q}}_y)\underline{r}(x, y; h) \quad (7)$$

where $\hat{\underline{r}}$ and \underline{r} are evaluated along the rough interface, $\underline{\underline{I}}$ is the identity matrix, and $\underline{\underline{Q}}_x$ and $\underline{\underline{Q}}_y$ are

$$\underline{\underline{Q}}_x = \begin{bmatrix} 0 & 0 & 0 & 0 & 0 & 0 \\ 0 & 0 & 0 & 0 & 0 & 0 \\ 0 & 0 & 0 & 0 & 0 & 0 \\ -\zeta\partial_x & \frac{-2\lambda\mu}{\lambda+2\mu}\partial_y & 0 & 0 & 0 & \frac{-\lambda}{\lambda+2\mu} \\ -\mu\partial_y & -\mu\partial_x & 0 & 0 & 0 & 0 \\ 0 & 0 & 0 & -1 & 0 & 0 \end{bmatrix} \quad (8)$$

and

$$\underline{\underline{Q}}_y = \begin{bmatrix} 0 & 0 & 0 & 0 & 0 & 0 \\ 0 & 0 & 0 & 0 & 0 & 0 \\ 0 & 0 & 0 & 0 & 0 & 0 \\ -\mu\partial_y & -\mu\partial_x & 0 & 0 & 0 & 0 \\ -\frac{2\lambda\mu}{\lambda+2\mu}\partial_x & -\zeta\partial_y & 0 & 0 & 0 & \frac{-\lambda}{\lambda+2\mu} \\ 0 & 0 & 0 & 0 & -1 & 0 \end{bmatrix} \quad (9)$$

The rough interface boundary conditions may then be expressed in the form

$$\hat{\underline{r}}^{(1)}(x, y; h) = \hat{\underline{r}}^{(2)}(x, y; h) \quad (10)$$

where superscripts indicate the respective media.

In order to relate the scattered field (the rough interface solution) to the background field (the mean planar interface solution), the scattered field at the mean planar interface $\underline{r}(0)$ is extrapolated to the rough interface by the power series expansion

$$\underline{r}(h) = \underline{r}(0) + h\underline{r}_{,z}(0) + \frac{h^2}{2!}\underline{r}_{,zz}(0) + \dots \quad (11)$$

Making use of the wave equation (3), (11) is reduced to the form

$$\underline{r}(h) = (\underline{I} + h\underline{A} + \frac{h^2}{2!}\underline{A}^2 + \dots)\underline{r}(0). \quad (12)$$

So far the formulation is exact as long as the series in (12) converges. It is easy to demonstrate convergence for the case of a planar interface. In this case h is constant and (12) can be easily Fourier transformed to the (k_x, k_y) domain to form the power series expansion of the exponential function, converging to

$$\underline{r}(k_x, k_y; h) = e^{h\underline{A}}\underline{r}(k_x, k_y; 0). \quad (13)$$

This is the standard form for the propagator matrix (Aki and Richards, 1980, p. 275), which is an exact extrapolation operator which forms the basis of the propagator matrix method for formulating wave equation solutions in plane layered media (Kennett, 1983).

After the displacement-stress vectors along the rough interface have been extrapolated to the mean planar interface, they are expanded in a perturbation series about $\underline{r}_0(0)$, the displacement-stress vector at the interface of the background planar interface model:

$$\underline{r}^{(j)}(0) = \underline{r}_0(0) + h\underline{r}_1^{(j)}(0) + h^2\underline{r}_2^{(j)}(0) + \dots, \quad (14)$$

where superscripts indicate the respective media and subscripts indicate the approximation order of the field. Since $\underline{r}_0(0)$ is the displacement-stress vector for the background planar interface model, it is continuous across the planar interface and needs no superscript. The higher order terms reflect the influence of the rough interface. Combining (7), (12), and (14), each side of the boundary condition expressed in (10) can be written as (omitting the superscripts)

$$\hat{\underline{L}}(h) = (\underline{I} + h_{,x}\underline{\underline{Q}}_x + h_{,y}\underline{\underline{Q}}_y) \quad (15)$$

$$\begin{aligned} & \cdot (\underline{I} + h\underline{A} + \frac{h^2}{2!}\underline{A}^2 + \dots) \\ & \cdot (\underline{r}_0 + h\underline{r}_1 + h^2\underline{r}_2 + \dots) \end{aligned}$$

$$\begin{aligned} & \approx (\underline{I} + h_{,x}\underline{\underline{Q}}_x + h_{,y}\underline{\underline{Q}}_y)\underline{r}_0 + h\underline{A}\underline{r}_0 + h\underline{r}_1 \\ & + O(h^2) + O(hh_{,x}) + O(hh_{,y}) \end{aligned} \quad (16)$$

where $O(\cdot)$ denotes order of accuracy.

Applying the boundary condition (10) to (16) results in

$$\begin{aligned} h(\underline{r}_1^{(2)} - \underline{r}_1^{(1)}) & \approx h(\underline{\underline{A}}^{(1)} - \underline{\underline{A}}^{(2)})\underline{r}_0 + h_{,x}(\underline{\underline{Q}}_x^{(1)} - \underline{\underline{Q}}_x^{(2)})\underline{r}_0 \\ & + h_{,y}(\underline{\underline{Q}}_y^{(1)} - \underline{\underline{Q}}_y^{(2)})\underline{r}_0, \end{aligned} \quad (17)$$

which is accurate to second-order in h and its derivatives. The right-hand side of (17) is clearly zero in a planar interface model. The presence of interface roughness results in discontinuities in the displacement-stress vector. Such discontinuities represent sources(Aki and Richards, 1980, p. 38). Thus, to first order in h , the effects of a rough interface can be duplicated by adding sources along the mean planar interface. These sources will be designated by $\underline{s} = h(\underline{r}_1^{(2)} - \underline{r}_1^{(1)})$. This use of sources to represent material deviations from a background model is shared with standard Born theoretical developments(Wu and Aki, 1985). The mapping of heterogeneity into source terms is also used in exact formulations based on Huygen's principle(Paul and Campillo, 1988).

Fourier transforming (17) to the k_x, k_y domain,

$$\underline{s}(k_x, k_y) = \frac{1}{4\pi^2} \int_{-\infty}^{\infty} h(k_x - k'_x, k_y - k'_y) \underline{\underline{L}}(k_x, k_y; k'_x, k'_y) \underline{r}_0(k'_x, k'_y) dk'_x dk'_y, \quad (18)$$

where $\underline{\underline{L}}$ is defined by

$$\underline{\underline{L}} = \begin{bmatrix} 0 & 0 & 0 \\ 0 & 0 & 0 \\ ik'_x(\frac{\lambda_1}{\lambda_1+2\mu_1} - \frac{\lambda_2}{\lambda_2+2\mu_2}) & -ik'_y(\frac{\lambda_1}{\lambda_1+2\mu_1} - \frac{\lambda_2}{\lambda_2+2\mu_2}) & 0 \\ k_xk'_x(\zeta_1 - \zeta_2) & 2k_xk'_y(\frac{\lambda_1\mu_1}{\lambda_1+2\mu_1} - \frac{\lambda_2\mu_2}{\lambda_2+2\mu_2}) & 0 \\ +k_yk'_y(\mu_1 - \mu_2) & +k'_xk_y(\mu_1 - \mu_2) & \\ -\omega^2(\rho_1 - \rho_2) & k_xk'_x(\mu_1 - \mu_2) & \\ k_xk'_y(\mu_1 - \mu_2) & +k_yk'_y(\zeta_1 - \zeta_2) & 0 \\ +2k'_xk_y(\frac{\lambda_1\mu_1}{\lambda_1+2\mu_1} - \frac{\lambda_2\mu_2}{\lambda_2+2\mu_2}) & -\omega^2(\rho_1 - \rho_2) & \\ 0 & 0 & -\omega^2(\rho_1 - \rho_2) \\ \frac{1}{\mu_1} - \frac{1}{\mu_2} & 0 & 0 \\ 0 & \frac{1}{\mu_1} - \frac{1}{\mu_2} & 0 \\ 0 & 0 & \frac{1}{\lambda_1+2\mu_1} - \frac{1}{\lambda_2+2\mu_2} \\ 0 & 0 & -ik_x(\frac{\lambda_1}{\lambda_1+2\mu_1} - \frac{\lambda_2}{\lambda_2+2\mu_2}) \\ 0 & 0 & -ik_y(\frac{\lambda_1}{\lambda_1+2\mu_1} - \frac{\lambda_2}{\lambda_2+2\mu_2}) \\ 0 & 0 & 0 \end{bmatrix} \quad (19)$$

Definition of the Scattering Kernel

For plane wave sources it is possible to define a factorization of the scattered field into a product of the wavenumber spectrum of the interface and a function that is called the scattering kernel. The scattering kernel is independent of the interface roughness function, and contains the features of the scattered field related to the material contrast and the source frequency and illumination angle. For a plane wave source of the form

$$\underline{r}_0(k'_x, k'_y) = 4\pi^2 \underline{r}_p(k_x^p, k_y^p) \delta(k'_x - k_x^p, k'_y - k_y^p), \quad (20)$$

equation (18) reduces to

$$\underline{s}(k_x, k_y) = h(k_x - k_x^p, k_y - k_y^p) \underline{\underline{L}}(k_x, k_y; k_x^p, k_y^p) \underline{r}_p(k_x^p, k_y^p). \quad (21)$$

The scattered field source term in this case is separated into a part associated with a particular

interface roughness function, $h(k_x - k_x^p, k_y - k_y^p)$, and a part associated with the material contrast and the source frequency and illumination angle, $\underline{\underline{L}}(k_x, k_y; k_x^p, k_y^p) \underline{\underline{r}}_0(k_x^p, k_y^p)$. The latter part is designated as the scattering kernel.

Knowledge of the scattering kernel allows one to evaluate the scattering potential of a model independent of any particular interface. For example, the transmission scattering kernels for the two-dimensional model in Figure 2 are given in Figure 3. The source is a normally incident, planar P wave. The scattering kernels here have been resolved into down-going P and S wave scattering coefficients using a technique described in the next section. Superimposed on these plots is the Fourier transform of the interface. The scattered field is simply the product of the two curves. From these plots it is clear that an interface with a smaller correlation length, and hence a broader spectrum in the transform domain, would result in large amplitude cusps for large scattering angles in P and S. For the transmitted P wave, the scattered wave amplitude increases for scattering angles larger than the P reflection critical angle. An amplitude boost at large angles may also be seen in the P and S reflection coefficients as it will be shown later with examples. This effect has also been demonstrated by Levander and Hill (1985) using finite difference methods and by Paul and Campillo (1988) using boundary integral equation methods.

Describing Reflection and Transmission

The source term given by (18) generates P and S waves above and below the interface. To determine the displacement coefficients of these waves requires a relation between the displacement-stress vector and the up- and down-going P, SV, and SH wave components, the form of which is given by

$$\underline{\underline{r}} = \underline{\underline{F}} \underline{\underline{b}} . \quad (22)$$

where $\underline{\underline{b}} = [\grave{P} \grave{S} \grave{T} \acute{P} \acute{S} \acute{T}]^T$, the grave and acute symbols : and : denote down- and up-going waves, respectively, and P, S, and T are the displacement coefficients of P, SV, and SH waves, respectively. Using the reflection coefficient sign conventions of Aki and Richards (1980), $\underline{\underline{F}}$ is given by

$$\underline{\underline{F}} = \begin{bmatrix} \frac{k_x\alpha}{\omega} & \frac{k_x\nu\beta}{\omega K} & -\frac{k_y}{K} & \frac{k_x\alpha}{\omega} & \frac{k_x\nu\beta}{\omega K} & -\frac{k_y}{K} \\ \frac{k_y\alpha}{\omega} & \frac{k_y\nu\beta}{\omega K} & \frac{k_x}{K} & \frac{k_y\alpha}{\omega} & \frac{k_y\nu\beta}{\omega K} & \frac{k_x}{K} \\ \frac{\gamma\alpha}{\omega} & -\frac{K\beta}{\omega} & 0 & -\frac{\gamma\alpha}{\omega} & \frac{K\beta}{\omega} & 0 \\ \frac{2ik_x\gamma\alpha\mu}{\omega} & \frac{ik_x(\nu^2-K^2)\beta\mu}{\omega K} & -\frac{ik_y\nu\mu}{K} & -\frac{2ik_x\gamma\alpha\mu}{\omega} & -\frac{ik_x(\nu^2-K^2)\beta\mu}{\omega K} & \frac{ik_y\nu\mu}{K} \\ \frac{2ik_y\gamma\alpha\mu}{\omega} & \frac{ik_y(\nu^2-K^2)\beta\mu}{\omega K} & \frac{ik_x\nu\mu}{K} & -\frac{2ik_y\gamma\alpha\mu}{\omega} & -\frac{ik_y(\nu^2-K^2)\beta\mu}{\omega K} & -\frac{ik_x\nu\mu}{K} \\ \frac{i(\nu^2-K^2)\alpha\mu}{\omega} & -\frac{2iK\nu\beta\mu}{\omega} & 0 & \frac{i(\nu^2-K^2)\alpha\mu}{\omega} & -\frac{2iK\nu\beta\mu}{\omega} & 0 \end{bmatrix} \begin{bmatrix} e^{i\gamma z} & 0 & 0 & 0 & 0 \\ 0 & e^{i\nu z} & 0 & 0 & 0 \\ 0 & 0 & e^{i\nu z} & 0 & 0 \\ 0 & 0 & 0 & e^{-i\gamma z} & 0 \\ 0 & 0 & 0 & 0 & e^{-i\nu z} \\ 0 & 0 & 0 & 0 & 0 \end{bmatrix} \quad (23)$$

with $K = \sqrt{k_x^2 + k_y^2}$, $\alpha = \sqrt{(\lambda + 2\mu)/\rho}$, $\beta = \sqrt{\mu/\rho}$, $\gamma = \sqrt{\omega^2/\alpha^2 - K^2}$, and $\nu = \sqrt{\omega^2/\beta^2 - K^2}$. To recover scattered field displacements from the source term note that

$$\underline{s} = \underline{r}^{(2)} - \underline{r}^{(1)} = \underline{\underline{F}}^{(2)} \underline{b}^{(2)} - \underline{\underline{F}}^{(1)} \underline{b}^{(1)} \quad (24)$$

and that \underline{s} generates no down-going waves in the upper medium and no up-going waves in the lower medium. Hence,

$$\underline{s} = \begin{bmatrix} F_{11}^{(2)} & F_{12}^{(2)} & F_{13}^{(2)} & -F_{14}^{(1)} & -F_{15}^{(1)} & -F_{16}^{(1)} \\ F_{21}^{(2)} & F_{22}^{(2)} & F_{23}^{(2)} & -F_{24}^{(1)} & -F_{25}^{(1)} & -F_{26}^{(1)} \\ F_{31}^{(2)} & F_{32}^{(2)} & F_{33}^{(2)} & -F_{34}^{(1)} & -F_{35}^{(1)} & -F_{36}^{(1)} \\ F_{41}^{(2)} & F_{42}^{(2)} & F_{43}^{(2)} & -F_{44}^{(1)} & -F_{45}^{(1)} & -F_{46}^{(1)} \\ F_{51}^{(2)} & F_{52}^{(2)} & F_{53}^{(2)} & -F_{54}^{(1)} & -F_{55}^{(1)} & -F_{56}^{(1)} \\ F_{61}^{(2)} & F_{62}^{(2)} & F_{63}^{(2)} & -F_{64}^{(1)} & -F_{65}^{(1)} & -F_{66}^{(1)} \end{bmatrix} \begin{bmatrix} \dot{P}^{(2)} \\ \dot{S}^{(2)} \\ \dot{T}^{(2)} \\ \dot{P}^{(1)} \\ \dot{S}^{(1)} \\ \dot{T}^{(1)} \end{bmatrix} = \hat{\underline{\underline{F}}} \hat{\underline{b}} \quad (25)$$

The wave displacement coefficients generated by \underline{s} are given by

$$\hat{\underline{b}} = \hat{\underline{\underline{F}}}^{-1} \underline{s} \quad (26)$$

The inverse of \hat{F} exists for all values of (k_x, k_y) except $(k_x, k_y) = (0, 0)$. At this point in the \underline{k} plane the scattered waves are propagating normal to the mean planar surface, and SV waves are indistinguishable from SH waves. For example, consider an S plane wave traveling in the z direction with particle motion in the x direction. If the wave direction is slightly perturbed in the x direction it becomes an SV wave. A perturbation in the y direction makes it an SH wave. These distinctions are true even when the perturbations are infinitesimal. Hence, to remove the singularity of \hat{F} , an arbitrary naming convention must be adopted for vertically propagating S waves. In this paper, the x component of such waves is labeled SV, and the y component is labeled SH. The \hat{F} matrix for vertical propagation is

$$\hat{F}(0,0) = \begin{bmatrix} 0 & 1 & 0 & 0 & -1 & 0 \\ 0 & 0 & 1 & 0 & 0 & -1 \\ 1 & 0 & 0 & 1 & 0 & 0 \\ 0 & i\omega\rho_2\beta_2 & 0 & 0 & i\omega\rho_1\beta_1 & 0 \\ 0 & 0 & i\omega\rho_2\beta_2 & 0 & 0 & i\omega\rho_1\beta_1 \\ i\omega\rho_2\alpha_2 & 0 & 0 & -i\omega\rho_1\alpha_1 & 0 & 0 \end{bmatrix} \quad (27)$$

COMPARISON WITH FINITE DIFFERENCE

The simple form of the scattered field source term (18) was made possible by the truncation of (15) to yield the second-order perturbation approximation given in (16). The error resulting from the exclusion of higher order terms is difficult to evaluate analytically. It is possible, though, to determine bounds on the domain of validity of this approximation. Kennett (1972) derived two conditions on the model which must hold in order for (18) to be valid. The first condition constrains the scattered field to be much weaker than the background field, a requirement for the single scattering approximation to apply. This condition is expressed by the relation

$$\underline{s}(k_x, k_y) \ll \max_{k_x, k_y} |\underline{\tau}_0(k_x, k_y)|, \quad (28)$$

where \underline{s} is the scattered field source term defined by (18). Kennett (1972) reduced this to a simpler, but stricter, form by replacing the convolution integral in (18) by an upper-bound approximation, yielding

$$\frac{\kappa_0\omega L}{\pi\beta_1}\eta_{12} \max_x |h(x)| \ll 1, \quad \max_x |h_{,x}(x)| \ll 1, \quad (29)$$

where

$$\eta_{12} = \max \left\{ \left| \frac{\alpha_1 \rho_1 - \alpha_2 \rho_2}{\alpha_1 \rho_1 + \alpha_2 \rho_2} \right|, \left| \frac{\beta_1 \rho_1 - \beta_2 \rho_2}{\beta_1 \rho_1 + \beta_2 \rho_2} \right| \right\},$$

L is the periodicity length of the rough interface, and the wavenumber spectrum of the incident field is bounded by $|k| \leq \kappa_0$. The second condition is that the background field must not contain wavenumbers so close to grazing incidence that shadow zones form. Shadow zones will be avoided if the radius of curvature of the interface is much longer than a wavelength. Such waves will then propagate as guided waves along the interface. This condition is expressed by

$$\frac{1}{\sqrt{\kappa_0^2 + k_z^2}} \max_x |h_{,xx}| \ll 1, \quad (30)$$

where k_z is the vertical wavenumber component associated with the maximum horizontal component κ_0 .

These conditions are not satisfactory for practical use, however. Approximations used in the derivation of (29) result in a much stricter bound than is necessary, and the practical limit imposed by (30) needs to be better defined. In order to empirically construct more realistic constraints on interface roughness, reflection and transmission coefficients obtained using the perturbation method described above will be compared with those derived from two-dimensional finite difference solutions. By comparing results for a range of interface height and slope statistics, the domain of validity of the perturbation method can be explored.

The finite difference algorithm used here is a two-dimensional, second-order formulation. To summarize, the wave equations (1) and (2) are solved in the time-space domain by replacing the time and space derivatives by their second-order centered-difference approximations. The accuracy is improved by using a staggered mesh formulation in which horizontal and vertical displacements are represented on separate grids, each shifted by half of the grid point spacing in both coordinate directions with respect to the other. This has the added benefit of increasing the grid-point density by a factor of two. The formulation differs from that of Virieux (1986) in that we use the second-order displacement/stress wave equations instead of the first-order velocity/stress equations. This modification improves efficiency, since the final solution was desired in terms of displacement. The stability conditions and grid dispersion relations are identical with those of Virieux's formulation. A low-order, staggered-mesh scheme was chosen because it is the most efficient method when dense grid point spacings are necessary, as is the case in our models where small interface irregularities must be represented. Higher order schemes, such as those which use fourth-order (Bayliss, *et al.*, 1986) or Fourier spatial derivative operators (Kosloff *et al.*, 1984; Fornberg, 1988), are generally

thought to be more efficient than second-order schemes, but this is not necessarily true. The dense grid point spacing used in modeling small interface perturbations puts the second-order derivative operator well within its domain of acceptable accuracy, and the short operator length makes it the most efficient scheme.

The finite difference method is known to be accurate when the wave fields and the model are both well discretized. Hence, when models with large interface irregularities are compared, the finite difference method will be used as the standard. On the other hand, the perturbation method is accurate for models with small interface height and slope irregularities and will be used as the standard for such models. The comparison with finite difference solutions will proceed in two parts. First it is necessary to show that the range of interface irregularities over which the finite difference method is accurate extends into the range over which the perturbation method is accurate. This will be done by showing that the finite difference method results match the perturbation method results for a model with very small height and slope irregularities. If the finite difference method works well in this case, results for larger interface irregularities will also be valid because they will be more accurately represented on the finite difference grid. Finite difference solutions will then be used a basis for comparison with perturbation solutions for a series of models with larger height and slope irregularities in order to probe the limits of validity of the perturbation approximation.

Accuracy of the Finite Difference Method

All results for scattering from a rough interface in this paper are expressed as reflection and transmission coefficients. The procedure for deriving these coefficients from the finite difference solution is similar to the method used for deriving them for the perturbation solution. In short, equation (22) is used to convert \underline{r} into \underline{b} , and then P and S wave amplitudes in \underline{b} are scaled by the source wave amplitude. The displacements and stresses in \underline{r} are computed by the finite difference method in the time-space domain along a horizontal linear array of uniformly spaced receivers that do not intersect the interface at any point. The receiver array should be located between the source and the interface in order to allow incident waves to be separated from reflected waves based on whether they are traveling downward or upward. \underline{r} is then Fourier transformed into the ω - k domain to yield a form suitable for use in (22). The distance of the receiver array from the interface is accounted for by the z term in the definition of \underline{F} in equation (23). If the finite difference model is such that reflections from the top or bottom edges of the grid will arrive within the seismogram time window, absorbing boundaries must be implemented which attenuate those reflections to a level

much smaller than the reflection and transmission coefficients to be measured. Periodic boundary conditions were applied on the horizontal boundaries of the grid in order to duplicate the periodicity of the spatial Fourier transform, and the length of the array, L , was set to the horizontal dimension of the finite difference grid to take advantage of this periodicity. For a point source, L controls the range of incidence and scattering angles that are within the receiver array, and the horizontal grid size should be large enough to capture the incidence and scattering angles of interest. Since the range of incident and scattering angles detected is also dependent on the distance of the source and the receiver array from the interface, it is best to put the source and the receiver array as close to the interface as possible in order to minimize the grid size and the seismogram length. Receiver spacing controls the maximum representable wavenumber in \underline{z} , and was set equal to the grid point spacing to avoid aliasing.

The reflection and transmission coefficients obtained from finite difference modeling are compared with analytical coefficients (Cerveny *et al.*, 1977) for the case of a planar interface model. The model is shown in Figure 4. The source has an 18 Hz Ricker time function of the form

$$R(t) = (1 - \frac{1}{2}\omega_0^2 t^2)e^{-\frac{1}{4}\omega_0^2 t^2}, \quad (31)$$

where ω_0 is the primary angular frequency of the wavelet. The source is implemented as a body force representing a point explosion source smoothed by a Gaussian with standard deviation equal to the grid point spacing. This smoothing is necessary to make the infinite bandwidth explosion source dipoles representable on the finite bandwidth finite difference grid. This source isotropically radiates pure P waves. It is located 20 grid points above the interface, and the two arrays of receivers are located 10 grid points above and 10 grid points below the interface. Reflection and transmission coefficients derived from the finite difference seismograms for this model are shown in Figure 5 along with analytical coefficients. There is generally good agreement for both pre- and post-critical waves. The small disagreement present at the larger scattering angles results from the finite aperture of the receiver array.

The finite difference and perturbation methods will now be compared for a model with very small height and slope perturbations shown in Figure 2. The source is a downward propagating, planar P wave with an 18 Hz Ricker time function. The interface roughness has a Gaussian autocorrelation function with a correlation length of $L = 100$ m and an RMS height deviation of $\sigma = 16.7$ m. The interface is periodic with a period of 2.70 km, the width of the model. The finite difference sampling parameters, $\Delta x = 6.67$ m, $\Delta z = 2.22$ m, and $\Delta t = 0.00156$ s, result in a maximum phase dispersion

error of -1.1 percent at 18 Hz. The two receiver arrays are located as close to the interface as is possible without intersection. The Fourier transform of the interface function which has been discretized for the finite difference grid is shown in Figure 6a as a function of horizontal slowness evaluated at 18 Hz. The zero spectral power at the origin results from the zero mean interface deviation. Histograms of interface height and slope are shown in Figures 6b and 6c. The largest deviation from the mean planar surface is 12 m, or 15 percent of the S wavelength in the upper medium. The largest slope is 0.16, while the mean and standard deviation of the slope are zero and 0.059, respectively. Since the maximum interface height and slope are fairly well approximated by twice their standard deviations, histograms will not be provided for the remaining rough interfaces used in this study. A comparison of the reflection and transmission coefficients derived from the finite difference and perturbation methods is shown in Figure 7. Agreement is very good, with both amplitude and shape predicted well by the perturbation method. "Ringing" appears to some degree on all of the finite difference coefficient plots, and is most apparent on the S wave coefficient plots. Another check on the accuracy of the reflection and transmission coefficient results is to plot the coefficients for the non-physical waves in the solution: the down-going S in the upper medium and the up-going S and P in the lower medium. Plots of the non-physical coefficients for the finite difference data are shown in Figure 8. In general, the amplitude of the non-physical waves increases with increasing scattering angle, since the wavenumbers corresponding to these larger angles are less well represented by the receiver array. The down-going P wave in the upper medium has unit amplitude at zero angle. It is clear from this figure that the maximum error is less than 0.1 percent, and that this error is associated with the S wave in the upper medium. This error is enough to explain the difference between the finite difference and perturbation results for the reflected S wave coefficient at large scattering angles.

Accuracy of the Perturbation Method in the ω - k Domain

The domain of validity of the perturbation method will be explored by comparing reflection and transmission coefficients generated using the perturbation method with those derived from finite difference modeling. Six rough interface models are used in this comparison, each having a Gaussian autocorrelation function and a uniform random phase. The interface functions are shown in Figure 9(a-f) with two times vertical exaggeration. RMS interface slope ranges from 0.037 to 0.99 and RMS interface height is 0.01 km for models A-E and 0.015 Km for model F. Since the accuracy of the perturbation method is sensitive to the smallest elastic wavelength in the model, interface

height is measured here in terms of S wavelengths in the upper medium (S_1), and thus the relative height of the irregularities changes as the frequency changes. The bandwidth of the 18 Hz Ricker wavelet time function used in the finite difference calculation allowed reflection and transmission coefficients to be computed at three frequencies (9.93, 16.5, and 26.5 Hz) in each of the six models, for a total of 18 comparisons for each coefficient. In these comparisons, RMS interface height ranges from 0.069 to 0.28 S_1 wavelengths. RMS height, correlation length, and RMS slope for the models used are listed in Table 2. The material parameters are $\alpha_1 = 2.50 \text{ km/s}$, $\beta_1 = 1.44 \text{ km/s}$, $\rho_1 = 1.00 \text{ g/cm}^3$, $\alpha_2 = 3.00 \text{ km/s}$, $\beta_2 = 1.73 \text{ km/s}$, and $\rho_2 = 1.00 \text{ g/cm}^3$, the same as in Figure 2. The source is a normally incident planar P wave in layer one. Plots of these comparisons are shown for the selected models A, D, and E in Figures 10(a-c). The reflection and transmission coefficients are the displacement coefficients \dot{P}_1 , \dot{S}_1 , \dot{P}_2 , and \dot{S}_2 are normalized so that $\dot{P}_1 = 1$.

In order to facilitate the comparison of the perturbation and finite difference coefficients, the curves are compared by finding the L_2 norm difference defined by

$$\|\dot{P}_{pt} - \dot{P}_{fd}\|_2 = 100 \times \left[\frac{\int_0^{\frac{\pi}{2}} [\dot{P}_{pt}(\theta_s) - \dot{P}_{fd}(\theta_s)]^2 d\theta_s}{\int_0^{\frac{\pi}{2}} \dot{P}_{fd}(\theta_s)^2 d\theta_s} \right]^{\frac{1}{2}} \quad (32)$$

where θ_s is the scattering angle and the \dot{P} coefficient is chosen for illustration. The differences between method results are plotted for each of the four coefficients in Figures 11(a-d) for a constant RMS interface height of 0.01 km, and in Figures 11(e-h) for a constant RMS interface slope of 0.1. The constant height plots show that the accuracy of the perturbation solution is not significantly degraded as RMS interface slope varies within the range tested. This L_2 norm result is verified in the coefficient comparison plots in Figures 10(a-d). The constant slope plots show that error increases rapidly with increasing RMS interface height, and in this particular example is acceptable for values of RMS height less than about 0.1 S_1 wavelengths.

Accuracy of the Perturbation Method in the t - x Domain

Error in time domain seismograms generated using the perturbation approximation cannot be directly estimated from the error results presented for the ω - k domain. This is because each seismogram contains energy from a broad spectrum of frequencies and wavenumbers. Here the time domain error will be estimated by comparing reflection seismograms generated by the perturbation method with those generated from the finite difference method. To generate reflection seismograms using the perturbation method, the scattering coefficients evaluated using the two-dimensional form

of (26) are converted to displacement by using (22) with $k_y = 0$. These displacements are then Fourier transformed in ω and k to yield

$$\begin{bmatrix} u_x \\ u_z \end{bmatrix} = \frac{1}{4\pi^2} \int_{-\infty}^{\infty} e^{-i\omega t} d\omega \int_{-\infty}^{\infty} e^{ikx} dk \begin{bmatrix} F_{14} & F_{15} \\ F_{34} & F_{35} \end{bmatrix} \begin{bmatrix} \hat{P} \\ \hat{S} \end{bmatrix} \quad (33)$$

Fourier transforms are evaluated using the discrete wavenumber method (Bouchon, 1977). Seismograms generated with (33) contain only the scattered field. The background field can be added if desired.

Seismograms were generated for each of the interface functions parameterized in Table 3 using both the perturbation and finite difference methods, and a subset of these are shown overlain in Figure 12. The source and receiver configurations and the material parameters are the same as those used in the last section. The source time function is an 18 Hz Ricker wavelet. These seismograms show that the shapes of the waveforms generated by the perturbation and finite difference methods agree fairly well for the range of models considered. Errors in amplitude and traveltimes seem to be positively correlated, both being larger at receivers that are over extrema in the interface height function than at other receiver locations. This feature will be explored next using an L_2 norm error measure. Since the total waveform is composed of the background field added to the scattered field, total field perturbation method seismograms minus the source waves are presented for comparison in Figure 13 for models A-I.

The L_2 norm was calculated as a measure of error between the perturbation and finite difference seismograms, using

$$\begin{aligned} E(x, \Delta t) &= \|u_z(x)^{pt} - u_z(x)^{fd}\|_2(\Delta t) \\ &= 100 \times \left[\frac{\int_{-t_{min}}^{t_{max}} dt' [u_z^{pt}(x, t' + \Delta t) - u_z^{fd}(x, t')]^2}{\frac{1}{L} \int_0^L dx \int_{t_{min}}^{t_{max}} dt' u_z^{fd}(t')^2} \right]^{\frac{1}{2}} \end{aligned} \quad (34)$$

where L is the length of the receiver array and Δt is the time shift between the two seismograms. The numerator was efficiently evaluated using the fast Fourier transform since the seismograms are periodic in space. The denominator is the average power of the entire array of finite difference seismograms in order to minimize the effect of low amplitude seismograms on $E(\Delta t)$. If $E(\Delta t)$ is normalized instead to the current seismogram, globally small error can overwhelm such low amplitude seismograms to produce large values of $E(\Delta t)$.

$E(\Delta t)$ is used to provide two separate measures of error for each seismogram: travel time error, which is defined as the time delay $\widehat{\Delta t}$ at which E is minimum; and amplitude error, which is defined as $\hat{E} = E(\widehat{\Delta t})$. A plot of $\widehat{\Delta t}$ versus seismogram offset x for Model A is shown in Figure 14. Overlain on this plot is a plot of the one-way, vertical P wave travel time associated with the interface function ($\frac{h(x)}{\alpha_1}$). In the absence of travel time error, $\widehat{\Delta t}$ would be zero for all the seismograms. The agreement between these two curves indicates that travel time from the interface to the receiver in the perturbation method is referenced to the mean planar interface, and not to the perturbed interface.

The reason for the travelttime error can easily be seen for the case where the interface perturbation function $h(x)$ is a constant. In this case, the perturbation expansion given by (15) transforms to an exact form in the $\omega-k$ domain:

$$\hat{r}(\omega, k_x, k_y; h) = \underline{I}(\underline{I} + h\underline{A} + \frac{h^2}{2!}\underline{A}^2 + \dots)\underline{r}(\omega, k_x, k_y; 0) \quad (35)$$

$$= e^{h\underline{A}}\underline{r}(\omega, k_x, k_y; 0) \quad (36)$$

$$= \underline{F}e^{h\underline{\Lambda}}\underline{F}^{-1}\underline{r}(\omega, k_x, k_y; 0). \quad (37)$$

Equation (36) is simply the definition of a propagator matrix which transforms the solution for \underline{r} at depth zero to the solution at depth h . Equation (37) uses a diagonal factorization of \underline{A} of the form

$$\underline{A} = \underline{F}\underline{\Lambda}\underline{F}^{-1} \quad (38)$$

where \underline{F} is defined by (23) and is always invertible, and $\underline{\Lambda}$ is a diagonal matrix whose diagonal elements in the three-dimensional case are $\Lambda_{11} = -\Lambda_{44} = i\gamma$ and $\Lambda_{22} = \Lambda_{33} = -\Lambda_{55} = -\Lambda_{66} = i\nu$. The exact form of the source term (18) valid for constant h is then

$$\underline{s}(\omega, k_x, k_y) = (e^{h\underline{\Lambda}^{(1)}} - e^{h\underline{\Lambda}^{(2)}})\underline{r}(\omega, k_x, k_y; 0) \quad (39)$$

$$= (\underline{F}^{(1)}e^{h\underline{\Lambda}^{(1)}}\underline{F}^{(1)-1} - \underline{F}^{(2)}e^{h\underline{\Lambda}^{(2)}}\underline{F}^{(2)-1})\underline{r}(\omega, k_x, k_y; 0) \quad (40)$$

$$\approx (\underline{F}^{(1)}(h\underline{\Lambda}^{(1)})\underline{F}^{(1)-1} - \underline{F}^{(2)}(h\underline{\Lambda}^{(2)})\underline{F}^{(2)-1})\underline{r}(\omega, k_x, k_y; 0) \\ + O(h^2). \quad (41)$$

The phase factors of the form $e^{h\underline{\Lambda}}$ in (40) are responsible for adjusting the travel time to account for the height of the interface. The accuracy of the first order approximation $e^{h\underline{\Lambda}} - \underline{I} \approx h\underline{\Lambda}$ in (41)

controls the accuracy of the travel time adjustment and influences the accuracy of the scattered field amplitude. The accuracy of the first and second order approximations to $e^{ih\Delta} - \underline{I}$ is illustrated in Figure 15. This figure shows that at least a second order approximation is required for accurate representation of phase, and therefore of traveltime, although both approximations converge to the exact solution as $h \rightarrow 0$. However, the modulus of the first order approximation is more accurate than that of the second order approximation, but this is a consequence of the non-monotonic improvement of accuracy as approximation order increases.

RMS amplitude error \hat{E} in the comparison of perturbation- and finite difference-derived seismograms is shown in Figure 16. RMS errors of the seismograms of each model were averaged, and these mean errors are plotted against RMS height for RMS slopes of 0.037 and 0.10, and against slope f_r - an RMS height of 0.125 S_1 wavelengths. Contrary to the results obtained in the ω - k domain, RMS amplitude error clearly increases with increasing RMS interface slope, as well as with increasing RMS interface height. Comparison of the rates of error growth for the fixed slope and fixed height error plots shows that error increases with increasing height nearly twice as fast as it does with increasing slope.

When the time shift error is removed, amplitude error is sensitive to two factors: the amplitude scale factor and the waveform character. Waveform character refers to the general shape of the waveform including the presence and length of the coda. It is fairly well approximated in all of the nine models considered here. With the exception of small amplitude arrivals, the shapes of the first arrivals generally agree well with the finite difference results, even for models with RMS slopes as high as one, and the complexity and decay rate of the coda are also well approximated. The amplitude scale factor, however, is generally overestimated by the perturbation method. This is true to the nature of the Born approximation, which violates conservation of energy by introducing the rough interface effects via a source term whose energy is added to the energy of the background field. With these points in mind, the range of validity spans the entire range of the models tested if the error criterion is based on waveform character. On the other hand, if the error criterion is based on amplitude scale or the absolute RMS error the range is limited to RMS slopes of less than about 0.3 and RMS heights of less than about 0.25 of the smallest wavelength present in the scattered field. Notice that the latter criterion results in a less restrictive range than the RMS error analysis on scattering coefficients done in the ω - k domain.

FEATURES OF THE 3-D SCATTERED FIELD

Three-dimensional scattering examples will now be presented for the model shown in Figure 17. The material and interface parameters are identical to those of model D (see Table 2 and Figure 9) with the Gaussian auto-correlation function having identical correlation lengths in the x and y directions. In general, a Gaussian rough interface whose major and minor axes coincide with the x and y axes has a Gaussian auto-correlation function of the form

$$h(k_x, k_y)h^*(k_x, k_y) \sim e^{-\frac{(k_x L_x)^2 + (k_y L_y)^2}{4}}. \quad (42)$$

where L_x and L_y are the major- and minor-axis correlation lengths. Equation (42) can be generalized to allow roughness trends at an angle θ to the x axis by applying a rotation transformation to get

$$h(k_x, k_y)h^*(k_x, k_y) \sim e^{-\frac{1}{4}[L_x^2(k_x \cos(\theta) + k_y \sin(\theta))^2 + L_y^2(-k_x \sin(\theta) + k_y \cos(\theta))^2]}. \quad (43)$$

In the first example, the source is an 18 Hz planar SV wave propagating downward along the z axis with particle motion in the x direction. The SV wave scatters into reflected and transmitted P, SV, and SH waves. The three-dimensional P, SV, and SH transmission coefficients for this model, found using the perturbation method, are given in Figure 18. The x and y scattering angles in these figures, referred to as ϕ_x and ϕ_y , are measured from the downward z axis in the x - z and y - z planes, respectively. They are defined by $\phi_x = \sin^{-1}(k_x v/\omega)$ and $\phi_y = \sin^{-1}(k_y v/\omega)$ where v is the body wave velocity of the transmitted wave concerned. Scattering in the z -direction, for example, is given by $\phi_x = \phi_y = 0$. The transmission coefficient plots cover scattering angles in the range $-90^\circ \leq \phi_x \leq 90^\circ$ and $0^\circ \leq \phi_y \leq 90^\circ$, and are symmetric about the $\phi_y = 0$ axis. For all three scattered wavetypes, these plots show that scattering is maximal in the direction that conserves source particle motion: for an SV source with particle motion in the x - z plane, P and SV are maximally scattered in the x - z plane, and SH is maximally scattered in the y - z plane. This effect is exaggerated by the use of the single scattering approximation. A null is present in the plane normal to maximal plane: the y - z plane for P and SV waves and the x - z plane for SH waves. An alternative display of the three-dimensional transmission coefficients is a cross-section of the coefficients for all scattering angles at a particular azimuth, where azimuth is measured clockwise in the x - y plane from the positive x -axis, and the scattering angle is defined by $\psi = \sin^{-1}(k_z v/\omega)$. Cross-sections of the reflection and transmission coefficients for the same model and source parameters are given for azimuthal angles of 10° , 45° , and 80° in Figure 19.

Transmission scattering kernels for the model in Figure 17 are given in Figure 20. Comparison with the SV and SH transmission coefficients in Figure 18 shows that the spatially band-limited nature of this particular interface damps out the large amplitude features present at large scattering angles. The P transmission coefficient exhibits a hint of the cusps present in the kernel. Consideration of another interface roughness function requires only a visual superposition of the new interface spectrum with the kernel. For the same SV source as above and a two-dimensional rough interface with variation in the x direction, the problem is truly two-dimensional, and waves are scattered into P and SV. If the interface is rotated 90 degrees so that variation is in the y direction, the problem is fully three-dimensional, and waves are scattered into P and SH. More general interfaces whose auto-correlation functions are described by (43), or perhaps a von Karman or exponential function, are handled with the same approach.

The second example is the same as the first, but with the SV source replaced by a P source. The three-dimensional P and SV transmission coefficients for this model are given in Figure 21. Since the source particle motion and the Gaussian auto-correlation function are azimuthally invariant, the scattering coefficients are also azimuthally invariant. Deviations of the contours from circular arcs are artifacts of the contouring program. Reflection and transmission coefficient cross-sections for this model are given in Figure 22. Note that scattered SH waves are not generated in this example. This is a consequence of the single-scattering approximation. For a normal incidence planar P wave, a minimum of two bounces are required to generate SH.

DISCUSSION AND CONCLUSIONS

A perturbation method has been presented here for computing three-dimensional body wave scattering from a rough interface. Its speed and simplicity are such that each of the examples in this paper was generated on a Macintosh SE computer in less than two minutes. Speed is an important consideration when three-dimensional modeling is necessary. For example, many of the two-dimensional finite difference computations done for comparison required 15 Mbytes of core and 23 hours of CPU time on a Vax 8800. In three dimensions, finite difference solutions for these models are beyond our resources at present. For the class of irregular interface models with small RMS height deviations, the perturbation method is a useful alternative.

Since interface height deviations in the models presented here are small, comparisons of the perturbation method with the finite difference method were preceded by careful testing of the finite difference method to show that it is valid for the small deviations used in these comparisons. It can

be shown that in the limit as the finite difference grid sampling interval goes to zero, and as the numerical precision of the computer goes to infinity, the finite difference solution converges to the exact solution as $O(\Delta x)$ (Brown, 1984). However, in order for the grid sampling interval to be small enough that the finite difference solution is sufficiently close to the exact solution, the number of grid points describing a fixed model must increase as the size of the interface height perturbations decreases. Therefore, the core size and speed of a computer are constraints in the minimum interface height perturbation that can be accurately modeled using finite difference method. Of course, a planar boundary is an exception to this limit. Another lower limit on interface perturbation size is imposed by numerical precision. As the size of interface height perturbations decreases, the amplitude of scattered seismic waves decreases. Since these scattered waves are added to the relatively large planar interface response, insignificant numerical noise in the planar interface response can be significant when compared with the scattered field. This is probably the cause of the "ringing" present in the finite difference-derived scattering coefficients. Comparisons of finite difference-derived scattering coefficients for a planar model against an analytical solution, and for a model with small interface height and slope perturbations against a perturbation method solution, show that this "ringing" tends to oscillate about the exact solution. Hence, the smoothed finite difference scattering coefficients are useful for comparisons.

Numerous two-dimensional model comparisons of finite difference and perturbation method scattering coefficients were made in order to determine the range of validity of the perturbation method. The L_2 norms of the differences were computed for varying RMS slope and constant RMS height, and for varying RMS height and constant RMS slope. There are two major trends in the L_2 norm results. Firstly, error increases strongly with increasing RMS height, with acceptable levels for RMS heights of less than about 0.1 shear wavelengths. Secondly, error appears to be roughly constant for increasing RMS slope for the tested range of from 0.037 to 0.99. Smaller trends, such as the apparent increase in accuracy with increasing RMS slope, are misleading. The L_2 norm is overly sensitive to the noise in the finite difference solution being used as the standard for comparison. This is apparent when the scattering coefficient plots are examined for the trend seen in the L_2 norm plots. The L_1 norm was also calculated to see whether it is less sensitive to this noise, but the improvements were minimal. Ultimately, all trends must be confirmed by the scattering coefficient plots.

Time domain seismograms generated by the perturbation method were compared with finite difference seismograms for the same models. The perturbation method was able to accurately predict waveform character for the entire range of models considered, including the shape of the

first arrival and the presence, duration, and complexity of the coda. Using RMS error analysis to determine traveltime error, it was shown that when first order perturbation theory is used, the travel time from the interface to the receiver is referenced to the mean planar interface, and not from the perturbed interface. Hence, traveltime error increases linearly with the height of the interface. It was shown that a second order theory is required for travel time to include the height of the perturbation. With this travel time error removed, the mean RMS error was determined for the perturbation seismograms in each of the models. If this mean RMS error is the criterion for determining the domain of validity of the perturbation method, it is valid for RMS slopes of less than about 0.25 and RMS heights of less than about 20 percent of the smallest wavelength in the scattered field.

Three-dimensional scattering kernels generated for an SV plane wave normally incident on a rough interface shows that waves are maximally scattered in directions for which the scattered wave particle motion coincides with that of the incident wave. A P wave in the same geometry induces azimuthally isotropic radiation. In the three-dimensional scattering example it was shown that there is a null in P and SV scattering in the y direction, and a null in SH scattering in the x direction. These nulls do not exist in the time-space domain, where a receiver in any location can detect waves traveling in all directions. These scattering kernels also show that scattered wave amplitudes tend to increase for scattering angles beyond the P wave critical angle (defined with respect to the planar interface model). This confirms the result of Paul and Campillo, 1988.

Acknowledgments

This work was supported by the Reservoir Delineation Consortium at the MIT Earth Resources Laboratory and by the Defense Advanced Research Projects Agency through contract F19628-87-K-0054 administered by the Air Force Geophysical Laboratory (AFGL). In addition, one of the authors gratefully acknowledges two years of fellowship support by the Amoco Foundation.

References

Aki, K., P.G.Richards, 1980, *Quantitative Seismology: Theory and Methods*, W. H. Freeman and Company, San Francisco, vols. 1 and 2, 932 pp.

Bayliss, A., K. Jordan, J. LeMesurier, and E. Turkel, 1986, A fourth-order accurate finite-difference scheme for the computation of elastic waves, *Bull. Seism. Soc. Am.*, 76, 1115-1132.

Bouchon, M., 1977, Discrete wavenumber representation of seismic-source wave fields, *Bull. Seism. Soc. Am.*, **67**, 259–277.

Brown, D.L., 1984, A note on the numerical solution of the wave equation with piecewise smooth coefficients, *Math. Comp.*, **42**, 369–391.

Cerveny, V., I.A. Molokov, and I. Psencik, 1977, *Ray Method in Seismology*, Univerzita Karlova, Praha.

DeSanto, J.A., and G.S. Brown, 1986, Analytical techniques for multiple scattering from rough surfaces, in *Progress in Optics, XXIII*, E. Wolf (ed.), Elsevier Science Publishers B.V.

Fornberg, B., 1988, The pseudospectral method: Accurate representation of interfaces in elastic wave calculations, *Geophysics*, **53**, 625–637.

Gilbert, F., and L. Knopoff, 1960, Seismic scattering from topographic irregularities, *J. Geophys. Res.*, **65**, 3437–3444.

Kennett, B.L.N., 1972, Seismic wave scattering by obstacles on interfaces, *Geophys. J. R. astr. Soc.*, **28**, 249–266.

Kennett, B.L.N., 1983, *Seismic Wave Propagation in Stratified Media*, Cambridge University Press, New York, 339.

Kosloff, D., M. Reshef, and D. Loewenthal, 1984, Elastic wave calculations by the Fourier method, *Bull. Seism. Soc. Am.*, **74**, 875–891.

Levander, A.R., and N.R. Hill, 1985, P-SV resonances in irregular low-velocity surface layers, *Bull. Seism. Soc. Am.*, **75**, 847–864.

Paul, A., and M. Campillo, 1988, Diffraction and conversion of elastic waves at a corrugated interface, *Geophysics*, **53**, 1415–1424.

Virieux, J., 1986, P-SV wave propagation in heterogeneous media: velocity-stress finite-difference method, *Geophysics*, **51**, 889–901.

Wu, R., and K. Aki, 1985, Scattering characteristics of elastic waves by an elastic heterogeneity, *Geophysics*, **50**, 582–595.

Symbol	Definition	Equation Introduced
ρ_j	Density in layer j	(1)
ω	Angular frequency	(1)
u_j	j th component of displacement	(1)
$\underline{\underline{\tau}}$	Cauchy stress tensor	(1)
λ_j, μ_j	Lamé parameters for layer j	(2)
\underline{r}	Displacement-stress vector	(3)
$\underline{\underline{A}}^{(j)}$	Wave equation coefficient matrix for layer j	(3)
∂_j	Partial derivative w.r.t. j th component	(4)
ζ_j	Simplification variable for layer j	(4)
$\underline{n}(x, y)$	Unit normal to interface	(5)
$h(x, y)$	Zero mean interface height function	(5)
T_j	j th component of traction	(6)
$\underline{\underline{Q}}_x^{(j)}, \underline{\underline{Q}}_y^{(j)}$	Rotation matrices for layer j	(7)
$\hat{r}^{(j)}$	Rotated displacement-stress vector in layer j	(7)
$\underline{r}_k^{(j)}$	k th order scattered field for layer j	(14)
\underline{r}_0	Displacement-stress vector for mean planar interface	(14)
\underline{s}	Scattered field source term	(18)
$\underline{\underline{L}}$	Kernel matrix for scattered field source term	(18)
k_x, k_y	x and y components of wavenumber	(18)
\underline{b}	Wave coefficient vector	(22)
$\underline{\underline{F}}$	Layer matrix	(22)
K	Magnitude of horizontal wavenumber	(23)
α_j, β_j	Compressional and shear wave speeds in layer j	(23)
γ_j	Vertical component of wavenumber for a compressional wave	(23)
ν_j	Vertical component of wavenumber for a shear wave	(23)
$\hat{\underline{b}}$	Scattering coefficient vector	(25)
$\hat{\underline{\underline{F}}}$	Scattering coefficient transformation matrix	(25)
κ_0	Maximum bound on source horizontal wavenumber	(29)
θ_s	Scattering angle	(32)
$\underline{\underline{\Lambda}}$	Diagonal eigenvalue matrix for $\underline{\underline{A}}$	(38)

Table 1: Table of symbols used in this paper.

Model	Correlation Length (km)	RMS Slope	RMS Height (km)	RMS Height in S ₁ Wavelengths at 9.93 Hz	RMS Height in S ₁ Wavelengths at 16.5 Hz	RMS Height in S ₁ Wavelengths at 26.5 Hz
A	0.010	0.30	0.037	0.069	0.11	0.18
B	0.010	0.10	0.10	0.069	0.11	0.18
C	0.010	0.050	0.20	0.069	0.11	0.18
D	0.010	0.033	0.30	0.069	0.11	0.18
E	0.010	0.010	0.99	0.069	0.11	0.18
F	0.015	0.15	0.10	0.10	0.17	0.28

Table 2: Interface parameters for the rough interfaces used in the ω - k domain comparisons. The interface height functions shown plotted in Figure 9.

Model	Correlation Length (km)	RMS Slope	RMS Height (km)	RMS Height in S ₁ Wavelengths at 18 Hz
A	0.30	0.037	0.010	0.125
B	0.10	0.10	0.010	0.125
C	0.050	0.20	0.010	0.125
D	0.033	0.30	0.010	0.125
E	0.010	0.99	0.010	0.125
F	0.15	0.10	0.015	0.188
G	0.45	0.038	0.015	0.188
H	0.60	0.039	0.020	0.25
I	0.20	0.10	0.020	0.25

Table 3: Interface parameters for the rough interfaces used in the t - x domain comparisons.

FIGURE CAPTIONS

Figure 1: Geometry of the rough interface model. The interface is defined by $z = h(x, y)$, and the downward-pointing unit normal to this surface at each point is denoted by $\underline{n}(x, y)$. The $z = 0$ plane is defined as the mean planar surface through the rough interface. $\alpha_1, \beta_1, \rho_1, \alpha_2, \beta_2$, and ρ_2 denote the compressional and shear wave speeds and density for the materials above and below the interface, respectively.

Figure 2: Two-dimensional rough interface model. The source is a normally incident, 18 Hz, plane wave. The rough interface has a Gaussian autocorrelation function with a correlation length of $L = 100$ m and an RMS height deviation of $\sigma = 16.7$ m. The interface is periodic with a period of 2.70 km, the width of the model above.

Figure 3: P and S wave transmission scattering kernels for a normally incident P wave for the model in Figure 2. The Fourier transform of the interface, mapped into scattering angle, is shown superimposed.

Figure 4: Planar interface model used to compare finite difference derived reflection and transmission coefficients with analytical solutions. The source is a point explosion with an 18 Hz Ricker wavelet time function. The sampling parameters, $\Delta x = \Delta z = 6.67$ m and $\Delta t = 0.00156$ s, result in a maximum phase dispersion error of -1.1 percent at 18 Hz. The source is located 20 grid points above the interface, and the receiver arrays are located 10 grid points on either side of the interface. The horizontal receiver interval is two grid points. All waves within the seismogram time window are contained within the finite difference grid, eliminating the need for absorbing boundaries.

Figure 5: Comparison between P and S wave reflection and transmission coefficients generated by finite difference and analytic methods for a planar interface. The model is shown in Figure 4. The small disagreement present at the larger scattering angles is "Gibb's ringing" that results from the finite aperture of the receiver array.

Figure 6: Properties of the interface shown in Figure 2: (a) Fourier transform, where the horizontal slowness is evaluated for 18 Hz, and histograms of (b) interface height and (c) interface slope.

Figure 7: Comparison between P and S wave reflection and transmission coefficients generated from the finite difference and perturbation methods for the model shown in Figure 2.

Figure 8: Amplitudes of waves incident on the interface corresponding to the scattered wave amplitudes shown in Figure 7. These are provided as a measure of the error versus angle. The

down-going P wave in the upper medium has unit amplitude at zero angle.

Figure 9: Interface functions used in comparison of reflection and transmission coefficients derived from the perturbation method with those derived from the finite difference method. The interfaces have a Gaussian autocorrelation function with RMS height, correlation length, and RMS slope for each interface listed in Table 2. The functions are displayed with two times vertical exaggeration.

Figure 10a: Comparison of reflection and transmission coefficients derived from the perturbation and finite difference methods for model A. The parameters of the rough interface are given in Table 2 and the interface function is illustrated in Figure 9.

Figure 10b: Comparison of reflection and transmission coefficients derived from the perturbation and finite difference methods for model D. The parameters of the rough interface are given in Table 2 and the interface function is illustrated in Figure 9.

Figure 10c: Comparison of reflection and transmission coefficients derived from the perturbation and finite difference methods for model E. The parameters of the rough interface are given in Table 2 and the interface function is illustrated in Figure 9.

Figure 11: L₂ norm comparison of finite difference and perturbation method derived reflection and transmission coefficients. (a-d) RMS interface height is a constant 0.01 km and RMS slope varies from 0.037 to 0.99. RMS interface height for three frequencies can be expressed as 0.069, 0.11, and 0.18 S₁ wavelengths. (e-h) RMS interface slope is a constant 0.1 and with RMS interface height varies from 0.069 to 0.28 S₁ wavelengths.

Figure 12: Representative scattered field seismograms generated for each of the interface functions parameterized in Table 3. The source is a normally incident plane wave with an 18 Hz Ricker time function. The bold curves are finite difference solutions, and the lighter curves are perturbation solutions. The four vertical component receivers are 0.0666 km above the mean planar interface at horizontal offsets of 0.0133, 1.35, 2.68, and 4.02 km. All seismograms are plotted at the same scale.

Figure 13: The seismograms of Figure 12 that were generated by the perturbation method are shown here with the background reflected field included in order to show the total waveform (minus the source wave). Plotted at the same scale as Figure 12.

Figure 14: Travel time error $\widehat{\Delta t}$ plotted against seismogram offset x for Model A. Shown overlain is a plot of the one-way, vertical P wave travel time associated with the interface function ($\frac{h(x)}{\alpha_1}$).

Figure 15: Comparison of first and second order approximations of $e^{ih\gamma} - 1$, which is the form of the term responsible for phase and amplitude shifts due to interface height. The first order

approximation is $e^{ih\gamma} - 1 \approx ih\gamma$, and the second order approximation is $e^{ih\gamma} - 1 \approx ih\gamma - \frac{1}{2!}(h\gamma)^2$.

(a) Modulus of the approximation. (b) Phase of the approximation in radians.

Figure 16: RMS amplitude error in the comparison of perturbation and finite difference derived seismograms. RMS amplitude error is measured after each perturbation method seismogram has been shifted in time relative to the complementary finite difference seismogram such that the RMS amplitude error is minimized. The error for each model is the average of the RMS errors of the seismograms in the model. This mean error is plotted against RMS height for two values of RMS slope, and against slope for a fixed RMS height. Interface height is in units of S_1 wavelengths. The data points are labeled with their model names.

Figure 17: Three-dimensional rough interface scattering model. The auto-correlation function of the interface is a two-dimensional Gaussian with x and y correlation lengths of 2.4 S_1 wavelengths (0.19 km), an RMS height of 0.125 S_1 wavelengths (0.010 km), and an RMS slope of 0.30. Contours and axes are labeled in kilometers.

Figure 18: Transmission coefficients for the model in Figure 17. The source is an 18 Hz SV plane wave at normal incidence with particle motion in the x -direction.

Figure 19: Cross-sections of the reflection and transmission coefficients in Figure 18 along 10°, 45°, and 80°azimuths. PU, SU, and TU and PD, SD, and TD are the up- and down-going P, SV, and SH scattering coefficients.

Figure 20: Transmission scattering kernels for the model in Figure 17.

Figure 21: Transmission coefficients for the model in Figure 17. The source is an 18 Hz P plane wave at normal incidence.

Figure 22: Cross-sections of the reflection and transmission coefficients in Figure 21 along 10°, 45°, and 80°azimuths. PU, SU, and TU and PD, SD, and TD are the up- and down-going P, SV, and SH scattering coefficients.

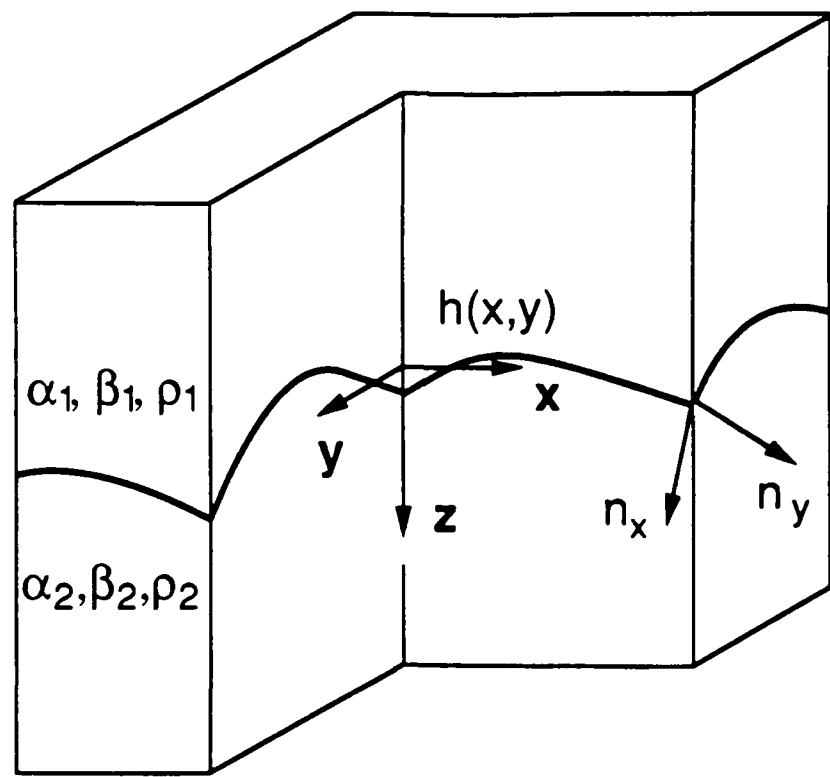


Figure 1.

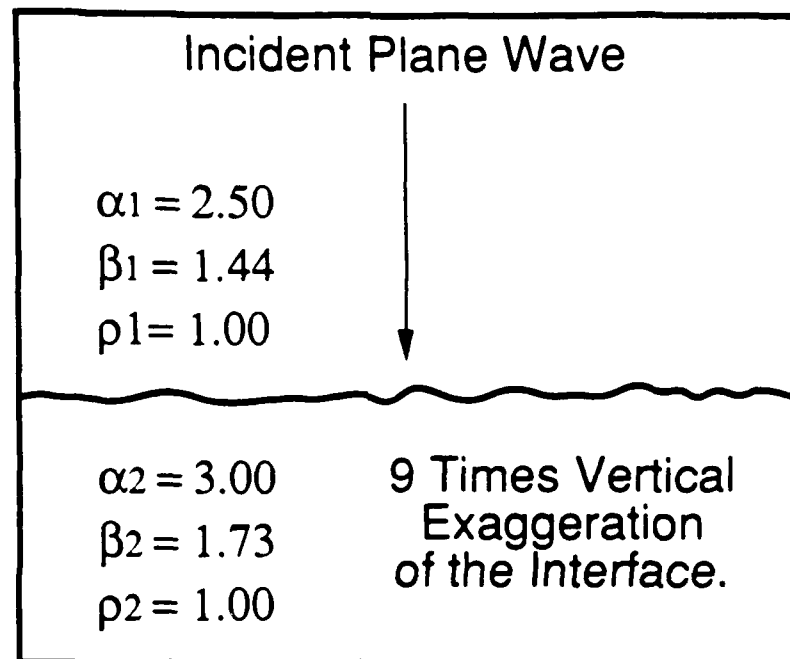


Figure 2.

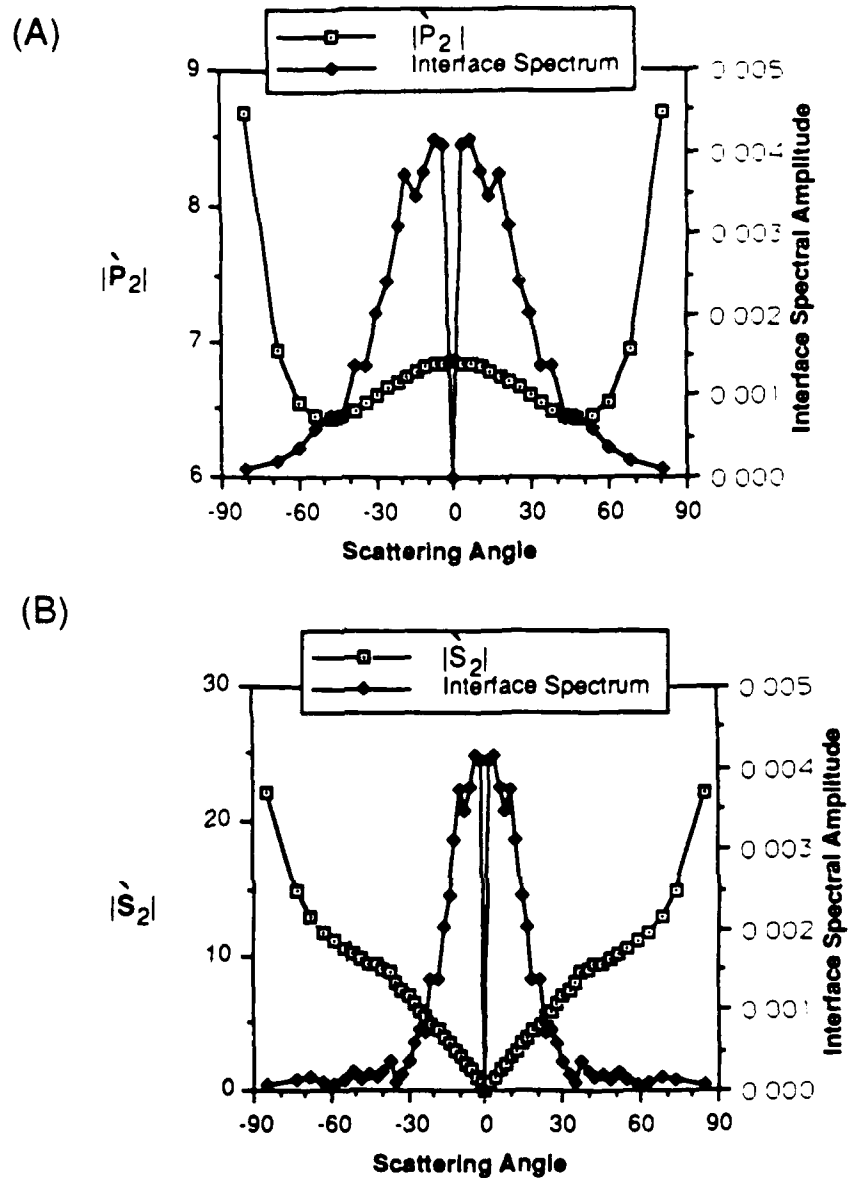


Figure 3.

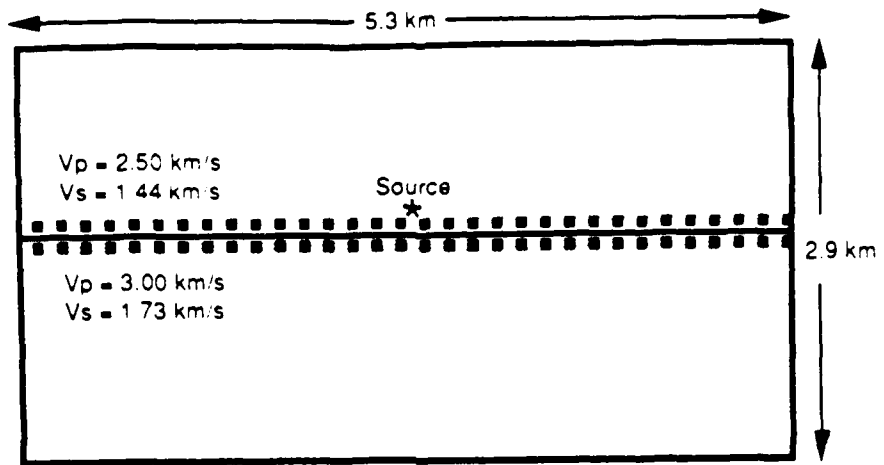


Figure 4.

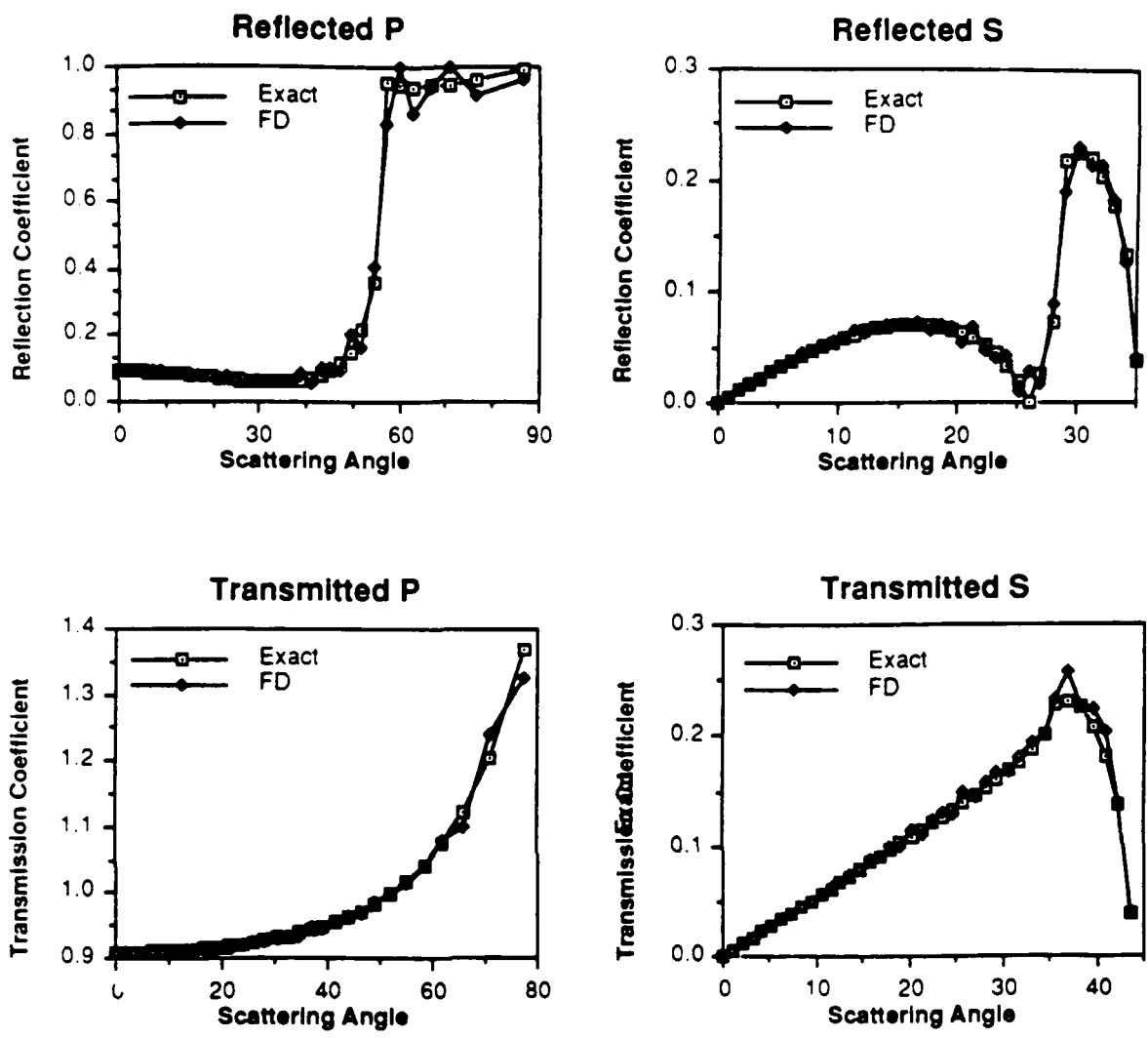


Figure 5.

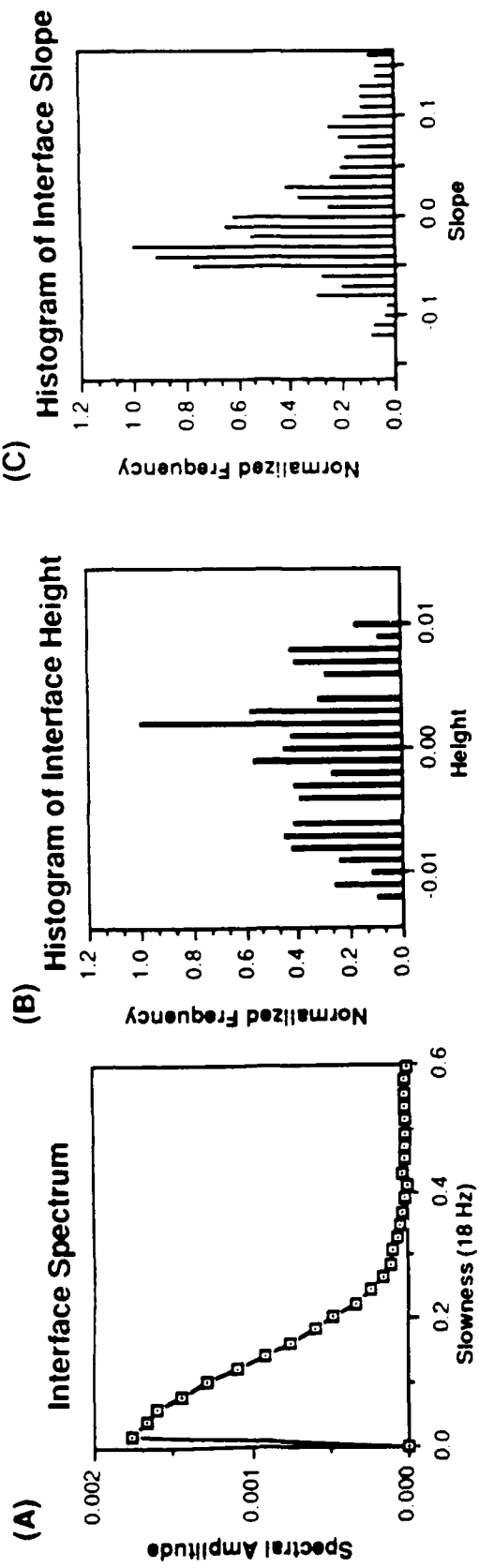


Figure 6.

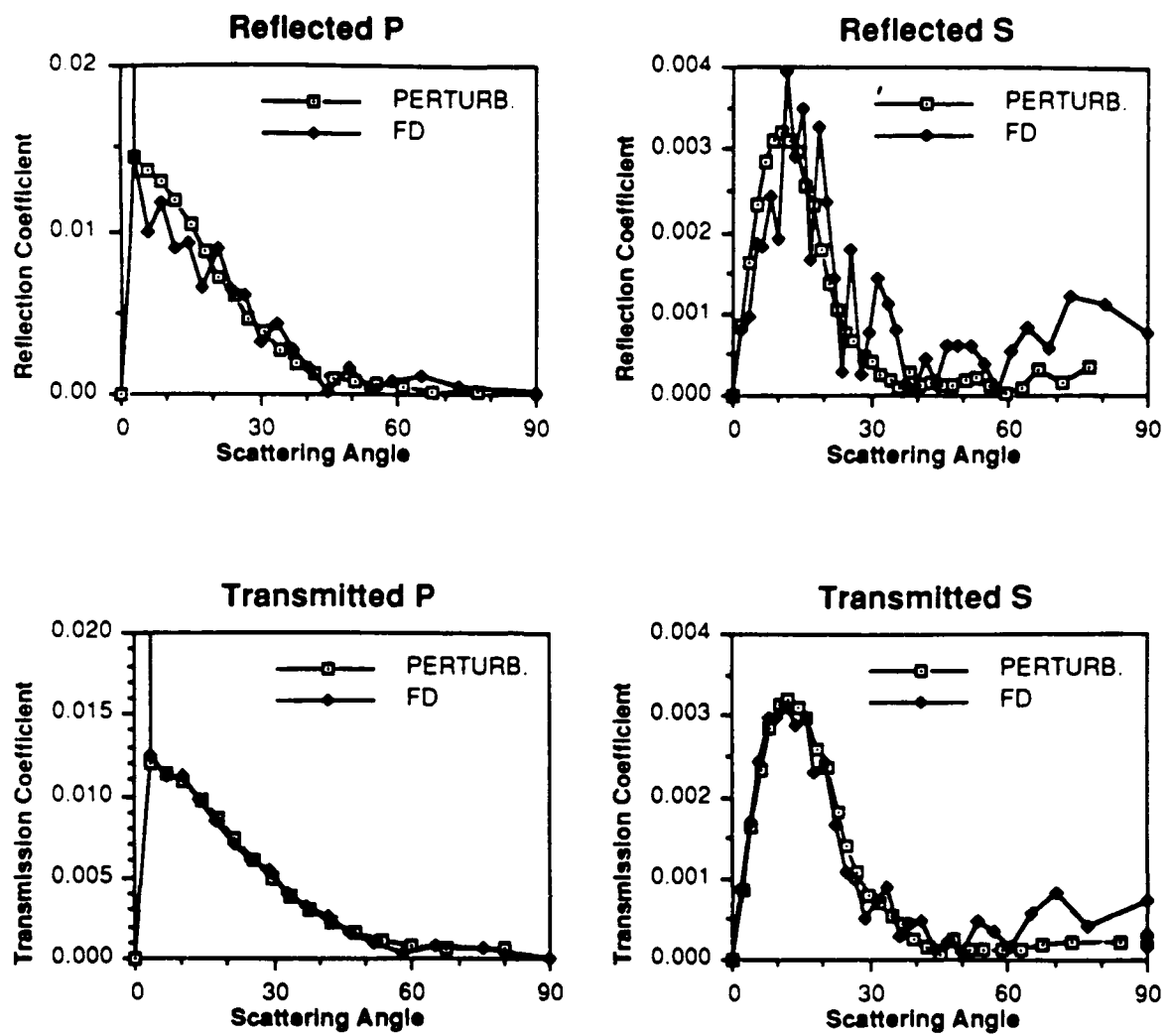


Figure 7.

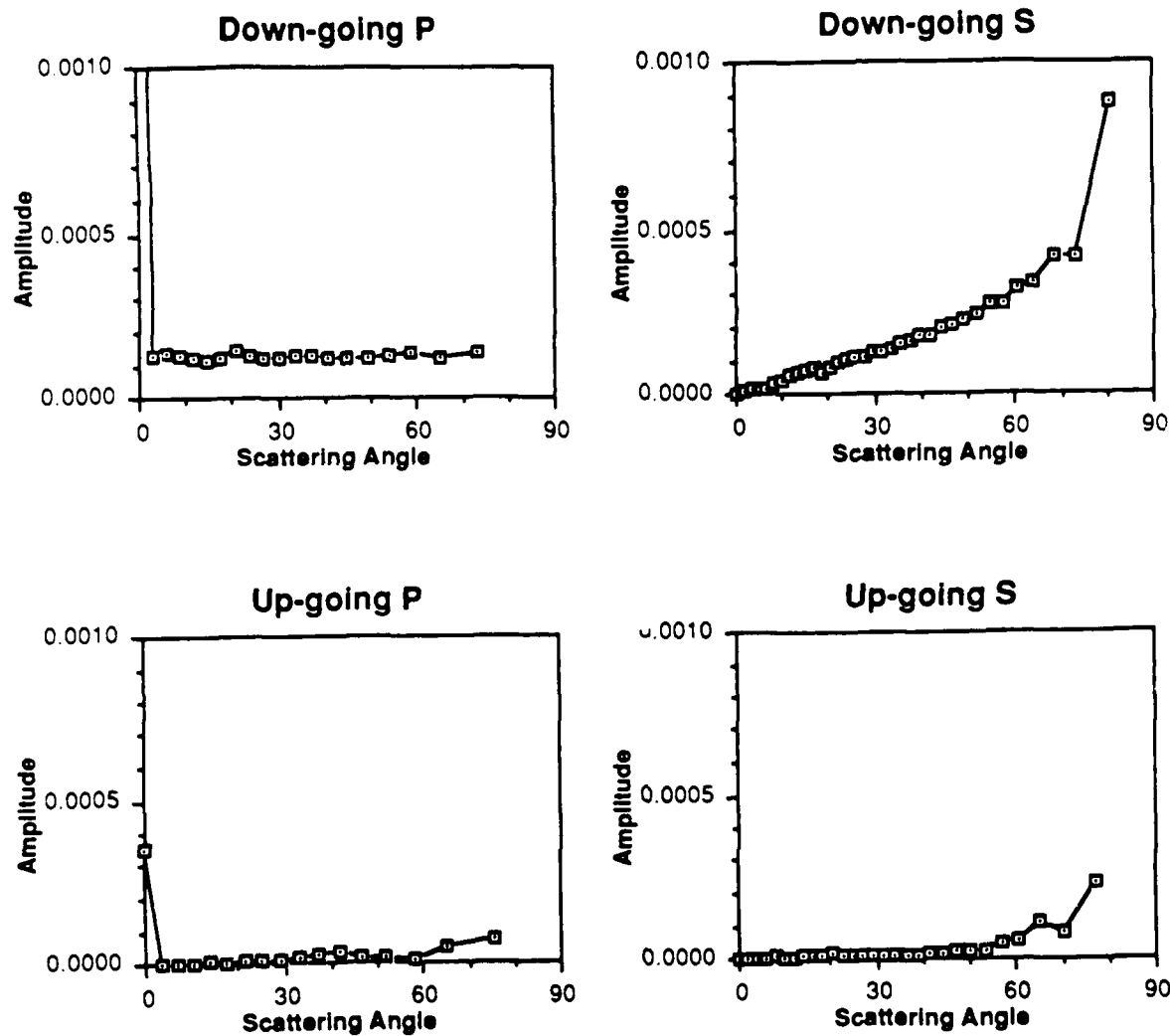
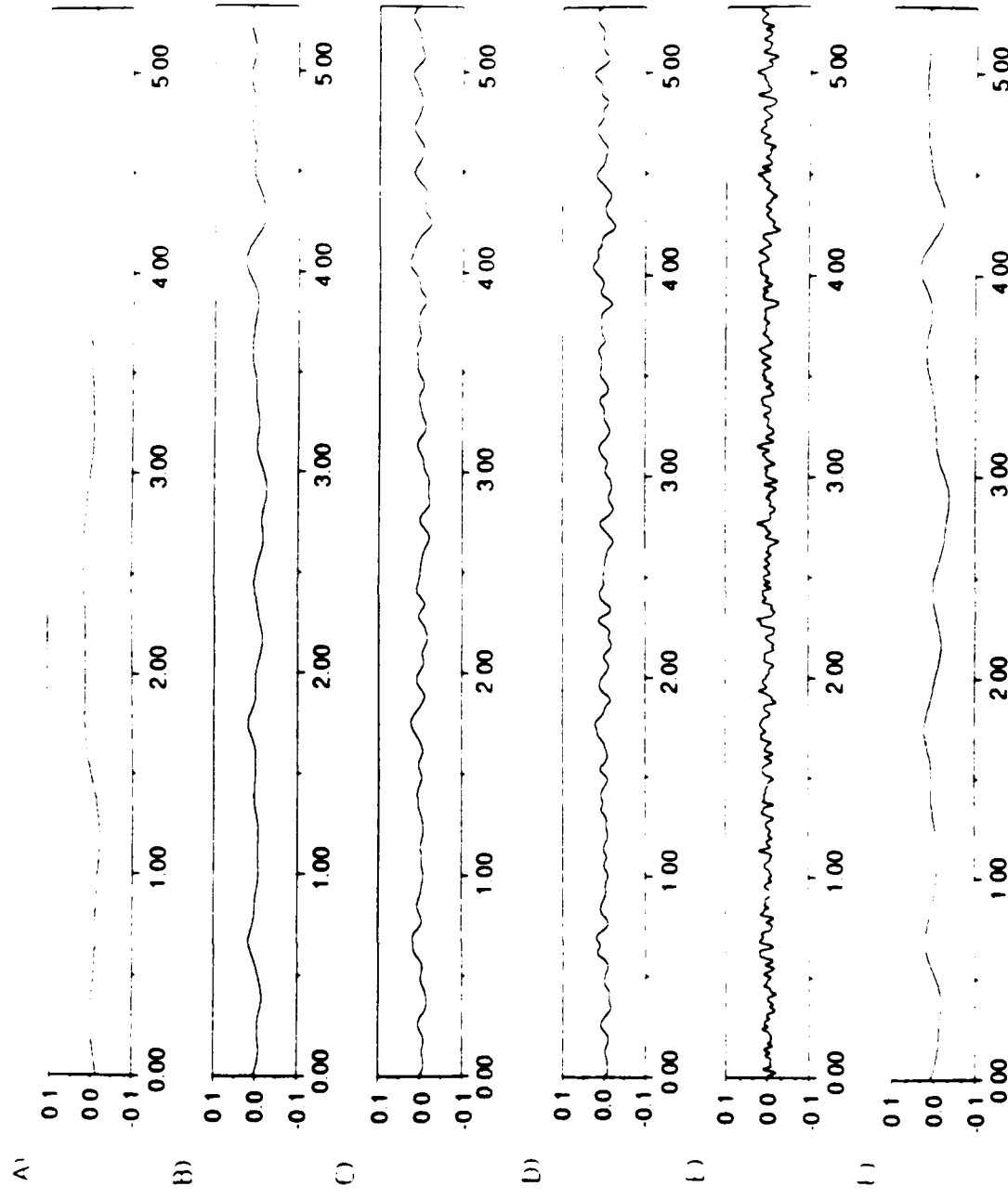


Figure 8.



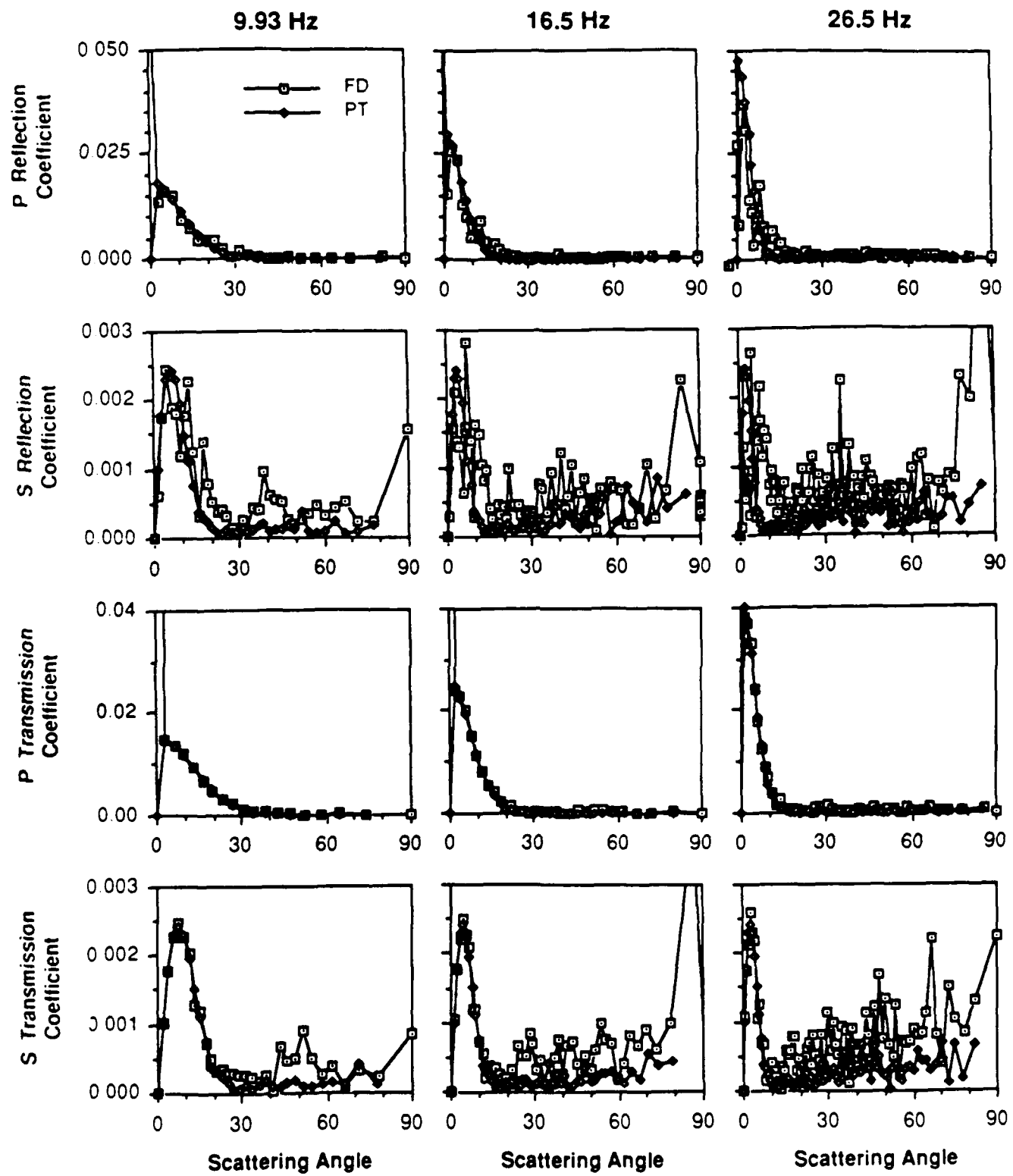


Figure 10a.

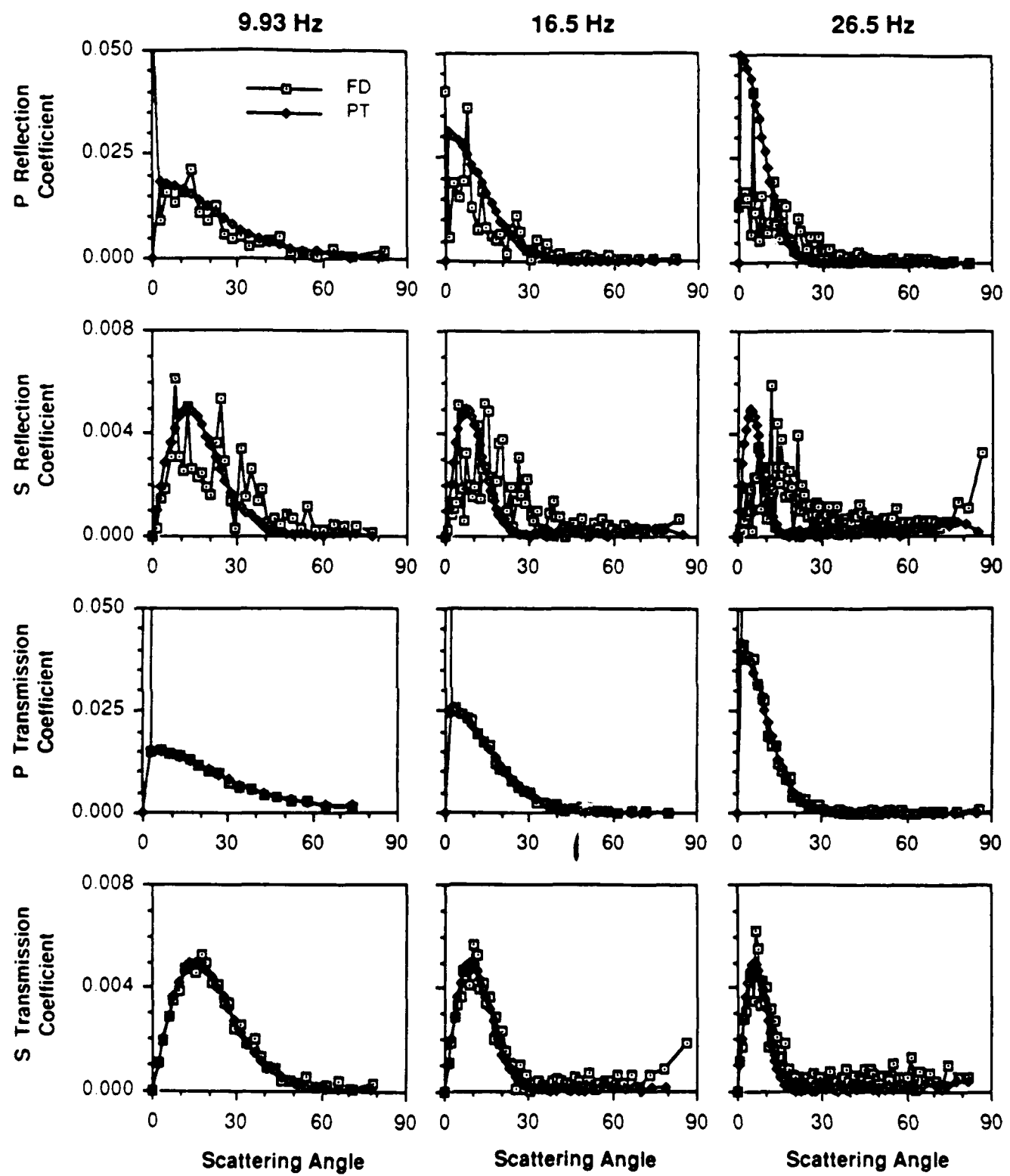


Figure 10b.

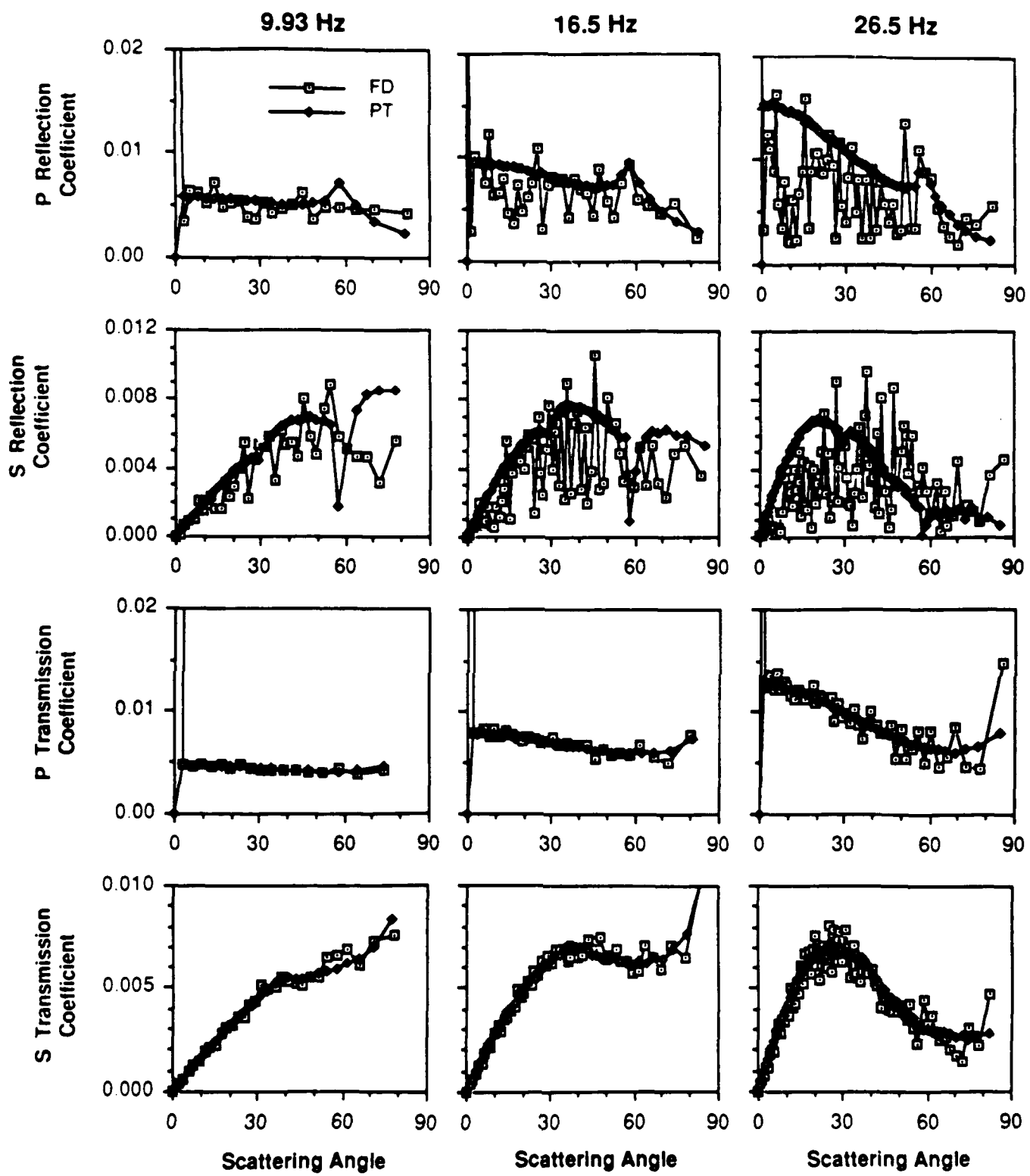


Figure 10c.

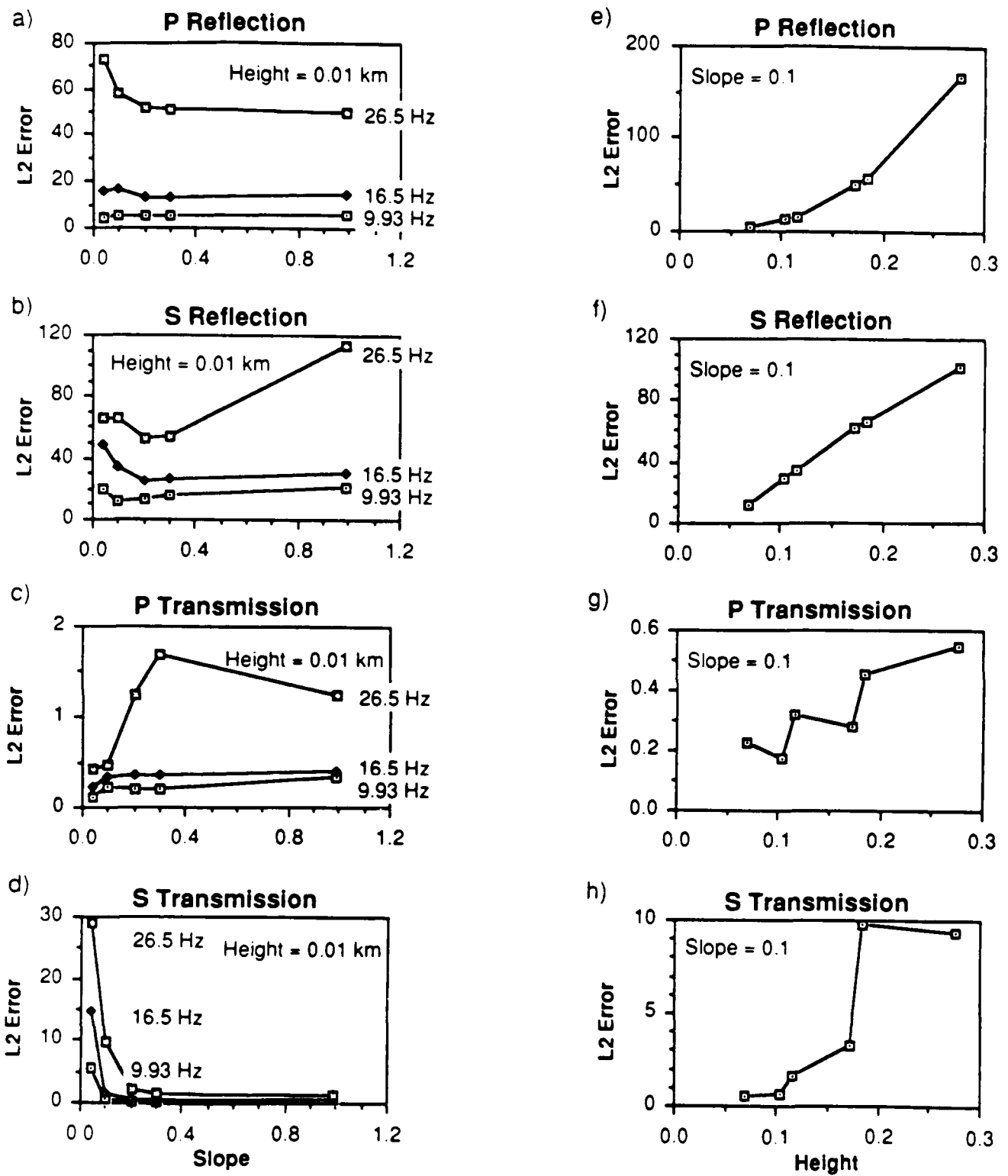


Figure 11.

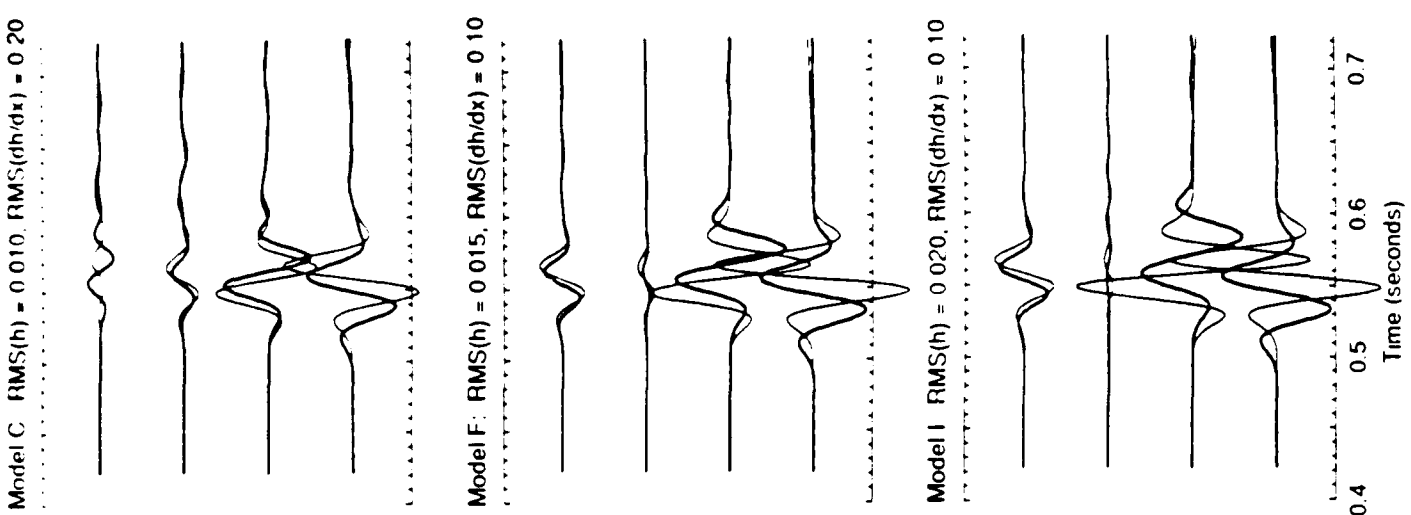
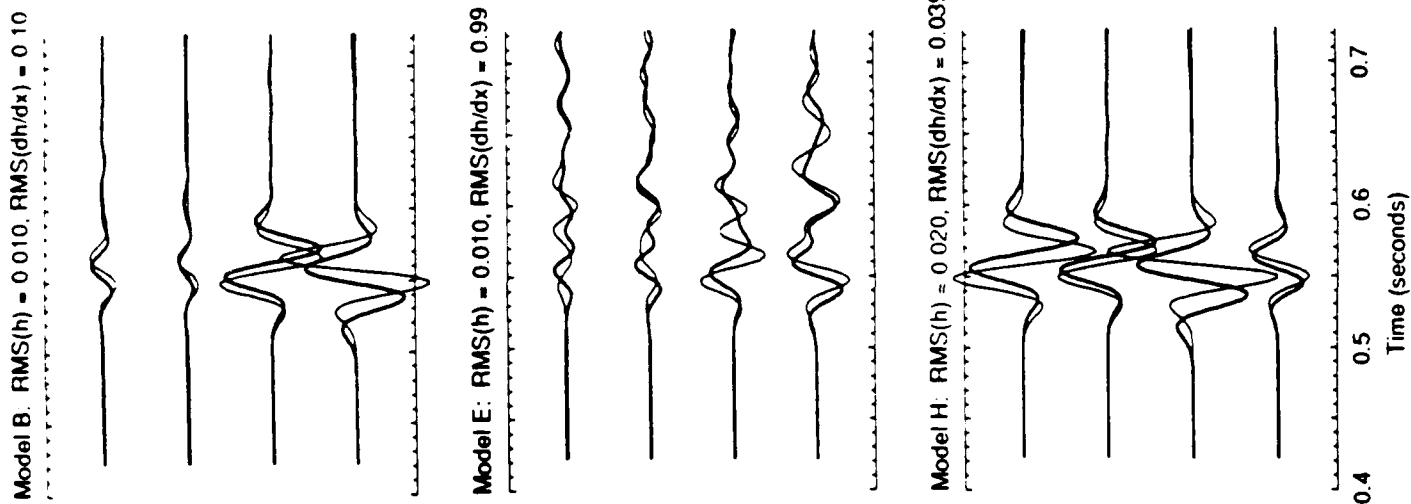
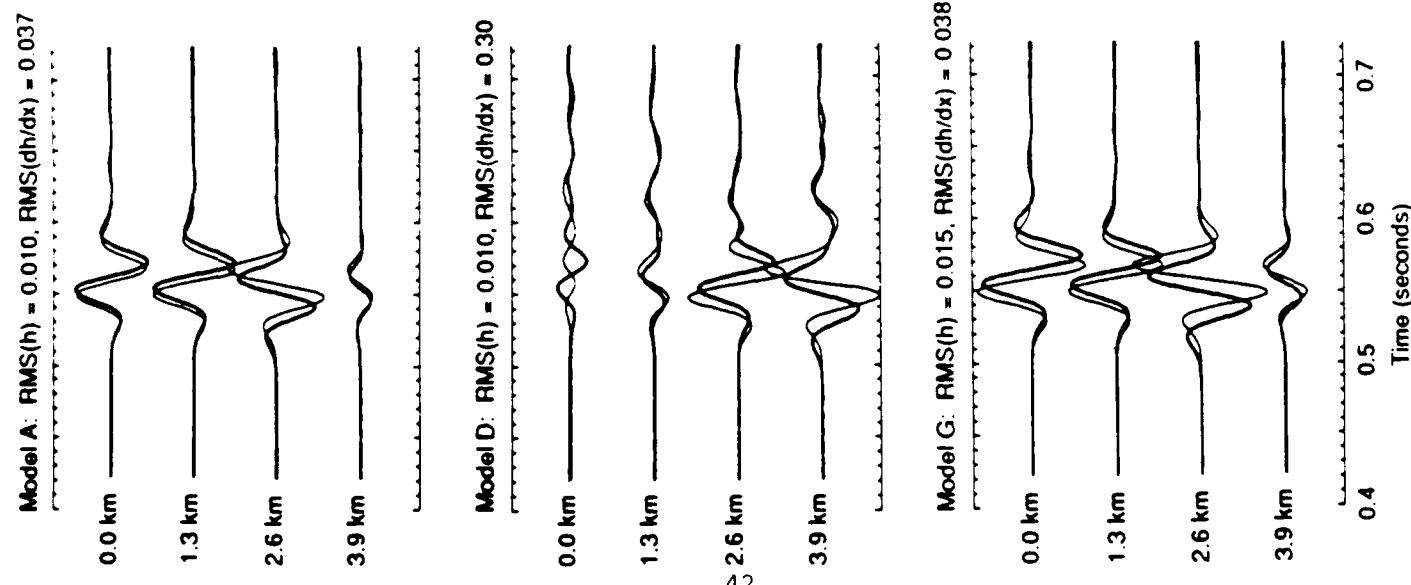
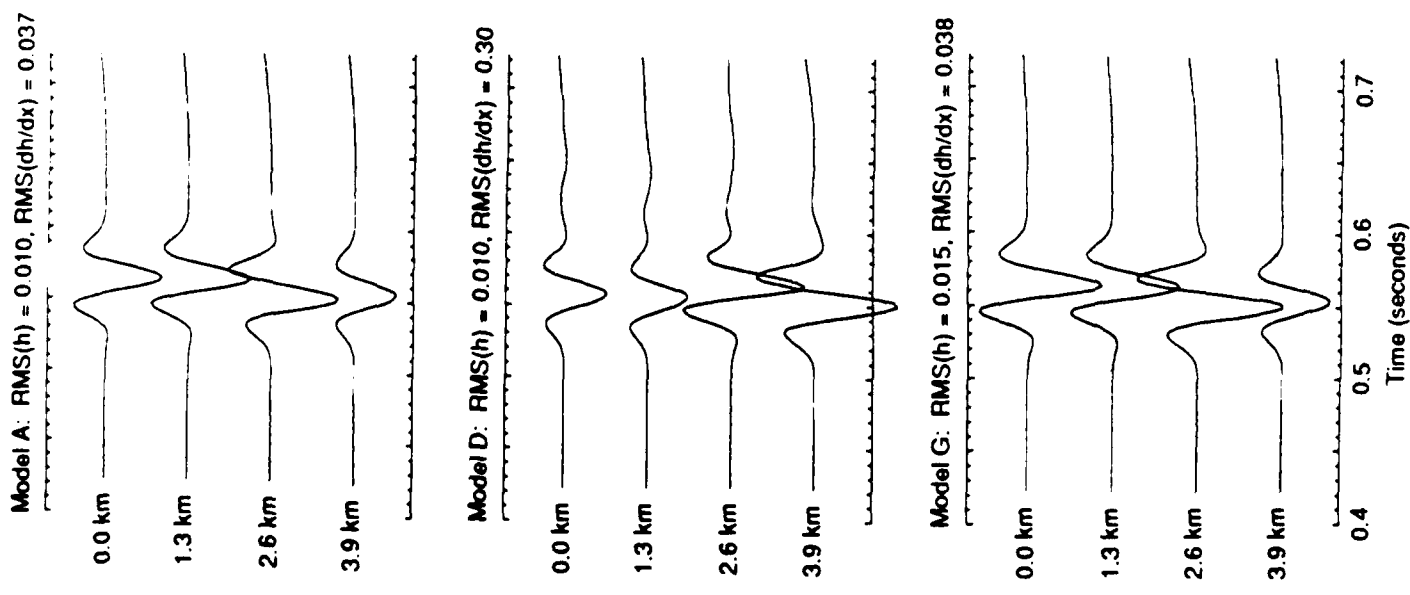
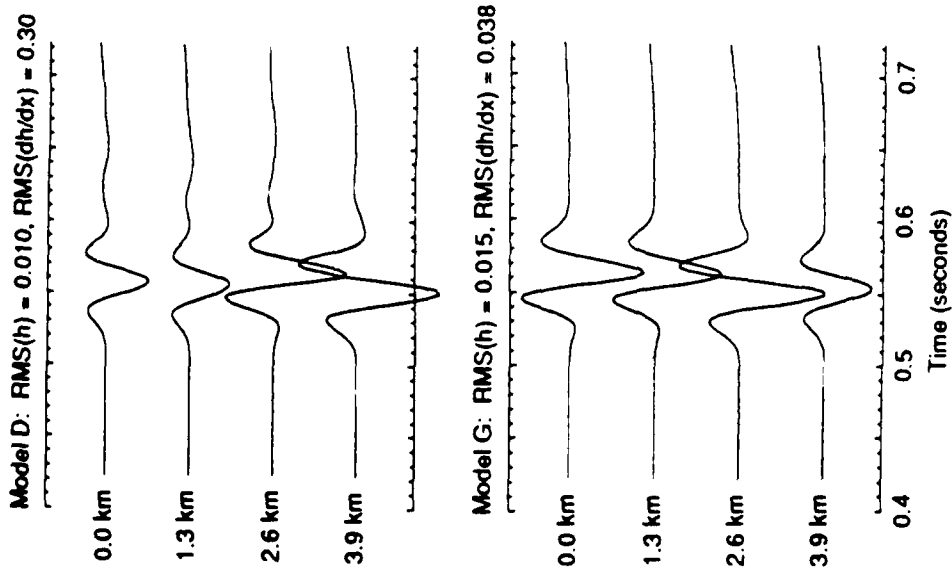


Figure 12.



Model B: RMS(h) = 0.010, RMS(dh/dx) = 0.10

Model C: RMS(h) = 0.010, RMS(dh/dx) = 0.20



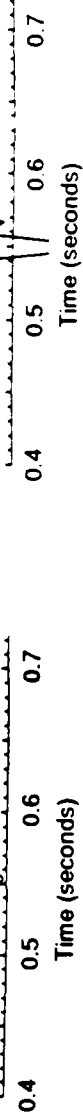
Model E: RMS(h) = 0.010, RMS(dh/dx) = 0.99

Model H: RMS(h) = 0.020, RMS(dh/dx) = 0.10

Model J: RMS(h) = 0.010, RMS(dh/dx) = 0.20

Model L: RMS(h) = 0.020, RMS(dh/dx) = 0.10

Figure 13.



Time (seconds)

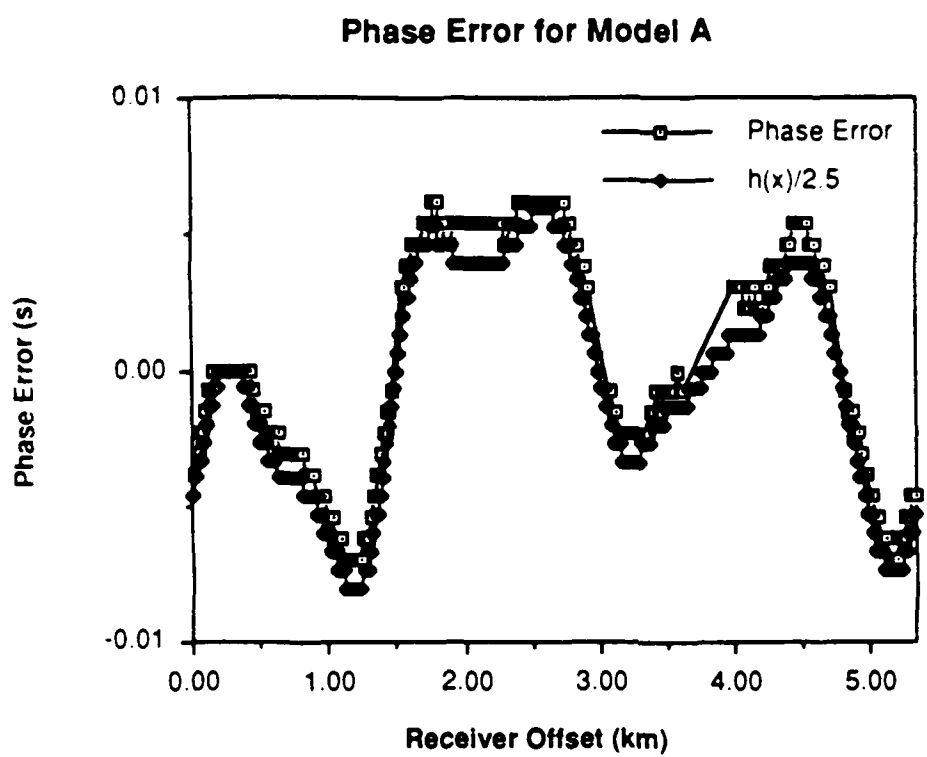


Figure 14.

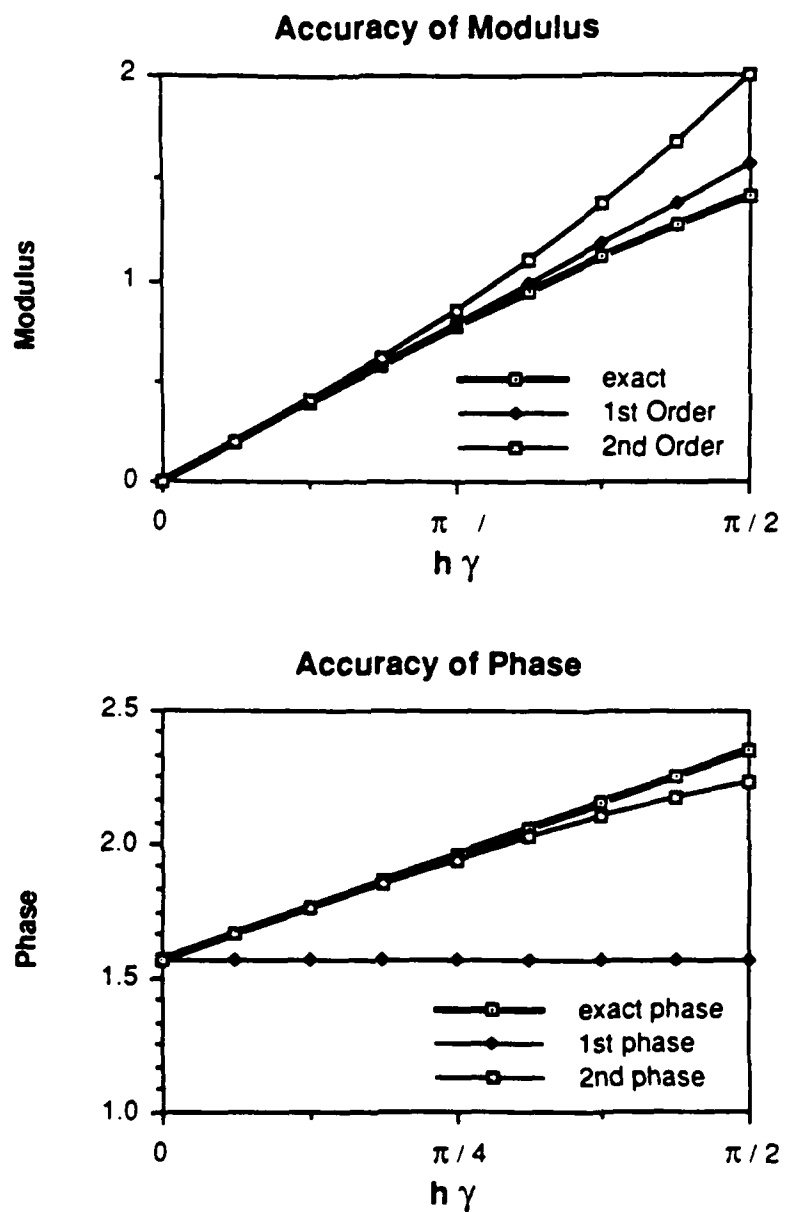
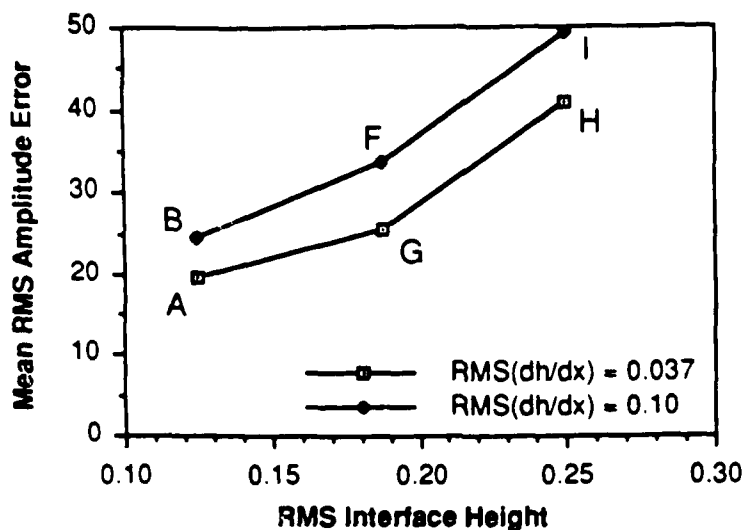


Figure 15

Error for Fixed Slope and Varying Height



Error for Fixed Height and Varying Slope

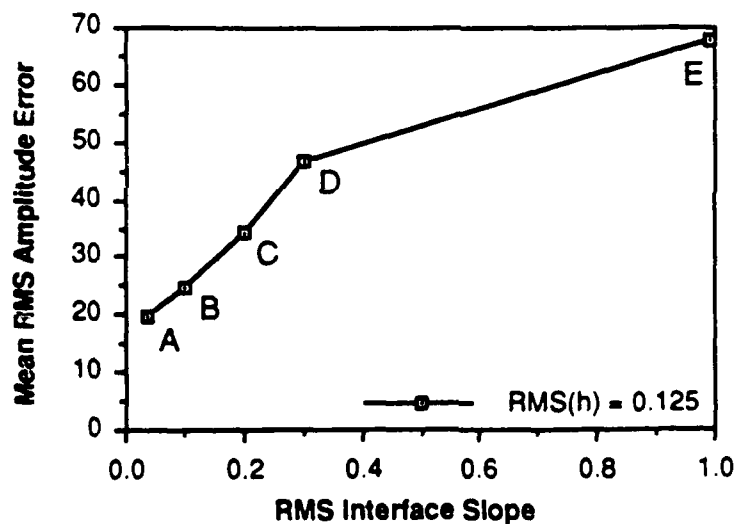


Figure 16.

← 18 Hz Normal Incidence Plane Wave →

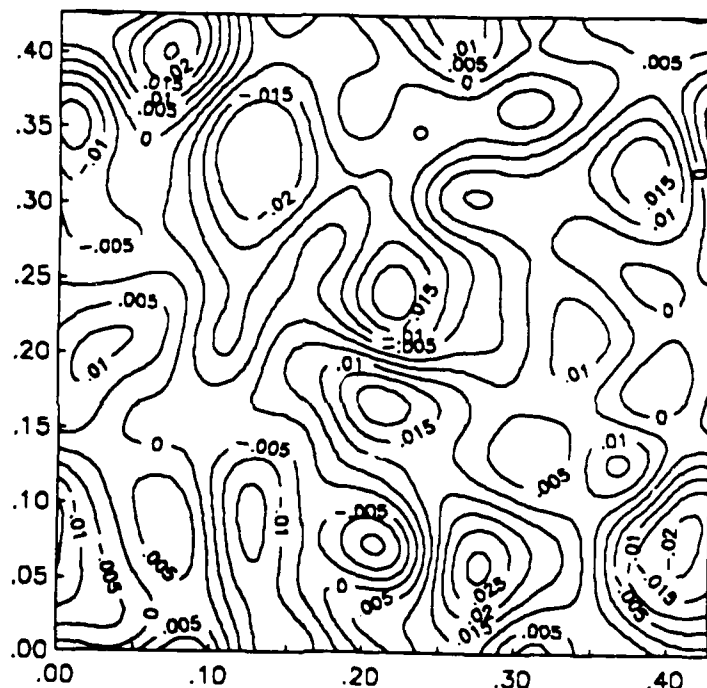
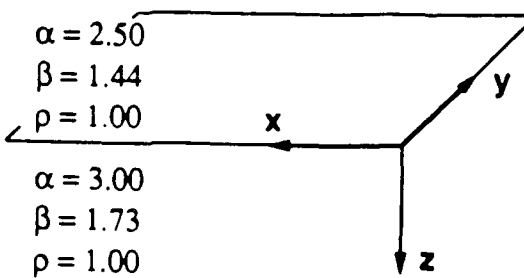


Figure 17.

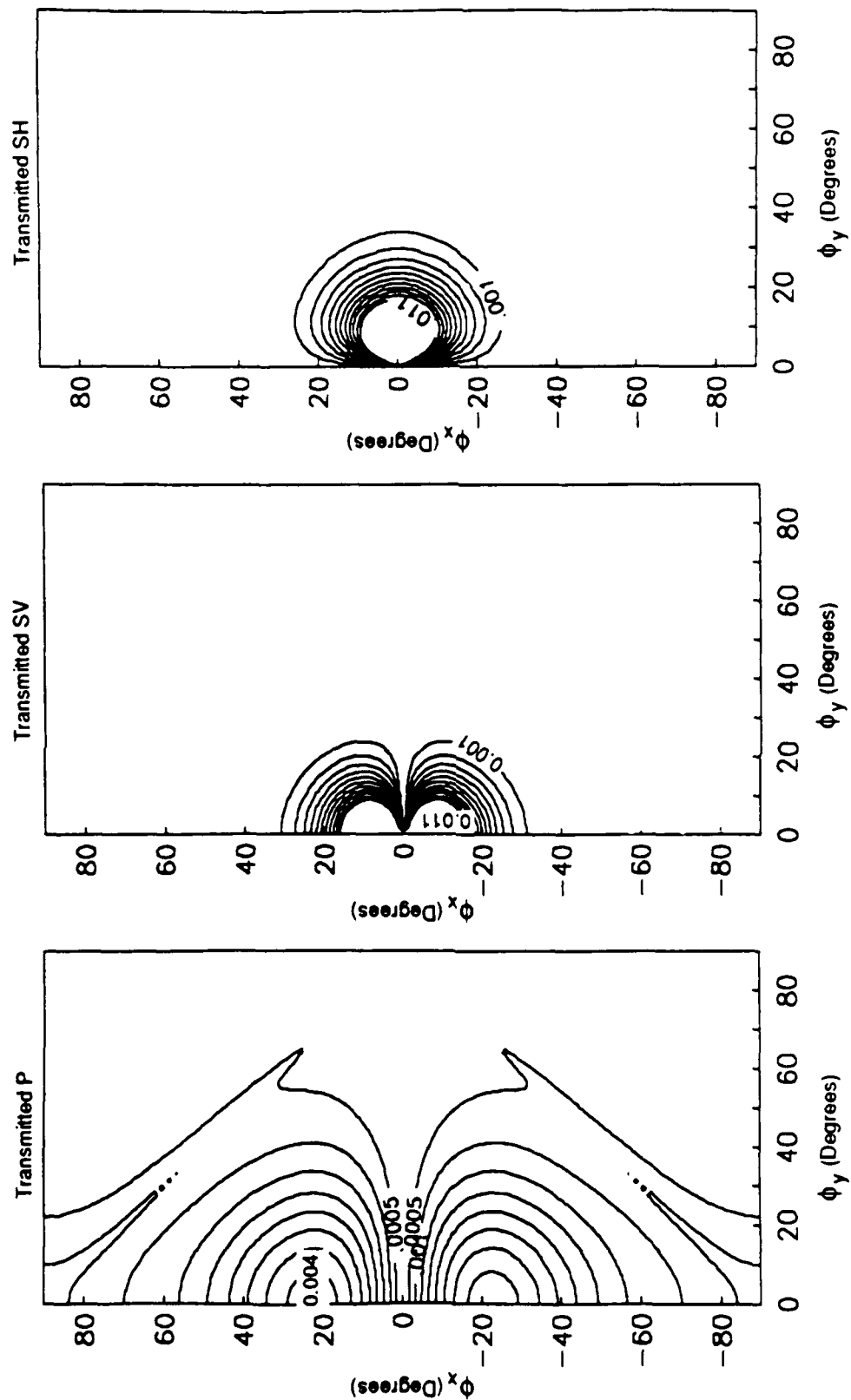


Figure 18.

SV Source

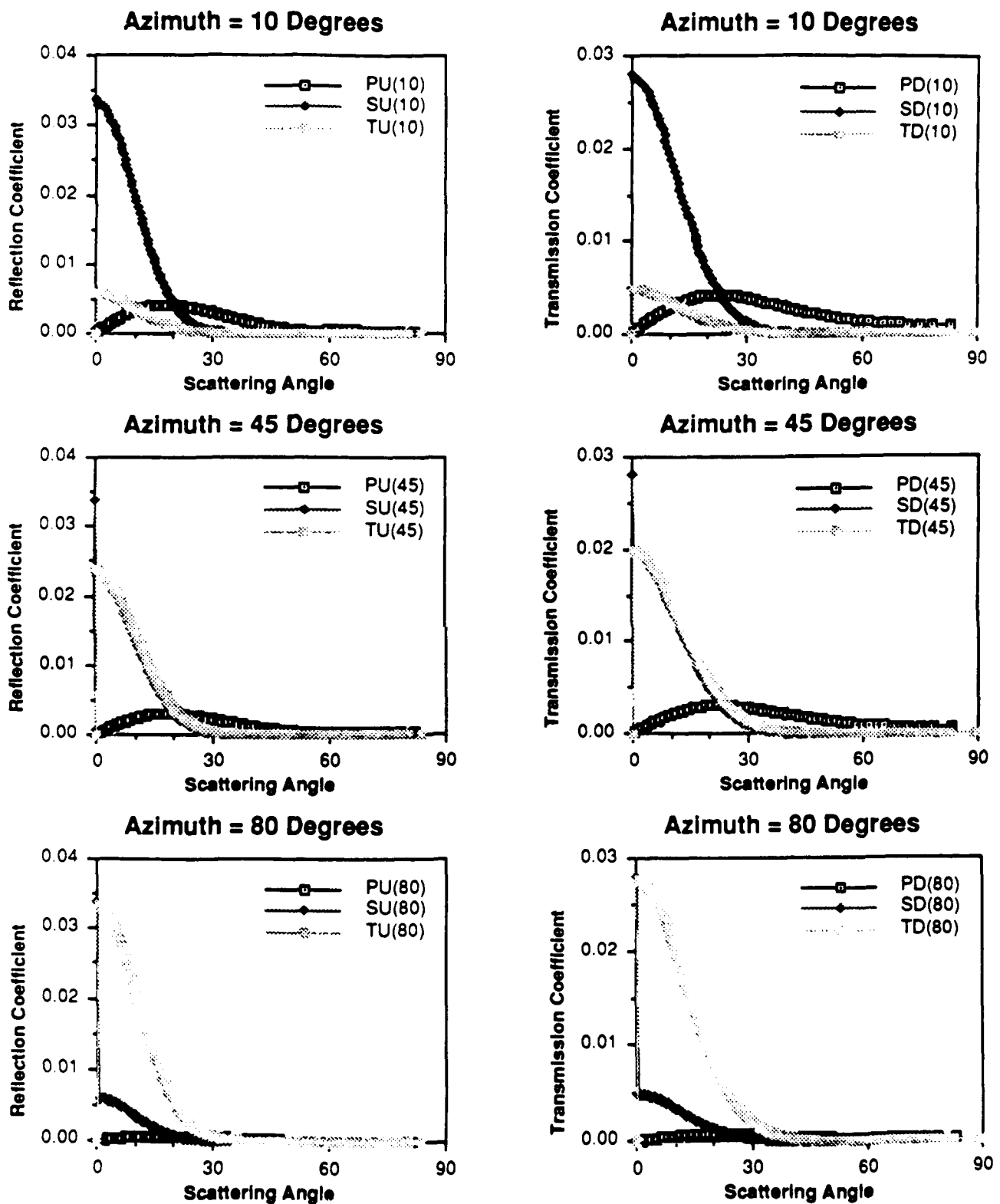


Figure 19

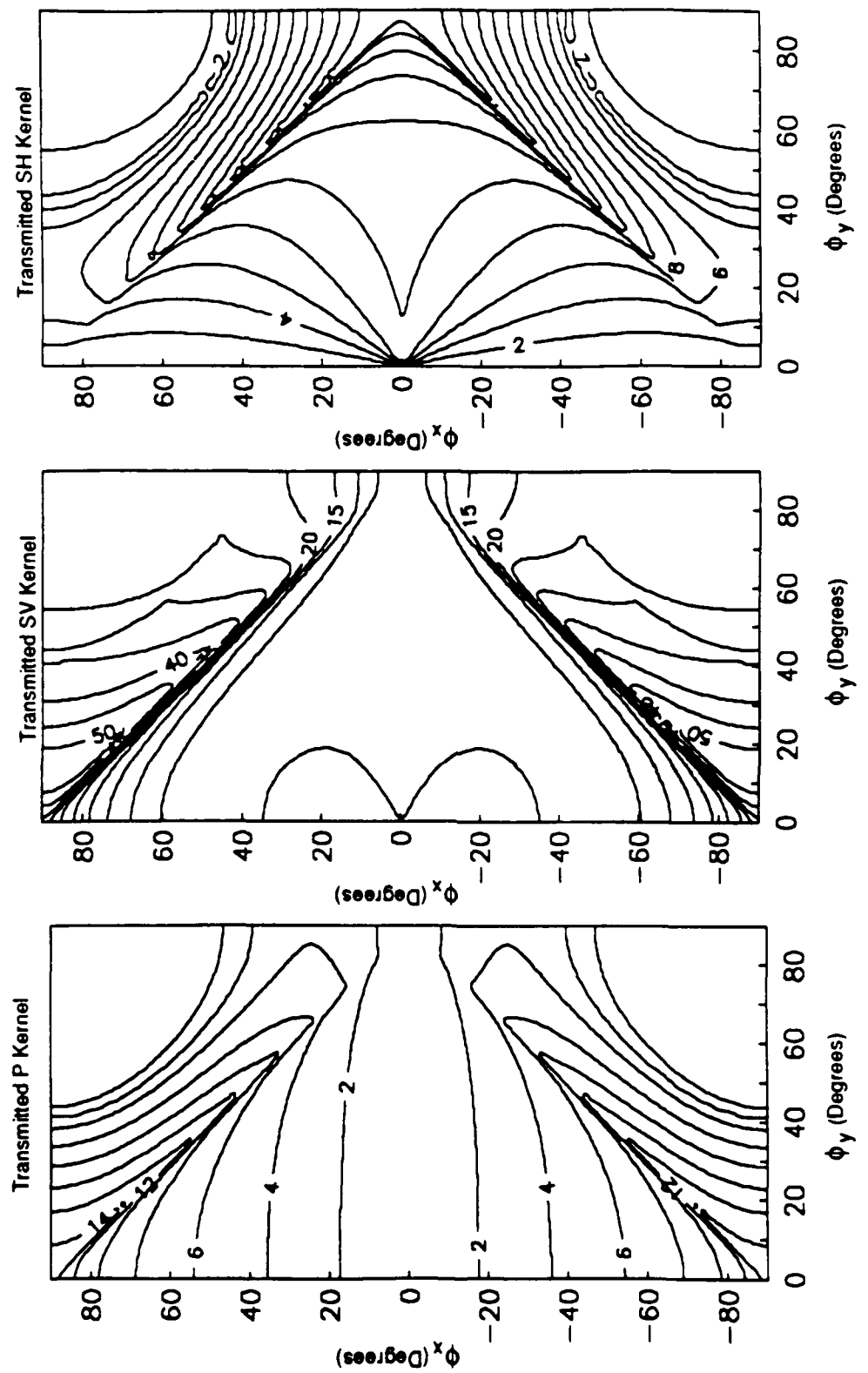
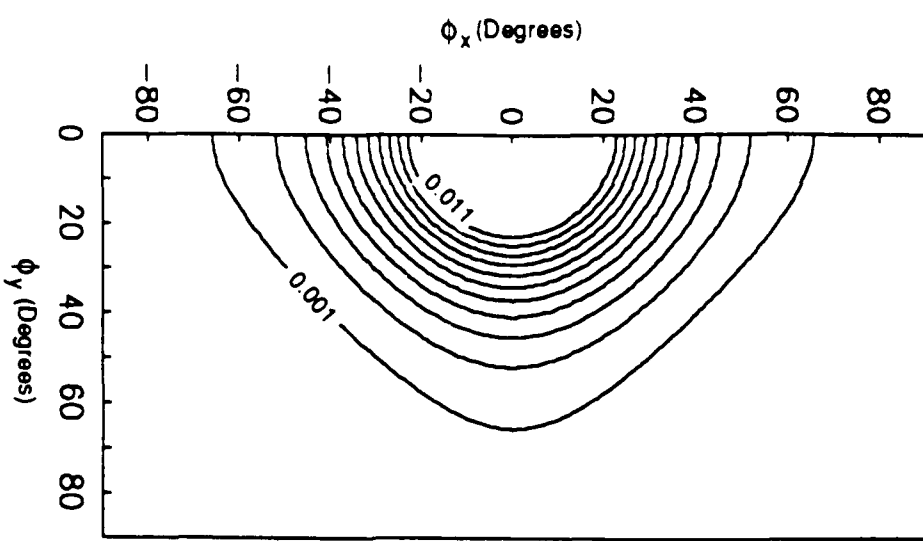


Figure 20.

Transmitted P



Transmitted SV

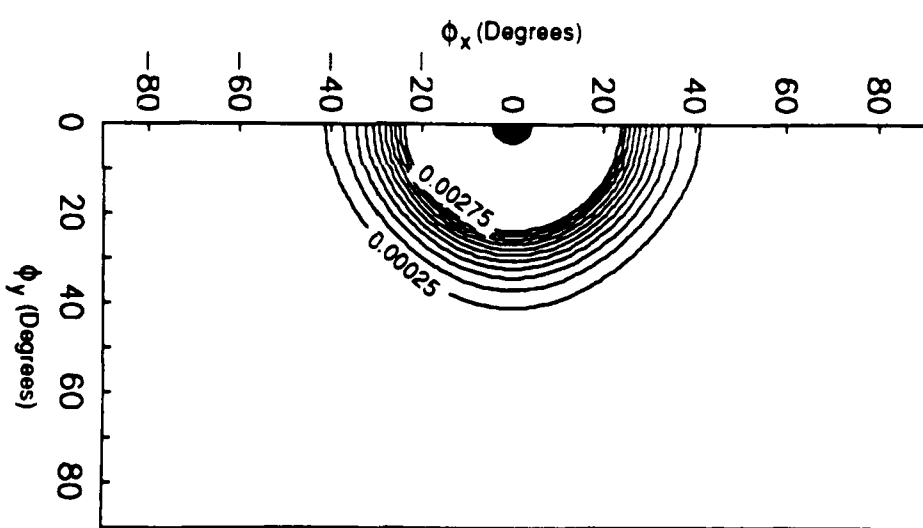


Figure 21.

P Source

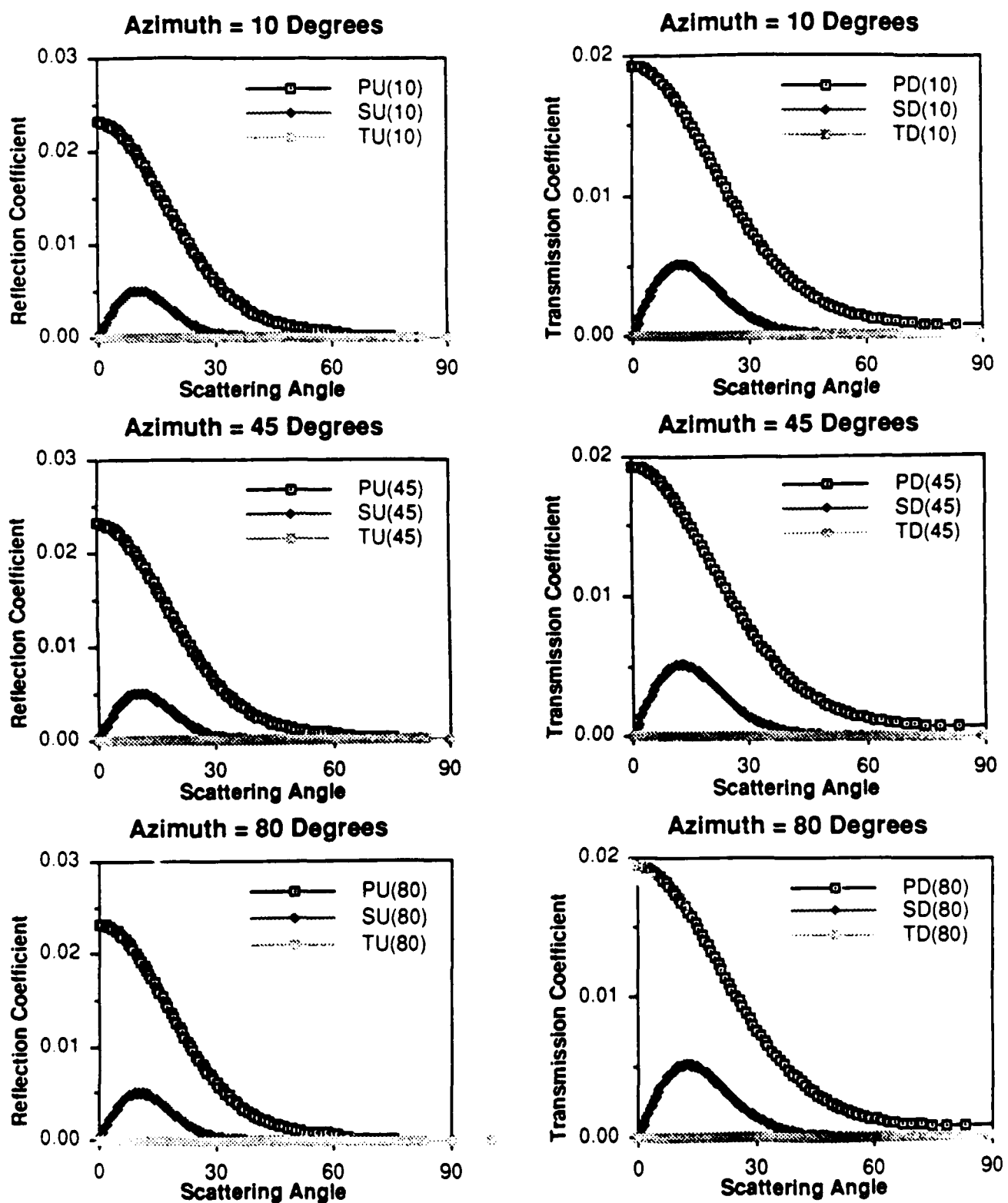


Figure 22.

SEISMIC SOURCE THEORY
IN INHOMOGENEOUS ANISOTROPIC MEDIA

Ari Ben-Menahem¹ and Arcangelo G. Sena

Earth Resources Laboratory
Department of Earth, Atmospheric, and Planetary Sciences
Massachusetts Institute of Technology
Cambridge, MA 02139

August, 1989

Submitted to the Journal of Geophysical Research

¹NRC Fellow, Earth Sciences Division, Air-Force Geophysics Laboratory, Hanscom Air Force Base, MA 02731. On leave from the Weizmann Institute of Science, Rehovot 76100, Israel.

ABSTRACT

A theoretical and computational tool is established for the numerical evaluation of spectral amplitudes of point sources in multilayered anisotropic crustal models. First, we obtain an explicit representation of the spectral elastodynamic Green's tensor in general anisotropic media as a sum of three integrals over the corresponding three slowness surfaces. The multidimensional stationary phase principle is then applied to derive an asymptotic approximation at the far-field. The theory is applied to azimuthally-isotropic media for which we offer an alternative representation of the Green's tensor and its ensuing displacements fields in the form of an exact Hankel transform over the horizontal wave-number variable. The total field is specified here in terms of two potentials: an SII potential and a mixed quasi transverse-quasi longitudinal potential, both of which assume the role of two scalar Green's functions. The availability of the *Green's tensor in analytical form* enables one to obtain readily numerical solutions for a wide selection of media and sources. Far-field spectral amplitude radiation patterns for various sources and displacement components are calculated and displayed. It is shown that the radiation field of an explosion has the following new features: (1) Quasi-transverse waves are created with four and eight lobe patterns; (2) Quasi-longitudinal waves are created for the collatitudinal displacement with four lobe patterns; (3) The energy ratio SV/P may reach the value of 20 for more than 50% of the azimuths in crustal structures such as tuff and shales; (4) Radiation patterns for vertical shear waves are created which are indistinguishable from corresponding waves produced by earthquake faults.

Haskell-type matrix algorithm is established for a multilayered azimuthally-isotropic half-space which enables one to calculate body waves and surface waves in real-earth crustal models.

1. INTRODUCTION

Measurements of seismic velocity anisotropy in exploration geophysics from travel-times of P, SV and SH waves (Weatherby *et al.*, 1934; McCollum and Snell, 1944; Ricker, 1953; White and Sengbush, 1953; Cholet and Richards, 1954; Uhrig and Van Melle, 1955; de Segonzac and Laherrere, 1959; Richards, 1960; Gretener, 1961; Van der Stoep, 1966; Robertson and Corrigan, 1983; White *et al.*, 1983; Helbig, 1984; Banik, 1984; Leary and Henyey, 1985; Stephen, 1985; Winterstein, 1986; Kerner *et al.*, 1989) have disclosed that many rocks in sedimentary basins exhibit significant degrees of anisotropy. Similar results were obtained for the earth's crust and deep mantle via earthquake seismology (Gupta, 1973; Crampin, 1985; Vinnik *et al.*, 1986; Kafka and Reiter, 1987), and laboratory ultrasonic velocity measurements (Giesel, 1963; Schock *et al.*, 1974; Levin, 1979; Jones and Wang, 1981; Carlson *et al.*, 1984; Lo *et al.*, 1986; Thomsen, 1986; Rai and Hanson, 1988). The conclusions for exploration seismology (Corrigan, 1989) are:

- Transverse isotropy¹ is ubiquitous, being observed over a wide range of depths, at many scales of length and in many basins of economic interest.
- Azimuthal anisotropy is present in some areas and can significantly impact the quality of shear wave data. Its utility as a tool for detecting fractural zones is still under active study.
- P-wave anisotropy is generally of the order 0-10 percent. Its effects may often be masked by heterogeneity and noise.

¹In exploration and earthquake seismology, the name *transverse isotropy* is usually associated with a vertical axis of symmetry (horizontal isotropy plane) while *azimuthal anisotropy* is associated with a vertical plane of symmetry (horizontal axis of symmetry).

- S-wave anisotropy is usually larger than P-wave anisotropy—it may easily reach 10–30 percent. Anisotropy *must* be taken into account for many applications of S-wave seismology.

It has also been previously known that large volumes of inherently isotropic rock may be micro-fractured by regional tectonic stresses, resulting in a system of oriented fractures along principal axes which in turn could lead to global anisotropy (Bamford and Nunn, 1979; Leary *et al.*, 1987). Mechanical anisotropy can also result from the presence of crystals of particular symmetries or periodic thin lamination. All these anisotropy types are susceptible of exhibiting shear wave splitting (birefringence) where the faster wave is polarized parallel to the fracture system, while the slower is polarized perpendicular to the fracture system.

The existing theoretical models lag far behind the observations. We can group it in three categories:

1. Propagation of plane-waves in homogeneous anisotropic structures (Musgrave, 1954, 1970; Fedorov, 1968).
2. Radiation from point-forces with no explicit analytical results (Yeatts, 1984; Hanyga, 1984).
3. Numerical evaluation of WKBJ seismograms (Garmann, 1988; Singh and Chapman, 1988).

Buchwald (1959) derived an integral representation of the field in terms of triple Fourier integrals. These were estimated asymptotically using the stationary phase approximation, following a method of Lighthill (1960). Yeatts (1984) solved the same problem using the Radon transform. His results are presented in a form that is suited exclusively for asymptotic ray theory. It is also suspected that his final formal solution in the frequency domain lacks that part which arises from integration

over imaginary plane-wave angles [see his equation (27)].

The present paper extends seismic source theory to general anisotropic media. It puts emphasis upon explicit exact and approximate analytic evaluation of the *Green's tensor*. The elastodynamic fields of various point-sources are then systematically constructed from this tensor. In this sense, our results go beyond the works mentioned above, since we equipped seismologists with a theoretical tool by which they can interpret observations of *amplitudes* of seismic waves as well as traveltimes. The theory was applied to media with azimuthal-isotropy: Here, due to the complexity of the analysis, it was necessary to provide two parallel theoretical approaches through which the numerical results could be checked and compared. To this end we have presented the displacement far-field, once in a form of a stationary-phase approximation and then alternatively in the form of an exact Hankel-Transform over the horizontal wave-number variable. The results of this paper are 'computer-ready' in the sense that the exact expressions for the displacements due to a variety of dipolar sources in an *homogeneous layer* are given. When applied to a multilayered media with proper boundary conditions, Haskell or matrizant type algorithms, would render an immediate generalization of our results.

2. INTEGRAL REPRESENTATION OF THE DISPLACEMENT FIELD

We consider the equation of motion for an elastic anisotropic medium (Ben-Menahem and Singh, 1981)

$$\rho \frac{\partial^2 u_i}{\partial t^2} - c_{ijkl} \frac{\partial^2 u_l}{\partial x_j \partial x_k} = f_i, \quad (2.1)$$

where $u_i = u_i(\vec{r}, t)$ is the i-th component of the displacement, $f_i = f_i(\vec{r}, t)$ is the i-th component of the applied body force per unit volume, ρ is the uniform mass density, and c_{ijkl} are the elements of the uniform elastic coefficient tensor which satisfy the symmetry conditions

$$c_{ijkl} = c_{jikl} = c_{ijlk} = c_{klji}, \quad (2.2)$$

so that only 21 independent constants are involved. The suffixes can take the values 1,2, or 3, and the summation convention for repeated suffixes is assumed.

Let the applied body force be an arbitrary point force $F_i(t)$ acting at the origin. Then

$$f_i(\vec{r}, t) = F_i(t) \delta(\vec{r}), \quad (2.3)$$

where $\delta(\vec{r})$ is the three-dimensional Dirac delta function.

We assume that the force and the displacement can be represented by the Fourier integrals

$$F_i(\omega) = \frac{1}{2\pi} \int_{-\infty}^{\infty} dt e^{-i\omega t} F_i(t), \quad (2.4)$$

and

$$u_i(\vec{k}, \omega) = \left(\frac{1}{2\pi} \right)^4 \int_{-\infty}^{\infty} dt \int \int d^3 \vec{r} e^{-i(\omega t - \vec{k} \cdot \vec{r})} u_i(\vec{r}, t). \quad (2.5)$$

In (2.4) we have used the notation F_i to describe two different functions, emphasizing with the

arguments the corresponding domain. The same applies to u_i in (2.5). Thus

$$F_i(t) = \int_{-\infty}^{\infty} d\omega e^{i\omega t} F_i(\omega), \quad (2.6)$$

and

$$u_i(\vec{r}, t) = \int_{-\infty}^{\infty} d\omega \int \int d^3 \vec{k} e^{i(\omega t - \vec{k} \cdot \vec{r})} u_i(\vec{k}, \omega), \quad (2.7)$$

where ω is the angular frequency and $i = \sqrt{-1}$.

Taking the Fourier transform of (2.1), and using (2.4) and (2.5), we obtain the matrix equation

$$(c_{ijk} k_l k_k - \rho \omega^2 \delta_{ij}) u_j(\vec{k}, \omega) = \left(\frac{1}{2\pi} \right)^3 F_i(\omega). \quad (2.8)$$

Letting

$$\vec{k} = k \hat{n}, \quad (2.9)$$

where \hat{n} is a unit vector in the direction of \vec{k} , and

$$A_{ij} = \frac{c_{ijk}}{\rho} n_l n_k, \quad (2.10)$$

Equation (2.8) takes the form

$$M_{ij} u_j = \left(\frac{1}{2\pi} \right)^3 F_i, \quad (2.11)$$

where

$$M_{ij} = \rho k^2 \left[A_{ij} - \left(\frac{\omega}{k} \right)^2 \delta_{ij} \right]. \quad (2.12)$$

The formal solution to (2.11) is

$$u_i = \left(\frac{1}{2\pi} \right)^3 M_{ij}^{-1} F_j. \quad (2.13)$$

We may write (2.13) in an explicit way by means of the *spectral resolution* (otherwise known as the "nonion form of a dyadic") of the matrix $\underline{A} = [A_{ij}]$; that is,

$$A_{ij} = \sum_{m=1}^3 C_m^2 A_{ij}^{(m)}, \quad (2.14)$$

where C_m^2 is the m -th eigenvalue of \underline{A} and $A_{ij}^{(m)}$ is the m -th projection matrix. Since \underline{A} is real, symmetric, and positive definite, its eigenvalues are real and positive.

The eigenvalue equation for \underline{A} is the Christoffel equation of plane-wave theory

$$A_{ij} T_j^{(m)} = C_m^2 T_i^{(m)}, \quad (2.15)$$

wherein C_m is the phase velocity of type- m waves and $T^{(m)}$ is the corresponding displacement polarization vector (Fedorov, 1968).

The eigenvectors can be taken as orthonormal,

$$T_i^{(p)} T_i^{(q)} = \delta_{pq}, \quad (2.16)$$

and the projection matrices, for symmetric \underline{A} , can be expressed as

$$A_{ij}^{(m)} = T_i^{(m)} T_j^{(m)}. \quad (2.17)$$

Consequently, the eigenvalues (β_m) of the matrix \underline{M} are

$$\beta_m = \rho k^2 \left[C_m^2 - \left(\frac{\omega}{k} \right)^2 \right], \quad m = 1, 2, 3 \quad (2.18)$$

and the eigenvectors of \underline{M} are the same as those of \underline{A} .

Therefore, we write for the inverse of the matrix \underline{M}

$$\underline{M}_{ij}^{-1} = \sum_{m=1}^3 \frac{1}{\beta_m} A_{ij}^{(m)}. \quad (2.19)$$

The solution in the (\vec{k}, ω) -domain, (2.13), is then written explicitly as

$$u_i(\vec{k}, \omega) = \frac{F_j(\omega)}{8\pi^3\rho} \sum_{m=1}^3 \frac{A_{ij}^{(m)}(\hat{n})}{C_m^2(\hat{n}) \left\{ k^2 - [\omega/C_m(\hat{n})]^2 \right\}}, \quad (2.20)$$

where we have emphasized the dependence of $A_{ij}^{(m)}$ and of C_m on \hat{n} .

3. THE SPECTRAL GREEN'S TENSOR AND ITS SLOWNESS-SURFACE INTEGRAL

Equation (2.20) can be transformed into the (\vec{r}, ω) -domain by standard procedures. Skipping the details of this lengthy operation, the end result for the *outgoing field* is

$$u_i(\vec{r}, \omega) = \frac{-i\omega F_j(\omega)}{8\pi^2 \rho} \sum_{m=1}^3 \int_{\Omega} d\Omega A_{ij}^{(m)} C_m^{-3} H(\vec{r} \cdot \hat{n}) e^{-i\omega \vec{r} \cdot \hat{n}/C_m}, \quad (3.1)$$

where $d\Omega$ is the solid angle element and H is the Heaviside unit-step function. We write

$$u_i(\vec{r}, \omega) = G_{ij}(\vec{r}, \omega) F_j(\omega), \quad (3.2)$$

where the Green's tensor $G_{ij}(\vec{r}, \omega)$ is given explicitly by

$$G_{ij}(\vec{r}, \omega) = \frac{-i\omega}{8\pi^2 \rho} \sum_{m=1}^3 \int_{\Omega} d\Omega A_{ij}^{(m)} C_m^{-3} H(\vec{r} \cdot \hat{n}) e^{-i\omega \vec{r} \cdot \hat{n}/C_m}. \quad (3.3)$$

If Ω is chosen as the *unit sphere*, the representation (3.3) can be written in the equivalent expression

$$G_{ij}(\vec{r}, \omega) = \frac{-i\omega}{8\pi^2 \rho} \sum_{m=1}^3 \int_0^{2\pi} d\bar{\phi} \int_{C^{\pm}} d\bar{\theta} \sin \bar{\theta} A_{ij}^{(m)}(\hat{n}) C_m^{-3}(\hat{n}) H(\vec{r} \cdot \hat{n}) \cdot \\ \cdot \exp \left\{ \frac{-i\omega}{C_m(\hat{n})} [\sin \bar{\theta}(x \cos \bar{\phi} + y \sin \bar{\phi}) + z \cos \bar{\theta}] \right\}, \quad (3.4)$$

where C^{\pm} in (3.4) is the Weyl contour $\{0 \leq \bar{\theta} \leq \pi\} \cup \{\bar{\theta} = \pi/2 \pm i\tau, (\tau \geq 0)\}$ specified in Figure 1.

In the particular case of an isotropic medium, the eigenvalues $C_m^2(\hat{n})$ and the projection operators $A_{ij}^{(m)}(\hat{n})$ assume the form

$$C_1^2 = \frac{\lambda + 2\mu}{\rho} \equiv a^2, \quad C_2^2 = C_3^2 = \frac{\mu}{\rho} \equiv b^2 \quad (3.5)$$

$$A_{ij}^{(1)}(\hat{n}) = n_i n_j, \quad A_{ij}^{(2)}(\hat{n}) = A_{ij}^{(3)}(\hat{n}) = \delta_{ij} - n_i n_j, \quad (3.6)$$

where λ and μ are the usual Lamé parameters. Then (3.4) renders

$$G_{ij}(\vec{r}, \omega) = \frac{-i\omega}{8\pi^2\rho} \int_0^{2\pi} d\bar{\phi} \int_{C^\pm} d\bar{\theta} \sin \bar{\theta} H(\vec{r} \cdot \hat{n}) [a^{-3} n_i n_j e^{-i\omega \vec{r} \cdot \hat{n}/a} + b^{-3} (\delta_{ij} - n_i n_j) e^{-i\omega \vec{r} \cdot \hat{n}/b}] . \quad (3.7)$$

Since the direction of the polar axis is arbitrary and $\int_{C^\pm} = \int_0^{\pi/2 \pm i\infty}$, we can omit the step function $H(\vec{r} \cdot \hat{n})$. Thus

$$G_{ij}(\vec{r}, \omega) = \frac{-i\omega b^{-3}}{8\pi^2\rho} \int_0^{2\pi} d\bar{\phi} \int_{C^\pm} d\bar{\theta} \sin \bar{\theta} \left\{ \delta_{ij} e^{-i\omega \vec{r} \cdot \hat{n}/b} + n_i n_j [(b/a)^3 e^{-i\omega \vec{r} \cdot \hat{n}/a} - e^{-i\omega \vec{r} \cdot \hat{n}/b}] \right\} \quad (3.8)$$

Equation (3.8) can be rewritten as

$$\begin{aligned} G_{ij}(\vec{r}, \omega) &= \frac{-i\omega b^{-3}}{8\pi^2\rho} \left\{ \delta_{ij} \int_0^{2\pi} d\bar{\phi} \int_{C^\pm} d\bar{\theta} \sin \bar{\theta} e^{-i\omega \vec{r} \cdot \hat{n}/b} \right. \\ &\quad \left. - \frac{\partial}{\partial x_i} \frac{\partial}{\partial x_j} \left[\frac{b^3}{a\omega^2} \int_0^{2\pi} d\bar{\phi} \int_{C^\pm} d\bar{\theta} \sin \bar{\theta} e^{-i\omega \vec{r} \cdot \hat{n}/a} - \left(\frac{b}{\omega} \right)^2 \int_0^{2\pi} d\bar{\phi} \int_{C^\pm} d\bar{\theta} \sin \bar{\theta} e^{-i\omega \vec{r} \cdot \hat{n}/b} \right] \right\} . \end{aligned} \quad (3.9)$$

Using the Weyl's integral representation

$$\int_0^{2\pi} d\bar{\phi} \int_{C^\pm} d\bar{\theta} \sin \bar{\theta} e^{-ik \vec{r} \cdot \hat{n}} = \frac{2\pi i}{kr} e^{-ikr} , \quad (3.10)$$

we obtain from (3.9)

$$G_{ij}(\vec{r}, \omega) = \frac{1}{4\pi\mu} \left[\frac{e^{-i\omega r/b}}{r} \delta_{ij} + \left(\frac{b}{\omega} \right)^2 \frac{\partial}{\partial x_i} \frac{\partial}{\partial x_j} \left(\frac{e^{-i\omega r/b} - e^{-i\omega r/a}}{r} \right) \right] , \quad (3.11)$$

which is the well-known expression for the Green's tensor in an isotropic medium (Ben-Menahem and Singh, 1981).

The Slowness Surface

The surface whose position vector has the magnitude $1/C_m$ is usually called the *slowness surface* (Synge, 1957).

Let \vec{s} be the position vector of a point on the slowness surface Γ_m of type-m waves, then

$$\vec{s} = \frac{\hat{n}}{C_m}. \quad (3.12)$$

A point P on the slowness surface with coordinates s_i represents a wave travelling in the direction OP with velocity $1/|\vec{s}|$. The slowness surface is given by $C_m = 1$, $m = 1, 2$, or 3 , and for each m , $C_m(\vec{s})$ represents a real sheet Γ_m . Since $C_m(\vec{s}) > 0$ depends continuously on \hat{n} , where $\vec{s} \in \Gamma_m$ if $\vec{s} = \hat{n}/C_m$, it follows that the Γ_m are three closed surfaces enclosing the origin.

Since the normal to the slowness surface coincides with the direction of the energy flux, we can introduce the unit normal vector \hat{N} (Musgrave, 1970),

$$w_i^{(m)} = w_m N_i, \quad (3.13)$$

where $\vec{w}^{(m)}$ is the group velocity vector

$$w_i^{(m)} = \frac{c_{ijkl}}{\rho C_m} T_j^{(m)} T_k^{(m)} n_l = \frac{c_{ijkl}}{\rho} A_{jk}^{(m)} s_l, \quad (3.14)$$

and w_m is its magnitude.

Next, we express the Green's tensor in (3.3) as an integration over the slowness surface. Using (3.12) we modify (3.3) as follows. First, from (2.10), we have on Γ_m

$$A_{ij}(\vec{s}) = C_m^{-2} A_{ij}(\hat{n}). \quad (3.15)$$

By comparing (3.15) with the eigenvalue equation (2.15), we find that on Γ_m the eigenvalues are equal to unity.

The second change involves the surface element on Γ_m

$$\text{surface element} = s_l d\sigma_l , \quad (3.16)$$

where $d\sigma_l$ is a component of the outwardly directed surface element of Γ_m and s_l is as in (3.12).

On the slowness surface

$$d\sigma_l = N_l d\sigma . \quad (3.17)$$

Then, using (3.12) and (3.13), we have

$$s_l d\sigma_l = n_l w_l^{(m)} \frac{d\sigma}{C_m w_m} = \frac{d\sigma}{w_m} , \quad (3.18)$$

where we have used the fact that (Lighthill, 1960),

$$n_l w_l^{(m)} = C_m , \quad (3.19)$$

i.e., the velocity of energy propagation normal to the wave fronts is equal to the phase velocity.

Using the above results in (3.3) we obtain for the Green's tensor

$$G_{ij}(\vec{r}, \omega) = \frac{-i\omega}{8\pi^2 \rho} \sum_{m=1}^3 \int_{\Gamma_m} d\sigma w_m^{-1}(\vec{s}) A_{ij}^{(m)}(\vec{s}) H(\vec{r} \cdot \vec{s}) e^{-i\omega \vec{r} \cdot \vec{s}} , \quad (3.20)$$

where the integration is now over the slowness surface Γ_m of type-m waves.

In this way, instead of specifying a wave normal \hat{n} and a velocity C_m of the wave parallel to \hat{n} , we employ the slowness vector $\vec{s} = \hat{n}/C_m$.

Equation (3.20) for the Green's tensor can be written as

$$G_{ij}(\vec{r}, \omega) = \underbrace{G_{ij}^P(\vec{r}, \omega)}_{m=1} + \underbrace{G_{ij}^{SV}(\vec{r}, \omega)}_{m=2} + \underbrace{G_{ij}^{SH}(\vec{r}, \omega)}_{m=3} . \quad (3.21)$$

This separation of the Green's tensor in three terms is merely mathematical and is not necessarily associated with true P, SV, or SH motions. However, for instance, in homogeneous media with hexagonal (azimuthal isotropy) and cubic symmetries, it is easy to show that true SH motion (understood as $\text{div} \vec{u} = 0$) is possible, and consequently, the concept of SH waves can still be maintained.

In this case, the SH part of the total Green's tensor is

$$G_{ij}^{SH}(\vec{r}, \omega) = \frac{-i\omega}{8\pi^2\rho} \int_{\Gamma_3} d\sigma w_3^{-1}(\vec{s}) A_{ij}^{(3)}(\vec{s}) H(\vec{r} \cdot \vec{s}) e^{-i\omega \vec{r} \cdot \vec{s}}. \quad (3.22)$$

4. AZIMUTHALLY ISOTROPIC MEDIA

4.1 SH Motion

In this section we apply the previously developed theory to the case of the azimuthally isotropic medium, where we only have five independent elastic constants

$$\begin{aligned}
 c_{1111} &= c_{2222} \equiv c_{11} \\
 c_{3333} &\equiv c_{33} \\
 c_{1122} &\equiv c_{12} \\
 c_{1133} &= c_{2233} \equiv c_{13} \\
 c_{1313} &= c_{2323} \equiv c_{44} \\
 c_{1212} &\equiv c_{66} = (c_{11} - c_{12})/2 .
 \end{aligned} \tag{4.1}$$

The remaining elastic constants are equal to zero if not related to the above by the basic symmetry relations (2.2).

In an azimuthally isotropic medium we have for the displacement polarization vector of SH waves

$$\hat{T}^{(3)}(\vec{s}) = (s_1^2 + s_2^2)^{-1/2} \begin{pmatrix} -s_2 \\ s_1 \\ 0 \end{pmatrix} . \tag{4.2}$$

Therefore, the corresponding projection operator takes the form

$$\underline{A}^{(3)}(\vec{s}) = (s_1^2 + s_2^2)^{-1} \begin{pmatrix} s_2^2 & -s_1 s_2 & 0 \\ -s_1 s_2 & s_1^2 & 0 \\ 0 & 0 & 0 \end{pmatrix} . \tag{4.3}$$

For these purely transverse waves, the phase velocity (eigenvalue) can be calculated from (2.15)

$$C_3(\vec{s}) = \left[\frac{c_{66}}{\rho + (c_{66} - c_{44})s_3^2} \right]^{1/2} \quad (4.4)$$

The group velocity vector for SH waves can be obtained from (3.14),

$$\vec{w}^{(3)}(\vec{s}) = \frac{c_{66}}{\rho}(s_1\hat{s}_1 + s_2\hat{s}_2) + \frac{c_{44}}{\rho}s_3\hat{s}_3 \quad (4.5)$$

We proceed to obtain the equation of the slowness surface. From (3.12) we can write

$$|\vec{s}|^2 = s_1^2 + s_2^2 + s_3^2 = C_3^{-2} . \quad (4.6)$$

Substituting (4.4) into (4.6) we find

$$\frac{c_{66}}{\rho}(s_1^2 + s_2^2) + \frac{c_{44}}{\rho}s_3^2 = 1 , \quad (4.7)$$

which represents the equation of the slowness surface for SH waves. This surface is an ellipsoid, and in the case of isotropy, ($c_{44} = c_{66} = \mu$), reduces to a sphere of radius $\sqrt{\rho/\mu}$.

To perform the integration in (3.22) over the slowness surface, we change to prolate spheroidal coordinates (η, θ, ϕ) , where

$$\begin{aligned} x &= a \sinh \eta \sin \theta \cos \phi \\ y &= a \sinh \eta \sin \theta \sin \phi \\ z &= a \cosh \eta \cos \theta \end{aligned} \quad (4.8)$$

with $0 \leq \eta < \infty$, $0 \leq \theta \leq \pi$, and $0 \leq \phi < 2\pi$. The corresponding metric coefficients are

$$\begin{aligned} g_{\eta\eta} &= g_{\theta\theta} = a^2(\sinh^2 \eta + \sin^2 \theta) \\ g_{\phi\phi} &= a^2 \sinh^2 \eta \sin^2 \theta \end{aligned} \quad (4.9)$$

For $\eta = \text{constant}$ we have the prolate spheroids

$$\frac{1}{a^2 \sinh^2 \eta} (x^2 + y^2) + \frac{1}{a^2 \cosh^2 \eta} z^2 = 1. \quad (4.10)$$

Thus, with the use of prolate spheroidal coordinates, the integration over the slowness surface is carried out at $\eta = \text{constant}$. From (4.7) and (4.10) we find that

$$a = \left[\frac{\rho}{c_{44}} \left(1 - \frac{c_{44}}{c_{66}} \right) \right]^{1/2} \quad (4.11)$$

and

$$\eta = tgh^{-1} \left(\frac{c_{44}}{c_{66}} \right)^{1/2}, \quad (4.12)$$

which is the equation of the slowness surface in prolate spheroidal coordinates.

For the area element on the slowness surface we have

$$d\sigma = (g_{\theta\theta} g_{\phi\phi})^{1/2} d\bar{\theta} d\bar{\phi} = \frac{\rho}{c_{66}} \sin \bar{\theta} \left(\cos^2 \bar{\theta} + \frac{c_{66}}{c_{44}} \sin^2 \bar{\theta} \right)^{1/2} d\bar{\theta} d\bar{\phi}, \quad (4.13)$$

whereas the magnitude of the group velocity on the slowness surface is

$$w_3(\bar{\theta}) = \left(\frac{c_{44}}{\rho} \right)^{1/2} \left(\cos^2 \bar{\theta} + \frac{c_{66}}{c_{44}} \sin^2 \bar{\theta} \right)^{1/2}. \quad (4.14)$$

Also, the projection matrix takes the form

$$\underline{A}^{(3)}(\bar{\phi}) = \begin{pmatrix} \sin^2 \bar{\phi} & -\sin \bar{\phi} \cos \bar{\phi} & 0 \\ -\sin \bar{\phi} \cos \bar{\phi} & \cos^2 \bar{\phi} & 0 \\ 0 & 0 & 0 \end{pmatrix}. \quad (4.15)$$

Therefore, from (3.22), (4.13), and (4.14) we have for the SH part of the Green's tensor

$$G_{ij}^{SH}(\vec{r}, \omega) = \frac{-i\omega}{8\pi^2 c_{66}} \left(\frac{\rho}{c_{44}} \right)^{1/2} \int_0^{2\pi} d\phi A_{ij}^{(3)}(\phi) \int_{C^\pm} d\theta \sin \theta H(\vec{r} \cdot \vec{s}) e^{-i\omega \vec{r} \cdot \vec{s}}. \quad (4.16)$$

Equation (4.16) represents essentially an integration over the complex unit sphere as we had in (3.4). Since the direction of the polar axis is arbitrary and $\int_{C^\pm} = \int_0^{\pi/2 \pm i\infty}$, we can omit the step function $H(\vec{r} \cdot \vec{s})$. Consequently,

$$G_{ij}^{SH}(\vec{r}, \omega) = \frac{-i\omega}{8\pi^2 c_{66}} \left(\frac{\rho}{c_{44}} \right)^{1/2} \int_0^{2\pi} d\phi A_{ij}^{(3)}(\bar{\phi}) \int_{C^\pm} d\bar{\theta} \sin \bar{\theta} e^{-i\omega \vec{r} \cdot \vec{s}}. \quad (4.17)$$

The projection operator in (4.15) can be rewritten as

$$\underline{A}^{(3)}(\bar{\phi}) = \underline{I} - \begin{pmatrix} \cos^2 \bar{\phi} & \sin \bar{\phi} \cos \bar{\phi} & 0 \\ \sin \bar{\phi} \cos \bar{\phi} & \sin^2 \bar{\phi} & 0 \\ 0 & 0 & 1 \end{pmatrix}, \quad (4.18)$$

where \underline{I} is the unit matrix.

We recast the exponential in (4.17) in the form

$$e^{-i\omega \vec{r} \cdot \vec{s}} = \exp \left\{ -i\omega \left(\frac{\rho}{c_{66}} \right)^{1/2} \left[(x \cos \bar{\phi} + y \sin \bar{\phi}) \sin \bar{\theta} + \left(\frac{c_{66}}{c_{44}} \right)^{1/2} z \cos \bar{\theta} \right] \right\} = e^{-i\omega \left(\frac{\rho}{c_{66}} \right)^{1/2} \vec{r}' \cdot \hat{n}'}, \quad (4.19)$$

where

$$\vec{r}' = (x, y, z'), \quad z' = z \left(\frac{c_{66}}{c_{44}} \right)^{1/2}, \quad (4.20)$$

and

$$\hat{n}' = (\cos \bar{\phi} \sin \bar{\theta}, \sin \bar{\phi} \sin \bar{\theta}, \cos \bar{\theta}). \quad (4.21)$$

Inserting (4.19) into (4.17), one shows that (4.18) can be put in the symbolic operational form

$$\underline{A}^{(3)}(\bar{\phi}) = \vec{I} - \hat{e}_z \hat{e}_z - \frac{\vec{\nabla}_t \vec{\nabla}_t}{\nabla_t^2}. \quad (4.22)$$

where

$$\frac{\vec{\nabla}_t \vec{\nabla}_t}{\nabla_t^2} g = i_\Delta i_\Delta g + (i_\phi i_\phi - i_\Delta i_\Delta) \frac{1}{\Delta^2} \int \Delta g(z, \Delta) d\Delta. \quad (4.23)$$

and $(\hat{e}_\Delta, \hat{e}_\phi, \hat{e}_z)$ is the unit vector triad in cylindrical coordinates. Note that $\frac{\vec{\nabla}_t \vec{\nabla}_t}{\nabla_t^2} g$ means $\vec{\nabla}_t \vec{\nabla}_t (\nabla_t^{-2} g)$ where the operation $\nabla_t^{-2} g$ precedes the operation $\vec{\nabla}_t \vec{\nabla}_t$. We then obtain at once

$$\vec{G}_{SH}(\vec{r}, \omega) = \left(\vec{I} - \hat{e}_z \hat{e}_z - \frac{\vec{\nabla}_t \vec{\nabla}_t}{\nabla_t^2} \right) g(z, \Delta) \quad (4.24)$$

where

$$g(z, \Delta) = \left(\frac{\rho}{c_{44}} \right)^{1/2} \frac{i\omega}{8\pi^2 c_{66}} \int_0^{2\pi} d\bar{\phi} \int_{C^\pm} d\bar{\theta} \sin \bar{\theta} e^{-i\omega(\rho/c_{66})^{1/2} \vec{r}' \cdot \hat{n}'} = \frac{e^{-i\omega(\rho/c_{66})^{1/2} \hat{R}}}{4\pi(c_{44}c_{66})^{1/2} \hat{R}} \quad (4.25)$$

and

$$\hat{R} = \left(x^2 + y^2 + \frac{c_{66}}{c_{44}} z^2 \right)^{1/2} = \left(\Delta^2 + \frac{c_{66}}{c_{44}} z^2 \right)^{1/2}. \quad (4.26)$$

Explicitly,

$$\vec{G}_{SH}(\vec{r}, \omega) = \hat{e}_\phi \hat{e}_\phi g(z, \Delta) + (\hat{e}_\Delta \hat{e}_\Delta - \hat{e}_\phi \hat{e}_\phi) \frac{1}{\Delta^2} \int \Delta g(z, \Delta) d\Delta, \quad (4.27)$$

which agrees with the result obtained by Ben-Menahem (1989). We also note that the integral in (4.27) renders

$$\int \Delta g(z, \Delta) d\Delta = \frac{i}{4\pi\omega(\rho c_{44})^{1/2}} e^{-i\omega(\rho/c_{66})^{1/2} \hat{R}}. \quad (4.28)$$

In Appendix A we give certain differential geometry results for the slowness surface based upon a general parameterization. These results will be useful for the evaluation of the Green's tensor in systems with lower symmetries.

4.2 Quasi-Longitudinal and Quasi-Transverse Motions

We represent the explicit Green's tensor in terms of a single field potential for the coupled P-SV field. The details of this operation are sidetracked to Appendix B.

We proceed to solve the simultaneous equations (B.8) and (B.9). To this end, we follow the notation

$$a_1 = \frac{c_{11}}{\rho} ; \quad a_2 = \frac{c_{33}}{\rho} , \quad a_3 = \frac{c_{13} + c_{44}}{\rho} , \quad a_4 = \frac{c_{66}}{\rho} , \quad a_5 = \frac{c_{44}}{\rho} \quad (4.29)$$

and put (B.8) and (B.9) in the form

$$(a_5 \nabla_t^2 + a_2 \partial_z^2 + \omega^2) \Gamma + a_3 \partial_z^2 \Theta = -f \hat{e} \cdot \{\hat{e}_z \partial_z \delta(\vec{r} - \vec{r}_0)\} , \quad (4.30)$$

$$a_3 \nabla_t^2 \Gamma + (a_1 \nabla_t^2 + a_5 \partial_z^2 + \omega^2) \Theta = -f \hat{e} \cdot \vec{\nabla}_t \delta(\vec{r} - \vec{r}_0) . \quad (4.31)$$

Denote

$$L_1 = a_5 \nabla_t^2 + a_2 \partial_z^2 + \omega^2 , \quad (4.32)$$

$$L_2 = a_1 \nabla_t^2 + a_5 \partial_z^2 + \omega^2 , \quad (4.33)$$

and assume a representation of the auxiliary potentials Θ and Γ in terms of a single *fundamental field potential* Ψ

$$\Theta = F \hat{e} \cdot [\hat{e}_z \partial_z a_3 \nabla_t^2 - \vec{\nabla}_t L_1] \Psi , \quad (4.34)$$

$$\Gamma = F \hat{e} \cdot [-\hat{e}_z \partial_z L_2 + a_3 \vec{\nabla}_t \partial_z^2] \Psi . \quad (4.35)$$

A substitution of (4.34) and (4.35) into (4.30) and (4.31) reveals that Ψ is the scalar Green's function of the equation.

$$(-L_1 L_2 + a_3^2 \partial_z^2 \nabla_t^2) \Psi = -\delta(\vec{r} - \vec{r}_0) . \quad (4.36)$$

In the derivation of (4.36), we were aided by the fact that the linear operations L_1 , L_2 , ∂_z , ∇_t^2 , and $\vec{\nabla}_t$, commute. Since Θ and Γ are expressible in terms of Ψ , so can the displacements. Indeed,

using (B.10) we have

$$\vec{u}_{P-SV} = \vec{\nabla}_t \{\nabla_t^{-2} \Theta\} + \hat{e}_z \int \Gamma dz = \vec{G}_{P-SV} \cdot F \hat{e}. \quad (4.37)$$

We put here the expressions for Θ, Γ from (4.34) and (4.35). Some rearrangements are necessary in order to arrive at the explicit expression for the P-SV part of the spectral Green's tensor

$$\vec{G}_{P-SV}(\vec{r}/\vec{r}_0; \omega) = \frac{1}{\rho} \left[a_3 \vec{\nabla} \vec{\nabla} - \hat{e}_z \hat{e}_z L_3 - \frac{\vec{\nabla}_t \vec{\nabla}_t}{\nabla_t^2} L_4 \right] \Psi, \quad (4.38)$$

with

$$L_3 = a_1 \nabla_t^2 + (a_3 + a_5) \partial_z^2 + \omega^2, \quad (4.39)$$

$$L_4 = (a_3 + a_5) \nabla_t^2 + a_2 \partial_z^2 + \omega^2, \quad (4.40)$$

$$\vec{\nabla} \vec{\nabla} = \left(\vec{\nabla}_t + \hat{e}_z \frac{\partial}{\partial_z} \right) \left(\vec{\nabla}_t + \hat{e}_z \frac{\partial}{\partial_z} \right) \quad (4.41)$$

$$= \hat{e}_z \hat{e}_z \partial_z^2 + \hat{e}_\Delta \hat{e}_\Delta \partial_\Delta^2 + \hat{e}_\phi \hat{e}_\phi \frac{1}{\Delta} \partial_\Delta + (\hat{e}_z \hat{e}_\Delta + \hat{e}_\Delta \hat{e}_z) \partial_{\Delta z}^2. \quad (4.42)$$

Clearly, $\partial_\phi = 0$ due to symmetry and differentiation is $w \cdot r \cdot t$ field coordinates. Nevertheless, one must note that the operators L_4 and $\vec{\nabla}_t \vec{\nabla}_t (\nabla_t^{-2})$ [see (B.32)] do *not* commute, i.e., $\vec{\nabla}_t \vec{\nabla}_t (\nabla_t^{-2} L_4) \neq L_4 \vec{\nabla}_t \vec{\nabla}_t \nabla_t^{-2}$. The total Green's tensor is the sum of the expressions in (4.38) and (B.36). Explicitly,

$$4\pi\rho \vec{G}(\vec{r}/\vec{r}_0; \omega) = 4\pi\rho \vec{G}_{iso} - 4\pi\rho \vec{G}_0 - \hat{e}_z \hat{e}_z \left[\frac{\mathcal{S}}{\eta_{SH} a_5} + 4\pi L_3 \{\Psi\} \right] - \hat{e}_\Delta \hat{e}_\Delta \left[\frac{\mathcal{S}}{\eta_{SH} a_5} + 4\pi L_4 \{\Psi\} \right], \quad (4.43)$$

$$4\pi\rho \vec{G}_{iso} = \frac{1}{\eta_{SH} a_5} \vec{I} \mathcal{S} + 4\pi a_3 \vec{\nabla} \vec{\nabla} \Psi, \quad (4.44)$$

$$4\pi\rho \vec{G}_0 = (\hat{e}_\phi \hat{e}_\phi - \hat{e}_\Delta \hat{e}_\Delta) \frac{1}{\Delta^2} \int \Delta \left[\frac{\mathcal{S}(\Delta, z)}{\eta_{SH} a_5} + 4\pi L_4 \{\Psi\} \right] d\Delta. \quad (4.45)$$

The arbitrary partition of the total Green's tensor in Eq. (4.43) is meaningful. In the *isotropic limit* ($\eta_{SH} = 1$, $a_1 = a_2 = \frac{\lambda+2\mu}{\rho}$, $a_4 = a_5 = \frac{\mu}{\rho}$, $a_3 = \frac{\lambda+\mu}{\rho}$), one finds that $\vec{G}_0 = 0$, \vec{G}_{iso} goes into the Green's tensor for unbounded isotropic media and $\vec{G} \equiv \vec{G}_{iso}$.

In (4.43), \vec{G} is symmetric in its indices and also invariant to an exchange of \vec{r} and \vec{r}_0 . We shall name \vec{G}_0 the *singularity tensor* of the medium. We also show in the next section that the potential Ψ splits naturally into a quasi-longitudinal part Ψ_p and a quasi-transverse part Ψ_s , such that

$$\Psi = \Psi_s - \Psi_p . \quad (4.46)$$

Accordingly, we effect a sub-partitioning of the singularity tensor into three constituents

$$\vec{G}_0 = \vec{G}_0^{SH} + \vec{G}_0^{SV} - \vec{G}_0^P , \quad (4.47)$$

where

$$\rho \vec{G}_0^{SH} = (\hat{e}_\phi \hat{e}_\phi - \hat{e}_\Delta \hat{e}_\Delta) \frac{i}{4\pi k_{SH} \eta_{SH} a_5} \frac{e^{-ik_{SH}\vec{R}}}{\Delta^2} , \quad (4.48)$$

$$\rho \vec{G}_0^j = (\hat{e}_\phi \hat{e}_\phi - \hat{e}_\Delta \hat{e}_\Delta) \frac{1}{\Delta^2} \int \Delta L_4 \{ \Psi_j(\Delta, z) \} d\Delta . \quad (4.49)$$

$$(j = P, SV)$$

We shall find it useful for a later development of the theory to recast (4.43) as

$$\vec{G} = \vec{G}_{SH} + \vec{G}_{SV} - \vec{G}_P \quad (4.50)$$

where

$$\begin{aligned} \rho \vec{G}_P &= -a_1 \hat{e}_z \hat{e}_z \left[\nabla_t^2 + \frac{a_5}{a_1} \partial_z^2 + k_p^2 \right] \Psi_p + a_3 (\hat{e}_z \hat{e}_\Delta + \hat{e}_\Delta \hat{e}_z) \partial_{\Delta z}^2 \Psi_p \\ &+ a_1 \hat{e}_\Delta \hat{e}_\Delta \left\{ \frac{a_3}{a_1} \partial_\Delta^2 \Psi_p - \left[\frac{a_3 + a_5}{a_1} \nabla_t^2 + \frac{a_2}{a_1} \partial_z^2 + k_p^2 \right] \Psi_p \right\} \\ &+ a_3 \hat{e}_\phi \hat{e}_\phi \frac{1}{\Delta} \partial_\Delta \Psi_p + \rho \vec{G}_0^P , \end{aligned} \quad (4.51)$$

and

$$\begin{aligned}
\rho \vec{G}_{SV} &= -a_5 \hat{e}_z \hat{e}_z \left[\frac{a_1}{a_5} \nabla_t^2 + \partial_z^2 + k_s^2 \right] \Psi_s + a_3 (\hat{e}_z \hat{e}_\Delta + \hat{e}_\Delta \hat{e}_z) \partial_{\Delta z}^2 \Psi_s \\
&+ a_5 \hat{e}_\Delta \hat{e}_\Delta \left\{ \frac{a_3}{a_5} \partial_\Delta^2 \Psi_s - \left[\frac{a_3 + a_5}{a_5} \nabla_t^2 + \frac{a_2}{a_5} \partial_z^2 + k_s^2 \right] \Psi_s \right\} \\
&+ a_3 \hat{e}_\phi \hat{e}_\phi \frac{1}{\Delta} \partial_\Delta \Psi_s - \rho \vec{G}_0^{SV}.
\end{aligned} \tag{4.52}$$

It can be shown that the singularity tensor has the following properties:

1. In the *absolute far-field* ($\Delta \rightarrow \infty, z \rightarrow \infty$)

$$\vec{G}_0 = \mathcal{O}\left(\frac{1}{\Delta^2}\right). \tag{4.53}$$

2. In the *axial far-field* ($\Delta = 0, z \rightarrow \infty$)

$$\vec{G}_0^{SH} = \mathcal{O}\left(\frac{1}{\Delta^2}\right) \text{ (exactly)} ; \quad \vec{G}_0^j = \mathcal{O}\left(\frac{1}{z}\right) \text{ (non-singular), } j = P, SV \tag{4.54}$$

3. In the *isotropic limit*

$$\vec{G}_0 = 0 \quad \left(\vec{G}_0^P \equiv 0, \vec{G}_0^{SH} = -\vec{G}_0^{SV} \right). \tag{4.55}$$

Developing the operators in (4.51) and (4.52), we find a simplified form of the P-SV Green's tensor (4.38)

$$\begin{aligned}
\vec{G}_{P-SV}(\vec{r}|\vec{r}_0; \omega) &= \frac{1}{\rho} \left\{ -\hat{e}_z \hat{e}_z [a_1 \nabla_t^2 + a_5 \partial_z^2 + \omega^2] \Psi + a_3 (\hat{e}_z \hat{e}_\Delta + \hat{e}_\Delta \hat{e}_z) \partial_{\Delta z}^2 \Psi \right. \\
&- \hat{e}_\phi \hat{e}_\phi \left[a_5 \frac{1}{\Delta} \partial_\Delta \Psi + (a_2 \partial_z^2 + \omega^2) \frac{1}{\Delta^2} \int \Delta \Psi d\Delta \right] \\
&\left. - \hat{e}_\Delta \hat{e}_\Delta \left[a_5 \partial_\Delta^2 \Psi + (a_2 \partial_z^2 + \omega^2) \left(\Psi - \frac{1}{\Delta^2} \int \Delta \Psi d\Delta \right) \right] \right\}.
\end{aligned} \tag{4.56}$$

Thus, in the absolute far-field, we have the approximation

$$\rho \vec{G}_P \approx -a_1 \hat{e}_z \hat{e}_z \left(\partial_\Delta^2 + \frac{a_5}{a_1} \partial_z^2 + k_p^2 \right) \Psi_p + a_3 (\hat{e}_z \hat{e}_\Delta + \hat{e}_\Delta \hat{e}_z) \partial_{\Delta z}^2 \Psi_p$$

$$- a_1 \hat{e}_\Delta \hat{e}_\Delta \left(\frac{a_5}{a_1} \partial_\Delta^2 + \frac{a_2}{a_1} \partial_z^2 + k_p^2 \right) \Psi_p, \quad (4.57)$$

$$\begin{aligned} \rho \vec{G}_{SV} \approx & -a_5 \hat{e}_z \hat{e}_z \left[\frac{a_1}{a_5} \partial_\Delta^2 + \partial_z^2 + k_s^2 \right] \Psi_s + a_3 (\hat{e}_z \hat{e}_\Delta + \hat{e}_\Delta \hat{e}_z) \partial_{\Delta z}^2 \Psi_s \\ & - a_5 \hat{e}_\Delta \hat{e}_\Delta \left(\partial_\Delta^2 + \frac{a_2}{a_5} \partial_z^2 + k_s^2 \right) \Psi_s. \end{aligned} \quad (4.58)$$

From (4.55) and (4.58) we may derive in a straightforward manner, the P-SV *far-field* of point forces in terms of the yet undetermined potentials Ψ_p and Ψ_s :

I. Force in the z -direction (axis of symmetry)

$$\begin{aligned} \vec{u} &= \frac{F(\omega)}{\rho} \vec{G} \cdot \hat{e}_z, \\ u_{pz} &= -\frac{F(\omega)}{\rho} \vec{G}_P: \hat{e}_z \hat{e}_z = \frac{F(\omega)}{\rho} a_1 \left(\partial_\Delta^2 + \frac{a_5}{a_1} \partial_z^2 + k_p^2 \right) \Psi_p, \\ u_{p\Delta} &= -\frac{F(\omega)}{\rho} \vec{G}_P: \hat{e}_z \hat{e}_\Delta = -\frac{F(\omega)}{\rho} a_3 \partial_{\Delta z}^2 \Psi_p, \\ u_{sz} &= \frac{F(\omega)}{\rho} \vec{G}_{SV}: \hat{e}_z \hat{e}_z = -\frac{F(\omega)}{\rho} a_5 \left(\frac{a_1}{a_5} \partial_\Delta^2 + \partial_z^2 + k_s^2 \right) \Psi_s, \\ u_{s\Delta} &= \frac{F(\omega)}{\rho} \vec{G}_{SV}: \hat{e}_z \hat{e}_\Delta = \frac{F(\omega)}{\rho} a_3 \partial_{\Delta z}^2 \Psi_s. \end{aligned} \quad (4.59)$$

II. Force in the x -direction (plane of isotropy; $\hat{e}_x \cdot \hat{e}_\Delta = \cos \phi$)

$$\begin{aligned} \vec{u} &= \frac{F(\omega)}{\rho} \vec{G} \cdot \hat{e}_x, \\ u_{pz} &= -\frac{F(\omega)}{\rho} \vec{G}_P: \hat{e}_x \hat{e}_z = -\frac{F(\omega)}{\rho} a_3 \cos \phi \partial_{\Delta z}^2 \Psi_p, \\ u_{p\Delta} &= -\frac{F(\omega)}{\rho} \vec{G}_P: \hat{e}_x \hat{e}_\Delta = \frac{F(\omega)}{\rho} a_1 \cos \phi \left[\frac{a_5}{a_1} \partial_\Delta^2 + \frac{a_2}{a_1} \partial_z^2 + k_p^2 \right] \Psi_p, \\ u_{sz} &= \frac{F(\omega)}{\rho} \vec{G}_{SV}: \hat{e}_x \hat{e}_z = \frac{F(\omega)}{\rho} a_3 \cos \phi \partial_{\Delta z}^2 \Psi_s, \\ u_{s\Delta} &= \frac{F(\omega)}{\rho} \vec{G}_{SV}: \hat{e}_x \hat{e}_\Delta = -\frac{F(\omega)}{\rho} a_5 \cos \phi \left[\partial_\Delta^2 + \frac{a_2}{a_5} \partial_z^2 + k_s^2 \right] \Psi_s. \end{aligned} \quad (4.60)$$

Expressions (4.57)–(4.60) can also be used in the *axial far-field* with insignificant error for most crustal models.

4.3 The Fundamental Field Potential

In the previous section, the non-SH field was found to depend on a single potential. Consequently, we have given the curvilinear components of the Green's tensor in terms of this potential. It remains, therefore, to solve (4.36). This is accomplished by means of the three-dimensional spatial Fourier integral. Assume the feasibility of the representation

$$\Psi = \frac{e^{i\omega t}}{8\pi^3} \int \int \int_{-\infty}^{\infty} \frac{1}{Y} e^{-i(\alpha x + \beta y + \gamma z)} d\alpha d\beta d\gamma , \quad (4.61)$$

and the known identity

$$\delta(\vec{r}) = \frac{1}{8\pi^3} \int \int \int_{-\infty}^{\infty} e^{-i(\alpha x + \beta y + \gamma z)} d\alpha d\beta d\gamma . \quad (4.62)$$

Inserting these in Eq. (4.36) it is found that

$$Y(\alpha, \beta, \gamma; \omega) = [a_5\gamma^2 + a_1(\alpha^2 + \beta^2) - \omega^2][a_5(\alpha^2 + \beta^2) + a_2\gamma^2 - \omega^2] - a_3^2\gamma^2(\alpha^2 + \beta^2) . \quad (4.63)$$

We assume here without loss of generality that $\vec{r}_0 = 0$, since it can be reinstalled in the final result.

We make a change of variable from (α, β, γ) to spherical coordinates in wave-number space

$$\begin{aligned} \alpha &= \frac{\omega}{C} \sin \bar{\theta} \cos \bar{\phi} ; & \beta &= \frac{\omega}{C} \sin \bar{\theta} \sin \bar{\phi} ; & \gamma &= \frac{\omega}{C} \cos \bar{\theta}, \\ \alpha^2 + \beta^2 + \gamma^2 &= \frac{\omega^2}{C^2} . \end{aligned} \quad (4.64)$$

The Jacobian of this transformation is $J = \left| \frac{\omega^3}{C^4} \sin \bar{\theta} \right|$. Some algebra is required to show that Y in (4.63) is indeed factorable

$$Y = \frac{\omega^4}{C^4} (C^2 - C_p^2)(C^2 - C_{SV}^2) , \quad (4.65)$$

where

$$C_p^2 = \frac{m + \sqrt{M}}{2} ; \quad C_{SV}^2 = \frac{m - \sqrt{M}}{2} ,$$

$$m = a_5 + a_2 \cos^2 \bar{\theta} + a_1 \sin^2 \bar{\theta}, \quad (4.66)$$

$$\begin{aligned} M &= \left[(a_1 - a_5) \sin^2 \bar{\theta} + \left(\frac{2a_3^2}{a_1 - a_5} + a_5 - a_2 \right) \cos^2 \bar{\theta} \right]^2 - 4a_3^2 \left[\frac{a_3^2 - (a_1 - a_5)(a_2 - a_5)}{(a_1 - a_5)^2} \right] \cos^4 \bar{\theta} \\ &= [(a_1 - a_5) \sin^2 \bar{\theta} - (a_2 - a_5) \cos^2 \bar{\theta}]^2 + a_3^2 \sin^2 2\bar{\theta}. \end{aligned}$$

Note that C_p and C_{SV} are the *plane-wave phase-velocities* of the respective quasi-longitudinal and quasi-transverse waves (e.g., Fedorov, 1968; Musgrave, 1970). Only in the isotropic limit do these velocities signify a true longitudinal and transverse motions, respectively.

It is apparent from (4.66) that for media in which

$$a_3^2 = (a_1 - a_5)(a_2 - a_5), \quad (4.67)$$

the phase velocities assume the simpler form

$$C_p^2 = (a_1 \sin^2 \bar{\theta} + a_2 \cos^2 \bar{\theta}) ; \quad C_{SV}^2 = a_s. \quad (4.68)$$

Such media are known as *ellipsoidally-anisotropic* (Gassman, 1964). The P-wave fronts are ellipsoids of revolution. Thomsen (1986) showed that it is a special case of *weak anisotropy*, obtained by a Taylor-series expansion of the phase-velocity functions in (4.66) and (B.21). Keeping the first few terms therein, one obtains:

$$C_p = \sqrt{a_2}[1 + \delta \sin^2 \bar{\theta} \cos^2 \bar{\theta} + \epsilon \sin^4 \bar{\theta}] + O(\epsilon^2, \delta^2), \quad (4.69)$$

$$C_{SV} = \sqrt{a_5} \left[1 + \frac{a_2}{a_5}(\epsilon - \delta) \sin^2 \bar{\theta} \cos^2 \bar{\theta} \right] + O \left[\frac{a_2}{a_5}(\epsilon - \delta) \right]^2, \quad (4.70)$$

$$C_{SH} = \sqrt{a_5} \left[1 + \frac{1}{2}(\eta_{SH}^2 - 1) \sin^2 \bar{\theta} \right] + O \left[\left(\frac{\eta_{SH}^2 - 1}{4} \right)^2 \right], \quad (4.71)$$

where

$$\epsilon = \frac{a_1 - a_2}{2a_2}; \quad \delta = \frac{a_3^2 - (a_2 - a_5)^2}{2a_2(a_2 - a_5)}; \quad \frac{a_2}{a_5}(\epsilon - \delta) = \frac{1}{2} \left(\frac{1}{\eta_s^2} - 1 \right) \frac{a_1 - a_5}{a_2 - a_5}. \quad (4.72)$$

The case $\epsilon = \delta$ corresponds to ellipsoidal anisotropy. It is appropriate at this point to introduce some measure of anisotropy in the form of percentage deviation from isotropy. We arbitrarily define this deviation in terms of the parameter ϵ .

Inserting (4.64) and (4.65) into (4.61), the fundamental integral becomes

$$\Psi = -\frac{1}{8\pi^3\omega} \int_0^\infty \frac{dC}{[C^2 - C_p^2(\bar{\theta})][C^2 - C_{SV}^2(\bar{\theta})]} \int_{C^\pm} d\bar{\theta} \sin \bar{\theta} e^{-i\frac{\omega}{C} z \cos \bar{\theta}} \int_0^{2\pi} e^{-i\frac{\omega}{C} \sin \bar{\theta}(x \cos \bar{\phi} + y \sin \bar{\phi})} d\bar{\phi}. \quad (4.73)$$

Since $\gamma = \sqrt{(\alpha^2 + \beta^2) - \frac{\omega^2}{C^2}}$, where $(\alpha^2 + \beta^2)$ vary from zero to infinity, γ can obtain pure imaginary values. The variation of γ is then mapped onto a corresponding variation of $\bar{\theta}$ along either C^+ or C^- (Fig. 1), depending on the sign of z , to secure finite values of $e^{-i\gamma z}$. For all values of $\bar{\theta}$, $C_p^2(\bar{\theta})$ and $C_{SV}^2(\bar{\theta})$ are real. In (4.73), C^\pm is the *modified Weyl contour*, as explained in Appendix B. The integral over $\bar{\phi}$ is immediate and equals $2\pi J_0(\frac{\omega}{C} \Delta \sin \bar{\theta})$, where J_0 is the Bessel function of the first kind and order zero. Then, the integral over C is evaluated through the method of residues at the contributing poles $C = C_p$ and $C = C_{SV}$. Using

$$\int_{-\infty}^\infty dC \frac{e^{-i\frac{\omega}{C} z \cos \bar{\theta}} J_0(\frac{\omega}{C} \Delta \sin \bar{\theta})}{(C^2 - C_p^2 + i\omega)(C^2 - C_{SV}^2 + i\omega)} = \frac{\pi i}{C_p^2 - C_{SV}^2} \left[\frac{1}{C_{SV}} e^{-i\frac{\omega}{C_{SV}} z \cos \bar{\theta}} J_0\left(\frac{\omega}{C_{SV}} \Delta \sin \bar{\theta}\right) - \frac{1}{C_p} e^{-i\frac{\omega}{C_p} z \cos \bar{\theta}} J_0\left(\frac{\omega}{C_p} \Delta \sin \bar{\theta}\right) \right]. \quad (4.74)$$

The net result of the two integrations is

$$\begin{aligned} \Psi &= \frac{-i}{4\pi\omega} \int_{C^\pm} \frac{d\bar{\theta} \sin \bar{\theta}}{C_p^2(\bar{\theta}) - C_{SV}^2(\bar{\theta})} \left\{ \frac{J_0\left(\frac{\omega}{C_{SV}} \Delta \sin \bar{\theta}\right)}{C_{SV}(\bar{\theta})} e^{-i\frac{\omega}{C_{SV}} z \cos \bar{\theta}} - \frac{J_0\left(\frac{\omega}{C_p} \Delta \sin \bar{\theta}\right)}{C_p(\bar{\theta})} e^{-i\frac{\omega}{C_p} z \cos \bar{\theta}} \right\} \\ &= \Psi_s - \Psi_p. \end{aligned} \quad (4.75)$$

In the isotropic limit $C_p \rightarrow a$, $C_{SV} \rightarrow b$ and the classical Sommerfeld-Weyl integral ($\sigma = a$ or b)

$$\frac{e^{-ik_\sigma R}}{-ik_\sigma R} = \int_{C^\pm} d\bar{\theta} \sin \bar{\theta} J_0\left(\frac{\omega}{\sigma} \Delta \sin \bar{\theta}\right) e^{-i\frac{\omega}{\sigma} z \cos \bar{\theta}}, \quad (4.76)$$

secures the reduction of Ψ to the isotropic limit. Note that the first integral on the r.h.s. of (4.75) represents the *quasi-transverse* part of the field while the second integral is due to the *quasi-longitudinal* motion. The explicit evaluation of Ψ_s and Ψ_p via (4.75) can be facilitated by reducing it to a *single* integral. Indeed, starting from (4.61) and changing variables and coordinates to (Fig. 2).

$$\alpha = k \cos \bar{\phi}, \quad \beta = k \sin \bar{\phi}, \quad x = \Delta \cos \phi, \quad y = \Delta \sin \phi; \quad \gamma = s, \quad (4.77)$$

one arrives at the representation

$$\begin{aligned} \Psi &= \frac{1}{8\pi^3} \int_{\infty}^{-\infty} ds e^{-isz} \int_0^{\infty} k dk \int_0^{2\pi} d\bar{\phi} e^{-ik\Delta \cos(\phi - \bar{\phi})} Y^{-1}(k^2, s^2) \\ &= \frac{1}{4\pi^2} \int_0^{\infty} J_0(k\Delta) k dk \int_{-\infty}^{\infty} ds e^{-isz} Y^{-1}(k^2, s^2) ds, \end{aligned} \quad (4.78)$$

where

$$Y = d_4 s^4 + d_2 s^2 + d_0,$$

$$\begin{aligned} d_4 &= a_2 a_5, \\ d_2 &= a_2 a_1 (k^2 - k_p^2) + a_5^2 (k^2 - k_s^2) - a_3^2 k^2, \\ d_0 &= a_5 a_1 (k^2 - k_p^2)(k^2 - k_s^2). \end{aligned} \quad (4.79)$$

The integral over s is evaluated by taking the residues at its s -poles. The final result has the form of a *Hankel transform*

$$\begin{aligned} \Psi(\Delta, z) &= \frac{1}{8\pi a_2 a_5} \int_0^{\infty} \frac{J_0(k\Delta) k dk}{\sqrt{A k^4 + B k^2 + E^2}} \left[\frac{e^{-|z|S_2(k)}}{S_2(k)} - \frac{e^{-|z|S_1(k)}}{S_1(k)} \right] \\ &= \Psi_s - \Psi_p, \end{aligned} \quad (4.80)$$

with

$$\left. \begin{aligned} S_1^2 = k^2 - \frac{\omega^2}{C_p^2(k)} &= -\frac{1}{2}k_p^2 \left(\left(1 + \frac{c_{11}}{c_{44}} \right) + nk^2 + \sqrt{Ak^4 + Bk^2 + E^2}, \right. \\ S_2^2 = k^2 - \frac{\omega^2}{C_{SV}^2(k)} &= -\frac{1}{2}k_p^2 \left(1 + \frac{c_{11}}{c_{44}} \right) + nk^2 - \sqrt{Ak^4 + Bk^2 + E^2}, \\ A &= n^2 - m, \\ B &= (m - n) \left(1 + \frac{c_{11}}{c_{44}} \right) k_p^2, \\ E^2 &= \frac{1}{4}k_p^4 \left[\left(1 + \frac{c_{11}}{c_{44}} \right)^2 - \frac{4c_{11}^2}{c_{33}c_{44}} \right], \quad B^2 - 4AE \geq 0 \\ m &= \frac{c_{11}}{c_{33}} ; \quad n = \frac{c_{11}}{2c_{44}} - \frac{c_{13}}{2c_{33}} \frac{c_{13}}{c_{44}} - \frac{c_{13}}{c_{33}}. \end{aligned} \right\} \quad (4.81)$$

The representation of the Green's tensor as a Hankel transform can be straightforwardly obtained by substituting Ψ from (4.80) into (4.56).

In the isotropic limit

$$m = n = 1, \quad A = B = 0, \quad E = \frac{1}{2}(k_b^2 - k_a^2), \quad S_1 = \sqrt{k^2 - k_a^2}, \quad S_2 = \sqrt{k^2 - k_b^2}, \quad (4.82)$$

and the *Sommerfeld integral*

$$\frac{e^{-ik_a R}}{R} = \int_0^\infty J_0(k\Delta) e^{-|z|\sqrt{k^2 - k_a^2}} \frac{k dk}{\sqrt{k^2 - k_a^2}}, \quad (4.83)$$

guarantees that (4.80) falls back on the isotropic limit. Otherwise, the integral in (4.80) cannot be evaluated in closed analytical form except for special cases. The integral representation of the potential in (4.80) is valid for *all* values of the elastic parameters and its numerical evaluation is the subject of a sequel to the present paper. Another advantage of (4.80) is its suitability for the numerical calculation of displacement fields of sources in multilayered azimuthally isotropic media, using the known Haskell-Thomson matrix algorithm.

Fields of Point Forces

I. Localized force in the direction of the symmetry axis

This force does not excite SH waves. The displacements are given by $\vec{u} = F(\omega) \vec{G} \cdot \hat{e}_z$. Starting from (4.57) and (4.58), we obtain for a force in the z -direction

$$\vec{u} = \frac{F(\omega)}{\rho(a_1 - a_5)} [a_3 \vec{\nabla} \partial_z - \hat{e}_z (\omega^2 + a_1 \nabla_t^2 + (a_3 + a_5) \partial_z^2)] \Psi . \quad (4.84)$$

The error term in all expressions is $\mathcal{O}\left(\frac{1}{k_\beta R}\right)^2$. Radial and collatitudinal motions are obtained via the relations

$$u_{Rp} = u_{zp} \cos \theta + u_{\Delta p} \sin \theta ; \quad u_{\theta p} = -u_{zp} \sin \theta + u_{\Delta p} \cos \theta , \quad (4.85)$$

with similar relations for the SV motion. In the isotropic limit $u_{Rs} \rightarrow 0$; $u_{\theta s} \rightarrow 0$. Consequently,

$$u_{\theta s} \rightarrow -\frac{F(\omega)}{4\pi\mu} \sin \theta \frac{e^{-ik_b R}}{R} ; \quad u_{Rp} \rightarrow \frac{F(\omega)}{4\pi(\lambda+2\mu)} \cos \theta \frac{e^{-ik_a R}}{R} . \quad (4.86)$$

II. Localized force in the isotropy plane (x direction, say)

In this case, the displacement field becomes more complicated due to the presence of SH waves, in addition to the usual quasi-transverse and quasi-longitudinal waves. These are obtained directly from (B.35):

$$u_{\Delta}^{SH} = \frac{iF(\omega)}{4\pi\rho\eta_{SH}a_5} \frac{\cos \phi}{k_{SH}\Delta^2} e^{-ik_{SH}\hat{R}} , \quad (4.87)$$

$$u_{\phi}^{SH} = \frac{iF(\omega)}{4\pi\rho\eta_{SH}a_5} \sin \phi \left[\frac{i}{\hat{R}} + \frac{1}{k_{SH}\Delta^2} \right] e^{-ik_{SH}\hat{R}} , \quad (4.88)$$

where k_{SH} is defined in (B.15). Note the *line-source singularity* at $\Delta = 0$. [This singularity arises from the incongruity of the axial symmetry of the medium and the geometry of the localized

source. It is already inherent in the operator ∇_t^{-2} in Eq. (4.23).] The P-SV part of the field is evaluated from (4.57) and (4.58) under the conditions $(k_s R) \gg 1$.

III. Explosion (center of compression)

Since \vec{G} is symmetric, displacements are given by (Ben-Menahem and Singh, 1981)

$$\vec{u} = -M_0 \operatorname{div}_r \vec{G}(\vec{r}|\vec{r}_0; \omega), \quad (4.89)$$

where M_0 is the source's moment. Applying the operator div_r to (4.43), we obtain

$$\vec{u} = \frac{M_0}{\rho} \left\{ \vec{\nabla}_r [\omega^2 + (a_2 - a_3)\partial_z^2 + a_5 \nabla_t^2] \Psi + \hat{e}_z \partial_z [(a_3 + a_5 - a_2)\partial_z^2 + (a_1 - a_3 - a_5)\nabla_t^2] \Psi \right\}. \quad (4.90)$$

In the isotropic limit, the $r \cdot h \cdot s$ of (4.90) goes to

$$\vec{u}_{isotropic} = \frac{M_0}{\rho} \nabla_r (\omega^2 + \beta^2 \nabla^2) \Psi. \quad (4.91)$$

The two fields differ in two respects:

1. In azimuthally-isotropic media the explosion sources produce also shear waves.
2. The field is no more a gradient of a potential.

In the isotropic limit $u_{zs} \rightarrow 0$, $u_{zp} \rightarrow -\frac{M_0}{4\pi(\lambda+2\mu)} \frac{\partial}{\partial z} \left(\frac{e^{-ik_a R}}{R} \right)$, as it should. Also, $u_{\theta s} \rightarrow 0$, $u_{Rs} \rightarrow 0$, and $u_{\theta p} \rightarrow 0$. In the *far-field*, one obtains from (4.90):

$$\begin{aligned} u_{pz} &= \frac{M_0 a_1}{\rho} \left[\left(1 - \frac{a_3}{a_1} \right) \partial_\Delta^2 + \frac{a_5}{a_1} \partial_z^2 + k_p^2 \right] \frac{\partial \Psi_p}{\partial z}, \\ u_{p\Delta} &= \frac{M_0 a_1}{\rho} \left[\frac{a_5}{a_1} \partial_\Delta^2 + \frac{a_2 - a_3}{a_1} \partial_z^2 + k_p^2 \right] \frac{\partial \Psi_p}{\partial \Delta}, \\ u_{sz} &= \frac{M_0 a_5}{\rho} \left[\frac{a_1 - a_3}{a_5} \partial_\Delta^2 + \partial_z^2 + k_s^2 \right] \frac{\partial \Psi_s}{\partial z}, \\ u_{s\Delta} &= \frac{M_0 a_5}{\rho} \left[\partial_\Delta^2 + \frac{a_2 - a_3}{a_5} \partial_z^2 + k_s^2 \right] \frac{\partial \Psi_s}{\partial \Delta}, \end{aligned} \quad (4.92)$$

where $k_p^2 = \omega^2/a_1$; $k_s^2 = \omega^2/a_5$.

IV. Torque (center of rotation)

Let the moment of the torque align with the z -axis. The displacements are then given by (Ben-Menahem and Singh, 1981)

$$\vec{u} = M_0 \hat{e}_z \cdot \operatorname{curl} \vec{G}. \quad (4.93)$$

Considering (4.38), it is apparent that the term $a_3 \vec{\nabla} \vec{\nabla} \Psi$ does not contribute to the field. Then, using the tensor identity [for a fixed vector \vec{m} and variable symmetric dyadic \vec{G} with trace p .]

$$\vec{m} \cdot \operatorname{curl} \vec{G} \equiv \operatorname{curl}(\vec{m} \cdot \vec{G}) - \vec{m} \times \operatorname{div}(\vec{G} - p \vec{I}), \quad (4.94)$$

one can show that the rest of \vec{G} contributes the displacement

$$\vec{u} = \frac{i k_{SH} M_0}{4\pi\rho\eta_{SH} a_5} [\operatorname{grad} h_0^{(2)}(k_{SH} \hat{R}) \times \hat{e}_z], \quad (4.95)$$

which renders SH waves only.

The radiation pattern in the absolute far-field is

$$u_\varphi = \frac{-i k_{SH} M_0}{4\pi\rho\eta_{SH} a_5} \left[\frac{\sin \theta}{\sin^2 \theta + \eta^2 \cos^2 \theta} \right] \frac{e^{-ik_{SH}\hat{R}}}{R}. \quad (4.96)$$

V. Strike-slip displacement dislocation

The displacement field is of the explicit form (Ben-Menahem and Singh, 1981)

$$\vec{u} = -M_0(\omega) \left[\hat{e}_x \cdot \frac{\partial \vec{G}}{\partial y} + \hat{e}_y \cdot \frac{\partial \vec{G}}{\partial x} \right], \quad (4.97)$$

where the slip is in the xz -plane with a normal in the y direction and a moment $M_0(\omega)$. Applying the operator $(\hat{e}_x \frac{\partial}{\partial y} + \hat{e}_y \frac{\partial}{\partial x})$ to the explicit expression of \vec{G} in (4.57)–(4.58), we can derive the various field components.

Note that in all expressions for the displacements we have not included the contribution of the singularity tensors $\overset{\leftrightarrow}{G}_0^P$ and $\overset{\leftrightarrow}{G}_0^{SV}$ [Eqs. (4.51)–(4.52)]. Although these terms are of order $\frac{1}{z}$ in the axial far-field, their values relative to the absolute far-field are less than a few percent for all the crustal models listed in Thomsen (1986). The use of the integral representation (4.80) enables one to represent the displacement fields in a form of a Hankel transform. The kernels of these integrals for different seismic sources are shown in Table 1.

4.5 The Exact Total Displacement Field

In Table 1, we have considered the *far-field* displacements for several seismic sources. In this subsection we show the exact total displacement field. In the case of a center of compression (explosion), we obtain, for the z component

$$u_z = \frac{M_0(\omega)}{8\pi\rho a_2 a_5} \int_0^\infty dk h_0(z; k) J_0(k\Delta), \quad (4.98)$$

where

$$h_0(z; k) = \frac{k sgn(z)}{\sqrt{Ak^4 + Bk^2 + E^2}} \{ [(a_1 - a_3)k^2 - a_5 S_2^2(k) - \omega^2] e^{-|z|S_2(k)} - [(a_1 - a_3)k^2 - a_5 S_1^2(k) - \omega^2] e^{-|z|S_1(k)} \}. \quad (4.99)$$

For a horizontal force in the x -direction we find for the Δ component of the P-SV displacement field,

$$\begin{aligned} u_\Delta &= \frac{F(\omega) \cos \phi}{8\pi\rho a_2 a_5} \int_0^\infty dk h_1(z; k) \left[J_0(k\Delta) - \frac{1}{k\Delta} J_1(k\Delta) \right] \\ &= \frac{F(\omega) \cos \phi}{8\pi\rho a_2 a_5} \frac{\partial}{\partial \Delta} \int_0^\infty dk \frac{h_1(z; k)}{k} J_1(k\Delta), \end{aligned} \quad (4.100)$$

where

$$h_1(z; k) = \frac{k}{\sqrt{Ak^4 + Bk^2 + E^2}} \left\{ [a_5 k^2 - a_2 S_2^2(k) - \omega^2] \frac{e^{-|z|S_2(k)}}{S_2(k)} - [a_5 k^2 - a_2 S_1^2(k) - \omega^2] \frac{e^{-|z|S_1(k)}}{S_1(k)} \right\} . \quad (4.101)$$

The expression for u_Δ in (4.100) must be supplemented by the corresponding SH counterpart (4.87).

The fields of other sources can be represented in a similar way. When this source representation is coupled to a multilayered structure by means of Haskell-type algorithms, one can compute the fields of point sources in inhomogeneous anisotropic media.

4.6 Extension of the Theory to Sources in Multilayered Media

In multilayered isotropic media, the spectral response to point sources is constructed from the known solution of a homogeneous layer and the source integral representation in a boundless domain [e.g., Haskell, 1964]. We wish to apply this matrix algorithm to azimuthally isotropic media in which the axis of symmetry coincides with the vertical axis. Let us therefore write the fundamental potential of the l -th layer in its Hankel transform representation

$$\Psi^{(l)} = \frac{1}{8\pi a_2^{(l)} a_5^{(l)}} \int_0^\infty h^{(l)}(z; k) J_0(k\Delta) k dk , \quad (4.102)$$

where $h^{(l)}(z, k)$ is given explicitly in (4.80). We then substitute (4.102), together with the known representation

$$\delta(\vec{r} - \vec{r}_0) = \delta(z - z_0) \int_0^\infty J_0(k\Delta) k dk , \quad (4.103)$$

in (4.36). The resulting equation for $h^{(l)}(z; k)$ is then

$$d_4^{(l)} \frac{d^4 h^{(l)}(z; k)}{dz^4} - d_2^{(l)} \frac{d^2 h^{(l)}(z; k)}{dz^2} + d_0^{(l)} h^{(l)}(z; k) = 8\pi \delta(z - z_0) . \quad (4.104)$$

where the $\{d_0^{(l)}, d_2^{(l)}, d_4^{(l)}\}$ are defined, for each layer, in (4.79). To obtain the surface displacements for either surface waves or body waves on the surface of a multilayered half-space, one follows the procedure outlined in Haskell (1964) and Ben-Menahem and Harkrider (1964). To this end, we need the explicit general solution (4.104) at $z \neq z_0$ in the form of a sum of four wave-types corresponding to upgoing and downgoing quasi-longitudinal and quasi-transverse plane-waves. To these we add the source representation in the source layer given via (4.102) for the particular source in question. One can then calculate the fields of point sources in a multilayered anisotropic media.

5. STATIONARY PHASE APPROXIMATION OF THE GREEN'S TENSOR

We shall next derive the asymptotic Green's tensor for $\omega r \rightarrow \infty$. When ωr is large, the contributions from the integration over complex angles (inhomogeneous waves) are negligible compared to the contributions from the homogeneous waves. Therefore, the important contributions to the integral in (3.20) will arise from points on the real surface (Buchwald, 1959; Lighthill, 1960).

To this end we use the method of stationary phase, which says that (3.20) is asymptotic as $\omega r \rightarrow \infty$ to a sum of contributions from points on the slowness surface Γ_m where $\vec{r} \cdot \vec{s}$ is stationary, namely, from points on the slowness surface where the normal is parallel to \vec{r} .

Denoting these points as

$$\vec{s}^{(1)}, \vec{s}^{(2)}, \vec{s}^{(3)}, \dots, \vec{s}^{(N)}, \quad (5.1)$$

we obtain the asymptotic solution

$$G_{ij}(\vec{r}, \omega) = \frac{1}{4\pi\rho r} \sum_{m=1}^3 \sum_{l=1}^N \frac{C(\vec{s}^{(l)})}{w_m(\vec{s}^{(l)}) |\mathcal{K}_m(\vec{s}^{(l)})|^{1/2}} A_{ij}^{(m)}(\vec{s}^{(l)}) H(\vec{r} \cdot \vec{s}^{(l)}) e^{-i\omega \vec{r} \cdot \vec{s}^{(l)}}, \quad (5.2)$$

where

$$C(\vec{s}^{(l)}) \equiv -i \exp \left\{ \frac{-\pi i}{4} [sgn(\kappa_1(\vec{s}^{(l)})) + sgn(\kappa_2(\vec{s}^{(l)}))] \right\}. \quad (5.3)$$

Here $\kappa_1(\vec{s}^{(l)})$ and $\kappa_2(\vec{s}^{(l)})$ are the *principal curvatures* of the slowness surface at $\vec{s} = \vec{s}^{(l)}$, and

$$\mathcal{K}_m(\vec{s}^{(l)}) = \kappa_1(\vec{s}^{(l)}) \kappa_2(\vec{s}^{(l)}), \quad (5.4)$$

is the *Gaussian curvature* of the slowness surface, assumed non-zero, evaluated at $\vec{s} = \vec{s}^{(l)}$. The principal curvatures κ_1 and κ_2 are positive if the surface is concave to the direction \vec{r} . The case of parabolic points of the slowness surface at which the Gaussian curvature is zero can also be handled using the stationary phase approximation, but will not be considered in this paper.

We can see from (5.2) that the asymptotic expression of the Green's tensor depends on the group velocity and the curvature of the slowness surface. Also, we note that the amplitudes are inversely proportional to the distance from the source for all waves corresponding to ordinary points of the slowness surface. The error in (5.2), is $\mathcal{O}(1/r^2)$. Besides, we have assumed that the integrand in (3.20) varies slowly near the stationary points. The availability of the Green's tensor, in its exact (equation (3.20)) and asymptotic form (equation (5.2)) enables one to obtain analytical and numerical solutions for a wide range of media and sources.

Location of Stationary Points

We now set to evaluate the stationary points. Let

$$p(\vec{s}) = \frac{\vec{r} \cdot \hat{n}}{C_m} = \vec{r} \cdot \vec{s}, \quad (5.5)$$

in the argument of the exponential in (3.20), and let

$$\Gamma_m(\vec{s}) = 0, \quad (5.6)$$

be the slowness surface equation. Since the stationary points of the integral in (3.20) must belong to the slowness surface, it follows that the stationary points satisfy

$$\vec{\nabla}_{\vec{s}}[p(\vec{s}) - \nu \Gamma_m(\vec{s})] = 0, \quad (5.7)$$

$$\Gamma_m(\vec{s}) = 0, \quad (5.8)$$

where ν is a Lagrangian multiplier. Since

$$\vec{\nabla}_{\vec{s}}p(\vec{s}) = \vec{r}, \quad (5.9)$$

and

$$\vec{\nabla}_{\vec{s}} \Gamma_m(\vec{s}) = q \vec{w} , \quad (5.10)$$

where \vec{w} is the group velocity and q is a scalar, (5.7) can be rewritten as

$$\vec{r} - \nu q \vec{w} = 0 . \quad (5.11)$$

Taking the scalar product of (5.11) with \vec{s} and using the fact that $\vec{w} \cdot \vec{s} = 1$, which follows from (3.12) and (3.19), we obtain

$$\vec{r} \cdot \vec{s} = \nu q . \quad (5.12)$$

Thus, (5.11) takes the form

$$\vec{r} - (\vec{r} \cdot \vec{s}) \vec{w}(\vec{s}) = 0 . \quad (5.13)$$

Therefore, the stationary points will be obtained by solving simultaneously (5.8) and (5.13).

Considering $\vec{r} = r \hat{e}_r$ in (5.13), we obtain

$$\hat{e}_r \cdot \vec{s} = \frac{1}{|\vec{w}(\vec{s})|} . \quad (5.14)$$

So, using (5.5) and (5.14), we find at the stationary points, the interesting result

$$p(\vec{s}) = \frac{r}{|\vec{w}(\vec{s})|} . \quad (5.15)$$

Azimuthal Isotropy

SH case:

The slowness surface is

$$\Gamma_m(\vec{s}) = \frac{c_{66}}{\rho} s^2 + \frac{c_{44}}{\rho} s_3^2 - 1 , \quad (5.16)$$

with $s = (s_1^2 + s_2^2)^{1/2}$.

Due to the azimuthal symmetry, we consider $\vec{r} = \Delta \hat{e}_\Delta + z \hat{e}_z$ and the stationary points are obtained by solving the system

$$\begin{aligned}\Delta - \nu \frac{\partial \Gamma_m}{\partial s} &= 0, \\ z - \nu \frac{\partial \Gamma_m}{\partial s_3} &= 0, \\ \Gamma_m(\vec{s}) &= 0.\end{aligned}\tag{5.17}$$

Thus, we find

$$s = \pm \left(\frac{\rho}{c_{66}} \right)^{1/2} \frac{\sin \theta}{\left(\sin^2 \theta + \frac{c_{66}}{c_{44}} \cos^2 \theta \right)^{1/2}},\tag{5.18}$$

$$s_3 = \pm \left(\frac{\rho}{c_{66}} \right)^{1/2} \frac{\frac{c_{66}}{c_{44}} \cos \theta}{\left(\sin^2 \theta + \frac{c_{66}}{c_{44}} \cos^2 \theta \right)^{1/2}},\tag{5.19}$$

where θ is the collatitudinal angle corresponding to the observation point.

P-SV case:

The slowness surface is

$$\Gamma_m(\vec{s}) = m + \epsilon \sqrt{M} - 2,\tag{5.20}$$

where $\epsilon = 1$ in the P case and $\epsilon = -1$ in the SV case, and

$$m = \left(\frac{c_{11} + c_{44}}{\rho} \right) s^2 + \left(\frac{c_{33} + c_{44}}{\rho} \right) s_3^2,\tag{5.21}$$

$$M = \left[\left(\frac{c_{11} - c_{44}}{\rho} \right) s^2 + \left(\frac{c_{33} - c_{44}}{\rho} \right) s_3^2 \right]^2 - 4 \left[\left(\frac{c_{11} - c_{44}}{\rho} \right) \left(\frac{c_{33} - c_{44}}{\rho} \right) - \left(\frac{c_{13} + c_{44}}{\rho} \right)^2 \right] s^2 s_3^2.\tag{5.22}$$

The stationary points are obtained by solving the system (5.17) with $\Gamma_m(\vec{s})$ given in (5.20).

Eliminating ν , we have the system

$$\Delta \left[\frac{\partial m}{\partial s_3} + \frac{\epsilon}{2\sqrt{M}} \frac{\partial M}{\partial s_3} \right] - z \left[\frac{\partial m}{\partial s} + \frac{\epsilon}{2\sqrt{M}} \frac{\partial M}{\partial s} \right] = 0 , \quad (5.23)$$

$$\Gamma_m(\vec{s}) = 0 .$$

The exact solution of (5.23) for the stationary points can only be achieved numerically. This task is now under study. In order to obtain analytical solutions for the stationary points we consider an approximate form of the slowness surface (or, equivalently, of the phase velocity), the justification of which is stated in sections 5.2 and 5.3. We assume

$$\Gamma_P(\vec{s}) = \frac{c_{11}}{\rho} \left(s^2 + \frac{1}{\eta_p^2} s_3^2 \right) - 1 , \quad (5.24)$$

in the P case and in the SV case

$$\Gamma_{SV}(\vec{s}) = \frac{c_{44}}{\rho} \left(s^2 + \frac{1}{\eta_s^2} s_3^2 \right) - 1 . \quad (5.25)$$

Here, η_p and η_s are given later in (5.42) and 5.60) respectively. Using these forms of the slowness surfaces, we find for the stationary points:

Quasi-longitudinal wave:

$$s = \pm \left(\frac{\rho}{c_{11}} \right) \frac{\sin \theta}{(\sin^2 \theta + \eta_p^2 \cos^2 \theta)^{1/2}} , \quad (5.26)$$

$$s_3 = \pm \left(\frac{\rho}{c_{11}} \right) \frac{\eta_p^2 \cos \theta}{(\sin^2 \theta + \eta_p^2 \cos^2 \theta)^{1/2}} . \quad (5.27)$$

Quasi-transverse wave:

$$s = \pm \left(\frac{\rho}{c_{44}} \right) \frac{\sin \theta}{(\sin^2 \theta + \eta_s^2 \cos^2 \theta)^{1/2}} , \quad (5.28)$$

$$s_3 = \pm \left(\frac{\rho}{c_{44}} \right) \frac{\eta_s^2 \cos \theta}{(\sin^2 \theta + \eta_s^2 \cos^2 \theta)^{1/2}} . \quad (5.29)$$

The particular case of ellipsoidal anisotropy (Gassman, 1964) can be easily obtained from the previous results by setting

$$\eta_p^2 = \frac{c_{11}}{c_{33}} \quad \text{and} \quad \eta_s^2 = 1, \quad (5.30)$$

in (5.24)–(5.29).

5.1 SH Motion

We shall estimate the asymptotic SH Green's tensor, using the results obtained in Section 5. Since the slowness surface is an ellipsoid, there is only one point on it where the normal is parallel to a given direction. Therefore, if (x, y, z) are the coordinates of a given observation point in space, there will be only one kind of wave passing through it, corresponding to a point $(s_1^{(1)}, s_2^{(1)}, s_3^{(1)})$ on the slowness surface. The coordinates of the stationary point that give rise to outgoing waves are obtained from (5.18) and (5.19) by choosing the positive sign.

The evaluation of the Gaussian curvature is simplified when the slowness surface is axially symmetric. It is sufficient to evaluate \mathcal{K}_3 in the case $s_2 = 0$, and owing to the symmetry, the value thus obtained holds for all values of s_2 . We obtain

$$\mathcal{K}_3(\vec{s}) = \frac{\frac{c_{44}}{c_{66}} (s_1^2 + s_2^2 + \frac{c_{44}}{c_{66}} s_3^2)}{\left[s_1^2 + s_2^2 + \left(\frac{c_{44}}{c_{66}} \right)^2 s_3^2 \right]^2}. \quad (5.31)$$

Evaluating Eq. (5.31) at the stationary point $\vec{s}^{(1)}$ we have

$$\mathcal{K}_3(\vec{s}^{(1)}) = \frac{c_{44}}{\rho} \left(\sin^2 \theta + \frac{c_{66}}{c_{44}} \cos^2 \theta \right)^2. \quad (5.32)$$

The magnitude of the group velocity at the stationary point can be obtained from (4.5). We

have

$$w_3(\vec{s}^{(1)}) = \left(\frac{c_{66}}{\rho}\right)^{1/2} \left(\sin^2\theta + \frac{c_{66}}{c_{44}}\cos^2\theta\right)^{-1/2}. \quad (5.33)$$

The projection tensor $\overset{\leftrightarrow}{A}^{(3)}$ can be written conveniently in cylindrical coordinates as

$$\overset{\leftrightarrow}{A}^{(3)}(\vec{s}) = \hat{e}_\phi \hat{e}_\phi. \quad (5.34)$$

In this case both principal curvatures are negative so that $C(\vec{s}^{(1)}) = 1$. Therefore, the asymptotic expression of the Green's tensor for SH waves becomes

$$\overset{\leftrightarrow}{G}^{SH}(\vec{r}, \omega) = \frac{1}{4\pi(c_{44}c_{66})^{1/2}} \frac{\exp\left[-i\omega(\rho/c_{66})^{1/2} \left(\sin^2\theta + \frac{c_{66}}{c_{44}}\cos^2\theta\right)^{1/2} r\right]}{\left(\sin^2\theta + \frac{c_{66}}{c_{44}}\cos^2\theta\right)^{1/2} r} \hat{e}_\phi \hat{e}_\phi, \quad (5.35)$$

or, since $\hat{R} = r \left(\sin^2\theta + \frac{c_{66}}{c_{44}}\cos^2\theta\right)^{1/2}$, (see (4.26)), we can write

$$\overset{\leftrightarrow}{G}^{SH}(\vec{r}, \omega) = \frac{1}{4\pi(c_{44}c_{66})^{1/2}} \frac{\exp\left[-i\omega(\rho/c_{66})^{1/2} \hat{R}\right]}{\hat{R}} \hat{e}_\phi \hat{e}_\phi = g(z, \Delta; \omega) \hat{e}_\phi \hat{e}_\phi, \quad (5.36)$$

where we have used the definition of $g(z, \Delta)$ given in (4.25). Using (4.93) we have in homogeneous anisotropic media

$$\tilde{u}_{torque} = \frac{-M_0}{4\pi(c_{44}c_{66})^{1/2}} \text{grad}_r \left[\frac{e^{-i\omega(\rho/c_{66})^{1/2} r'}}{r'} \right] \times \hat{e}_z. \quad (5.37)$$

Therefore, in the *far field* we have for the displacement field of SH waves

$$\tilde{u}_{torque} = \frac{-i\omega(\rho/c_{66})^{1/2} M_0}{4\pi(c_{44}c_{66})^{1/2}} \left(\frac{\sin\theta}{\sin^2\theta + \frac{c_{66}}{c_{44}}\cos^2\theta} \right) \frac{\exp\left[-i\omega(\rho/c_{66})^{1/2} \left(\sin^2\theta + \frac{c_{66}}{c_{44}}\cos^2\theta\right)^{1/2} r\right]}{r} \hat{e}_\phi, \quad (5.38)$$

in agreement with Ben-Menahem (1989).

5.2 Quasi-Longitudinal Motion

The asymptotic expression corresponding to the P part of the total Green's tensor (equation (3.21)) is

$$\vec{G}_P(\vec{r}, \omega) = \frac{1}{4\pi\rho r} \sum_{l=1}^N \frac{C(\vec{s}^{(l)})}{w_p(\vec{s}^{(l)})|\mathcal{K}_p(\vec{s}^{(l)})|^{1/2}} \overset{(p)}{\vec{A}}(\vec{s}^{(l)}) H(\vec{r} \cdot \vec{s}^{(l)}) e^{-i\omega \vec{r} \cdot \vec{s}^{(l)}}. \quad (5.39)$$

We have stated earlier that the analytic determination of the stationary points in the case of azimuthally-isotropic media is hampered by the special algebraic form of C_p^2 (equation (4.66)).

We now consider an approximation of the phase velocity that enables us to find closed form expressions for the stationary points. Assume that we can write the P phase velocity as

$$C_p^2 = a_1(\sin^2 \bar{\theta} + \frac{1}{\eta_p^2} \cos^2 \bar{\theta}), \quad (5.40)$$

where η_p^2 is still unknown. It then follows algebraically from (4.66) that

$$\sqrt{M} = (a_1 - a_5) \sin^2 \bar{\theta} + \left(\frac{2a_1}{\eta_p^2} - a_2 - a_5 \right) \cos^2 \bar{\theta}. \quad (5.41)$$

When we compare (5.41) with M in (4.66) without the last term $\left\{ -4a_3^2 \frac{a_3^2 - (a_1 - a_5)(a_2 - a_5)}{(a_1 - a_5)^2} \cos^4 \bar{\theta} \right\}$, the solution for the unknown η_p^2 is

$$\eta_p^2 = \frac{a_1(a_1 - a_5)}{a_5(a_1 - a_5) + a_3^2}. \quad (5.42)$$

We then conclude that our approximation is valid whenever the neglect of the above term in the expression of the phase velocity is justified. For isotropic and ellipsoidally anisotropic media (equation (4.67)), this term is identically zero. In Figure 3a, we show the relative error in the quasi-longitudinal phase velocity when using this approximation for some earth materials considered by Thomsen (1986) (see Table 2). We can see that this approximation is uniformly valid for a wide range of angles and the error increases as we approach the axis $\bar{\theta} = 0$.

From (5.40) we obtain the equation of the slowness surface for quasi-longitudinal waves

$$a_1(s_1^2 + s_2^2 + \frac{1}{\eta_p^2} s_3^2) = 1. \quad (5.43)$$

This surface is an ellipsoid, and in the case of isotropy ($\eta_p = 1$), it reduces to a sphere of radius

$$\sqrt{\frac{1}{a_1}} = \sqrt{\frac{\rho}{\lambda+2\mu}}.$$

The coordinates of the stationary point that correspond to outgoing waves, are obtained from (5.26) and (5.27) by choosing the positive sign. In Figure 4, we show the geometry of the slowness surface in a generic case for which $\eta_p > 1$.

The magnitude of the group velocity is easily found by differentiation of the expression of the phase velocity

$$w_p(\vec{s}) = a_1 \left(s^2 + \frac{1}{\eta_p^4} s_3^2 \right)^{1/2}. \quad (5.44)$$

Evaluating (5.44) at the stationary point, we obtain

$$w_p(\vec{s}^{(1)}) = \frac{a_1^{1/2}}{(\sin^2 \theta + \eta_p^2 \cos^2 \theta)^{1/2}}. \quad (5.45)$$

Next, we calculate the Gaussian curvature. The axial symmetry simplifies the evaluation and we find

$$\mathcal{K}_p(\vec{s}) = \frac{1}{\eta_p^2} \frac{s^2 + s_3^2/\eta_p^2}{(s^2 + s_3^2/\eta_p^4)^2}. \quad (5.46)$$

At the stationary point

$$\mathcal{K}_p(\vec{s}^{(1)}) = \frac{a_1}{\eta_p^2} (\sin^2 \theta + \eta_p^2 \cos^2 \theta)^2. \quad (5.47)$$

We consider the eigenvector corresponding to quasi-longitudinal waves. For azimuthal isotropy, we can write, after some algebra, the displacement polarization eigenvector at the stationary point

as

$$\hat{T}^{(p)} = \sin \sigma_p \hat{e}_\Delta + \cos \sigma_p \hat{e}_z , \quad (5.48)$$

where

$$\sin \sigma_p = \sin \theta \frac{d_1(\theta)}{D(\theta)} , \quad (5.49)$$

$$\cos \sigma_p = \eta_p^2 \cos \theta \frac{d_2(\theta)}{D(\theta)} , \quad (5.50)$$

$$d_1(\theta) \equiv (a_1 - a_5) \sin^2 \theta + [a_1 - \eta_p^2(a_2 - a_3)] \eta_p^2 \cos^2 \theta , \quad (5.51)$$

$$d_2(\theta) \equiv a_3 \sin^2 \theta + (a_1 - a_5 \eta_p^2) \eta_p^2 \cos^2 \theta , \quad (5.52)$$

$$D(\theta) \equiv [d_1^2(\theta) \sin^2 \theta + d_2^2(\theta) \eta_p^4 \cos^2 \theta]^{1/2} . \quad (5.53)$$

In the isotropic limit $\sigma_p = \theta$, and we obtain the usual form of the displacement polarization vector for P waves.

Using (5.48) we have for the projection operator

$$\overset{\leftrightarrow}{A}^{(p)} = \vec{T}^{(p)} \vec{T}^{(p)} = \sin^2 \sigma_p \hat{e}_\Delta \hat{e}_\Delta + \sin \sigma_p \cos \sigma_p (\hat{e}_\Delta \hat{e}_z + \hat{e}_z \hat{e}_\Delta) + \cos^2 \sigma_p \hat{e}_z \hat{e}_z . \quad (5.54)$$

Then, substituting (5.45), (5.47) and (5.54) into (5.39), and using the fact that $C(\vec{s}^{(1)}) = 1$, we obtain the asymptotic expression of the Green's tensor for quasi-longitudinal waves

$$\overset{\leftrightarrow}{G}_P(\vec{r}, \omega) = \frac{\eta_p}{4\pi\rho a_1} \overset{\leftrightarrow}{A}^{(p)}(\theta) \frac{e^{-i\omega R_p/a_1^{1/2}}}{R_p} , \quad (5.55)$$

where

$$R_p \equiv r(\sin^2 \theta + \eta_p^2 \cos^2 \theta)^{1/2} . \quad (5.56)$$

5.3 Quasi-Transverse Motion

In this case the asymptotic expression of the Green's tensor is

$$\vec{G}_{SV}(\vec{r}, \omega) = \frac{1}{4\pi\rho r} \sum_{l=1}^N \frac{C(\vec{s}^{(l)})}{w_{SV}(\vec{s}^{(l)})|\mathcal{K}_{SV}(\vec{s}^{(l)})|^{1/2}} \vec{A}^{(SV)}(\vec{s}^{(l)}) H(\vec{r} \cdot \vec{s}^{(l)}) e^{-i\omega \vec{r} \cdot \vec{s}^{(l)}}, \quad (5.57)$$

and the corresponding phase velocity

$$C_{SV}^2 = \frac{1}{2}(m - \sqrt{M}), \quad (5.58)$$

with m and M given in (4.66).

At this point we follow the same arguments considered for approximating the phase velocity in the quasi-longitudinal case. Assuming that we can write the SV phase velocity as

$$C_{SV}^2 = a_5(\sin^2 \bar{\theta} + \frac{1}{\eta_s^2} \cos^2 \bar{\theta}), \quad (5.59)$$

with η_s^2 still unknown, it follows algebraically from (5.58) that

$$\eta_s^2 = \frac{a_5(a_1 - a_5)}{a_2(a_1 - a_5) - a_3^2}, \quad (5.60)$$

as long as the last term in M in (4.66) can be neglected. In Figure 3b we show the relative error in phase velocity when using the approximate expression (5.59) for some earth materials considered by Thomsen (1986) (see Table 2). Again, we observe that the approximation is uniformly valid for a wide range of angles except along the axis $\bar{\theta} = 0$.

From (5.60) we know that this approximation for the quasi-transverse waves fails whenever

$$a_2(a_1 - a_5) \leq a_3^2, \quad (5.61)$$

yielding unbounded or imaginary values of η_s at those points. Although (5.61) is not excluded by the physical realizability conditions,² media of this type are rare in earth sedimentary rocks (only 2 out of 58 cases; Thomsen, 1986).

The equation of the slowness surface is obtained from (5.59)

$$a_5 \left(s_1^2 + s_2^2 + \frac{s_3^2}{\eta_s^2} \right) = 1 , \quad (5.62)$$

with the corresponding stationary point for outgoing waves given in (5.28) and (5.29), choosing again the positive sign. The magnitude of the group velocity at the stationary point takes the form

$$w_{SV}(s^{(1)}) = \frac{a_5^{1/2}}{(\sin^2 \theta + \eta_s^2 \cos^2 \theta)^{1/2}} , \quad (5.63)$$

and the Gaussian curvature is

$$\mathcal{K}_{SV}(\bar{s}^{(1)}) = \frac{a_5}{\eta_s^2} (\sin^2 \theta + \eta_s^2 \cos^2 \theta)^2 . \quad (5.64)$$

Next, we consider the displacement polarization eigenvector for the quasi-transverse waves at the stationary point. After some algebra, one obtains

$$\vec{T}^{SV} = \cos \sigma_s \hat{e}_\Delta - \sin \sigma_s \hat{e}_z , \quad (5.65)$$

where

$$\sin \sigma_s = \sin \theta \frac{b_1(\theta)}{E(\theta)} , \quad (5.66)$$

$$\cos \sigma_s = \eta_s^2 \cos \theta \frac{b_2(\theta)}{E(\theta)} , \quad (5.67)$$

² $c_{11}c_{33} > c_{13}^2$, $c_{11} > c_{33}$, $(c_{11} + c_{12})c_{33} > 2c_{13}^2$
 $c_{11} > 0$, $c_{33} > 0$, $c_{44} > 0$, $c_{66} > 0$, $|c_{12}| > 0$

$$b_1(\theta) \equiv (a_1 - a_5) \sin^2 \theta + \left[\left(\frac{\eta_s}{\eta_p} \right)^2 a_1 - \eta_s^2 (a_2 - a_3) \right] \eta_s^2 \cos^2 \theta , \quad (5.68)$$

$$b_2(\theta) \equiv a_3 \sin^2 \theta + \left[\left(\frac{\eta_s}{\eta_p} \right)^2 a_1 - a_5 \eta_s^2 \right] \eta_s^2 \cos^2 \theta , \quad (5.69)$$

$$E(\theta) \equiv [b_1^2(\theta) \sin^2 \theta + b_2^2(\theta) \eta_s^4 \cos^2 \theta]^{1/2} . \quad (5.70)$$

In the isotropic limit $\sigma_s = \theta$ and the conventional expression of the displacement polarization vector for SV waves follows.

From (5.65) the corresponding projector operator is

$$\overleftrightarrow{A}^{(SV)} = \vec{T}^{(SV)} \vec{T}^{(SV)} = \cos^2 \sigma_s \hat{e}_\Delta \hat{e}_\Delta - \sin \sigma_s \cos \sigma_s (\hat{e}_\Delta \hat{e}_z + \hat{e}_z \hat{e}_\Delta) + \sin^2 \sigma_s \hat{e}_z \hat{e}_z . \quad (5.71)$$

Therefore, using (5.63), (5.64), (5.71) and (5.57), together with the fact that $C(s^{(1)}) = 1$, the asymptotic Green's tensor for the quasi-transverse SV waves is

$$\vec{G}_{SV}(\vec{r}, \omega) = \frac{\eta_s^2}{4\pi\rho a_5} \overleftrightarrow{A}^{(SV)}(\theta) \frac{e^{-i\omega R_s/a_5^{1/2}}}{R_s} , \quad (5.72)$$

where

$$R_s \equiv r(\sin^2 \theta + \eta_s^2 \cos^2 \theta)^{1/2} . \quad (5.73)$$

5.4 Divergence Coefficients and Wave Surfaces

We have noticed in (5.36), (5.55), and (5.72) a typical divergence coefficient for the Green's tensor of the form

$$\frac{1}{r(\sin^2 \theta + \eta^2 \cos^2 \theta)^{1/2}} , \quad (5.74)$$

where $\eta = \eta_p$, η_s , or η_{SH} . In order to give a geometrical interpretation to the angular dependence of (5.74), we consider the corresponding wave surface. Its equation can be obtained by following

waves for which the phase $\omega(\vec{r} \cdot \vec{s} - t)$ is zero. then, at $t = 1$,

$$\vec{r} \cdot \vec{s} = 1 . \quad (5.75)$$

The waves at point \vec{r} in space are generated by a point \vec{s} of the slowness surface, satisfying $\Gamma_m(\vec{s}) = 0$, at which the normal is parallel to the vector \vec{r} , namely,

$$\vec{r} = q \vec{\nabla} \Gamma_m , \quad (5.76)$$

q being a scalar. Taking the scalar product of (5.76) with \vec{s} and using (5.75), we obtain

$$q = \frac{1}{\vec{\nabla} \Gamma_m \cdot \vec{s}} . \quad (5.77)$$

Therefore, the coordinates of a point of the wave surface, at $t = 1$, will be given by

$$\vec{r} = \frac{\vec{\nabla} \Gamma_m}{\vec{\nabla} \Gamma_m \cdot \vec{s}} = \frac{\vec{w}}{\vec{w} \cdot \vec{s}} = \vec{w} , \quad (5.78)$$

where \vec{w} is the group velocity vector.

Since, under the approximations considered in this paper, the P, SV and SH slowness surfaces are ellipsoids, it is sufficient to exhibit only one example. For the P case it follows from (5.78) that the equation of the wave surface is

$$\frac{1}{a_1} (x^2 + y^2 + \eta_p^2 z^2) = 1 . \quad (5.79)$$

In Figure 5 we show the geometry of the wave surface in a generic case for which $\eta_p > 1$. We can easily see that

$$\frac{a_1^{1/2}}{|\vec{r}_\omega|} = \frac{|\vec{w}^{isotropic}|}{|\vec{w}^{(p)}(\vec{s})|} = (\sin^2 \theta + \eta_p^2 \cos^2 \theta)^{1/2} = \frac{R_p}{r} . \quad (5.80)$$

Therefore, we find that the ratio $\frac{|\text{position on isotropic wave surface}|}{|\text{position on anisotropic wave surface}|}$ or, equivalently, the ratio $\frac{|\text{magnitude of isotropic group velocity}|}{|\text{magnitude of anisotropic group velocity}|}$, along the direction of the observation point gives the angular dependence of the divergence coefficient (5.74).

5.5 Anisotropy Data

In order to apply our theory we consider an exhaustive listing of measurements of anisotropy for 58 earth materials, including mostly sedimentary rocks, reported in Thomsen (1986). These data were interpreted by the original investigators in terms of the five elastic constants of azimuthal isotropy. About 70% of these models have a maximum error below 30% at $\bar{\theta} = 0$ and 180° when we use the approximate expression for the phase velocities given in (5.40) and (5.59). However, in the range $30^\circ \leq \bar{\theta} \leq 150^\circ$, the error is approximately below 10% (see Figure 3). In Table 2 we show a partial list of these models, including the elastic constants, η_p^2 , η_s^2 , and the anisotropy parameter ϵ (percentage)

$$\epsilon(\%) = \frac{c_{11} - c_{33}}{2c_{33}} \times 100 , \quad (5.81)$$

as a, somewhat arbitrary, measure of anisotropy.

As another indicator of the fit of the approximation of the phase velocities, we show in Figure 6 the exact and approximate slowness surfaces for four selected models (see Table 2). The good fit of the approximation for a wide range of angles centered at $\bar{\theta} = 90^\circ$ is again apparent. Besides, we can see that this approximation induces ellipsoidal slowness surfaces, and therefore excludes the possibility of parabolic points.

In the next subsection we evaluate the displacement fields and radiation patterns of some

common seismic sources.

5.6 Radiation Patterns

I. Localized force in the direction of the symmetry axis.

The representation of this field in terms of the fundamental potential Ψ was discussed already in Section 4.3. It can also be given directly in terms of the Green's tensor

$$\vec{u} = F(\omega)[\vec{G}_P + \vec{G}_{SV}] \cdot \vec{e}_z . \quad (5.82)$$

Using the asymptotic expressions in (5.55) and (5.72), we obtain the results shown in Tables 3 and 4.

In Figures 7a and 7b we show the vertical radiation patterns of the amplitude spectrum, namely, the dependence of the spectral displacement field of u_{zp} and u_{zs} , respectively, on θ for fixed azimuth and r . The isotropic limit is marked by a broken line. The deviation of the results from the isotropic case demonstrates that these patterns can be used as diagnostic aids for the identification of anisotropic regions in the earth's crust and mantle.

II. Localized force in the isotropy plane (x -direction).

Here, the displacement field is determined by

$$\vec{u} = F(\omega)[\vec{G}_P + \vec{G}_{SV}] \cdot \hat{e}_x , \quad (5.83)$$

and using (5.55) and (5.72) we obtain the results shown in Tables 3 and 4.

In Figures 8a and 8b we show the vertical radiation patterns corresponding to the amplitude spectrum of $u_{\theta p}$ and u_{rs} , respectively. These components are null in the isotropic limit, and may

thus be used to diagnose azimuthal isotropy provided a powerful enough source is used and the collatitudinal coverage in the recordings is adequate.

III. Explosion (center of compression)

Since \vec{G} is symmetric, the displacement field is given by (4.92). Using the asymptotic expressions for the Green's tensor in (5.55) and (5.72), we find the results indicated in Tables 3 and 4.

Contrary to the isotropic case, explosion sources in azimuthally isotropic media also produce shear waves. In Figures 9a and 9b we show the vertical radiation patterns corresponding to the u_{zp} and u_{zs} (not present in the isotropic case) components, respectively. Using these two components, we can evaluate the SV/P ratio of the displacement field. The results are shown in Figure 10. We observe that SV/P ratios as large as 4.5 are predicted (Model 5, Robertson and Corrigan, 1983). This indicates that explosion sources can be used diagnostically to establish anisotropy provided that sufficiently strong quasi-longitudinal waves are generated.

In Figures 11a, 11b, 12a, and 12b, we present the vertical radiation patterns corresponding to the $u_{\Delta s}$, $u_{\theta p}$, $u_{\theta s}$ and u_{rs} components, respectively. All these components are null in the isotropic limit. For anisotropic media we have a variety of new radiation patterns including an "eight lobe" pattern for Model 3 (Lin, 1985). This behavior can therefore be used effectively in the identification of azimuthal isotropy.

IV. Strike-slip displacement dislocation

The displacement field in this case has already been given in Section 4.3. Applying the operator

$(\vec{e}_x \cdot \frac{\partial}{\partial y} + \vec{e}_y \cdot \frac{\partial}{\partial x})$ to the asymptotic expressions (5.55) and (5.72), we derive the various field components. The corresponding results are given in Tables 3 and 4.

In Figure 13 we compare the radiation patterns of $u_{\theta p}$ for two sources in tuff (Model 7, Table 2). The analytic form of this pattern is listed in Table 4. The sources are: a point strike-slip dislocation in the xz plane and a point-explosion. The patterns are almost identical in shape.

In Figure 14 we compare the radiation patterns of the same sources in Mesaverde clayshale (Model 1, Table 2). Here we display the u_{zs} displacement component (Table 3). Again, the patterns are indistinguishable.

These results show that even in weak anisotropic media, explosions can masquerade for strike-slip earthquake faults. The ramifications of these results are discussed elsewhere (Ben-Menahem and Toksöz, 1989).

Note that our radiation patterns were calculated for the case where both source and receivers are in the same anisotropic medium. This may seem a rather specific case. Nevertheless, the results are useful, among other applications, in geophysical exploration for oil. For example, in the situation where the source is located in an open hole section of a borehole.

6. DISCUSSION AND CONCLUSIONS

We have derived analytic approximations for the far field of point sources in azimuthally-isotropic media. Our results exhibit the strong effects that anisotropy has on the source's directional energy radiation and the partition of energy between the longitudinal and shear components of the motion. We have also shown that Haskell matrix method is applicable, without modification, to multilayered azimuthally isotropic media in which the axis of symmetry and inhomogeneity coincide.

In our study we have employed the multidimensional stationary phase approximation which limits the results to frequency and spatial domains such that ωr is large. Also, in the process of determining the stationary points we found it convenient to approximate the phase velocities itself. The price payed for this artifice was the lesser accuracy of the spectral amplitudes on and near the axis of symmetry. This restriction can be removed by solving numerically for the stationary points. The alternative for the stationary phase approximation is the numerical calculation of the Hankel transform in the exact analytical solution. Note that by our simultaneous use of the stationary phase approximation and the approximated phase velocities we avoid the parabolic points on the slowness surface since these surfaces are approximated by ellipsoids. In general, however, the stationary phase approximation fails at parabolic points of the slowness surface and a higher order approximation must be made at these points.

The availability of the Green's tensor in closed form enables one to extend the results to anisotropic half-space configurations where the axis of symmetry is not necessarily normal to the free surface. This will be used to model azimuthal anisotropy

Acknowledgments

Discussions held with Drs. M. N. Toksöz and W. Beydoun are gratefully acknowledged. We wish to thank Dr. Don Eckhardt and James F. Lewkowicz at the Earth Sciences Division of the Air Force Geophysics Laboratory for their encouragement throughout this work. Ms. Liz Henderson, at the M.I.T. Earth Resources Laboratory, kindly typed the manuscript. This research was supported by the Defense Advanced Research Projects Agency through contract F19628-87-K-0054 administered by the Air Force Geophysics Laboratory.

REFERENCES

Bamford, D. and K.R. Nunn, 1979, In-situ seismic measurements of crack anisotropy in the carboniferous limestone of northwest England, *Geophysical Prospecting*, **27**, 322-338.

Banik, N.C., 1984, Velocity anisotropy of shales and depth estimation in the North Sea basin, *Geophysics*, **49**, 1411-1419.

Ben-Menahem, A., 1987, Green's tensor for inhomogeneous elastic media, *Proc. Roy. Soc. London A*, **409**, 287-327.

Ben-Menahem, A., 1989, SH waves from point sources in anisotropic inhomogeneous media, *Geophysics*, in press.

Ben-Menahem, A. and D.G. Harkrider, 1964, Radiation patterns of seismic surface waves from buried dipolar sources in flat stratified earth, *Jour. Geophys. Res.*, **69**, 2605-2620.

Ben-Menahem, A. and S.T. Singh, 1981, *Seismic Waves and Sources*, Springer Verlag, New York.

Ben-Menahem, A. and M.N. Toksöz, 1989, Radiation patterns from explosions in anisotropic media, submitted to *Science*.

Buchwald, V.T., 1959, Elastic waves in anisotropic media, *Proc. Roy. Soc. London A*, **253**, 563-580.

Carlson, R.L., C.H. Schaftenaar, and R.P. Moore, 1984, Causes of compressional-wave anisotropy in carbonate-bearing, deep-sea sediments, *Geophysics*, **49**, 525-532.

Cholet, J. and H. Richard, 1954, A test on elastic anisotropy measurement at Berriane (North Sahara), *Geophys. Prospecting*, **2**, 232-246.

Corrigan, D., 1989, Anisotropy in exploration seismology: Experimental evidence (M.I.T. seminar, April 27).

Crampin, S., 1985, Evaluation of anisotropy by shear wave splitting, *Geophysics*, **50**, 383-411.

de Segonzac, P.D. and J. Laherrere, 1959, Application of the continuous velocity log to anisotropy measurements in Northern Sahara; Results and consequences, *Geophys. Prospecting*, **7**, 202-217.

Fedorov, F.I., 1968, *Theory of Elastic Waves in Crystals*, Plenum Press, New York.

Garmay, J., 1988, Seismograms in stratified anisotropic media, *Jour. Geophys. Res.*, **92**, 365-377.

Gassman, F., 1964, Introduction to seismic travel-time methods in anisotropic media, *Pure and App. Geophysics*, **58**, 53-112.

Giesel, W., 1963, Elastische Anisotropie in tektonisch verformten Sedimentgesteinen, *Geophys. Prospecting*, **1**, 423-458.

Gretener, P.E.F., 1961, An analysis of the observed time discrepancies between continuous and conventional well velocity surveys, *Geophysics*, **26**.

Gupta, I.N., 1973, Premonitory variations in S-wave anisotropy before earthquakes in Nevada, *Science*, **182**, 1129-132.

Hanyga, A., 1984, Point source in anisotropic medium, *Gerlands Beitrage zur Geophysik*, **93**, 463-479.

Haskell, N.A., 1964, Radiation patterns of surface waves from point sources in a multilayered medium, *Bull. Seism. Soc. Amer.*, **54**, 377-393.

Helbig, K., 1984, Transverse isotropy in exploration seismics, *Geophys. J.R. Astr. Soc.*, **76**, 79-88.

Jones, L.E.A. and H.F. Wang, 1981, Ultrasonic velocities in cretaceous shales from the Williston basin, *Geophysics*, **46**, 288-297.

Kafka, A.L. and E.C. Reiter, 1987, Dispersion of Rg waves in southeastern Maine: Evidence for

lateral anisotropy in the shallow crust, *Bull. Seism. Soc. Amer.*, 77, 925-941.

Kerner, C., B. Dyer and M. Worthington, 1989, Wave propagation in a vertical transversely isotropic medium: field experiment and model study, *Geophys. J.R. Astr. Soc.*, 97, 295-309.

Leary, P.C. and T.L. Henyey, 1985, Anisotropy and fracture zones about a geothermal well from P-wave velocity profiles, *Geophysics*, 50, 25-36.

Leary, P.C., Y.-G. Li and K. Aki, 1987, Observation and modeling of fault-zone fracture seismic anisotropy—I. P, SV and SH travel times, *Geophys. J.R. Astr. Soc.*, 91, 461-484.

Levin, F.K., 1979, Seismic velocities in transversely isotropic media, *Geophysics*, 44, 918-936.

Lighthill, M.J., 1960, Studies on magneto-hydrodynamic waves and other anisotropic wave motions, *Phil. Trans. Roy. Soc. London A*, 252, 297-430.

Lin, W., 1985, Ultrasonic velocities and dynamic elastic moduli of Mesaverde rock, *Lawrence Livermore Nat. Lab., Rep. 20273*, rev. 1.

Lo, T.-W., K.B. Coyner, and M.N. Toksöz, 1986, Experimental determination of elastic anisotropy of Berea sandstone, Chicopee shale and Chelmsford granite, *Geophysics*, 51, 164-171.

McCollum, B. and Snell, F.A., 1944, Asymmetry of sound velocity in stratified formation, Early geophysical papers, Society of Exploration Geophysicists, 216-227.

Musgrave, M.J.P., 1954, On the propagation of elastic waves in aelotropic media: II. Media of hexagonal symmetry, *Proc. Roy. Soc. London A*, 226, 356-366.

Musgrave, M.J.P., 1970, *Crystal Acoustics*, Holden-Day, San Francisco.

Rai, C.S. and K.E. Hanson, 1988, Shear-wave velocity anisotropy in sedimentary rocks, *Geophysics*, 53, 800-806.

Richards, T.C., 1960, Wide angle reflections and their application to finding limestone structures in the foothills of Western Canada, *Geophysics*, 25, 385-407.

Ricker, N., 1953, The form and laws of propagation of seismic wavelets, *Geophysics*, 18, 10-40.

Robertson, J.D. and D. Corrigan, 1983, Radiation patterns of a shear-wave vibrator in near-surface shale, *Geophysics*, 48, 19-26.

Schock, R.N., B.P. Bonner, and H. Louis, 1974, collection of ultrasonic velocity data as a function of pressure for polycrystalline solids, Lawrence Livermore Nat. Lab. Rep. UCRL-51508.

Singh, S.C. and C.H. Chapman, 1988, WKBJ seismogram theory in anisotropic media, *J. Acoust. Soc. Am.*, 84, 732-741.

Stephen, R.A., 1985, Seismic anisotropy in the upper oceanic crust, *Jour. Geophys. Res.*, 66, 3487-3496.

Struik, D. J., 1961, *Lectures on Classical Differential Geometry*, Addison-Wesley, Massachusetts.

Synge, J.L., 1957, Elastic waves in anisotropic media, *Journal of Mathematics and Physics*, 35, 323-334.

Thomsen, L., 1986, Weak elastic anisotropy, *Geophysics*, 51, 1954-1966.

Uhrig, L.F. and F.A. Van Melle, 1955, Velocity anisotropy in stratified media, *Geophysics*, 20, 774-779.

Van der Stoep, D.M., 1966, Velocity anisotropy measurements in wells, *Geophysics*, 31, 900-916.

Vinnik, L.P., G.L. Kosarev, and L.I. Makeyeva, 1986, Azimuthal anisotropy of the earth's interior from observations of long-period body waves: Izvestia, *Earth Physics*, 22, 955-960.

Weatherby, B.B., W.T. Born, and Harding, 1934, Granite and limestone velocity determination in

Arbuckle Mountains, Oklahoma, *Bull. Am. Assn. Petr. Geol.*, 18, 106-118.

White, J.E. and R.L. Sengbush, 1953d, Velocity measurements in near-surface formations, *Geophysics*, 18, 54-70.

White, J.E., Martineau-Nicoletis, and C. Monash, 1983, Measured anisotropy in Pierre shale, *Geophys. Prospecting*, 31, 709-725.

Winterstein, D.R., 1986, Anisotropy effects in P-wave and SH-wave stacking velocities containing information on lithology, *Geophysics*, 51, 661-672.

Yeatts, F.R., 1984, Elastic radiation from a point source in an anisotropic medium, *Phys. Rev. B.*, 29, 1674-1684.

APPENDIX A. DIFFERENTIAL GEOMETRY OF THE SLOWNESS SURFACE

Some differentio-geometrical properties of the slowness surface are needed for the evaluation of the Green's tensor. Let the position vector of a point on the slowness surface be parameterized as

$$\begin{aligned}s_1 &= R(\theta, \phi) \sin \theta \cos \phi, \\ s_2 &= R(\theta, \phi) \sin \theta \sin \phi, \\ s_3 &= R(\theta, \phi) \cos \theta\end{aligned}\tag{A.1}$$

with $0 \leq \theta \leq \pi$, $0 \leq \phi < 2\pi$.

From (3.12) we have

$$|\vec{s}| = \frac{1}{C_m} \tag{A.2}$$

where C_m is the phase velocity of type- m waves. It then follows from A.1 and A.2 that

$$R(\theta, \phi) = \frac{1}{C_m(\theta, \phi)}. \tag{A.3}$$

We shall omit the subscript m in $R(\theta, \phi)$ for convenience but it is understood that the function $R(\theta, \phi)$ will be different depending on the sheet of the slowness surface under discussion.

We now evaluate the two vectors $\frac{\partial \vec{s}}{\partial \theta}$ and $\frac{\partial \vec{s}}{\partial \phi}$ which lie in the tangent plane. We obtain

$$\frac{\partial \vec{s}}{\partial \theta} = \frac{\partial R}{\partial \theta} \hat{e}_r + R \hat{e}_\theta, \tag{A.4}$$

and

$$\frac{\partial \vec{s}}{\partial \phi} = \frac{\partial R}{\partial \phi} \hat{e}_r + R \sin \theta \hat{e}_\phi. \tag{A.5}$$

The slowness surface normal is then obtained from (Struik, 1961)

$$\vec{N} = \frac{\partial \vec{s}}{\partial \theta} \times \frac{\partial \vec{s}}{\partial \phi} = R \left(R \sin \theta \hat{e}_r - \frac{\partial R}{\partial \theta} \sin \theta \hat{e}_\theta - \frac{\partial R}{\partial \phi} \hat{e}_\phi \right). \tag{A.6}$$

From A.6, the surface element on the slowness surface can be easily evaluated (see (3.17))

$$d\sigma = |\vec{N}| d\theta d\phi \Rightarrow \\ \Rightarrow d\sigma = R^2 \left\{ \sin^2 \theta \left[1 + \left(\frac{1}{R} \frac{\partial R}{\partial \theta} \right)^2 \right] + \left(\frac{1}{R} \frac{\partial R}{\partial \phi} \right)^2 \right\}^{1/2} d\theta d\phi . \quad (\text{A.7})$$

Another important quantity in evaluating the Green's tensor is the group velocity. We obtain it by differentiation of the phase velocity of type- m waves

$$\vec{w}^{(m)} = C_m \hat{e}_r + \frac{\partial C_m}{\partial \theta} \hat{e}_\theta + \frac{1}{\sin \theta} \frac{\partial C_m}{\partial \phi} \hat{e}_\phi . \quad (\text{A.8})$$

Its magnitude takes the form

$$w_m(\theta, \phi) = \left[C_m^2 + \left(\frac{\partial C_m}{\partial \theta} \right)^2 + \frac{1}{\sin^2 \theta} \left(\frac{\partial C_m}{\partial \phi} \right)^2 \right]^{1/2} , \quad (\text{A.9})$$

or, in terms of $R(\theta, \phi)$,

$$w_m(\theta, \phi) = \frac{1}{R^2} \left[R^2 + \left(\frac{\partial R}{\partial \theta} \right)^2 + \frac{1}{\sin^2 \theta} \left(\frac{\partial R}{\partial \phi} \right)^2 \right]^{1/2} . \quad (\text{A.10})$$

From (A.6) and (A.8), we also find

$$\vec{N} = \frac{\sin \theta}{C_m^3} \vec{w}^{(m)} , \quad (\text{A.11})$$

as expected, since the group velocity vector is normal to the slowness surface.

Finally, we give the necessary expressions for the evaluation of the Gaussian curvature. We start with the first and second fundamental forms of the slowness surface (Struik, 1961)

$$I = E(d\theta)^2 + 2Fd\theta d\phi + G(d\phi)^2 = d\vec{s} \cdot d\vec{s} , \quad (\text{A.12})$$

$$II = e(d\theta)^2 + 2fd\theta d\phi + g(d\phi)^2 = -d\vec{s} \cdot \vec{N} . \quad (\text{A.13})$$

where

$$E = \frac{\partial \vec{s}}{\partial \theta} \cdot \frac{\partial \vec{s}}{\partial \theta}, \quad (\text{A.14})$$

$$F = \frac{\partial \vec{s}}{\partial \theta} \cdot \frac{\partial \vec{s}}{\partial \phi}, \quad (\text{A.15})$$

$$G = \frac{\partial \vec{s}}{\partial \phi} \cdot \frac{\partial \vec{s}}{\partial \phi}, \quad (\text{A.16})$$

$$e = \frac{\partial^2 \vec{s}}{\partial \theta^2} \cdot \vec{N}, \quad (\text{A.17})$$

$$f = \frac{\partial^2 \vec{s}}{\partial \theta \partial \phi} \cdot \vec{N}, \quad (\text{A.18})$$

$$g = \frac{\partial^2 \vec{s}}{\partial \phi^2} \cdot \vec{N}. \quad (\text{A.19})$$

The Gaussian curvature is then given by

$$\mathcal{K} = \frac{eg - f^2}{EG - F^2}. \quad (\text{A.20})$$

The second derivatives needed in (A.17)–(A.19) can be evaluated using our general parameterization

$$\frac{\partial^2 \vec{s}}{\partial \theta^2} = \left(\frac{\partial^2 R}{\partial \theta^2} - R \right) \hat{e}_r + 2 \frac{\partial R}{\partial \theta} \hat{e}_\theta, \quad (\text{A.21})$$

$$\frac{\partial^2 \vec{s}}{\partial \theta \partial \phi} = \frac{\partial^2 R}{\partial \theta \partial \phi} \hat{e}_r + \frac{\partial R}{\partial \phi} \hat{e}_\theta + \left(\frac{\partial R}{\partial \theta} \sin \theta + R \cos \theta \right) \hat{e}_\phi, \quad (\text{A.22})$$

$$\frac{\partial^2 \vec{s}}{\partial \phi^2} = \left(\frac{\partial^2 R}{\partial \phi^2} - R \sin^2 \theta \right) \hat{e}_r - R \sin \theta \cos \theta \hat{e}_\theta + 2 \frac{\partial R}{\partial \phi} \sin \theta \hat{e}_\phi. \quad (\text{A.23})$$

Thus, we have

$$E = \left(\frac{\partial R}{\partial \theta} \right)^2 + R^2, \quad (\text{A.24})$$

$$F = \frac{\partial R}{\partial \theta} \frac{\partial R}{\partial \phi}, \quad (\text{A.25})$$

$$G = \left(\frac{\partial R}{\partial \phi} \right)^2 + R^2 \sin^2 \theta. \quad (\text{A.26})$$

$$e = \frac{R \sin \theta}{|\vec{N}|} \left[R \left(\frac{\partial^2 R}{\partial \theta^2} - R \right) - 2 \left(\frac{\partial R}{\partial \theta} \right)^2 \right], \quad (\text{A.27})$$

$$f = \frac{R \sin \theta}{|\vec{N}|} \left[R \left(\frac{\partial^2 R}{\partial \theta \partial \phi} - ctg \theta \frac{\partial R}{\partial \phi} \right) - 2 \frac{\partial R}{\partial \theta} \frac{\partial R}{\partial \phi} \right], \quad (\text{A.28})$$

$$g = \frac{R \sin \theta}{|\vec{N}|} \left[R \left(\frac{\partial^2 R}{\partial \phi^2} - R \sin^2 \theta + \frac{\partial R}{\partial \theta} \sin \theta \cos \theta \right) - 2 \left(\frac{\partial R}{\partial \phi} \right)^2 \right]. \quad (\text{A.29})$$

Substituting (A.24)–(A.29) into (A.20), the Gaussian curvature of the slowness surface can be evaluated for the general case.

The results in this appendix can be used to evaluate the Green's tensor in the case of general anisotropy provided a suitable expression of the phase velocity is obtained.

APPENDIX B. AUXILIARY POTENTIALS FOR AZIMUTHALLY-ISOTROPIC MEDIA

The Fourier-transformed Cauchy equation of motion for an elastic solid under a body-force distribution $\vec{F}(\vec{r}, \omega)$, is

$$\operatorname{div} \vec{T} + \rho\omega^2 \vec{u} = -\rho\vec{F}; \quad (\text{B.1})$$

where ρ is the density, ω is the angular frequency, $\vec{u}(\vec{r}, \omega)$ is the displacement at field point \vec{r} and \vec{T} is the dynamic stress-tensor. Choosing a cartesian coordinate system with the z axis as the axis of symmetry, the stress-strain relations for an azimuthally-isotropic medium can be put in the convenient form:

$$\begin{aligned} \vec{T} &= [c_{13} \vec{I} \operatorname{div} \vec{u} + c_{44}(\nabla \vec{u} + \vec{u} \nabla)] + \vec{T}_{\text{anis}}, \\ \vec{T}_{\text{anis}} &= (c_{11} - c_{13} - 2c_{44})(\vec{I} - \hat{e}_z \hat{e}_z) \left(\frac{\partial u_x}{\partial x} + \frac{\partial u_y}{\partial y} \right) \\ &\quad + (c_{33} - c_{13} - 2c_{44}) \frac{\partial u_z}{\partial z} \hat{e}_z \hat{e}_z \\ &\quad + (c_{44} - c_{66}) \left[2 \frac{\partial u_x}{\partial x} \hat{e}_y \hat{e}_y + 2 \frac{\partial u_y}{\partial y} \hat{e}_x \hat{e}_x - \left(\frac{\partial u_x}{\partial y} + \frac{\partial u_y}{\partial x} \right) (\hat{e}_x \hat{e}_y + \hat{e}_y \hat{e}_x) \right]. \end{aligned} \quad (\text{B.2})$$

Here (u_x, u_y, u_z) are the cartesian displacement components and $\{c_{11}, c_{13}, c_{33}, c_{44}, c_{66}\}$ are the five elastic constants of the medium. The unit dyadic is \vec{I} and $\{\hat{e}_x, \hat{e}_y, \hat{e}_z\}$ are the three cartesian unit vectors along the respective axes.

We now take the divergence of \vec{T} in (B.2). Using some vector and tensor identities (Ben-Menahem, 1987), we find that (B.1) can be recast in the form

$$(c_{13} + c_{44}) \operatorname{grad} \operatorname{div} \vec{u} + \operatorname{curl}(\hat{e}_z L) + \hat{e}_z B + \vec{\nabla}_t N + \rho\omega^2 \vec{u} = -\rho\vec{F}, \quad (\text{B.3})$$

where

$$\left. \begin{aligned} L &= -c_{66}\Lambda - c_{44}\partial_z^2\{\nabla_t^{-2}\Lambda\}, \\ B &= (c_{33} - c_{13} - c_{44})\frac{\partial\Gamma}{\partial z} + c_{44}\nabla_t^2 u_z, \\ N &= (c_{11} - c_{13} - c_{44})\Theta + c_{44}\partial_z^2\{\nabla_t^{-2}\Theta\}, \end{aligned} \right\} \quad (\text{B.4})$$

$$\left. \begin{aligned} \Lambda &= \hat{e}_z \cdot \operatorname{curl} \vec{u} = \frac{\partial u_y}{\partial x} - \frac{\partial u_x}{\partial y}, \\ \Gamma &= \frac{\partial u_x}{\partial z}, \\ \Theta &= \frac{\partial u_x}{\partial x} + \frac{\partial u_y}{\partial y} \end{aligned} \right\} \quad (\text{B.5})$$

$$\vec{\nabla}_t = \nabla - \hat{e}_z\partial_z = \hat{e}_x\partial_x + \hat{e}_y\partial_y \quad ; \quad \nabla_t^2 = \nabla^2 - \partial_z^2, \quad (\text{B.6})$$

and ∇_t^{-2} is the inverse transverse Laplace operator, to be given explicitly in (B.33).

We apply to (B.3) the linear operator $\{\hat{e}_z \cdot \operatorname{curl}\}$. This yields a single wave equation for Λ

$$c_{66}\nabla_t^2\Lambda + c_{44}\partial_z^2\Lambda + \rho\omega^2\Lambda = -\rho\left(\frac{\partial Y}{\partial x} - \frac{\partial X}{\partial y}\right), \quad (\text{B.7})$$

where (X, Y, Z) are the cartesian components of \vec{F} .

Next, we take the z -component of (B.3) and differentiate it with respect to z . The result is a coupled wave equation in the potentials Θ and Γ

$$[c_{44}\nabla_t^2 + c_{33}\partial_z^2]\Gamma + (c_{13} + c_{44})\partial_z^2\Theta + \rho\omega^2\Gamma = -\rho\frac{\partial Z}{\partial z}. \quad (\text{B.8})$$

A second equation is obtained from (B.3) by taking its transverse divergence

$$[c_{44}\partial_z^2 + c_{11}\nabla_t^2]\Theta + (c_{13} + c_{44})\nabla_t^2\Gamma + \rho\omega^2\Theta = -\rho\left(\frac{\partial X}{\partial x} + \frac{\partial Y}{\partial y}\right). \quad (\text{B.9})$$

We shall obtain explicit solutions for the three potentials. Once these are known, the components of \vec{u} are expressible in terms of these functions:

$$u_x = \nabla_t^{-2}\left(\frac{\partial\Theta}{\partial x} - \frac{\partial\Lambda}{\partial y}\right); \quad u_y = \nabla_t^{-2}\left(\frac{\partial\Theta}{\partial y} + \frac{\partial\Lambda}{\partial x}\right); \quad u_z = \int \Gamma dz. \quad (\text{B.10})$$

Equation (B.7) can readily be solved in closed-form. Let us specify the body force distribution as a localized force of magnitude $F(\omega)$ and fixed direction \hat{e} , at $\vec{r} = \vec{r}_0$

$$\rho \vec{F} = F(\omega) \hat{e} \delta(\vec{r} - \vec{r}_0) , \quad (\text{B.11})$$

where \vec{F} is a force per unit mass, but $F(\omega)$ is force proper. Assume

$$\Lambda = -F \hat{e} \cdot \operatorname{curl}(\hat{e}_z g) , \quad (\text{B.12})$$

where g is an unknown function. A substitution of (B.12) in (B.7) renders at once the equation for g

$$c_{66} \nabla_t^2 g + c_{44} \partial_z^2 g + \rho \omega^2 g = -\delta(\vec{r} - \vec{r}_0) . \quad (\text{B.13})$$

Its exact solution is the scalar Green's function,

$$g(\vec{r}, \omega) = \frac{e^{-ik_{SH}\hat{R}}}{4\pi \hat{R} \eta_{SH} \rho a_5} , \quad (\text{B.14})$$

with

$$\begin{aligned} \hat{R} &= \sqrt{\Delta^2 + \eta_{SH}^2(z - z_0)^2} , \quad \Delta^2 = (x - x_0)^2 + (y - y_0)^2 , \\ \eta_{SH}^2 &= \frac{c_{66}}{c_{44}} , \quad k_{SH}^2 = \frac{\omega^2}{a_4} . \end{aligned} \quad (\text{B.15})$$

An alternative way to derive (B.14) is instructive at this point. Assume a Fourier-integral representation of the solution of (B.13)

$$g(\vec{r}, \omega) = \frac{1}{8\pi^3 \rho} \int_{-\infty}^{\infty} \int \int \frac{d\alpha d\beta d\gamma}{h(\alpha, \beta, \gamma; \omega)} e^{-i[\alpha(x-x_0) + \beta(y-y_0) + \gamma(z-z_0)]} d\alpha d\beta d\gamma , \quad (\text{B.16})$$

and use the known identity

$$\delta(\vec{r} - \vec{r}_0) = \frac{1}{8\pi^3} \int_{-\infty}^{\infty} \int \int e^{-i[\alpha(x-x_0) + \beta(y-y_0) + \gamma(z-z_0)]} d\alpha d\beta d\gamma . \quad (\text{B.17})$$

Inserting these into (B.13), yields

$$h(\alpha, \beta, \gamma; \omega) = a_*(\alpha^2 + \beta^2) + \frac{1}{\eta_{SH}^2} a_4 \gamma^2 - \omega^2. \quad (\text{B.18})$$

We make a change of variables from (α, β, γ) to spherical coordinates in wave-number space (Figure 2)

$$\begin{aligned} \alpha &= \frac{\omega}{C} \sin \bar{\theta} \cos \bar{\phi}; & \beta &= \frac{\omega}{C} \sin \bar{\theta} \sin \bar{\phi}; & \gamma &= \frac{\omega}{C} \cos \bar{\theta} \\ \alpha^2 + \beta^2 + \gamma^2 &= \frac{\omega^2}{C^2}. \end{aligned} \quad (\text{B.19})$$

The Jacobian of this transformation is $J = \left| \frac{\omega^3}{C^4} \sin \bar{\theta} \right|$, and

$$h(\alpha, \beta, \gamma) = \frac{\omega^2}{C^2} (C_{SH}^2 - C^2), \quad (\text{B.20})$$

where

$$C_{SH} = [a_4 \sin^2 \bar{\theta} + a_5 \cos^2 \bar{\theta}]^{1/2}, \quad (\text{B.21})$$

is the *plane-wave phase-velocity* of the SH wave. Substituting (B.20) and (B.21) into (B.16), the integral becomes

$$g = -\frac{\omega}{8\pi^3 \rho} \int_0^\infty \frac{dC}{C^2 [C^2 - C_{SH}^2(\bar{\theta})]} \int_{C^\pm} \sin \bar{\theta} d\bar{\theta} e^{-i\frac{\omega}{c} z \cos \bar{\theta}} \int_0^{2\pi} e^{-i\frac{\omega}{c} \sin \bar{\theta} (x \cos \bar{\phi} + y \sin \bar{\phi})} d\bar{\phi} \quad (\text{B.22})$$

Since $\gamma = \sqrt{\frac{\omega^2}{C^2} - (\alpha^2 + \beta^2)}$, where $(\alpha^2 + \beta^2)$ varies from zero to infinity, γ can take on pure imaginary values. In isotropic media C^\pm is the usual Weyl contour (Fig. 1). However, in our anisotropic medium, there are two *branch points* on C^\pm at $\tau_0 = \pm \tan h^{-1} \eta_{SH}$. One can see this as one puts $\bar{\theta} = \frac{\pi}{2} \pm i\tau$ into the expression for $C_{SH}^2(\bar{\theta})$ via Eq. (B.21). At these branch points C_{SH} vanishes. For this reason the integration along τ on C^\pm must stop at $\frac{\pi}{2} \pm i\tau_0$. As $\eta_{SH} \rightarrow 1$ (isotropy) $\tau_0 \rightarrow \pm\infty$ and the original Weyl contour is re-established. The variation of γ is then

mapped onto a corresponding variation of $\bar{\theta}$ along either of the modified Weyl contours C^+ or C^- (Fig. 1), depending on the sign of z , to secure finite values of $e^{-\imath \gamma z}$. The function $C_{SH}^2(\bar{\theta})$ is *real* for all complex and real values of $\bar{\theta}$ along C^\pm .

The integral over $\bar{\phi}$ is immediate and equals $2\pi J_0(\frac{\omega}{c}\Delta \sin \bar{\theta})$, where J_0 is the Bessel function of the first kind and order zero. Then, the integral over C is evaluated through the method of residues at the contributing pole $C = C_{SH}$, yielding

$$\int_{-\infty}^{\infty} dc \frac{e^{-\imath \frac{\omega}{c} z \cos \bar{\theta}} J_0(\frac{\omega}{c}\Delta \sin \bar{\theta})}{C^2[C^2 - C_{SH}^2(\bar{\theta}) + \imath 0]} = \frac{\pi \imath}{C_{SH}^3} e^{-\imath \frac{\omega}{C_{SH}} z \cos \bar{\theta}} J_0\left(\frac{\omega}{C_{SH}} \Delta \sin \bar{\theta}\right). \quad (\text{B.23})$$

The net result of both integrations over $\bar{\phi}$ and C is

$$g = \frac{-\imath \omega}{4\pi\rho} \int_{C^\pm} \frac{d\bar{\theta} \sin \bar{\theta}}{C_{SH}^3(\bar{\theta})} J_0\left(\frac{\omega}{C_{SH}} \Delta \sin \bar{\theta}\right) e^{-\imath \frac{\omega}{C_{SH}} z \cos \bar{\theta}}. \quad (\text{B.24})$$

In the isotropic limit $C_{SH} \rightarrow b$. Then the classical *Sommerfeld-Weyl* integral

$$\frac{e^{-\imath kR}}{-\imath k_b R} = \int_{C^\pm} d\bar{\theta} \sin \bar{\theta} J_0\left(\frac{\omega}{b} \Delta \sin \bar{\theta}\right) e^{-\imath \frac{\omega}{b} z \cos \bar{\theta}}, \quad (\text{B.25})$$

secures the reduction of g to its isotropic limit. We effect another change of variable

$$\sin u = \sin \bar{\theta} \frac{C_{SH}(\frac{\pi}{2})}{C_{SH}(\bar{\theta})}; \quad \eta_{SH} \cos u = \cos \bar{\theta} \frac{C_{SH}(\frac{\pi}{2})}{C_{SH}(\bar{\theta})}; \quad \sin u \, du = \frac{a_4^{3/2}}{\eta_{SH}} \frac{\sin \bar{\theta} d\bar{\theta}}{[C_{SH}(\bar{\theta})]^3} \quad (\text{B.26})$$

where $C_{SH}^2(\frac{\pi}{2}) = a_4$ and $k_{SH} = \frac{\omega}{\sqrt{a_4}}$. One can easily show that this transformation restores the modified Weyl contour into the standard Weyl contour C^\pm (Fig. 1). Therefore, using (B.25)

$$g = \frac{-\imath \omega \eta_{SH}}{4\pi\rho a_4^{3/2}} \int_{C^\pm} \sin u \, du J_0(k_{SH} \Delta \sin u) e^{-\imath k_{SH} z \eta_{SH} \cos u} = \frac{1}{\rho \eta_{SH} a_5} \frac{e^{-\imath k_{SH} \hat{R}}}{4\pi \hat{R}} \quad (\text{B.27})$$

in agreement with (B.14).

The ensuing displacements are obtained from (B.14) via (B.12) and (B.10)

$$\vec{u}_{SH} = \frac{F(\omega)}{4\pi \eta_{SH} \rho a_5} \operatorname{curl}(\hat{e}_z \chi), \quad (\text{B.28})$$

$$\chi = \text{curl}(\hat{e}_z \tau) \cdot \hat{e}, \quad \tau = \nabla_t^{-2} \mathcal{S}, \quad \mathcal{S}(\Delta, z) = \frac{e^{-ik_{SH}\hat{R}}}{\hat{R}}. \quad (\text{B.29})$$

Next we use the tensor identities (Ben-Menahem, 1987)

$$\text{curl}(\vec{G} \cdot \vec{F}) \equiv (\text{curl } \vec{G}) \cdot \vec{F} \quad (\text{B.30})$$

$$\text{curl}[\hat{e}_z \text{curl}(\hat{e}_z \tau)] \equiv \left[\vec{I} - \hat{e}_z \hat{e}_z - \frac{\vec{\nabla}_t \vec{\nabla}_t}{\nabla_t^2} \right] \mathcal{S}, \quad (\text{B.31})$$

$$\frac{\vec{\nabla}_t \vec{\nabla}_t}{\nabla_t^2} \mathcal{S} \equiv \hat{e}_\Delta \hat{e}_\Delta \mathcal{S} + (\hat{e}_\phi \hat{e}_\phi - \hat{e}_\Delta \hat{e}_\Delta) \frac{1}{\Delta^2} \int \Delta \mathcal{S}(\Delta, z) d\Delta, \quad (\text{B.32})$$

$$\frac{1}{\nabla_t^2} \mathcal{S}(\Delta, z) \equiv \int \frac{d\Delta}{\Delta} \int \Delta \mathcal{S}(\Delta, z) d\Delta, \quad (\text{B.33})$$

valid for a fixed vector \vec{F} , a variable dyadic \vec{G} and remembering that \mathcal{S} is independent of the azimuth angle ϕ . Here $(\hat{e}_\Delta, \hat{e}_\phi, \hat{e}_z)$ are the unit-vector triad of cylindrical polar coordinates. We note that the integral in (B.32) renders

$$\int \Delta \mathcal{S}(\Delta, z) d\Delta = -\frac{1}{ik_{SH}} e^{-ik_{SH}\hat{R}}. \quad (\text{B.34})$$

Using (B.32), one may rewrite (B.28) as

$$\begin{aligned} \vec{u}_{SH} &= \frac{F(\omega)}{4\pi\rho\eta_{SH}a_5} \left[\left(\vec{I} - \hat{e}_z \hat{e}_z - \frac{\vec{\nabla}_t \vec{\nabla}_t}{\nabla_t^2} \right) \mathcal{S} \right] \cdot \hat{e} \\ &= F(\omega) \vec{G}_{SH} \cdot \hat{e}, \end{aligned} \quad (\text{B.35})$$

where

$$\vec{G}_{SH}(\vec{r}|\vec{r}_0; \omega) = \frac{1}{4\pi\eta_{SH}\rho a_5} \left(\vec{I} - \hat{e}_z \hat{e}_z - \frac{\vec{\nabla}_t \vec{\nabla}_t}{\nabla_t^2} \right) \frac{e^{-ik_{SH}\hat{R}}}{\hat{R}}, \quad (\text{B.36})$$

is the SH part of the total Green's tensor. Note that since $\Delta = r \sin \theta$, $z - z_0 = r \cos \theta$ [θ is the spherical collatitude angle measured from the z axis], we have

$$\hat{R} = r \left(\sin^2 \theta + \frac{C_{66}}{C_{44}} \cos^2 \theta \right). \quad (\text{B.37})$$

Also note that the *frequency* enters into the displacements only via the source function $F(\omega)$ and the phase $e^{-i\frac{\omega}{\sqrt{a_4}}R}$.

APPENDIX C. LIST OF SYMBOLS

a	P-wave velocity in isotropic media ($= \sqrt{\frac{\lambda+2\mu}{\rho}}$).
$a_1 = c_{11}/\rho$	
$a_2 = c_{33}/\rho$	
$a_3 = (c_{13} + c_{44})/\rho$	Square of velocities in Azimuthally-Isotropic Media (AIM).
$a_4 = c_{66}/\rho$	
$a_5 = c_{44}/\rho$	
A_{ij}, \vec{A}	Plane-wave response tensor (2.10).
b	S-wave velocity in isotropic media ($= \sqrt{\frac{\mu}{\rho}}$).
c_{ijkl}	Tensor of elastic coefficients.
c_{pq}	Matrix of elastic coefficients in Voigt abbreviated notation.
C^\pm	Weyl contours.
C_m	Phase-velocity of type-m waves ($m = 1, 2, 3$) in general anisotropic media.
$(C_m)^2$	Eigenvalues of A_{ij} .
C_P	Quasi-longitudinal phase velocity in AIM, ($m = 1$).
C_{SV}	Quasi-transverse phase velocity in AIM, ($m = 2$).
C_{SH}	SH-wave phase velocity in AIM, ($m = 3$).
\hat{e}	Unit vector in the direction of a point-force source.
$\hat{e}_x, \hat{e}_y, \hat{e}_z$	Unit vectors in cartesian coordinates.

$\hat{e}_\Delta, \hat{e}_\phi, \hat{e}_z$	Unit vectors in cylindrical coordinates.
$\hat{e}_\tau, \hat{e}_\theta, \hat{e}_\phi$	Unit vectors in spherical coordinates.
$F(t)$	Time-function of applied point-force source per unit-volume.
$F(\omega)$	Fourier-transform of $F(t)$.
\vec{F}	Applied force.
g	Scalar SH Green's function for AIM.
g_{ij}	Tensor of metric coefficients.
G_{ij}, \vec{G}	Spectral Green's tensor in general anisotropic media.
\vec{G}_0	Singularity tensor for AIM.
\vec{G}_{iso}	Green's tensor for homogeneous-isotropic elastic solid.
\vec{G}_P	Quasi P-wave Green's tensor for AIM at far-field.
\vec{G}_{SV}	Quasi SV-wave Green's tensor for AIM at far-field.
\vec{G}_{SH}	SH Green's tensor for AIM at far-field.
H	Heaviside unit-step function.
$\vec{I}; I$	Unit dyadic; unit matrix.
J_0, J_1	Bessel functions.
k_P	$\omega/a_1^{1/2}$.
k_{SV}	$\omega/a_5^{1/2}$.
k_{SH}	$\omega/a_4^{1/2}$.

\vec{k}	Wave-number vector.
k	Horizontal wave-number.
m	Index of wave-type in general anisotropic medium (also used in (4.65)).
M_{ij}	Christoffel tensor (2.12).
$M_0(\omega)$	Spectral moment of dipolar source.
\hat{n}	Unit vector in \vec{k} direction.
$\hat{N}(\vec{s})$	Unit normal to slowness surface.
P-wave	Abbreviation for the quasi-longitudinal wave (Section 4.2).
$\vec{r}(x, y, z)$	Coordinates of field-point.
\vec{r}_0	Coordinates of source-point.
$\vec{r}'(x, y, z)$	Coordinates of field-point in AIM metric.
r	Magnitude of field-point position vector.
$R = \vec{r} - \vec{r}_0 $	
\hat{R}	Effective source-receiver distance in AIM for SH-waves.
R_p	Effective source-receiver distance in AIM for quasi P-waves (5.60).
R_s	Effective source-receiver distance in AIM for quasi SV-waves (5.79).
$\vec{s}(s_1, s_2, s_3)$	Slowness vector and its components ($s = \sqrt{s_1^2 + s_2^2}$).
$\hat{s}_1, \hat{s}_2, \hat{s}_3$	Unit vectors in the direction of the (s_1, s_2, s_3) respectively.
SV-wave	Abbreviation for the quasi-transverse wave (Section 4.2).

t	Time
$\vec{T}^{(m)}$	Displacement polarization vector of type-m waves.
\vec{u}	Displacement vector.
\vec{w}	Group-velocity vector in general anisotropic media.
$w_p(\vec{s})$	Magnitude of group-velocity of quasi P-waves in AIM.
$w_s(\vec{s})$	Magnitude of group-velocity of quasi SV-waves in AIM.
α, β, γ	Direction cosines of wave-number vector.
β_m	Eigenvalues of M_{ij} .
Γ	Auxiliary potential in AIM.
Γ_m	Slowness surface for type-m waves ($m = 1, 2, 3$).
Γ_p	Slowness surface in AIM for quasi P-waves.
Γ_s	Slowness surface in AIM for quasi SV-waves.
δ_{ij}	Kronecker's delta.
$\delta(\vec{r})$	Dirac's delta-function in 3D.
$\partial_z = \frac{\partial}{\partial z}$; $\partial_\Delta = \frac{\partial}{\partial \Delta}$	
(Δ, ϕ, z)	Cylindrical coordinates.
ϵ	Parameter of azimuthal-isotropy.
η_{SH}	Coordinate scaling factor for SH motion in AIM (B.15).

η_p	Coordinate scaling factor for quasi P-motion in AIM (5.44).
η_s	Coordinate scaling factor for quasi SV-motion in AIM (5.64).
Θ	Auxiliary potential in AIM.
(θ, ϕ)	Spherical polar angles.
$(\bar{\theta}, \bar{\phi})$	Spherical polar angles in wave-number space.
$\kappa_1; \kappa_2$	Principal curvatures of slowness surface.
\mathcal{K}_m	Gaussian curvature of type-m slowness surface.
λ, μ	Lamé parameters in isotropic elastic solid.
ρ	Uniform mass density.
Ω	Solid angle.
$d\sigma$	Scalar surface element in Γ_m .
$\vec{d\sigma}$	Surface-element vector in Γ_m .
σ_p	Generalized collatitudinal angle in AIM for quasi P-waves.
σ_s	Generalized collatitudinal angle in AIM for quasi SV-waves.
Ψ	Fundamental potential in AIM.
Ψ_p	Quasi P-wave potential in AIM.
Ψ_s	Quasi SV-wave potential in AIM.
ω	Angular frequency.
$\vec{\nabla}_t$	Transverse gradient.

∇_t^{-2}

Integration operator.

LEGEND OF FIGURES

Figure 1. Path of integration in the complex $\bar{\theta}$ plane of the Sommerfeld-Weyl integral for anisotropic media.

Figure 2. Cartesian (α, β, γ) vs. spherical $(\frac{\omega}{C}, \bar{\theta}, \bar{\phi})$ coordinates in wave-number space. On the same axes we also show cartesian (x, y, z) vs. spherical (r, θ, ϕ) in real space.

Figure 3. Relative error of phase velocities for four earth materials as a function of the collatitudinal (zenithal) angle (see Table 2). Top: Quasi P velocity. Bottom: Quasi SV velocity.

Figure 4. Geometry of the slowness surface in a generic case for which $\eta_p > 1$.

Figure 5. Geometry of the wave surface in a generic case for which $\eta_p > 1$.

Figure 6. Exact and approximate slowness surfaces for four earth models (see Table 2).

Figure 7. Top: Vertical radiation patterns in the far-field for the vertical quasi-longitudinal displacement due a vertical point force for two types of anisotropic media. Broken lines indicate isotropic limit. Force is directed from origin toward 0° along the positive symmetry z-axis and θ is measured in vertical plane positively counterclockwise. Bottom: Same as above for the vertical quasi-transverse displacement component.

Figure 8. Top: Vertical radiation patterns in the far-field for the collatitudinal quasi-longitudinal displacement due a horizontal point force in the x direction. Displacement field vanishes in the isotropic limit. Bottom: Vertical radiation patterns for the radial quasi-transverse displacement due a horizontal point force in the x direction. Displacement field vanishes in the isotropic limit.

Figure 9. Top: Vertical radiation patterns in the far-field for the vertical quasi-longitudinal displacement due to an explosion point source. Broken lines indicate isotropic limit. Bottom:

Vertical radiation patterns for the vertical quasi-transverse displacement due to an explosion point source. Displacement field vanishes in the isotropic limit.

Figure 10. Vertical radiation patterns in the far-field for the SV/P ratio of vertical quasi-transverse to quasi-longitudinal components of displacement field due to an explosion point source. SV/P ratio vanishes in the isotropic limit.

Figure 11. Top: Vertical radiation patterns in the far-field for the horizontal-radial quasi-transverse displacement due to an explosion point source. Displacement field vanishes in the isotropic limit. Bottom: Vertical radiation patterns for the collatitudinal quasi-longitudinal displacement due to an explosion point source. Displacement field vanishes in the isotropic limit.

Figure 12. Top: Vertical radiation patterns in the far-field for the collatitudinal quasi-transverse displacement due to an explosion point source. Displacement field vanishes in the isotropic limit. Bottom: Vertical radiation patterns for the radial quasi-transverse displacement due to an explosion point source. Displacement field vanishes in the isotropic limit.

Figure 13. A comparison of $u_{\theta p}$ radiation patterns in the far-field due to two sources in azimuthally isotropic Timber Mountain tuff. Left: Strike-slip dislocation in the xz plane. Right: Explosion.

Figure 14. A comparison of u_{zs} radiation patterns in the far-field due to two sources in azimuthally isotropic Mesaverde clayshale. Left: Strike-slip dislocation in the xz plane. Right: Explosion.

LEGEND OF TABLES

Table 1. Kernels of the Hankel-Transform representation of displacement fields of various sources in unbounded azimuthally isotropic media.

Table 2. Structural constants of some azimuthally isotropic earth materials reported by Thomsen (1986).

Table 3. Cylindrical components of displacement field and radiation patterns of point sources in unbounded azimuthally isotropic media.

Table 4. Spherical components of displacement field and radiation patterns of point sources in unbounded azimuthally isotropic media.

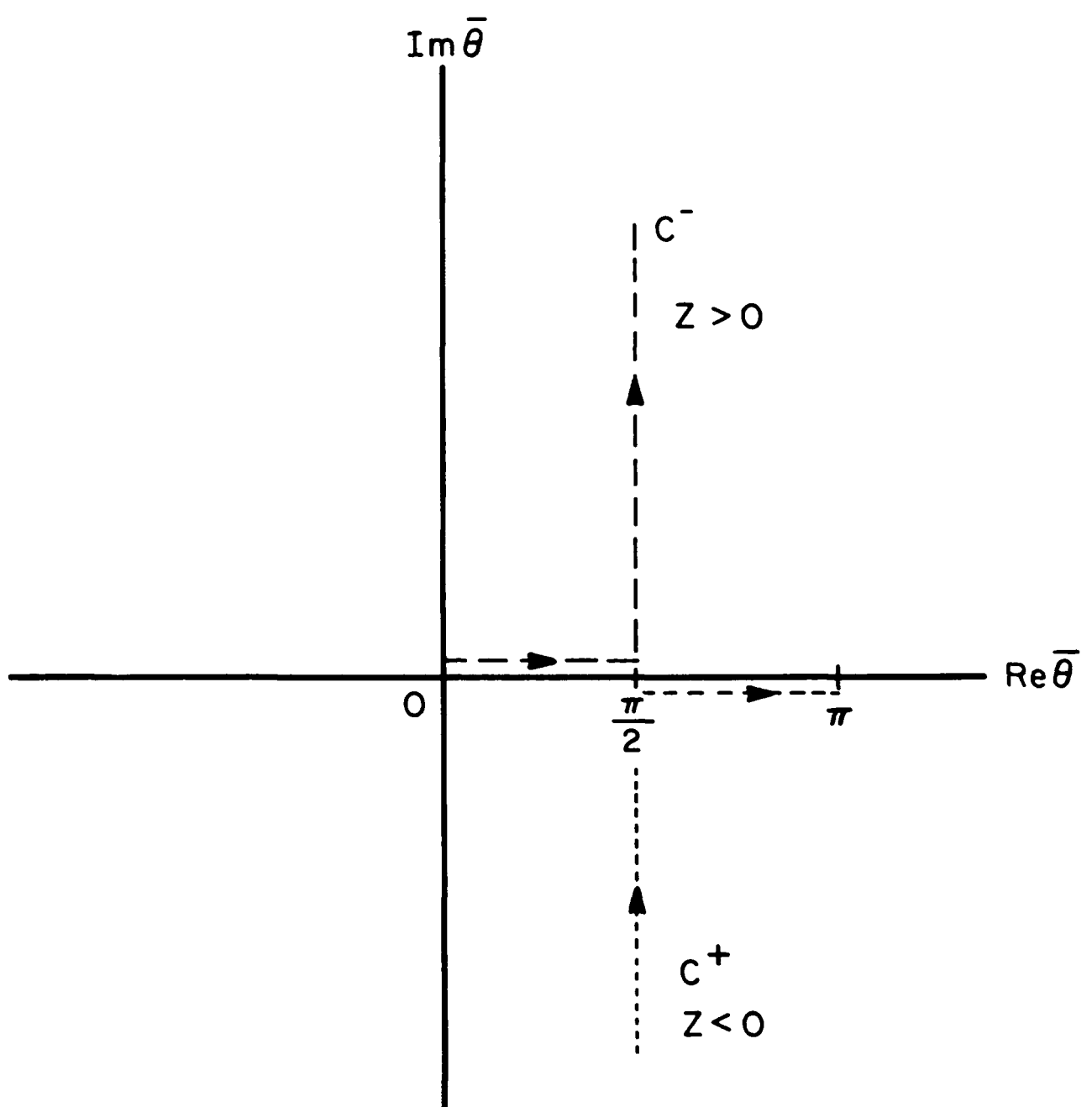


Figure 1.

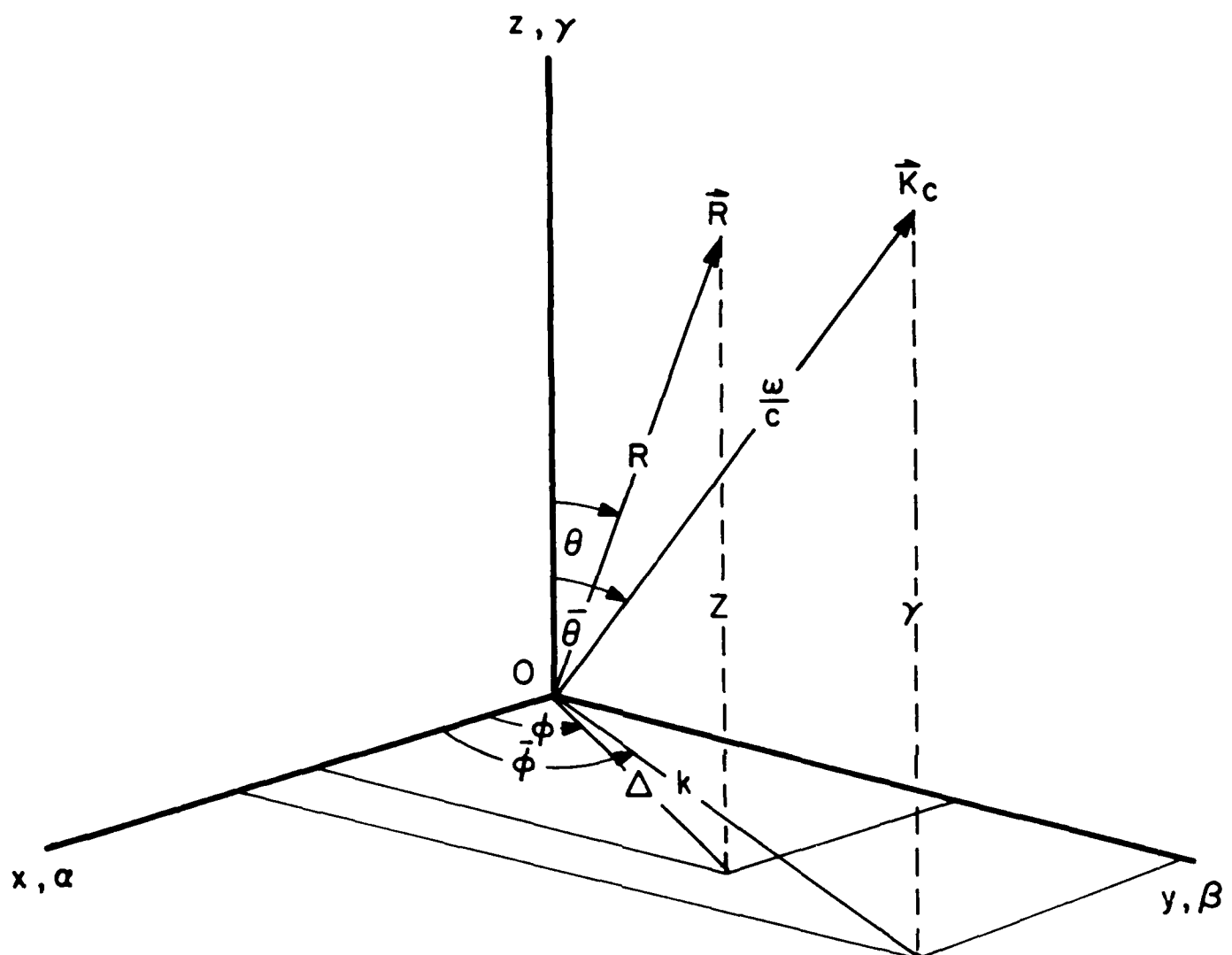
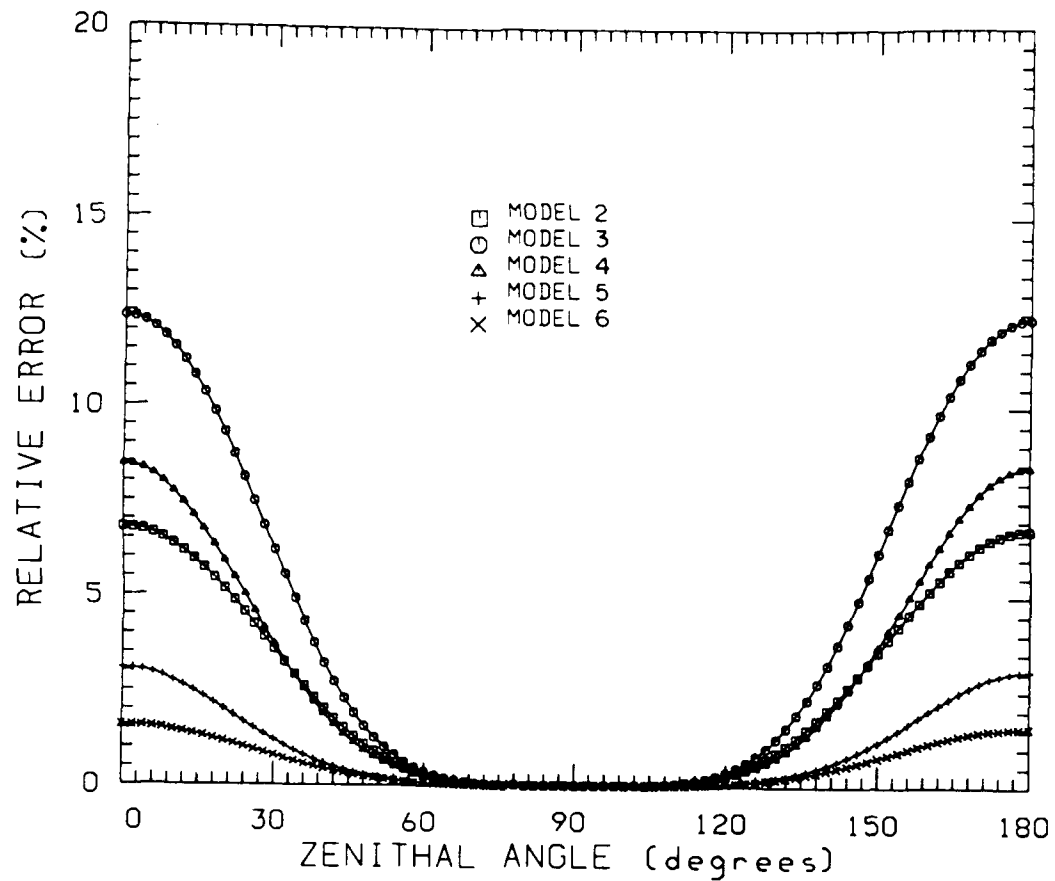


Figure 2.

QUASI P-VELOCITY



QUASI SV-VELOCITY

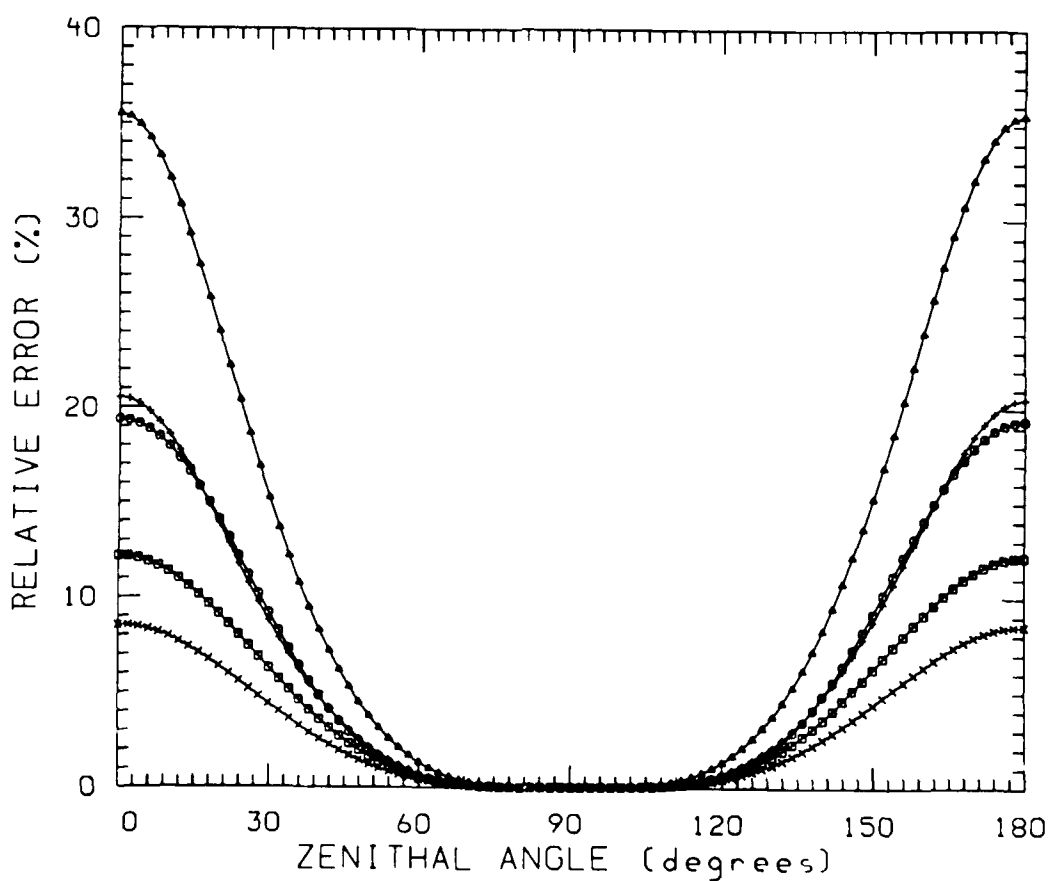


Figure 3.

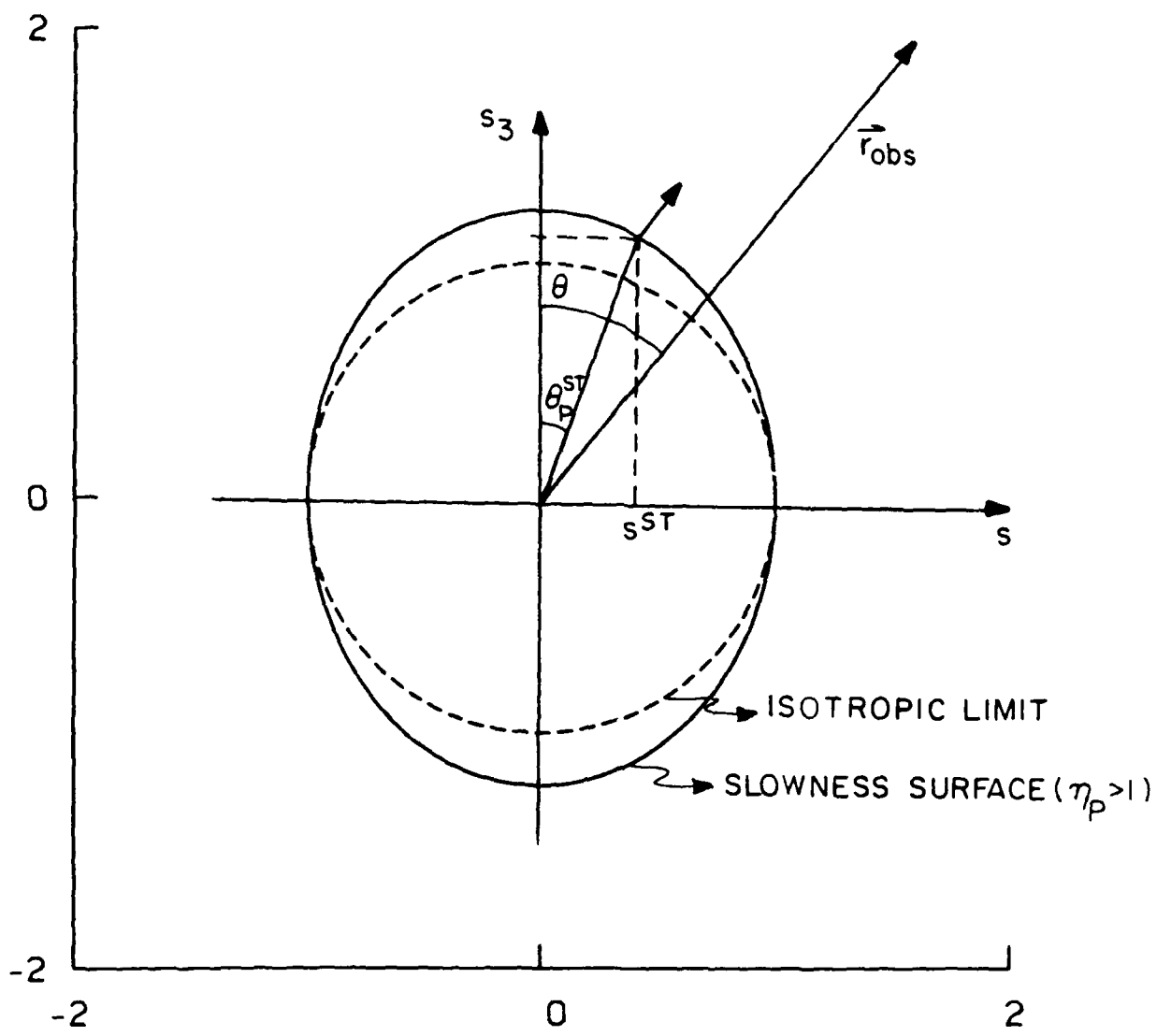


Figure 4.

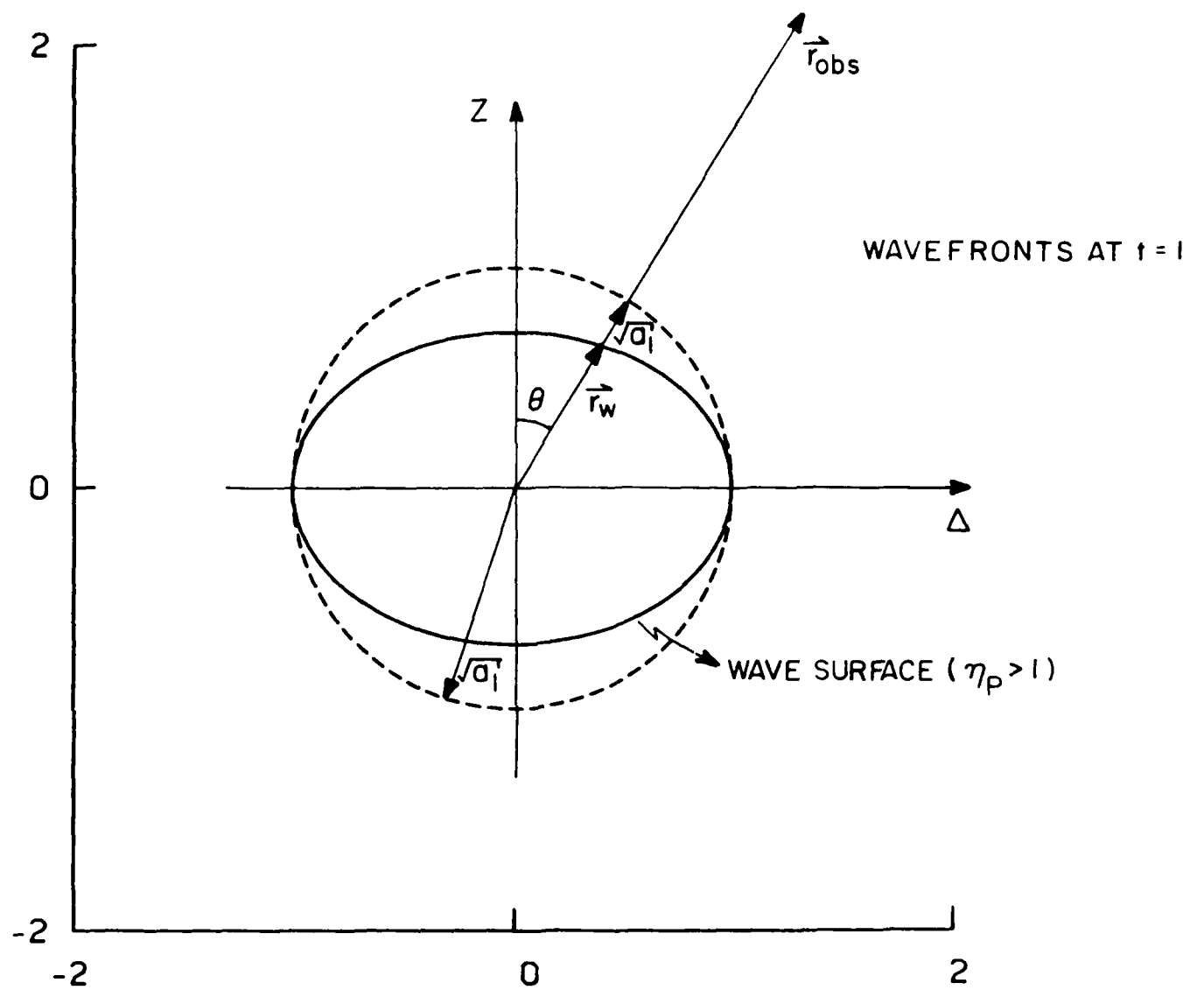
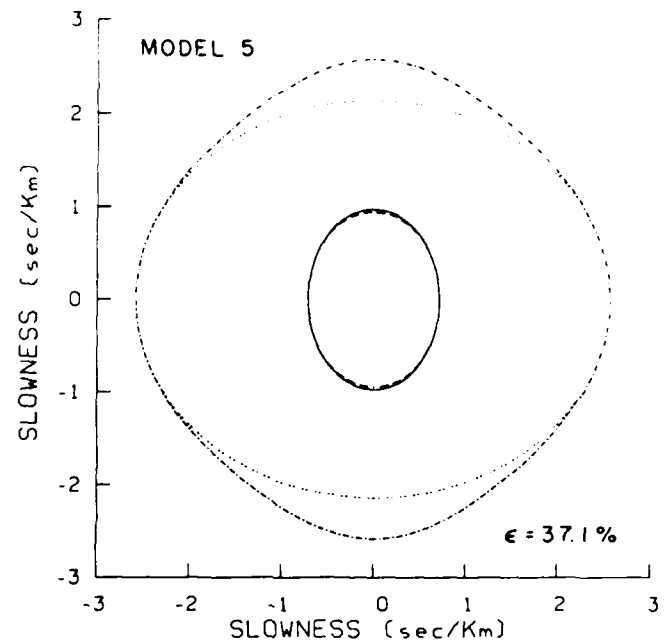
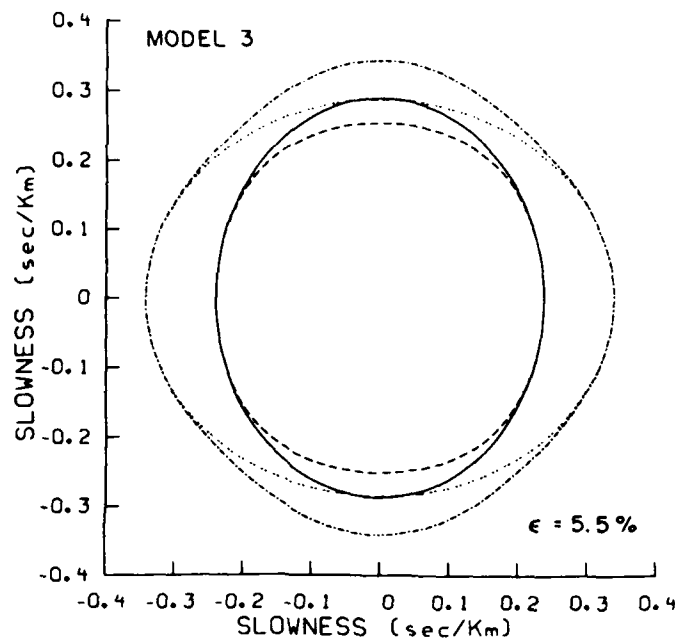


Figure 5.



-- EXACT P
 --- EXACT SV
 — APPROX. P
 ... APPROX. SV

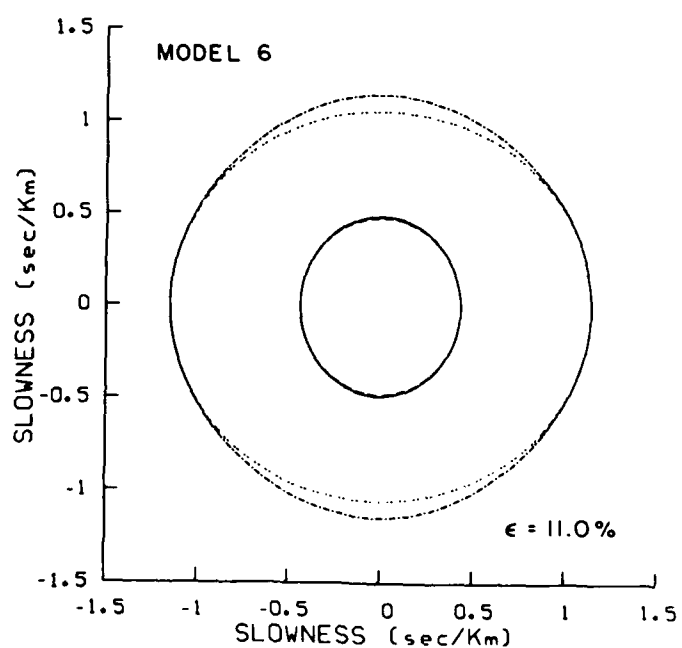
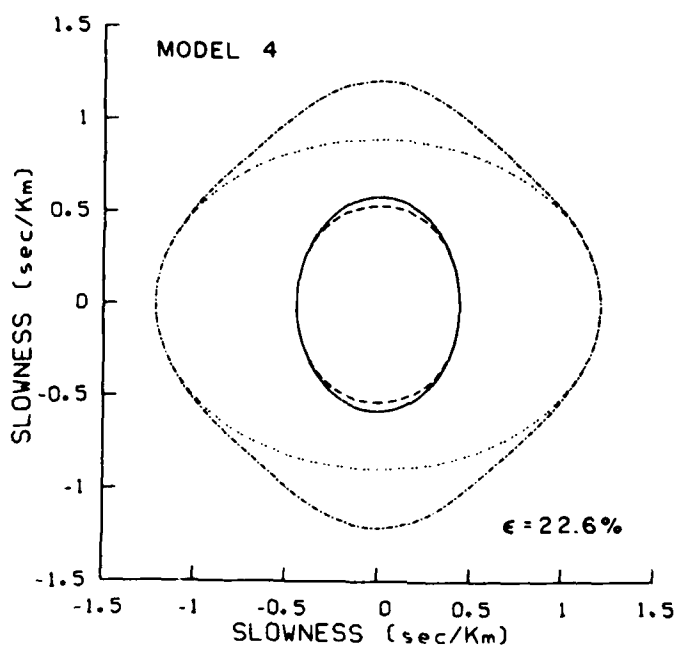
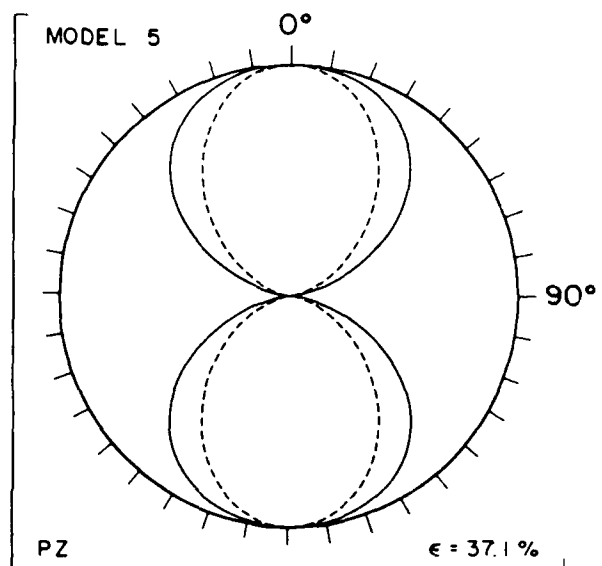
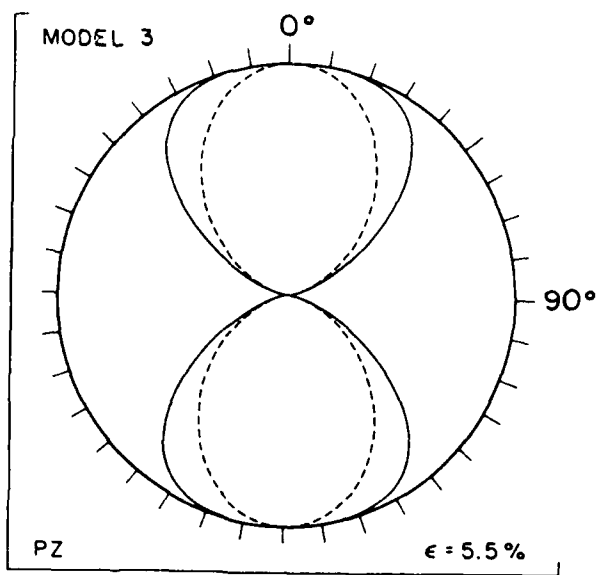


Figure 6.



VERTICAL FORCE

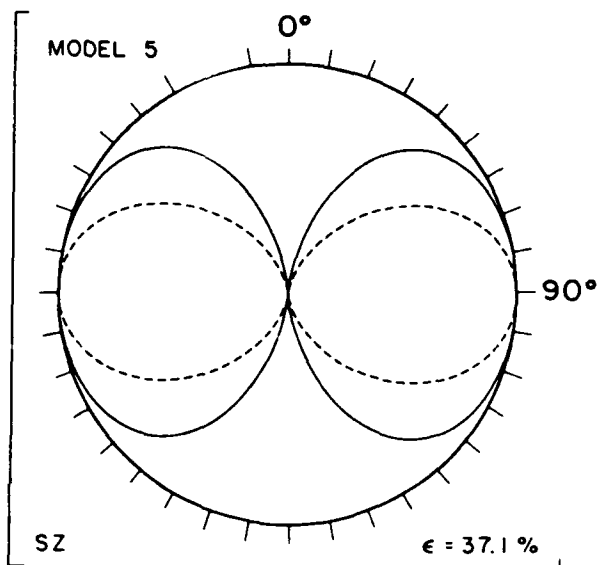
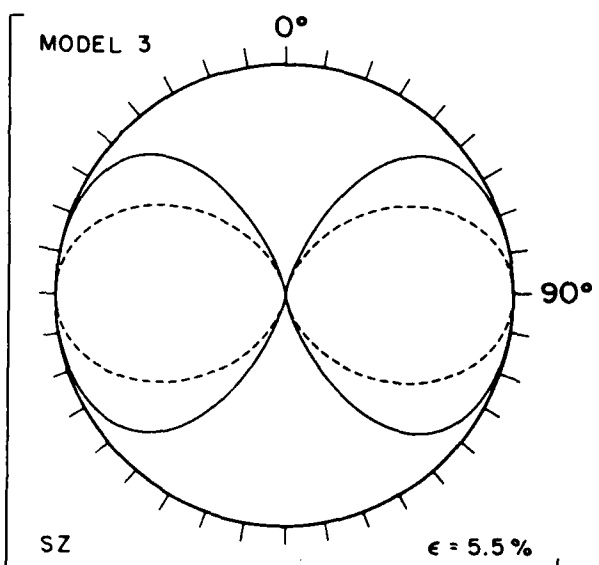
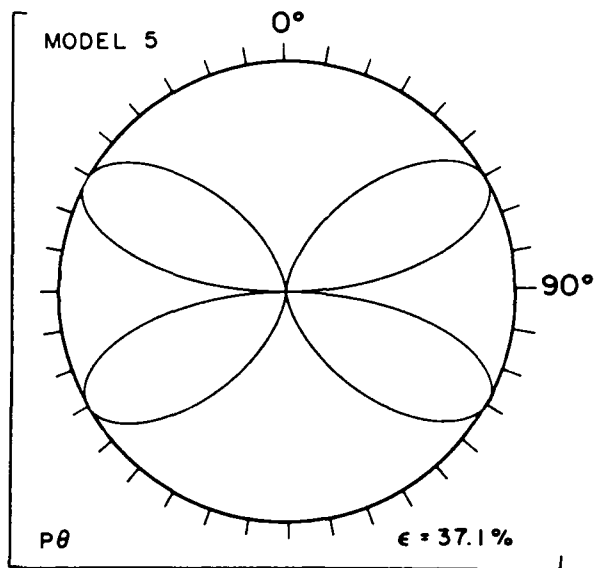
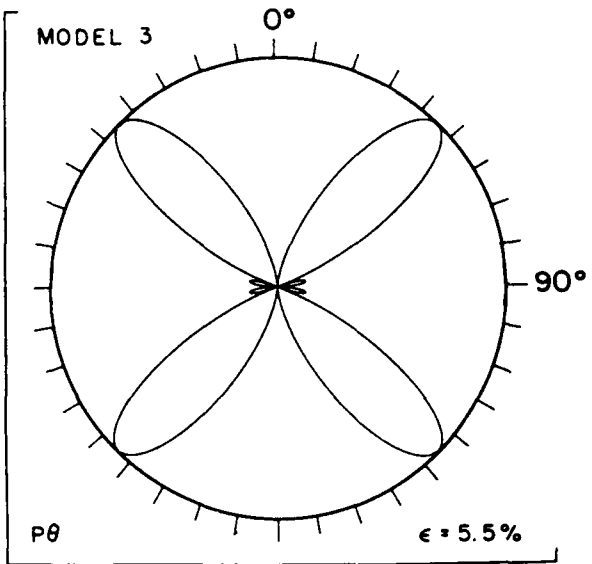


Figure 7.



HORIZONTAL FORCE

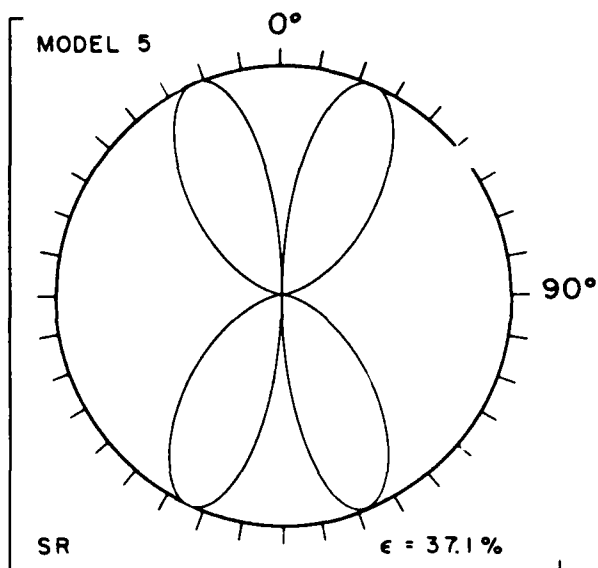
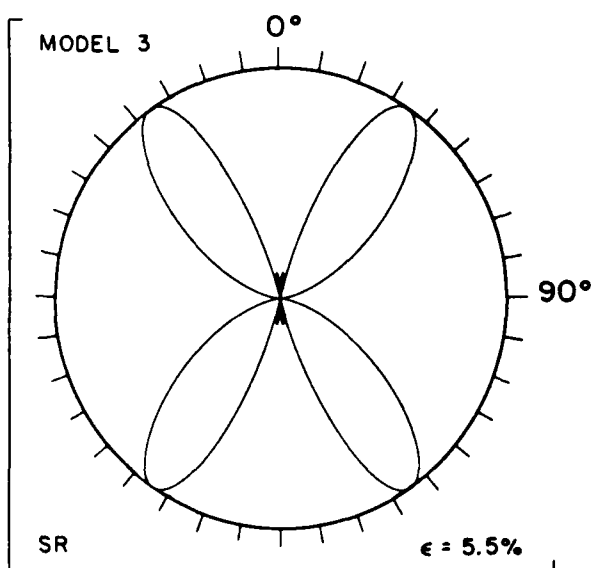
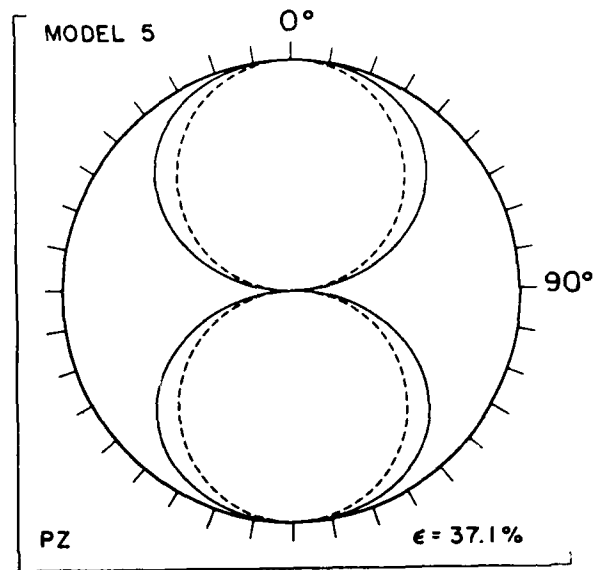
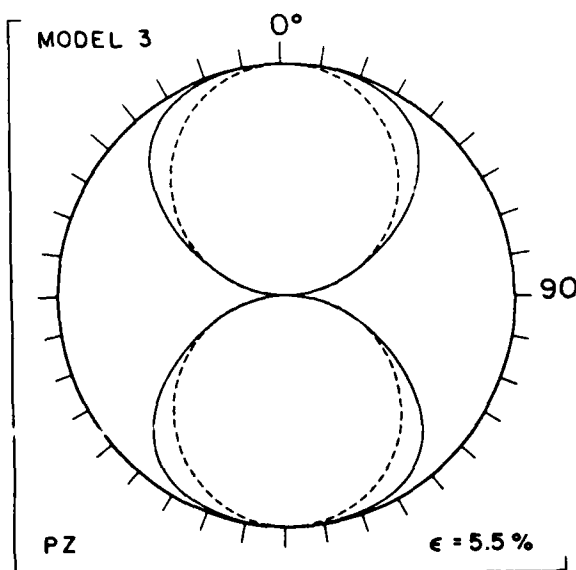


Figure 8.



EXPLOSION

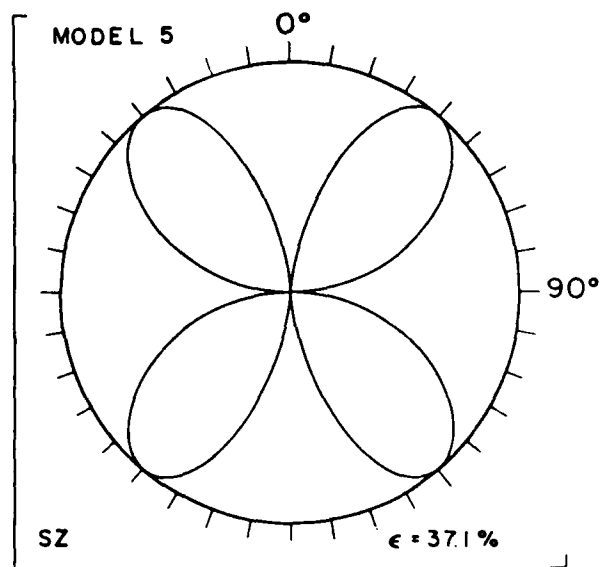
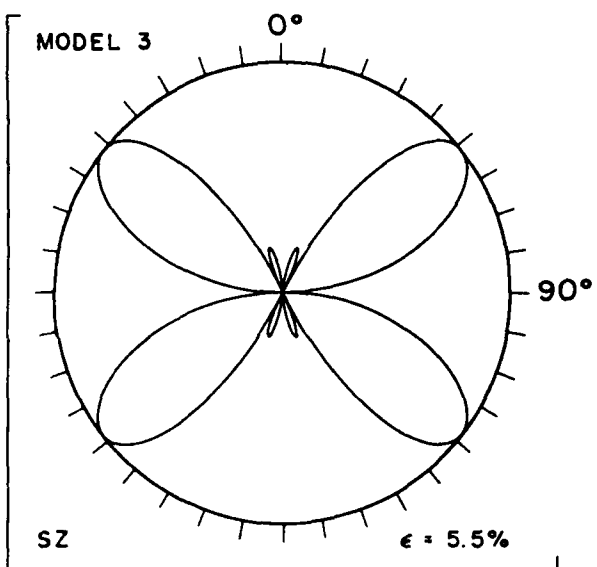


Figure 9.

SV/P RATIO (VERT. COMP.) - EXPLOSION

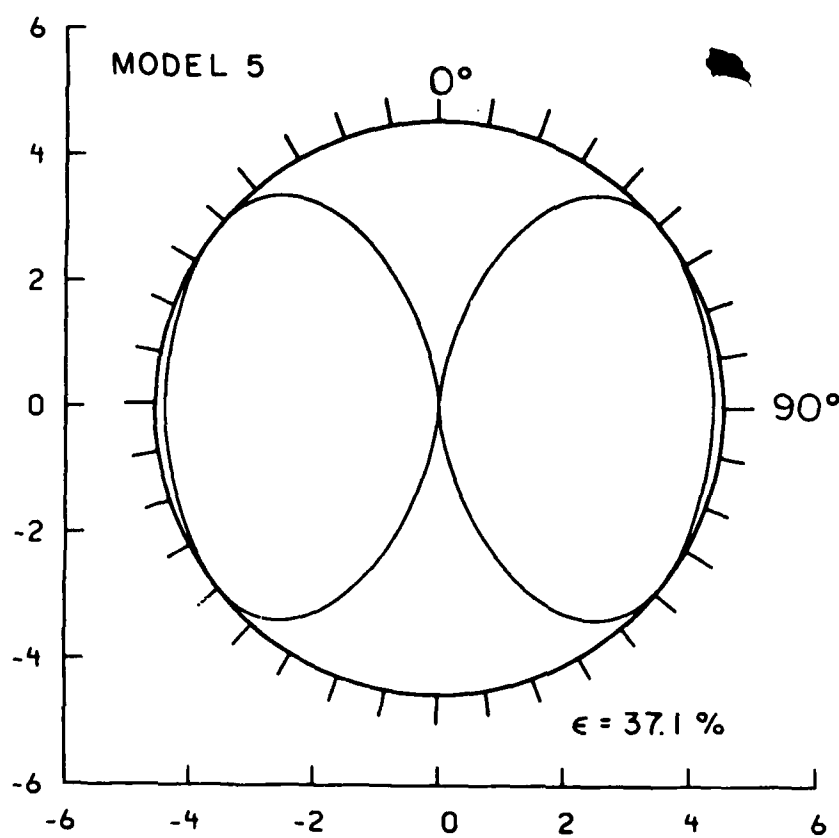
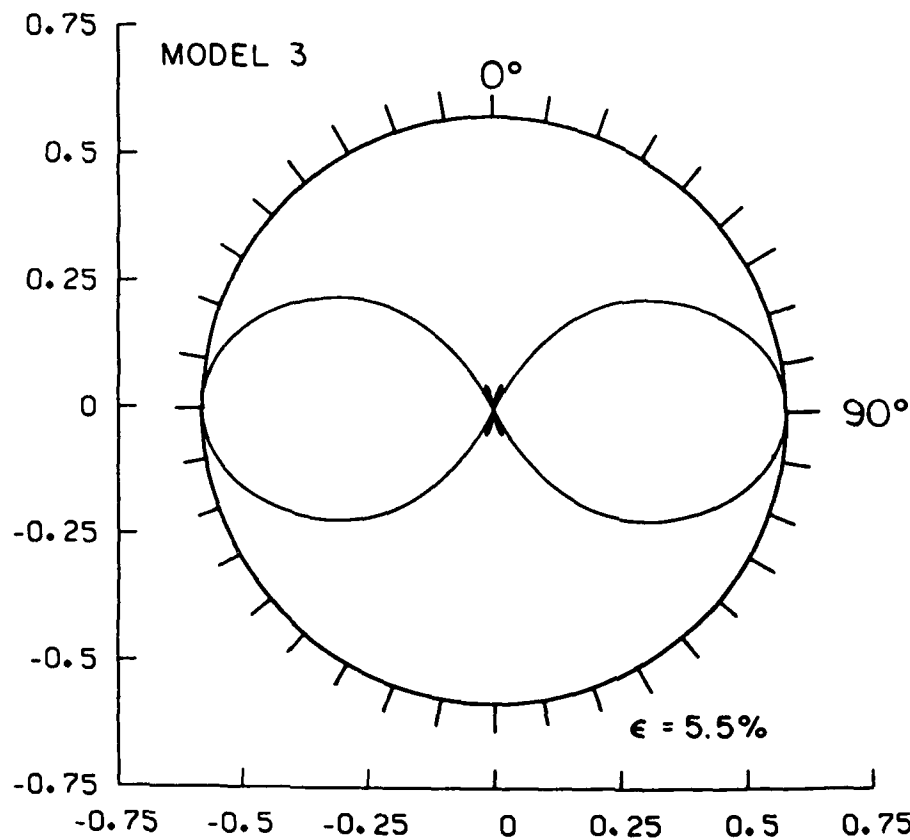
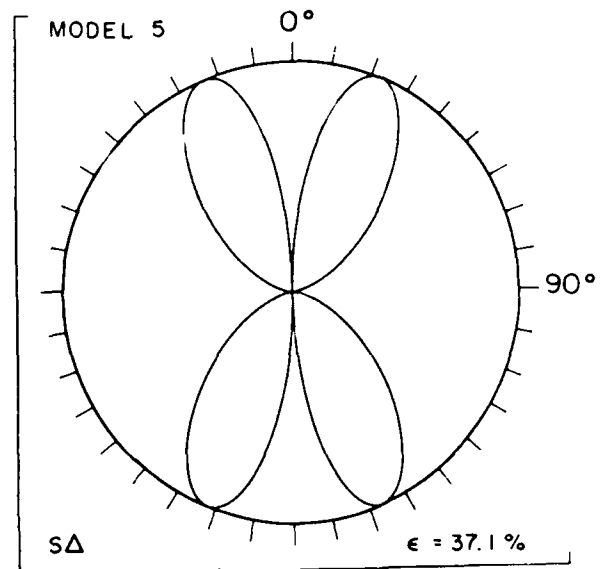
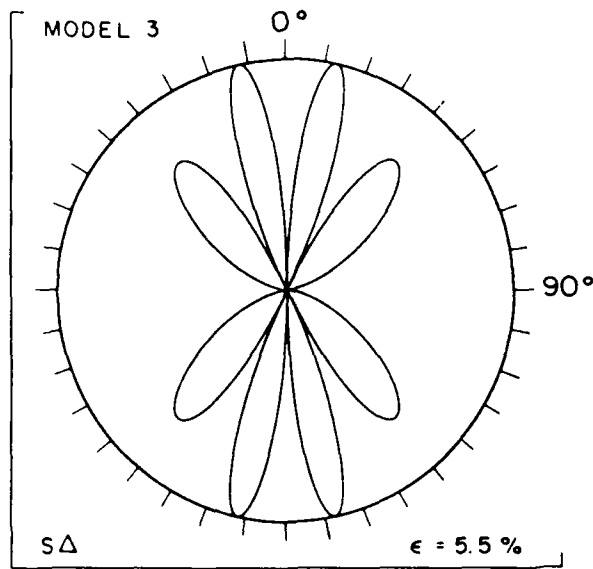


Figure 10.



EXPLOSION

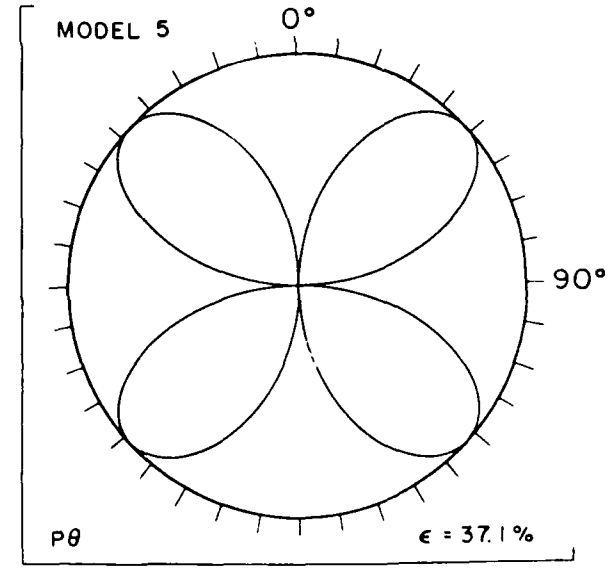
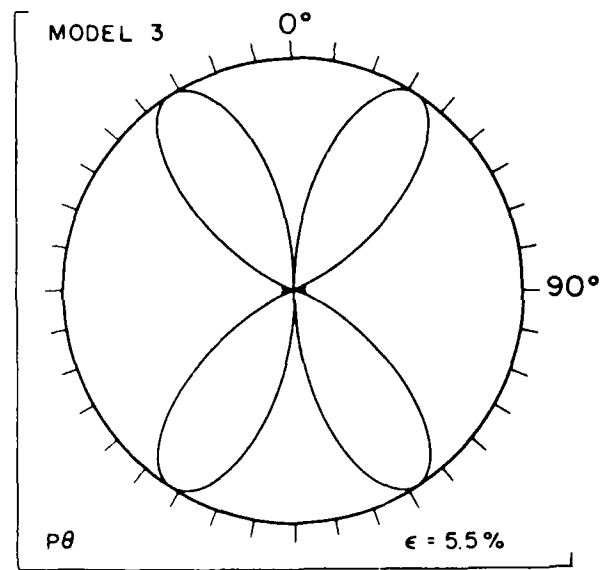
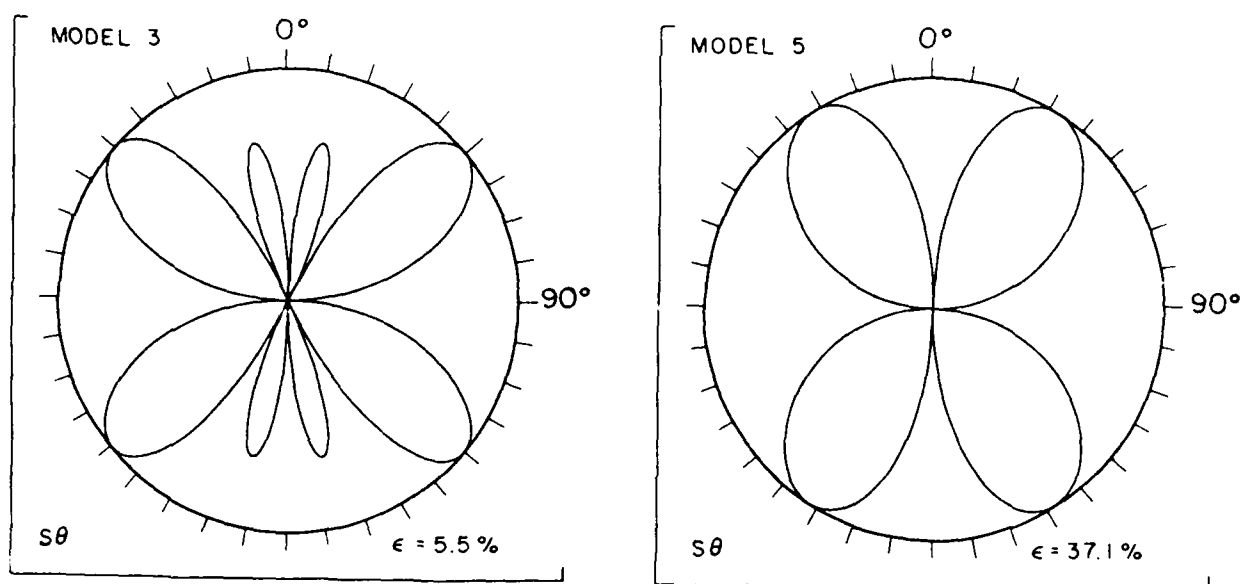


Figure 11.



EXPLOSION

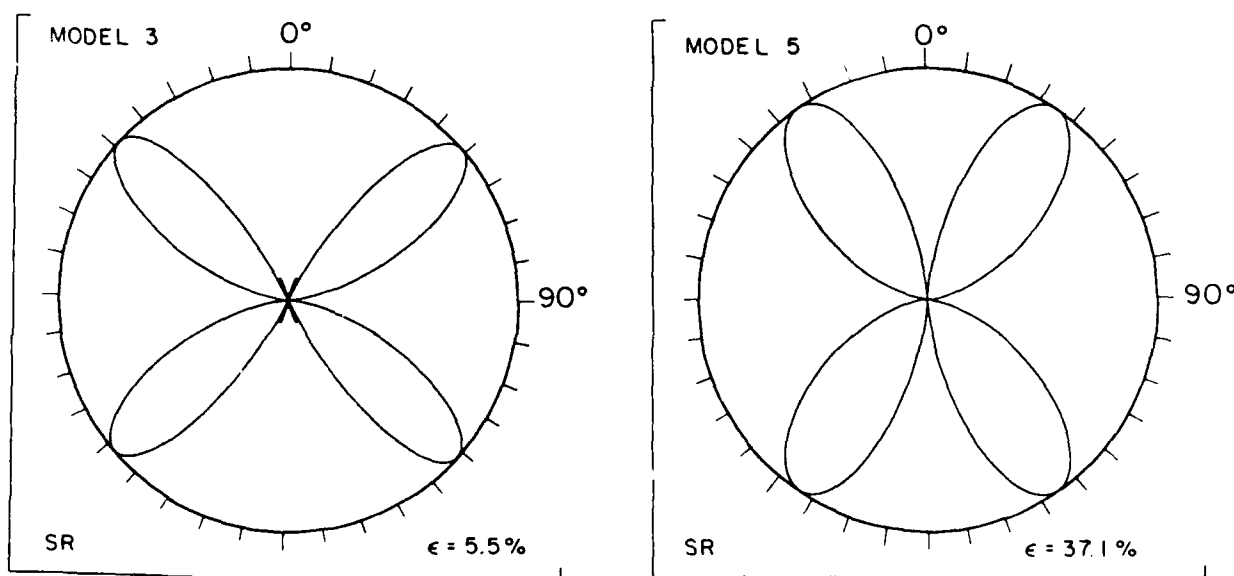
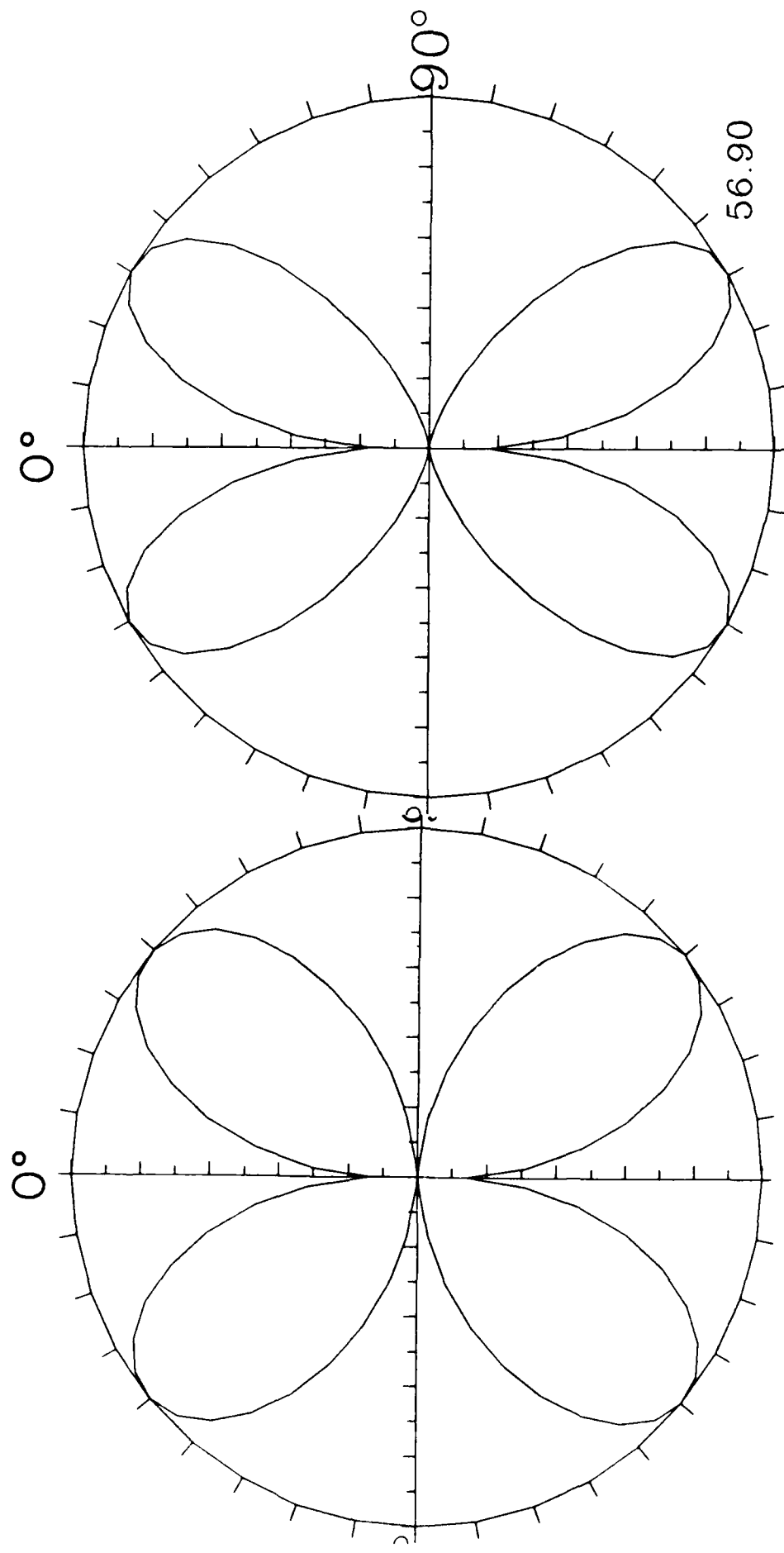


Figure 12.

MODEL 7

U-THETAP(DISL)

U-THETAP(EXPL)

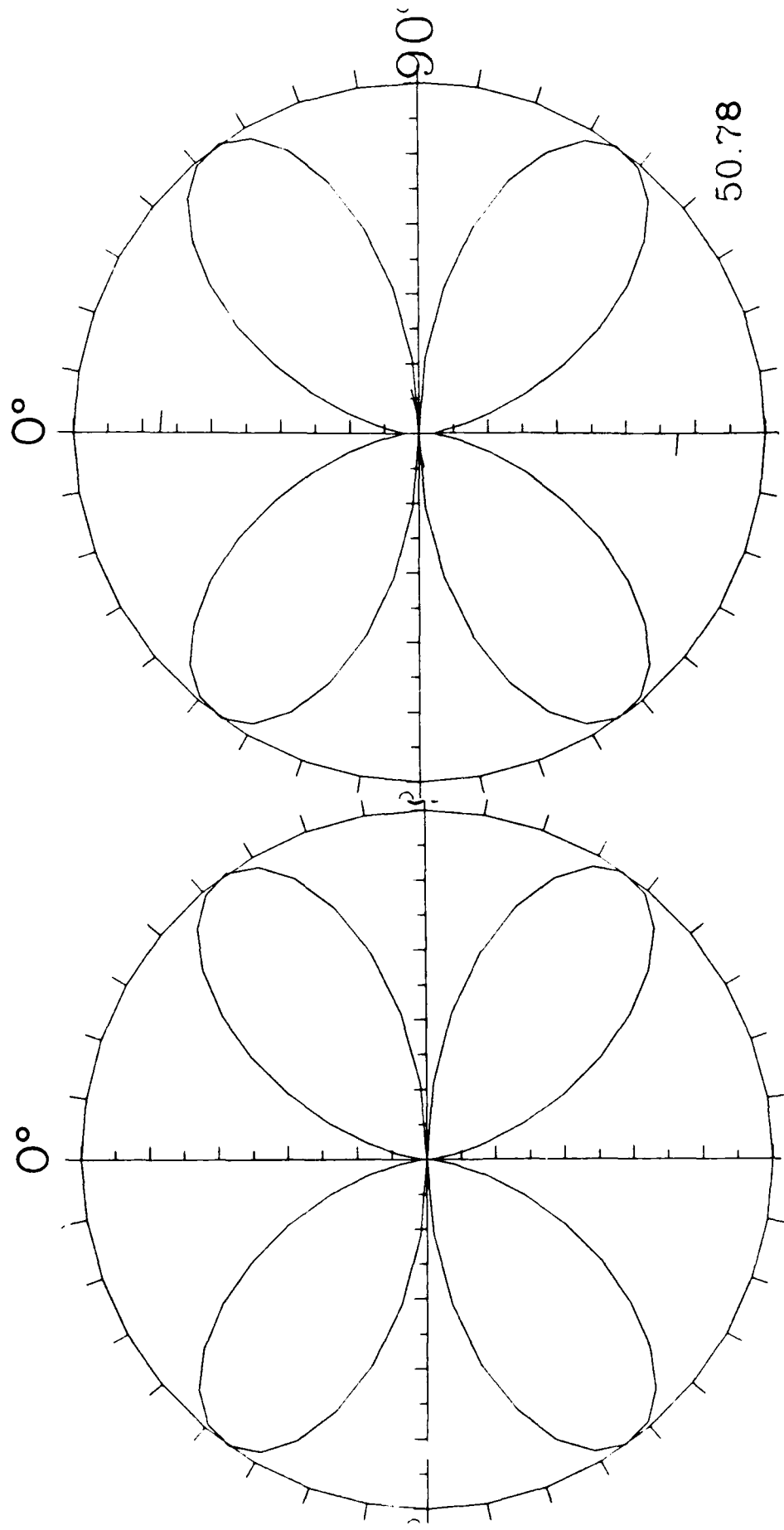


tuff (8.5%)

MODEL I

U-ZS(DISL)

U-ZS(EXPL)



MESAVERDE CLAYSHALE (20%)

Figure 14.

TABLE 1. Kernel functions $Q(k; c_{ij})$ for the displacements in the absolute far field.

$$u_j(\Delta, z; \omega) = \frac{1}{8\pi a_2 a_3} \int_0^\infty dk \frac{k e^{-|k|S_j(k)}}{S_j(k)\sqrt{\Delta k^2 + BE^2 + E^2}} [Q_0(k; c_{ij})J_0(k\Delta) + Q_1(k; c_{ij})J_1(k\Delta)]; \quad j = 1(P), 2(SV)$$

Source	ZP	Cylindrical components (Δ, ϕ, z)		ΔS
		ΔP	ZS	
Force in the direction of symmetry axis (z)	$Q_0 = -F(\omega)[a_1 k^2 - a_5 S_1^2(k) - a_1 k_p^2]$ $Q_1 = 0$	$Q_0 = 0$ $Q_1 = -F(\omega)a_3 sgn(z)kS_1(k)$	$Q_0 = F(\omega)[a_1 k^2 - a_5 S_2^2(k) - a_5 k_s^2]$ $Q_1 = 0$	$Q_0 = 0$ $Q_1 = F(\omega)a_3 sgn(z)kS_2(k)$
	$Q_0 = 0$ $Q_1 = -F(\omega)a_3 sgn(z) \cos \phi kS_1(k)$	$Q_0 = -F(\omega) \cos \phi [a_5 k^2 - a_2 S_1^2(k) - a_1 k_p^2]$ $Q_1 = 0$	$Q_0 = 0$ $Q_1 = F(\omega)a_3 sgn(z) \cos \phi kS_2(k)$	$Q_0 = F(\omega) \cos \phi [a_5 k^2 - a_2 S_2^2(k) - a_5 k_s^2]$ $Q_1 = 0$
Force in the isotropy plane (τ)	$Q_0 = M_0 sgn(z)[(a_3 - a_1)k^2 + a_5 S_1^2(k) + a_1 k_p^2]S_1(k)$ $Q_1 = 0$	$Q_0 = 0$ $Q_1 = -M_0 k[a_5 k^2 - (a_2 - a_3)S_1^2(k) - a_1 k_p^2]$	$Q_0 = -M_0 sgn(z)[(a_3 - a_1)k^2 + a_5 S_2^2(k) + a_5 k_s^2]S_2(k)$ $Q_1 = 0$	$Q_0 = 0$ $Q_1 = M_0 k[a_5 k^2 - (a_2 - a_3)S_2^2(k) - a_5 k_s^2]$
	$Q_0 = M_0 sgn(z)[(a_3 - a_1)k^2 + a_5 S_1^2(k) + a_1 k_p^2]S_1(k)$ $Q_1 = 0$	$Q_0 = 0$ $Q_1 = -M_0 k[a_5 k^2 - (a_2 - a_3)S_1^2(k) - a_1 k_p^2]$	$Q_0 = -M_0 sgn(z) \sin 2\phi k^2 S_2(k)$ $Q_1 = 0$	$Q_0 = 0$ $Q_1 = M_0 k \sin 2\phi [a_5 k^2 - a_2 S_2^2(k) - a_5 k_s^2]$

TABLE 2. Structural constants of some azimuthally-isotropic earth materials.

(Density in $\text{g} \cdot \text{cm}^{-3}$; C_{ij} in units of $10^{10} \text{ dyn} \cdot \text{cm}^{-2}$).

(\\$)	(†)	(*)	(**) (1)	(2)	(3)	(4)	(5)	(6)	(7)		
c_{11}	A	ρa_1	$\lambda + 2\mu$	50.78	51.77	50.01	10.20	3.52	11.81	56.91	
c_{33}	C	ρa_2	$\lambda + 2\mu$	36.85	48.29	45.05	7.02	2.02	9.68	54.72	
c_{13}	F	-	λ	21.49	-2.68	-8.60	4.95	2.03	7.11	36.99	
c_{66}	N	ρa_4	μ	14.87	25.97	26.59	2.31	0.42	2.26	9.71	
c_{44}	L	ρa_5	μ	11.01	24.50	24.57	1.37	0.27	1.70	8.03	
$c_{13} + c_{44}$		ρa_3	$\lambda + \mu$	32.50	21.82	15.97	6.32	2.30	8.81	45.02	
ρ	-	-	ρ	2.56	2.69	2.87	2.00	1.80	2.25	2.33	
η				1.000	1.162	1.030	1.040	1.298	1.247	1.153	1.100
η_s				1.000	1.034	0.891	0.838	0.741	0.829	0.921	0.779
η_p				1.000	1.163	1.111	1.202	1.315	1.362	1.122	1.072
ϵ (percent)	0	18.9		3.6	5.5	22.5	37.1	11.0	2.0		

(\\$) Crystallographer's notation	(1) Mesaverde clayshale (Thomsen, 1986)
(†) Stoneley's notation	(2) Mesaverde sandstone (Lin, 1985)
(*) Musgrave-Buchwald's notation	(3) Mesaverde sandstone (Lin, 1985)
(**) Isotropic limit	(4) Fog Creek shale (Robertson & Corrigan, 1983)
	(5) Eocene Wills Point shale (Robertson & Corrigan, 1983)
	(6) Pierre shale (White <i>et al.</i> , 1983)
	(7) Timber Mtn. tuff (Shock <i>et al.</i> , 1974)

TABLE 3. Far-field radiation patterns^(1,2) of point sources in unbounded anisotropic media.

Stationary phase approximation.

Source	Cylindrical components (Δ, ϕ, z)		
	ZP	ΔP	ZS
Force in the direction of symmetry axis (z), $s(\omega) = F(\omega)$	$\frac{\eta_p \sin \sigma_p \cos \sigma_p}{a_1 A_p^{1/2}}$	$\frac{\eta_p \sin^2 \sigma_p}{a_1} \frac{A_p}{A_s^{1/2}}$	$-\frac{\eta_p}{a_3} \frac{\sin \sigma_s \cos \sigma_s}{A_s^{1/2}}$
Force in the isotropy plane (x), $s(\omega) = F(\omega)$	$\frac{\eta_p \sin \sigma_p \cos \sigma_p}{a_1 A_p^{1/2}} \cos \phi$	$\frac{\eta_p \sin^2 \sigma_p}{a_1} \frac{A_p}{A_s^{1/2}} \cos \phi$	$-\frac{\eta_p}{a_3} \frac{\sin \sigma_s \cos \sigma_s}{A_s^{1/2}} \cos \phi$
Center of compression, $s(\omega) = iM_0(\omega)$	$\frac{k_p \eta_p}{a_1} \left(\frac{\sin \theta \sin \sigma_p + \eta_p^2 \cos \theta \cos \sigma_p}{A_p} \right) \cos \sigma_p$	$\frac{k_p \eta_p}{a_1} \left(\frac{\sin \theta \sin \sigma_p + \eta_p^2 \cos \theta \cos \sigma_p}{A_p} \right) \sin \sigma_p$	$-\frac{k_p \eta_p}{a_3} \left(\frac{\sin \theta \cos \sigma_s - \eta_p^2 \cos \theta \sin \sigma_s}{A_s} \right) \sin \sigma_s$
Torque parallel to symmetry axis (z)		$u_\phi = -\frac{i k_{SH} M_0}{4 \pi \eta_p S H a_3} \frac{\sin \theta}{\sin^2 \theta + \eta_p^2 S H} \frac{\sin \theta}{\cos^2 \theta}$	$e^{-i k SH R} \frac{\sin \theta}{r}$
Dislocation in xz plane, $s(\omega) = iM_0(\omega)$	$\frac{k_p \eta_p \sin \sigma_p \cos \sigma_p}{a_1} \sin \theta \sin 2\phi$	$\frac{k_p \eta_p \sin^2 \sigma_p}{a_1} \sin \theta \sin 2\phi$	$-\frac{k_p \eta_p}{a_3} \frac{\sin \sigma_s \cos \sigma_s \sin \theta \sin 2\phi}{A_s}$
			$\frac{k_p \eta_p}{a_3} \frac{\cos^2 \sigma_s \sin \theta \sin 2\phi}{A_s}$

(1) A common frequency dependent factor $\left\{ \frac{s(\omega)}{4\pi\rho} \frac{e^{-i k_p R_p}}{r} \right\}$ is suppressed in all quasi-longitudinal (P) displacements.

(2) A common frequency dependent factor $\left\{ \frac{s(\omega)}{4\pi\rho} \frac{e^{-i k_s R_s}}{r} \right\}$ is suppressed in all quasi-transverse (S) displacements.

Ad-hoc notation:

$$A_p = \sin^2 \theta + \eta_p^2 \cos^2 \theta \quad ; \quad k_p^2 = \frac{\omega^2}{a_1} \quad ; \quad k_{SH}^2 = \frac{\omega^2}{a_3}$$

$$A_s = \sin^2 \theta + \eta_s^2 \cos^2 \theta \quad ; \quad k_s^2 = \frac{\omega^2}{a_3}$$

TABLE 4. Far-field radiation patterns of point sources in unbounded anisotropic media.

Stationary phase approximation. (Notation and convention as in Table 3.)

Source	Spherical components (r, θ, ϕ)		
	RP	θP	RS
Force in the direction of symmetry axis (z), $s(\omega) = F(\omega)$	$\frac{2e}{a_1} \frac{B_{RF}(\theta)}{A_p} \cos \sigma_p$	$\frac{2e}{a_1} \frac{B_{RF}(\theta)}{A_p} \cos \sigma_p$	$\frac{2e}{a_3} \frac{B_{RS}(\theta)}{A_p} \sin \sigma_s$ $- \frac{2e}{a_3} \frac{B_{RS}(\theta)}{A_p} \sin \sigma_s$
Force in the isotropy plane (z), $s(\omega) = F(\omega)$	$\frac{2e}{a_1} \frac{B_{RF}(\theta)}{A_p} \sin \sigma_p \cos \phi$	$\frac{2e}{a_1} \frac{B_{RF}(\theta)}{A_p} \sin \sigma_p \cos \phi$	$\frac{2e}{a_3} \frac{B_{RS}(\theta)}{A_p} \cos \sigma_s \cos \phi$ $- \frac{2e}{a_3} \frac{B_{RS}(\theta)}{A_p} \cos \sigma_s \cos \phi$
Center of compression, $s(\omega) = iM_0(\omega)$	$\frac{k_p \eta_p}{a_1} \frac{B_{RF}(\theta)}{A_p} (\sin \theta \sin \sigma_p + \eta_p^2 \cos \theta \cos \sigma_p)$	$\frac{k_p \eta_p}{a_1} \frac{B_{RF}(\theta)}{A_p} (\sin \theta \cos \sigma_s + \eta_p^2 \cos \theta \cos \sigma_p)$	$\frac{k_p \eta_p}{a_3} \frac{B_{RS}(\theta)}{A_p} (\sin \theta \cos \sigma_s - \eta_p^2 \cos \theta \sin \sigma_s)$ $- \frac{k_p \eta_p}{a_3} \frac{B_{RS}(\theta)}{A_p} (\sin \theta \cos \sigma_s - \eta_p^2 \cos \theta \sin \sigma_s)$
Torque parallel to symmetry axis (z)		$u_\phi = -\frac{ik_{SH} M_0}{4\pi \rho c H a_3} \frac{\sin \theta}{\sin^2 \theta + \frac{1}{4} k_H^2 H^2 \cos^2 \theta} \frac{e^{-ik_{SH} R}}{r}$	
Dislocation in zz plane, $s(\omega) = iM_0(\omega)$	$\frac{k_p \eta_p}{a_1} \frac{B_{RF}(\theta)}{A_p} \sin \sigma_p \sin \theta \sin 2\phi$	$\frac{k_p \eta_p}{a_1} \frac{B_{RF}(\theta)}{A_p} \sin \sigma_p \sin \theta \sin 2\phi$	$\frac{k_p \eta_p}{a_3} \frac{B_{RS}(\theta)}{A_p} \cos \sigma_s \sin \theta \sin 2\phi$ $- \frac{k_p \eta_p}{a_3} \frac{B_{RS}(\theta)}{A_p} \cos \sigma_s \sin \theta \sin 2\phi$

$$B_{RP}(\theta) = \cos \theta \cos \sigma_p + \sin \theta \sin \sigma_p$$

$$B_{\theta P}(\theta) = \cos \theta \sin \sigma_p - \sin \theta \cos \sigma_p$$

$$B_{RS}(\theta) = \cos \theta \sin \sigma_s - \sin \theta \cos \sigma_s$$

$$B_{\theta S}(\theta) = \cos \theta \cos \sigma_s + \sin \theta \sin \sigma_s$$

Computation of complete waveforms in general anisotropic media – Results from an explosion source in anisotropic medium

B. Mandal and M. N. Toksöz

Earth Resources Laboratory, Dept. of Earth Atmospheric & Planetary Sciences, Massachusetts Institute of Technology, 42 Carleton St, E34-400, Cambridge, MA-02142, USA.

Submitted to Geophysical Journal, September, 1989

SUMMARY

An algorithm of generating complete waveforms in general anisotropic media (21 constants) is presented. Complete waveforms have been computed including a point source in anisotropic medium and the reflection and transmission properties of individual interfaces. A recursive scheme of scatterer operators and the numerical wavenumber integration technique are used. The 6×6 system matrix \mathbf{A} of each layer is derived, and each element of \mathbf{A} is expressed in terms of coefficients of two horizontal wavenumbers. This form of system matrix \mathbf{A} reduces the computation time and uses the wavenumber as an inner loop (vectorizing loop). The complex upper Hessenberg Matrix and QR algorithm are used to compute simultaneously the eigenvalues and eigenvectors of \mathbf{A} . The upgoing and downgoing eigenvalues are separated according to radiation condition and the properties of z -component Poynting vector. Filon integration is applied to evaluate the integrals over two horizontal wavenumbers. Since wave propagation in anisotropic medium is a three

dimensional problem, it requires an enormous number of computations. To reduce the computation time, the wavenumber loop is used as the deepest loop. An efficient computer code has been developed for vectorization in the super computer. Both source and receivers can be placed at arbitrary depths. Three component synthetic seismograms are computed from an explosion in the anisotropic medium. Examples are calculated for half-space multilayered anisotropic media. Theoretical seismograms show that radiation patterns are strongly affected by the anisotropy. For example, an explosion in an anisotropic medium with horizontal axes of symmetry generates P, SV, and Rayleigh waves, all whose amplitudes vary with azimuths, and significant transverse (SH) waves at certain azimuths. These effects could be explained by the non-spherical behavior of source due to the direction dependence of elastic moduli. The waveforms are further complicated by the reflection and conversion phenomena of waves propagating in anisotropic media.

Key words: general anisotropy, complete waveforms, explosion source, wavenumber integration, vertical fractures

INTRODUCTION

This paper presents the computation of complete wavefield in general anisotropic media due to a point source. It also investigates the effects of anisotropy on the synthetic seismograms. In recent years increasing numbers of observational studies in seismology have required interpretations in terms of anisotropic elastic properties since a small degree can significantly affect the imaging of the wave field. This variation may be caused by a variety of mechanisms, including mineralization/deposition orientations, tectonic stress or preferentially oriented fracture patterns. An anisotropic medium has some distinct effects on data which cannot be explained by an isotropic

or heterogeneous medium. The existence of anisotropy in the crust has been widely detected in field data, as well as in laboratory experiments (e.g. Robertson and Corrigan, 1983; Crampin *et al.*, 1984; Gaiser *et al.*, 1984; Babuska, 1981). The theoretical developments of wave motion in anisotropic media for last 50 years were reviewed by Crampin (1981) and Pao (1983). Recently, computation of synthetic seismograms in anisotropic media have been developed by Booth and Crampin (1983) and by Fryer and Frazer (1984) which further advances toward complete waveform computation in general anisotropic media.

To compute complete synthetic waveforms, we use the numerical wavenumber integration method (e.g. Bouchon and Aki, 1977). In this method the computation can be divided into three steps. First, the steady-state wave field radiation by a seismic source is represented as a superposition of waves propagating with discrete phase velocities. In this way a single source is replaced by a periodic array of sources. The effect of secondary sources is removed by introducing both a small constant imaginary part of the frequency and proper wavenumber step size. Then each phase velocity component of the source wave field is propagated through a stack of layers from the reflection and transmission properties of individual interfaces using a recursion scheme of scatterer operators and scatterer products (e.g. Saastamoinen, 1980; Kennett, 1983, Fryer and Frazer, 1984). The resulting contributions are summed for each wavenumber to transform from the wavenumber domain to the space domain. Finally, the solution obtained is Fourier transformed to the time domain, and the unwanted effects of source periodicity and complex frequency are removed. This final solution yields the complete wavefield within the medium for the particular source considered over a specified time length. This method is common for isotropic and anisotropic media except for

the computation of the eigensolutions. In an isotropic medium or transversely isotropic medium with a vertical axis of symmetry, this computation of eigensolutions can be performed analytically (e.g. Mandal and Mitchell, 1986). The energy propagating from source to receiver is restricted to the sagittal plane. However, in azimuthal anisotropic media, the energy generally propagates out of the sagittal plane causing the transverse component of the wavenumber vector to be non-zero (e.g. Auld, 1973). This phenomenon forces us to compute three-dimensional eigensolutions to achieve complete wavefields in anisotropic media. In general, the elastodynamic solutions are computed from the Christoffel equation of six order polynomial (e.g. Fedorov, 1968; Musgrave, 1970; Frayer and Frazer, 1987). This procedure needs a high degree of numerical precession. To avoid these problems, we derived the system matrix A in a spatial form and calculated the elastodynamic solutions by computing the eigenvalues and eigenvectors of the system matrix A using QR algorithm (e.g. Golub, 1983). This method is very stable and eigenvalues and its eigenvectors are computed simultaneously. We then substitute these eigensolutions in the reflectivity and numerical wavenumber integration algorithm to get the complete wave field. To reduce the computation time, we used Filon quadrature (1928) relation for numerical integration in wavenumber domain. This technique will allow us to use larger wavenumber step size and smaller oscillation of the kernel of the integral.

In this computation we choose to use a Cartesian coordinate system. Although a cylindrical coordinate is the right choice to compute a synthetic wavefield for modeling elastic waves, there is no simple solution for general anisotropic media. The problem of wave propagation in general anisotropic media is thus much more conveniently addressed in Cartesian coordinates, with the wavenumber to space transformation accomplished by numerical integration and the frequency to

time transformation by inverse Fourier transformation.

Investigated is the complexity of seismic radiation patterns and the generation of transversely polarized (SH) waves by an explosion in anisotropic medium. The causes of the azimuthal dependence of radiation patterns of P, SV, and Rayleigh waves and the generation of SH and Love waves by underground nuclear explosions have been studied extensively (Kisslinger *et al.*, 1961; Archambeau *et al.*, 1970; Toksöz and Kehrein, 1972; Massé, 1981; Wallace *et al.*, 1983; Gupta and Blandford, 1983; Lynnes and Lay, 1988; Johnson, 1988). Various mechanisms including: tectonic strain energy release by relaxation or triggering of an earthquake; dislocation across cracks; spallation and "slapdown"; and scattering from heterogeneities have been proposed and found to explain some of the data. No single mechanism has been identified that could satisfactorily explain all the data (Massé, 1981; Gupta and Blandford, 1983; Johnson, 1988.)

The evidence for seismic anisotropy in the earth's crust has been also increasing. Recent observational studies showed that the crust material may have seismic anisotropy due to aligned fractures randomly distributed (e.g., Stephen, 1981; Crampin, 1984; Thomsen, 1986; Winterstein, 1986). Several major factors contribute to seismic anisotropy including: (1) preferred orientation of the minerals due to deposition or metamorphism; (2) geometric effects, such as alternating high and low velocity thin beds (e.g., shales, carbonates); and (3) stress-induced preferred orientation of micro- and macro-fractures in shallow crust. The complete seismogram synthesis in transversely isotropic media with a vertical axis of symmetry (Mandal and Mitchell, 1986) showed that the most simple kind of anisotropy can alter the waveform significantly. The reflection and transmission phenomena for anisotropic media are very much different than isotropic case (e.g. Rokhlin *et al.*, 1986,

Mandal, 1989). In addition, the some radiation patterns are altered if the source is located in an anisotropic medium. For example, an explosion source in anisotropic full space could generate a significant amount of shear wave energy where none would be generated in an isotropic medium (Mandal, 1988; Ben-Menahem and Toksöz, 1989). These studies also show that the radiation pattern of P waves from an explosion in a transversely isotropic medium is not spherical.

In this paper we investigate the effect of anisotropy on seismic radiation by computing complete synthetic seismograms from an explosion source. We take a simple half-space or a layer on a half-space where the axis of symmetry is horizontal and velocities vary with azimuth. Such a medium can be derived from aligned vertical fractures. We show that anisotropy could have significant effects on radiation patterns of all phases producing a transverse component of P-wave and generating a strong SH-type transverse wave.

THEORETICAL BACKGROUND

I. Wave Equation and Plane Wave Solution

We consider a layered, anisotropic media bounded above by a free surface and below by a half-space (Figure 1). The material properties within each layer is homogeneous. Any sublayer is characterized by a thickness H , a density ρ , and 21 independent stiffness coefficients C_{ijkl} with a 6×6 (symmetric) matrix. We take z-axis positive downward and assume density and elastic constants are functions of z only. The wave equation without body force will be:

$$\rho \partial_t^2 u_i = \tau_{ij,j} = (C_{ijkl} u_{k,l})_j \quad (1)$$

where displacements: $\mathbf{u} = (u_x, u_y, u_z)^T$, stress tensor: $\tau_{ij} = C_{ijkl}e_{kl}$ (Generalized Hook's Law), and strain tensor: e_{kl} .

We assume a displacement-stress vector \mathbf{b} whose variables are continuous across any horizontal plane, and whose trial plane wave solutions is

$$\mathbf{b} = \begin{pmatrix} \mathbf{u} \\ \boldsymbol{\tau} \end{pmatrix} = \begin{pmatrix} \mathbf{U} \\ \mathbf{T} \end{pmatrix} e^{i\omega(p_x x + p_y y - t)}, \quad (2)$$

where \mathbf{U} and \mathbf{T} are new coefficients of the displacement-stress vector. They are expressed as,

$\mathbf{U} = (U_x, U_y, U_z)^T$ coefficients of component of displacement, $\boldsymbol{\tau} = \frac{-1}{i\omega}(\tau_{xz}, \tau_{yz}, \tau_{zz})^T$ and $\mathbf{T} = \frac{-1}{i\omega}(T_{xz}, T_{yz}, T_{zz})^T$ vertical components of stress tensor and its coefficients. The p_x and p_y are horizontal phase slownesses and ω is the angular frequency.

The substitution of these trail solutions (2) on the wave equation (1) and after some algebraic mesh (Appendix A), we will end up a set of linear differential equations with simple form

$$\partial_z \mathbf{b}(z) = i\omega \mathbf{A}(z) \mathbf{b}(z). \quad (3)$$

\mathbf{A} is the system (6×6) matrix consisting of medium elastic constants (C_{ijkl}), density, and horizontal phase slownesses. From the definition of \mathbf{b} , the system matrix \mathbf{A} in (3) is in the form (Appendix A)

$$\mathbf{A} = \begin{pmatrix} \mathbf{O} & \mathbf{P} \\ \mathbf{Q} & \mathbf{O}^T \end{pmatrix}, \quad (4)$$

where \mathbf{O} , \mathbf{P} , and \mathbf{Q} are 3×3 submatrices and \mathbf{P} and \mathbf{Q} are symmetric.

The formulation of differential system as Eq.(3) as derived in Appendix A followed the approach of Alterman et al. (1959). The advantages of this approach are as follows: there are no derivatives of elastic constants and densities, and the \mathbf{U} and \mathbf{T} are proportional to displacement and stress so

that they behave same at the boundary. Takeuchi and Saito (1972) used same approach to solve the differential system for transversely isotropic media.

The differential system (3) can be solved subject to specified boundary conditions to compute the displacement-stress field (**b**) at any depth provided the medium parameters vary with z-direction. The classical propagator matrix method can be used to transmit the wavefield from one point to other. The techniques of propagator matrix method are well defined (e.g. Gilbert and Backaus, 1966). For vertical stratified medium, using a propagator matrix approach, the response at depth z may be written

$$\begin{aligned} b(z) &= e^{i\omega A(z)(z-z_o)} b(z_o) \\ &= P(z, z_o) b(z_o), \end{aligned} \quad (5)$$

where $P(z, z_o) = e^{i\omega A(z)(z-z_o)}$ is the stress-displacement propagator (also called matricant and matrizant of layer matrix for a homogeneous medium) at depth z from a reference depth z_o . The detail properties of the propagator has been given in many previous articles (e.g. Gilbert and Backaus, 1966, Woodhouse, 1974).

From the definition of the propagator (e.g. Gilbert and Backaus, 1966) we may write

$$\begin{aligned} \partial_z P(z, z_o) &= i\omega A(z) P(z, z_o), \\ P(z, z_o) &= I, \\ P(z, z_o) &= D e^{i\omega(z-z_o)\Lambda} D^{-1}, \end{aligned} \quad (6)$$

where I is a 6×6 identity matrix; D is the eigenvector matrix of A (i.e., each column of D is an eigenvector) and Λ is the diagonal matrix of eigenvalues. We can write the relation between D , A ,

and Λ as,

$$D^{-1}AD = \Lambda. \quad (7)$$

Some properties of eigenvectors (D) are identified provided they are normalized correctly with respect to vertical energy flux (e.g. Chadwick and Smith 1977; Garmany 1983; Fryer and Frazer 1984).

II. Eigensolutions

A vertically stratified medium may be defined by a series of homogeneous layers. To propagate wavefield from one point to another, we need to evaluate eigenvalues and eigenvectors of the system matrix (A) for each layer. There are six eigenvalues with six corresponding eigenvectors. In general anisotropic medium, major portions of the computation has been devoted to compute the eigenvalues and eigenvectors of the system matrix. There is no simplified solution for this in anisotropic medium. Hence, one has to go for numerical solution and the present computer revolution allows us to do that job efficiently. There are some practical analytical solutions for the medium with a higher degree of symmetry (Mandal and Mitchell, 1986; Fryer and Frazer, 1987).

In general, the eigenvalue problem in anisotropic medium may be expressed as in terms of wave normal

$$(C_{ijkl}n_j n_l - \rho v^2 \delta_{ik}) P_k = 0 \quad (8)$$

and in terms of slowness vector

$$(C_{ijkl}p_j p_l - \rho \delta_{ik}) P_k = 0 \quad (9)$$

where P_k is the polarization unit displacement vector (eigen vectors), n is the wave normal, and v

is the phase velocity. These equation (8) or (9) have non trivial solutions for $P_k \neq 0$ only if the determinant of the system equals zero, know as Christoffel's matrix:

$$|C_{ijkl}n_j n_l - \rho v^2 \delta_{ik}| = 0 \quad (10)$$

$$|C_{ijkl}p_j p_l - \rho \delta_{ik}| = 0 \quad (11)$$

These equations (10-11) are used to determine three unknown phase velocities and corresponding vectors of the permissible elastic waves in the given wave direction \mathbf{n} .

The nature of the wave phenomenon in anisotropic media is significantly different from that in isotropic media. The properties of wave phenomena in anisotropic medium are discussed elsewhere (e.g. Fedorov, 1968; Musgrave, 1970; Auld, 1973; Crampin, 1981). The Christoffel equation (11) gives 6 roots in each medium, three of which are up-going (U) and three of which are down-going (D) corresponding to three fundamental waves. They are a quasilongitudinal wave (qP) and two quasitransverse waves ($S1$ - faster and $S2$ - slower transverse wave). In general, none of these will be purely longitudinal or purely transverse waves. Each of the waves has different phase and group or energy (ray) velocities. The group or energy velocity is greater than or equal to the phase velocity and its direction does not coincide with the wave normal (e.g. Fedorov, 1968; Auld, 1973, Rokhlin, et al., 1968). The determination of the eigenvalues and eigenvectors using equations (10) and (11) have been reported by many authors (e.g. Fedorov, 1968; Musgrave, 1970; Frayer and Frazer, 1987; Rokhlin, et al., 1986). To solve the six order polynomial (11), a very high degree precision is necessary using an analytical method especially when waves are in an evanescent regime. The Laguerre's numerical method (Press et al., 1986) may be used to compute the roots of the polynomial even in normal precision (Mandal, 1988).

Here, we are using a simultaneous method of computation of eigenvalues and eigenvectors of system matrix A . The algorithm of this method is taken from EISPACK routines (e.g. Smith, et al., 1976; Golub and Van Loan, 1983). The algorithm has few steps. First, it balances the 6×6 complex matrix (A) to reduce the overall norm of the matrix. Second, it establishes the balanced matrix in an *upper Hessenberg* form (e.g. Wilkinson and Reinsch, 1971). Finally, the QR algorithm (e.g. Golub and Van Loan, 1983) is used to compute simultaneously the eigenvalue and eigenvectors of the upper Hessenberg matrix. The QR transformation preserves the upper Hessenberg form of the original matrix. This method is very stable and computes faster ($O(n^2)$) than the general matrix method ($O(n^3)$) (e.g. Press, et al., 1986).

The up-going and down-going wave field may be separated by the radiation condition for $\omega > 0$

$$Im(q^D) > 0 \quad \text{and} \quad Im(q^U) < 0, \quad (12)$$

where q^D and q^U are the vertical slownesses or eigenvalues for down-going and up-going waves respectively.

The above-mentioned radiation conditions are not sufficient, especially when there is no imaginary component of the eigenvalues for propagating modes through a nonattenuative medium. Another set of necessary conditions should be available to make sure that the propagating modes carry energy into the other solid medium and that the evanescent modes decay into the other solid medium as a function of depth. The Poynting vector approach is found to be more appropriate to separate the up- and down-going waves along with the radiation conditions (e.g. Musgrave, 1970; Henneke, 1972). This vector is in the direction of the gradient of the slowness surface, not along the normal to the wavefront. For separating up- and down-going vectors, the z -component of the

wave vector is sufficient. This component is given by

$$P_z = -\frac{1}{2}(v_x^*T_{yz} + v_y^*T_{xz} + v_z^*T_{zz}) \quad (13)$$

where the v_i^* 's are conjugates of the respective particle velocities. The criteria of the evanescent and nonevanescent modes are: (1) a negative imaginary part for the evanescent mode; (2) a positive real part for the nonevanescent mode. These characteristics, along with the other radiation conditions (Eq. 12), will ensure separate correct up- and down-going wave fields.

III. Reflection and Transmission Response

Our model is composed of a series of uniform anisotropic layers with a free surface $z = 0$ and a halfspace at $z > z_L$ (Figure 1). We calculate the propagator forms using reflectivity coefficients as described by Kennett and Kerry (1979) and Kennett (1983). We compute the response at the uppermost interface and then adding the effects of successive deeper layers.

Ignoring the free surface effects, the relation between the stress-displacement vector at depth 0 and z_L from (5) and (6)

$$b(z_L) = D(z_L+)W(z_L+, 0+)D^{-1}(0+)b(0), \quad (14)$$

where + (plus)-sign refers to the expression just below the interface. $W = e^{i\omega(z_L-0)\Lambda}$ is known as 'wave-propagator' and it depends on the difference between the current depth z_L (half-space) and 0 (free-surface). In terms of the wavevector in the half-space, the relation looks like

$$\mathbf{v}(z_L+) = W(z_L+, 0+)\mathbf{v}(0+), \quad (15)$$

In terms of the up- and down-going wavevector, the above equation can be expressed as

$$\begin{pmatrix} v_U(z_L+) \\ v_D(z_L+) \end{pmatrix} = \begin{pmatrix} W_{11} & W_{12} \\ W_{21} & W_{22} \end{pmatrix} \begin{pmatrix} v_U(0+) \\ v_D(0+) \end{pmatrix}, \quad (16)$$

where we partition the wave propagator into 3×3 submatrices. We can apply the obvious boundary conditions for the wavevector at the free surface (up-going energy will equal to down-going reflection energy) and at the half-space (no up-going energy) as

$$v_U(0+) = R_D v_D(0+), \quad v_D(z_L+) = T_D v_D(0+) \quad (17)$$

where R and T are reflection and transmission matrices. If we consider the source originating inside the layer medium then from the equations (16 and 17), all the reflection and transmission coefficients will be

$$\begin{pmatrix} 0 & I \\ T_D & R_U \end{pmatrix} = \begin{pmatrix} W_{11} & W_{12} \\ W_{21} & W_{22} \end{pmatrix} \begin{pmatrix} R_D & T_U \\ I & 0 \end{pmatrix}. \quad (18)$$

We can write a scatterer or reflection matrix of the equation as

$$\mathbf{R} = \begin{pmatrix} T_U & R_D \\ R_U & T_D \end{pmatrix} = \begin{pmatrix} W_{11}^{-1} & -W_{11}^{-1}W_{12} \\ W_{21}W_{11}^{-1} & W_{22} - W_{21}W_{11}^{-1}W_{12} \end{pmatrix} \quad (19)$$

(e.g. Kennett, 1974; Kennett and Kerry, 1979). It is useful to present equation (19) in the symbolic form

$$\mathbf{R} = \varphi(\mathbf{W}) \quad (20)$$

The term, φ , is known as a scatterer operator which maps the propagator \mathbf{W} into scatterers \mathbf{R} . The properties of the operator are discussed in an article by Saastamoinen (1980). This concept of

a “scatterer product” can be introduced for studying the scattering properties of a stack of layers which may be anisotropic media (Saastamoinen, 1980; Fryer and Frazer, 1984).

Due to continuity of stress and displacement at an interface, the wave propagator \mathbf{W} at depth z_i takes a form

$$W(z_i+, z_i-) = D^{-1}(z_i+)D(z_i-). \quad (21)$$

The interface scatterer, which includes, the reflection and transmission effects is from equations (20) and (21)

$$R(z_i+, z_i-) = \varphi [W(z_i+, z_i-)]. \quad (22)$$

The total response of the interface and the uniform medium by using the scatter product (\star) is

$$\mathbf{R}(z_i-, z_{i-1}+) = \mathbf{R}(z_i+, z_i-) \star \mathbf{R}(z_i-, z_{i-1}+). \quad (23)$$

Thus, the overall response of the layered structure can be computed from the above relations by adding succession of layer-interface scatterers from the top of the layer as going downward or from half-space going upward, so that for step i we have a form

$$\mathbf{R}(z_i+, 0+) = \mathbf{R}(z_i+, z_{i-1}+) \star \mathbf{R}(z_{i-1}+, 0+). \quad (24)$$

In this approach, there are no growing exponentials (Saastamoinen, 1980) so that we will get a stable result even at high frequencies.

IV. Point Source in Anisotropic Medium

Our main goal is to compute the seismic response at several receivers located in other arbitrary positions from an arbitrarily placed source. The basic method used in this case for a single receiver

is described in detail by Kennett (1983, Ch. 7). A Cartesian coordinate system (x, y, z) is used to compute the complete wavefield in anisotropic media. Here, we do not consider any approximation of propagation in anisotropic media. To account for all kinds of anisotropic effects, we must integrate both horizontal wavenumbers (k_x, k_y) to achieve full response from a point source. Attenuation is introduced by specifying imaginary parts to the elastic constants (Crampin, 1981).

The inclusion of a source in an anisotropic medium is discussed by Frayer and Frazer (1984). Choosing a Cartesian coordinate is very helpful to introduce a point source in anisotropic media. The original homogeneous differential equation (3) is no-longer valid for the presence of any source and the equation (3) will take an inhomogeneous form

$$\frac{\partial \mathbf{b}}{\partial z} = i\omega \mathbf{A}\mathbf{b} + \mathbf{F} \quad (25)$$

where $\mathbf{F} = \frac{-1}{i\omega} (0, 0, 0, f_x, f_y, f_z)^T$ is a source term containing the body forces. With the presence of a point source in the medium, we will have a discontinuity across the plane containing the source (depth z_s). A point source at $r = (0, 0, z_s)$ can be represented by a point force $\mathbf{h} = (h_x, h_y, h_z)^T$ and a symmetric moment tensor \mathbf{M} , with a body force equivalent given by (Burridge and Knopoff, 1964)

$$f = h\delta(r - r_s) \text{ for simple point force,} \quad (26)$$

$$f = -M \cdot \nabla \delta(r - r_s) \text{ for double couple source,} \quad (27)$$

where δ and ∇ are the delta function and gradient operator respectively. If S is stress-displacement discontinuity at depth z_s , then an equivalent wave vector discontinuity is

$$\Sigma(z_s) = \begin{pmatrix} -\Sigma_U \\ \Sigma_D \end{pmatrix} = D^{-1}(z_s)S(z_s). \quad (28)$$

This vector $S(z_s)$ is obtained from equations (26-27), by the Fourier transform over x and y , in the form (e.g. Frayer and Frazer, 1984)

$$S(z_s) = -\frac{1}{i\omega} \begin{pmatrix} 0 \\ 0 \\ 0 \\ h_x \\ h_y \\ h_z \end{pmatrix} \quad \text{for point force,} \quad (29)$$

$$S(z_s) = \begin{pmatrix} 0 \\ 0 \\ 0 \\ p_x M_{xx} + p_y M_{xy} \\ p_x M_{xy} + p_y M_{yy} \\ p_x M_{zx} + p_y M_{zy} \end{pmatrix} + A(z_s) \begin{pmatrix} 0 \\ 0 \\ 0 \\ M_{xz} \\ M_{yz} \\ M_{zz} \end{pmatrix} \quad \text{for double couple source.} \quad (30)$$

For example, for an explosion source, point forces \mathbf{h} will vanish and only diagonal components of equal magnitude moment tensors (M_{xx}, M_{yy}, M_{zz}) will contribute to the source. This discontinuity wave vector is used to compute the radiation pattern for different kinds of sources in an anisotropic medium.

For example, in general anisotropic medium, the source vector for explosion source will be (from

Appendix A),

$$S(z_s) = \begin{pmatrix} -(\mathcal{D}_z^{-1})_{13} \\ -(\mathcal{D}_z^{-1})_{23} \\ -(\mathcal{D}_z^{-1})_{33} \\ p_x [1 - (\mathcal{D}_x^T \mathcal{D}_z^{-1})_{13}] - p_y (\mathcal{D}_y^T \mathcal{D}_z^{-1})_{13} \\ -p_x (\mathcal{D}_x^T \mathcal{D}_z^{-1})_{23} + p_y [1 - (\mathcal{D}_y^T \mathcal{D}_z^{-1})_{23}] \\ -p_x (\mathcal{D}_x^T \mathcal{D}_z^{-1})_{33} - p_y (\mathcal{D}_y^T \mathcal{D}_z^{-1})_{33} \end{pmatrix}. \quad (31)$$

($)_{13}$ denotes the 13 element of the 3×3 matrix.

For example in orthorhombic medium (9 elastic constants), source vector will be

$$S = \begin{pmatrix} 0 \\ 0 \\ -\frac{1}{C_{33}} \\ p_x \left(1 - \frac{C_{13}}{C_{33}}\right) \\ p_y \left(1 - \frac{C_{23}}{C_{33}}\right) \\ 0 \end{pmatrix}. \quad (32)$$

V. Response at the Receivers

Computation of a seismic wavefield in anisotropic media involves a very large number of computations. Without a supercomputer it is almost impossible to compute synthetic wavefields. An algorithm of generating complete seismograms for fast computation on a super computer (CRAY) is used. In this method, Kennett's derivation of response (Chapter 7, Kennett, 1983) at the receiver is modified to express a better structured algorithm for multiple receivers (e.g. for VSP types of

geometry). This formulation allows us to compute all the matrices in a single pass through the layer loop and helps to increase the speed of computation in vector and parallel computers. New relations at the receiver are as follows:

for receiver depth $z_R < z_s$,

$$u(z_R) = \left(M_{UR} + M_{DR} R_U^{fR} \right) \left(T_U^{fR} \right)^{-1} T_U^{fs} \left(I - R_D^{sL} R_U^{fs} \right)^{-1} \left[R_D^{sL} \Sigma_D(z_s) + \Sigma_U(z_s) \right], \quad (33)$$

and for $z_R > z_s$,

$$u(z_R) = \left(M_{DR} + M_{UR} R_D^{RL} \right) \left(I - R_U^{Rs} R_D^{RL} \right)^{-1} T_D^{Rs} \left(I - R_U^{fs} R_D^{sL} \right)^{-1} \left[R_U^{fs} \Sigma_U(z_s) + \Sigma_D(z_s) \right], \quad (34)$$

where R_D^{RL} is expressed in the algorithm

$$R_D^{RL} = \left[T_D^{sR} \left(R_D^{sL} - R_D^{sR} \right)^{-1} T_U^{sR} + R_U^{sR} \right]^{-1}.$$

These notations are explained in Kennett (1983). These modified relations (33–34) are also used by Mallick and Frazer (1988).

VI. Numerical Integration and Time domain Response

Finally, we get a time domain response due to a point source at the receiver by the relation

$$u(x, y, z_R; t) = \frac{1}{(2\pi)^3} \int_{-\infty}^{+\infty} \int_{-\infty}^{+\infty} \int_{-\infty}^{+\infty} u(k_x, k_y, z_R, \omega) e^{i(k_x x + k_y y - \omega t)} dk_x dk_y d\omega, \quad (35)$$

where $u(k_x, k_y, z_R, \omega)$, the displacement (Green's function) of the entire medium at the receiver, is computed for each k_x, k_y , and ω (from relation 33–34) and for the algorithm in Figure 2. Denoting by ω_R and ω_I , the real and imaginary parts of the frequency, the impulse response $u(x, y, z_R; t)$ can

then be written in terms of a wavenumber summation form (e.g. Bouchon and Aki, 1977)

$$u(x, y, z_R; t) = \frac{e^{-\omega_I t}}{2\pi} \int_{-\infty}^{+\infty} e^{i\omega_R t} d\omega_R \cdot \frac{4\pi}{L_x L_y} \left[\sum_{n=-N}^N \sum_{m=-M}^M u(k_{x_n}, k_{y_m}, z_R; \omega) e^{ik_{x_n} x} e^{ik_{y_m} y} \right], \quad (36)$$

where L_x and L_y are the secondary source intervals along the x - and y -directions and

$$k_{x_n} = \frac{2\pi}{L_x} n \quad \text{and} \quad k_{y_m} = \frac{2\pi}{L_y} m.$$

The N and M are wavenumber loops and their values will depend on the convergence of the integral kernel $u(k_x, k_y, z_R; \omega)$. The imaginary part of the frequency is used to avoid the influence of singularities of the integration kernel (Bouchon, 1981). We later remove the imaginary part of the frequency from the time-domain solution.

This numerical summation (36) is only applicable to the ranges (R) where the product of the kernel and the exponential function is well represented by a linear function. To ensure these criteria, the wavenumber sampling has to satisfy the following inequalities (e.g. Bouchon and Aki, 1977; Mallick and Frazer, 1987),

$$\Delta k R < \frac{\pi}{4}, \quad R < \frac{L}{2} \quad \text{and} \quad \sqrt{(L-R)^2 + z^2} > V_{max} t.$$

V_{max} is the fastest velocity of the media. For larger distance, the wavenumber step size will be smaller and hence computation time will increase. However, to overcome this problem, we can solve wavenumber integration by using Filon's quadrature formula (e.g. Filon, 1928; Frazer and Gettrust, 1984). In this method, we can use a large step size which reduces the computational time. Some important features of Filon's quadrature formula had been discussed in previous articles (e.g. Frazer and Gettrust, 1984; Mallick and Frazer, 1988).

Since we use the discrete wavenumber summation to substitute a wavenumber integration, we need to compute the eigensolutions and reflection and transmission matrices of each medium for a large number of wavenumbers for each frequency. We use wavenumber (k) as an inner loop with the main intent to vectorize. At first, we compute the maximum value of wavenumber which is sufficient to explain all types of waveform within a given time window for each frequency. We determine the total number of wavenumber steps (N_{kmax}) for the proper wavenumber step size. These N_{kmax} -loops are again subdivided into sets of small k -loops which can be a variable according to the machine memory requirement. This code can be executed on any size computer. However, each small k -loop vectorizes well on a super computer such as a CRAY. A schematic flow chart of this algorithm in Figure 2 describes the flow of this algorithm.

In summary, the depth-dependent Green's function is computed for each frequency and wavenumber using reflectivity technique, and the transformation from wavenumber domain to space domain is performed by numerical integration which requires both truncation and discretization of the wavenumber interval. Finally, the complete response in a time domain has been achieved by inverse Fourier transformation of the product of frequency domain Green's function with required source-time function.

We used a simple crustal model for testing this algorithm with the isotropic model. The velocities of the top layer $Vp = 6.15$ km/sec and $Vs = 3.55$ km/sec and density $\rho = 2.8$ gm/cc. The velocities of the half-space $Vp = 8.09$ km/sec and $Vs = 4.67$ km/sec and density $\rho = 3.3$ gm/cc. After the responses are computed by wavenumber and frequency integration with 0-2 Hz band, the synthetic seismograms are generated by convolving it with a Ricker wavelet-type pulse centered at

1 Hz. The comparisons of synthetic seismograms at a distance of 75 km for an explosion source depth of 10 km are shown in Fig. 3. The synthetic seismograms on the left are representing the vertical (top) and radial (bottom) components for the isotropic computation with cylindrical coordinates (Mandal and Mitchell, 1986). The waveforms in the right represent the results for the same medium using anisotropic algorithm of this article. This comparison shows that the present algorithm of general anisotropic medium provides results which are consistent with other methods for a model with isotropic elastic parameters.

SYNTHETIC SEISMOGRAMS FROM AN EXPLOSION SOURCE IN ANISOTROPIC MEDIUM

To understand the effects of anisotropy on seismic waves from an explosion source, we use two relatively simple test models: an anisotropic half-space and an anisotropic layer over an isotropic half-space. For an anisotropic half-space, we investigate the effects of two different anisotropic degrees of the anisotropy.

I. Half-Space

The anisotropic half-space is our simplest test model. The anisotropy is assumed to be due to a parallel set of thin vertical fractures filled by a fluid. The aspect ratio of the fractures is 0.001. The degree of anisotropy of the models is determined by the fracture densities. The two models we use have fracture densities of 5% and 20%. The elastic constants are computed using the theoretical formulation of Hudson (1981) and Crampin (1984). Properties of the anisotropic medium with parallel vertical fractures are described by a set of five elastic constants with a horizontal symmetry

axis. Models for estimating the effects of cracks have been developed (Hudson, 1981; Schoenberg and Douma, 1988; Douma, 1988). We use Hudson's (1981) formulation for small aspect ratio fractures. We also assume fractures are fluid-filled. Anisotropic velocities are affected by fluid properties such as air, water, etc. (Hudson, 1981; Shearer and Chapman, 1989).

The five elastic constants in terms of velocities ($v_{ij} = \sqrt{\frac{c_{ij}}{\rho}} \text{ km/sec}$) are:

1. 5% fracture density:

$$v_{11} = 6.12 \quad v_{22} = v_{33} = 6.15 \quad v_{12} = v_{13} = 3.53$$

$$v_{44} = 3.55 \quad v_{55} = v_{66} = 3.35$$

2. 20% fracture density:

$$v_{11} = 5.94 \quad v_{22} = v_{33} = 6.13 \quad v_{12} = v_{13} = 3.43$$

$$v_{44} = 3.55 \quad v_{55} = v_{66} = 2.85$$

The density (ρ) is 2.8 gm/cc in both cases.

An explosion source is placed at a depth of 1 km below the surface. Let us assume the fracture planes are parallel to an east-west direction as shown in Fig. 4, and the Y axis (North) is normal to the fracture plane. We calculate seismograms for five different azimuths ($N0^\circ$, $N22.5^\circ E$, $N45^\circ E$, $N67.5^\circ E$ and $N90^\circ E$) with stations at distances 5 and 50 km from the epicenter. After the responses are calculated by wavenumber and frequency integration in 0-10 Hz frequency band, the synthetic seismograms are generated by convolving these with a Ricker wavelet-type pulse centered at 1 Hz, 2 Hz, 3 Hz, and 4 Hz. The seismograms are shown in Figures 5-6 for 5% and Figures 7-8 for 20% fracture densities, respectively, for the five azimuths (ϕ) in the 0° to 90° range. Prominent transverse component motion is observed at azimuths of 22.45 and 67° . At 5 km offsets, the arrival

times between longitudinal and transverse waves are small. In the high frequency seismograms (4 Hz), wave types can be differentiated by comparing transverse components with vertical or radial components. In this and subsequent figures, the seismograms in the direction of the symmetry axis ($\phi = 90^\circ$) correspond exactly to that of an isotropic medium with appropriate velocities. As the degree of anisotropy increases, the intensity of the transverse component also increases. In an anisotropic medium, the three wave types are: qP (quasi-longitudinal), qSP (transverse wave polarized within the symmetry plane), and qSR (transverse wave polarized perpendicular to the symmetry plane).

The seismograms at a distance of 50 km from the source (Figure 6) show that qP waves show a variation of travel times (velocities) and amplitudes as a function of azimuth on both vertical and radial components. There is a small transverse component of P wave at $\phi = 22.5^\circ$, 45° , and 67.5° azimuths for 20% fracture density (Figure 8). The large pulse in the vertical component is a combination of shear (qSP) and Rayleigh waves. The velocity variation with azimuth is clearly observable as is the amplitude variation. The transverse component seismograms clearly show the large transverse shear wave (qSR) at $\phi = 67.5^\circ$ for 20% fracture density. Also, the shear-wave-splitting diagnostic of an anisotropic medium is observable.

The frequency dependence of compressional, shear, and Rayleigh wave amplitudes may be explained by the depth of the source and the free surface effects. In seismograms at 90° azimuth (i.e., the isotropic case), we see that the Rayleigh wave amplitudes decrease exponentially with frequency. At other azimuths (22.5° , 45° , 67.5°), the qSR and Rayleigh wave amplitudes change rapidly. These changes are less for 5% fractured medium (Figure 6). In anisotropic media, reflection

of waves from an interface is more complex than for the case of isotropic media. For example, there is a cusp on the shear wave velocity surface (qSP) for fluid-filled fractures (Crampin, 1984; Shearer and Chapman, 1989). Other complexities of reflection and transmission properties in an anisotropic medium have been described elsewhere (e.g., Rokhlin *et al.*, 1986; Mandal, B., 1989).

The generation of transverse components by an explosion in an anisotropic half-space is due to azimuthal variation of elastic constants which results in non-spherical displacements at the source. Although we construct the explosion source using three equal orthogonal moment tensors, the final source vector is a product of the moment tensor matrix and the system matrix whose components contain medium elastic constants (c_{ijkl}), density, and phase slownesses.

II. Layer Over Half-Space

This model consists of a 2 km thick anisotropic layer over an isotropic half-space. The source is an explosion at 1 km depth in the anisotropic layer, as shown in Figure 9. The anisotropic layer contains aligned, vertical, fluid-filled fractures with an aspect ratio of 0.001 and fracture density 20%, the same as in the previous model. The five elastic constants in terms of velocities ($v_{ij} = \sqrt{\frac{c_{ij}}{\rho}}$) are: $v_{11} = 5.35$, $v_{22} = v_{33} = 5.47$, $v_{12} = v_{13} = 3.4$, $v_{44} = 3.00$, $v_{55} = v_{66} = 2.42$. The density (ρ) is 2.7 gm/cc. The isotropic half-space has the P- and S-wave velocities of: $V_p = 6.2$ and $V_s = 3.5$ km/sec. The density is 2.8 gm/cc.

Synthetic seismograms are calculated for the same source and receivers arrangements, as in the previous half-space example. Figures 10 and 11 show the synthetic seismograms at distances 5 km and 50 km, respectively. The transverse motion due to anisotropy is very prominent. The seismograms are more complex due to the presence of multiple reflections and normal modes.

The phenomena for anisotropic media have some very different features. The behavior of polarizations of the three fundamental waves (qP , qSP and qSR) in vertical fluid-filled fracture medium has been studied by Shearer and Chapman (1989). These computations of complete wave synthesis show us many features of anisotropic wave propagation.

CONCLUSIONS

The reflection matrix and the numerical wavenumber integration are used to compute complete wavefields in stratified anisotropic media due to a point source. The point source may be an explosion, point force, or double couple source. The source and receivers can be placed at any arbitrary place in the medium.

An explosion in an anisotropic medium has a non-uniform radiation pattern and generates significant transverse motion at certain azimuths because: (1) A spherical explosion in an anisotropic medium becomes non-spherical due to the directional dependence of elastic compliance. (2) The reflection (especially at free surface) and conversion of seismic waves propagating in an anisotropic medium further complicates the seismograms and their frequency dependence. These examples show that anisotropy may be a significant factor in contributing to the generation of transverse waves by explosions. From these synthetic computations, it is clear that anisotropy takes a major roll in wave propagation.

The complete wavefield in anisotropic media is now possible with the help of a super computer and an efficient computational algorithm. We hope that the high speed super computer and efficient code will give us the opportunity to study wave propagation in general anisotropic media.

Acknowledgments

This work is partially supported by the Reservoir Delineation - Vertical Seismic Profiling Consortium at M.I.T. Partial support was provided by the Defence Advanced Research Projects Agency through contract F19628-87-K-0054 administered by the Air Force Geophysical Laboratory. Some of the computations have been done on the CRAY at the Pittsburgh Supercomputing Center under NSF Grant EAR-8804355.

References

Alterman, Z., Jarosch, H., Pekeris, C. L., 1959. Oscillations of the earth. *Proc. Roy. Soc. Ser. A* 252, 80-95.

Archambeau, C.G. and C. Sammis, 1970. Seismic radiation from explosions in prestressed media and the measurement of tectonic stress in the Earth, *Rev. Geophys.*, 6, 241-288.

Auld, B.A., 1973. *Acoustic Fields and Wave in Solids*, Vol. 1, Wiley, New York.

Babuska, V., 1981. Anisotropy of v_p and v_s in rock-forming minerals, *J. Geophys.*, 50, 1-6.

Ben-Menahem, A. and M.N. Toksöz, 1989. Radiation patterns from explosions in anisotropic media, submitted to *Science*.

Booth, D.C. and Crampin, S., 1983. The anisotropic reflectivity technique: theory, *Geophys. J. R. astr. Soc.*, 72, 755-766.

Bouchon, M., 1981. A simple method to calculate Green's functions for elastic layered media, *Bull. Seism. Soc. Am.*, 73, 959-971.

Bouchon, M. and K. Aki, 1977. Discrete wavenumber representation of seismic source wave fields,

Bull. Seism. Soc. Am., 67, 259-277.

Burridge, R. and Knopoff, L., 1964. Body force equivalents for seismic dislocations, *Bull. seism. Soc. Am.*, 54, 1875-1888.

Chadwick, P. and Smith, G. D., 1977. Foundations in the theory of surface waves in anisotropic elastic materials, in *Advances in Applied Mechanics*, 17, ed. Yih, C. S., Academic Press, New York.

Crampin, S., 1984. Effective elastic constants for wave propagation through cracked solids, *Geophys. J. R. astr. Soc.*, 78, 691-710.

Crampin, S., 1981. A review of wave motion in anisotropic and cracked elastic-media, *Wave Motion*, 3, 343-391.

Crampin, S., E.M. Chesnokov and R.G. Hipkin, 1984. Seismic anisotropy—the state of the art: II, *Geophys. J. R. astr. Soc.*, 76, 1-16.

Douma, J., 1988. The effect of the aspect ratio on crack-induced anisotropy, *Geophy. Prospecting*, 36, 614-632.

Fedorov, F.I., 1968. *Theory of Elastic Waves in Crystals*, Plenum Press, New York.

Filon, L.N.G., 1928. On a quadrature method for trigonometric integrals, *Proc. Roy. Soc. Edinburgh*, 49, 38-47.

Frazer, L.N. and J.F. Gettrust, 1984. On a generalization of Filon's method and the computation of oscillatory integrals of seismology, *Geophys. J. R. astr. Soc.*, 76, 461-481.

Fryer, G.J. and L.N. Frazer, 1984. Seismic waves in stratified anisotropic media, *Geophys. J. R. astr. Soc.*, 78, 691-710.

Fryer, G.J. and L.N. Frazer, 1987. Seismic waves in stratified anisotropic media - II: Elastodynamic eigensolutions for some anisotropic systems, *Geophys. J. R. astr. Soc.*, 81, 73-101.

Gaiser, J.E., R.W. Ward, and J.P. DiSiena, 1984. Three-component vertical seismic profiles: Velocity anisotropy estimates from P wave particle motion, *Handbook of Geophysical Exploration*, section I, Vol. 14B, 189-204.

Garmann, J., 1983. Some properties of elastodynamic eigensolutions in stratified media, *Geophys. J. R. astr. Soc.*, 75, 565-569.

Gilbert, F. and G.E. Backaus, 1966. Propagator matrices in elastic wave and vibration problems, *Geophysics*, 31, 326-332.

Golub, G. H. and Van Loan, C. F., 1983. *Matrix Computations*, The Johns Hopkins University Press, Baltimore.

Gupta, I.N. and R.R. Biandford, 1983. A mechanism for generation of short-period transverse motion from explosions, *Bull. Seism. Soc. Am.*, 73, 571-591.

Johnson, L.R., 1988. Source characteristics of two underground nuclear explosions, *Geophys. J.*, 95 15-30.

Henneke, E.G., 1972. Reflection-refraction of stress wave at a plane boundary between anisotropic media, *J. Acoust. Soc. Am.*, 51, 210-217.

Hudson, J. A., 1981. Wave speeds and attenuation of elastic waves in material containing cracks, *Geophys. J. Roy. astr. Soc.*, 64, 133-150.

Kausel, E., 1986. Wave propagation in Anisotropic layered media, *Inter. J. Num. Methods in Eng.*, 23, 1567-1578.

Kennett, B. L. N., 1974. Reflections, rays, and reverberations, *Bull. seism. Soc. Am.*, **64**, 1685-1696.

Kennett, B.L.N., 1983. *Seismic Wave Propagation in Stratified Media*, Cambridge University Press.

Kennett, B. L. N. and Kerry, N. J., 1979. Seismic waves in a stratified half space, *Geophys. J. R. astr, Soc.*, **57**, 557-583.

Kisslinger, C., E.J. Mateker, Jr., and T.V. McEvilly, 1961. SH motion from explosions in soil, *J. of Geophys. Res.*, **66**, 3487-3496.

Lynnes, C.S. and T. Lay, 1988. Analysis of amplitude and travel-time anomalies for short-period P-waves from NTS explosions, *Geophys. J.*, **92**, 431-443.

Mallick, S. and L.N. Frazer, 1987. Practical aspects of reflectivity modeling, *Geophysics*, **52**, 1355-1364.

Mallick, S. and L.N. Frazer, 1988. Rapid computation of multioffset vertical seismic profile synthetic seismograms for layered media, *Geophysics*, **53**, 479-491.

Malvern, L.F., 1969. *Introduction to the Mechanics of a Continuous Media*, Prentice-Hall, Englewood Cliffs.

Mandal, B., 1989. Reflection and transmission properties of elastic waves on a plane interface for general anisotropic media, annual report, *Reservoir Delineation Consortium, ERL, MIT*, 2-1,2-48.

Mandal, B., 1988. Computation of the complete wavefield in anisotropic media, annual report, *Reservoir Delineation- Vertical Seismic Profiling Consortium, ERL, MIT*, 2-1.2-31.

Mandal, B. and B.J. Mitchell, 1986. Complete seismogram synthesis for transversely isotropic media, *J. Geophys.*, **59**, 149-156.

Massé, B.P., 1981. Review of seismic source models for underground nuclear explosions, *Bull. Seism. Soc. Am.*, **71**, 1249–1268.

Musgrave, M.J.P., 1970. *Crystal Acoustics*, Holden-Day, San Francisco.

Pao, Y., 1983. Elastic waves in solids, *Journal of Applied Mechanics*, **50**, 1152–1164.

Press, W.H., B.P. Flannery, S.A. Teukolsky, and W.T. Vetterling, 1986. *Numerical Recipes*, Cambridge University Press.

Robertson, J.D. and D. Corrigan, 1983. Radiation patterns of a shear-wave vibrator in near-surface shale, *Geophysics*, **48**, 19–26.

Rokhlin, S. I., Bolland, T. K., and Adler, L., 1986. Reflection and refraction of elastic waves on a plane interface between two generally anisotropic media, *J. Acoust. Soc. Am.*, **79**, 906–918.

Saastamoinen, P.R., 1980. On propagators and scatterers in wave problems of layered elastic media: a spectral approach, *Bull. Seism. Soc. Am.*, **70**, 1125–1135.

Schoenberg, M. and Douma, J., 1988. Elastic wave propagation in media with parallel fractures and aligned cracks, *Geophys. Prospecting*, **36**, 571–590.

Shearer, P. M. and Chapman, C. H., 1989. Ray tracing in azimuthally anisotropic media-I. Results for models of aligned cracks in the upper crust, *Geophys. J.*, **96**, 51–64.

Smith, B. T., 1976. *Matrix Eigensystem Routines -EISPACK Guide*, 2nd ed., Vol 6 of Lecture Notes in Computer Science (New York: Springer-Velag).

Stephen, R. A., 1981. Seismic anisotropy observed in upper oceanic crust, *Geophys. Res. Lett.*, **8**, 865–868.

Takeuchi, H., and Saito, M., 1972. Seismic surface waves, *Methods in computational Physics*, Academic.

demic Press, New York, 11, 217-295.

Thomsen, L., 1986. Weak elastic anisotropy, *Geophysics*, 51, 1954-1966.

Toksöz, M.N. and H.H. Khrer, 1972. Tectonic strain release by underground nuclear explosions and its effect on seismic discrimination, *Geophys. J. R. astr. Soc.*, 31, 141-161.

Wallace, T.C., D.V. Helmberger, and G.R. Engen, 1983. Evidence of tectonic release from underground nuclear explosions in long-period *P* waves, *Bull. Seism. Soc. Am.*, 73, 593-613.

Wilkinson, J. H. and Reinsch, C., 1971. *Linear Algebra, vol II of Handbook of Automatic Computation*, Springer-Verlag, New York.

Winterstein, D. F., 1986. Anisotropy effects in P-wave and SH-wave stacking velocities contain information on lithology, *Geophysics*, 51, 661-672.

Woodhouse, J. H., 1974. Surface waves in a laterally varying layered structure, *Geophys. J. R. astr. Soc.*, 37, 461-490.

APPENDIX A.

Wave equation with out body force (1)

$$\rho \partial_t^2 u_i = \tau_{ij,j} = L^T \tau_{ij} = L^T C_{ijkl} e_{kl} = L^T C_{ijkl} L u_k \quad (\text{A-1})$$

where

$$\tau_{ij} = (\tau_{xx}, \tau_{yy}, \tau_{zz}, \tau_{yz}, \tau_{zx}, \tau_{xy})^T \quad (\text{A-2})$$

$$e_{ij} = (e_{xx}, e_{yy}, e_{zz}, 2e_{yz}, 2e_{zx}, 2e_{xy})^T \quad (\text{A-3})$$

$$u_k = (u_x, u_y, u_z)^T \quad (\text{A-4})$$

$$L = L_x \frac{\partial}{\partial x} + L_y \frac{\partial}{\partial y} + L_z \frac{\partial}{\partial z}. \quad (\text{A-5})$$

The matrices L_x, L_y, L_z are

$$\begin{aligned} L_x^T &= \begin{pmatrix} 1 & 0 & 0 & 0 & 0 & 0 \\ 0 & 0 & 0 & 0 & 0 & 1 \\ 0 & 0 & 0 & 0 & 1 & 0 \end{pmatrix}, \\ L_y^T &= \begin{pmatrix} 0 & 0 & 0 & 0 & 0 & 1 \\ 0 & 1 & 0 & 0 & 0 & 0 \\ 0 & 0 & 0 & 1 & 0 & 0 \end{pmatrix}, \\ L_z^T &= \begin{pmatrix} 0 & 0 & 0 & 0 & 1 & 0 \\ 0 & 0 & 0 & 1 & 0 & 0 \\ 0 & 0 & 1 & 0 & 0 & 0 \end{pmatrix}. \end{aligned} \quad (\text{A-6})$$

Wave equation (e.g. Kausel, 1986),

$$\rho \partial_t^2 u = \left(L_x^T \frac{\partial}{\partial x} + L_y^T \frac{\partial}{\partial y} + L_z^T \frac{\partial}{\partial z} \right) \mathcal{C} \left(L_x \frac{\partial}{\partial x} + L_y \frac{\partial}{\partial y} + L_z \frac{\partial}{\partial z} \right) u \quad (\text{A-7})$$

$$= \left(C_{xx} \frac{\partial^2}{\partial x^2} + C_{yy} \frac{\partial^2}{\partial y^2} + C_{zz} \frac{\partial^2}{\partial z^2} + 2C_{xy} \frac{\partial^2}{\partial x \partial y} + 2C_{yz} \frac{\partial^2}{\partial y \partial z} + 2C_{zx} \frac{\partial^2}{\partial z \partial x} \right) u \quad (\text{A-8})$$

where

$$C_{ij} = \frac{1}{2} \left(L_i^T \mathcal{C} L_j + L_j^T \mathcal{C} L_i \right) \quad i, j = x, y, z \quad (\text{A-9})$$

The 6 (C_{ij}) matrices are

$$\begin{aligned} C_{xx} &= \begin{pmatrix} C_{11} & C_{16} & C_{15} \\ & C_{66} & C_{56} \\ \boxed{\text{SYM}} & & C_{55} \end{pmatrix}, \quad C_{yy} = \begin{pmatrix} C_{66} & C_{26} & C_{46} \\ & C_{22} & C_{24} \\ \boxed{\text{SYM}} & & C_{44} \end{pmatrix}, \\ C_{zz} &= \begin{pmatrix} C_{55} & C_{45} & C_{35} \\ & C_{44} & C_{34} \\ \boxed{\text{SYM}} & & C_{33} \end{pmatrix}, \quad 2C_{xy} = \begin{pmatrix} 2C_{16} & C_{12} + C_{66} & C_{14} + C_{56} \\ & 2C_{26} & C_{25} + C_{46} \\ \boxed{\text{SYM}} & & 2C_{45} \end{pmatrix}, \quad (\text{A-10}) \\ 2C_{yz} &= \begin{pmatrix} 2C_{56} & C_{25} + C_{46} & C_{36} + C_{45} \\ & 2C_{24} & C_{23} + C_{44} \\ \boxed{\text{SYM}} & & 2C_{34} \end{pmatrix}, \quad 2C_{zx} = \begin{pmatrix} 2C_{15} & C_{14} + C_{56} & C_{13} + C_{55} \\ & 2C_{46} & C_{45} + C_{36} \\ \boxed{\text{SYM}} & & 2C_{35} \end{pmatrix}. \end{aligned}$$

Stresses will take the new form as

$$\begin{aligned} \tau &= \mathcal{C} L u = \mathcal{C} \left(L_x \frac{\partial}{\partial x} + L_y \frac{\partial}{\partial y} + L_z \frac{\partial}{\partial z} \right) u \\ &= \left(C_x \frac{\partial}{\partial x} + C_y \frac{\partial}{\partial y} + C_z \frac{\partial}{\partial z} \right) u, \end{aligned} \quad (\text{A-11})$$

where

$$\mathcal{C}_x = \begin{pmatrix} C_{11} & C_{16} & C_{15} \\ C_{12} & C_{26} & C_{25} \\ C_{13} & C_{36} & C_{35} \\ C_{14} & C_{46} & C_{45} \\ C_{15} & C_{56} & C_{55} \\ C_{16} & C_{66} & C_{56} \end{pmatrix}, \quad \mathcal{C}_y = \begin{pmatrix} C_{16} & C_{12} & C_{14} \\ C_{26} & C_{22} & C_{24} \\ C_{36} & C_{23} & C_{34} \\ C_{46} & C_{24} & C_{44} \\ C_{56} & C_{25} & C_{45} \\ C_{66} & C_{26} & C_{46} \end{pmatrix},$$

$$\mathcal{C}_z = \begin{pmatrix} C_{15} & C_{14} & C_{13} \\ C_{25} & C_{24} & C_{23} \\ C_{35} & C_{34} & C_{33} \\ C_{45} & C_{44} & C_{34} \\ C_{55} & C_{45} & C_{35} \\ C_{56} & C_{46} & C_{36} \end{pmatrix}. \quad (\text{A-12})$$

Now stresses in equation 2 (main text) take the form

$$-i\omega\tau = \begin{pmatrix} \tau_{xz} \\ \tau_{yz} \\ \tau_{zz} \end{pmatrix} = \begin{pmatrix} C_{15} & C_{56} & C_{55} \\ C_{14} & C_{46} & C_{45} \\ C_{13} & C_{36} & C_{35} \end{pmatrix} \frac{\partial}{\partial x} \begin{pmatrix} u_x \\ u_y \\ u_z \end{pmatrix}$$

$$+ \begin{pmatrix} C_{56} & C_{25} & C_{45} \\ C_{46} & C_{24} & C_{44} \\ C_{36} & C_{23} & C_{34} \end{pmatrix} \frac{\partial}{\partial y} \begin{pmatrix} u_x \\ u_y \\ u_z \end{pmatrix} + \begin{pmatrix} C_{55} & C_{45} & C_{35} \\ C_{45} & C_{44} & C_{34} \\ C_{35} & C_{34} & C_{33} \end{pmatrix} \frac{\partial}{\partial z} \begin{pmatrix} u_x \\ u_y \\ u_z \end{pmatrix} \quad (\text{A-13})$$

In the simpler form

$$-i\omega\tau = \mathcal{D}_x u_x + \mathcal{D}_y u_y + \mathcal{D}_z u_z. \quad (\text{A-14})$$

Substitute the trial solutions, we will get

$$\begin{pmatrix} T_{xz} \\ T_{yz} \\ T_{zz} \end{pmatrix} = i\omega(p_x\mathcal{D}_x + p_y\mathcal{D}_y) \begin{pmatrix} U_x \\ U_y \\ U_z \end{pmatrix} + \mathcal{D}_z \frac{\partial}{\partial z} \begin{pmatrix} U_x \\ U_y \\ U_z \end{pmatrix} \quad (\text{A-15})$$

or,

$$\frac{\partial}{\partial z} \begin{pmatrix} U_x \\ U_y \\ U_z \end{pmatrix} = i\omega \mathcal{D}_z^{-1} \left[- (p_x\mathcal{D}_x + p_y\mathcal{D}_y) \begin{pmatrix} U_x \\ U_y \\ U_z \end{pmatrix} - \frac{1}{-i\omega} \begin{pmatrix} T_{xz} \\ T_{yz} \\ T_{zz} \end{pmatrix} \right] \quad (\text{A-16})$$

In a simplified form

$$\begin{aligned} U_{,z} &= i\omega(-\mathcal{D}_z^{-1}\mathcal{D}_{xy}U - \mathcal{D}_z^{-1}T), \text{ or} \\ &= i\omega(OU + PT), \end{aligned} \quad (\text{A-17})$$

where

$$\mathcal{D}_{xy} = p_x\mathcal{D}_x + p_y\mathcal{D}_y$$

and

$$P = -\mathcal{D}_z^{-1} \text{ and } O = P\mathcal{D}_{xy}$$

Now substitute the trial solution in the wave equation (A-8),

$$-\omega^2\rho U = -\omega^2(p_x^2\mathcal{C}_{xx} + p_y^2\mathcal{C}_{yy} + 2p_xp_y\mathcal{C}_{xy})U + \mathcal{C}_{zz}U_{,zz} + 2i\omega(p_x\mathcal{C}_{zx} + p_y\mathcal{C}_{yz})U_{,z} \quad (\text{A-18})$$

Substitute $U_{,z}$ and $U_{,zz}(=\frac{\partial^2 U}{\partial z^2})$ from eqn (A-17) in equation (A-18)

$$\begin{aligned} i\omega\mathcal{C}_{zz}PT_{,z} &= \omega^2(p_x^2\mathcal{C}_{xx} + p_y^2\mathcal{C}_{yy} + 2p_xp_y\mathcal{C}_{xy} - \rho I)U \\ &\quad + \omega^2\mathcal{C}_{zz}(O^2U + OPT) + 2\omega^2(p_x\mathcal{C}_{zx} + p_y\mathcal{C}_{yz})(OU + PT) \end{aligned} \quad (\text{A-19})$$

Note that $\mathcal{C}_{zz} = \mathcal{D}_z$, then $\mathcal{C}_{zz}P = -I$ and $\mathcal{C}_{zz}O = -\mathcal{D}_{xy}$. The I is 3×3 identity matrix. After some algebra we will get a relation between T_{xz} and (U, T) ,

$$T_{xz} = i\omega(QU + RT) \quad (\text{A-20})$$

where

$$\begin{aligned} Q &= p_x^2 \mathcal{C}_{xx} + p_y^2 \mathcal{C}_{yy} + 2p_x p_y \mathcal{C}_{xy} - \rho I \\ &\quad - (-\mathcal{D}_{xy} + 2p_x \mathcal{C}_{zx} + 2p_y \mathcal{C}_{yz}) \mathcal{D}_z^{-1} \mathcal{D}_{xy}, \end{aligned} \quad (\text{A-21})$$

$$R = -(-\mathcal{D}_{xy} + 2p_x \mathcal{C}_{zx} + 2p_y \mathcal{C}_{yz}) \mathcal{D}_z^{-1}. \quad (\text{A-22})$$

The simplification forms of O, Q and R may be written as

$$\begin{aligned} O &= p_x O_1 + p_y O_2 \\ Q &= p_x^2 Q_1 + p_y^2 Q_2 + p_x p_y Q_3 - \rho I \\ R &= - (p_x \mathcal{D}_x^T + p_y \mathcal{D}_y^T) \mathcal{D}_z^{-1} = O^T \end{aligned} \quad (\text{A-23})$$

where

$$\begin{aligned} O_1 &= -\mathcal{D}_z^{-1} \mathcal{D}_x \\ O_2 &= -\mathcal{D}_z^{-1} \mathcal{D}_y \\ Q_1 &= \mathcal{C}_{xx} - \mathcal{D}_x^T \mathcal{D}_z^{-1} \mathcal{D}_x \\ Q_2 &= \mathcal{C}_{yy} - \mathcal{D}_y^T \mathcal{D}_z^{-1} \mathcal{D}_y \\ Q_3 &= 2\mathcal{C}_{xy} - \mathcal{D}_x^T \mathcal{D}_z^{-1} \mathcal{D}_y - \mathcal{D}_y^T \mathcal{D}_z^{-1} \mathcal{D}_x \end{aligned} \quad (\text{A-24})$$

The final form of the differential system will be expressed as

$$\frac{\partial}{\partial z} \begin{pmatrix} U \\ T \end{pmatrix} = i\omega \begin{pmatrix} O & P \\ Q & O^T \end{pmatrix} \begin{pmatrix} U \\ T \end{pmatrix} = i\omega Ab, \quad (\text{A-25})$$

which is the equation (3). The matrix P and Q are symmetric.

Figure Captions

Figure 1: Anisotropic layered model.

Figure 2: Schematic flowchart of the algorithm.

Figure 3: Synthetic seismograms at a distance of 75 km, for a source at a depth of 10 km, using the results of Mandal and Mitchell (1986) (left traces) and present anisotropic algorithm (right traces). Both seismograms are computed for the same isotropic model.

Figure 4: Schematic diagram of an anisotropic half-space model. Dashed lines represent fractures.

Figure 5: Three-component synthetic seismograms at a 5 km epicentral distance, for five azimuths and at frequencies of 1, 2, 3, and 4 Hz. The anisotropic model has 5% fracture density. The seismograms at $\phi = 90^\circ$ are equivalent to those of an isotropic reference medium.

Figure 6: Three-component synthetic seismograms at a 50 km epicentral distance, for five azimuths and at frequencies of 1, 2, 3, and 4 Hz for 5% fractured model. The seismograms at $\phi = 90^\circ$ are equivalent to those of an isotropic reference medium.

Figure 7: Three-component synthetic seismograms at a 5 km epicentral distance, for five azimuths and at frequencies of 1, 2, 3, and 4 Hz. The anisotropic medium has 20% fracture density. The seismograms at $\phi = 90^\circ$ are equivalent to those of an isotropic reference medium.

Figure 8: Three-component synthetic seismograms at a 50 km epicentral distance, for five azimuths and at frequencies of 1, 2, 3, and 4 Hz for 20% fracture density. The seismograms at

$\phi = 90^\circ$ are equivalent to those of an isotropic reference medium.

Figure 9: Schematic diagram of an anisotropic layer over isotropic half-space.

Figure 10: Three-component synthetic seismograms for a layer over half-space at a 5 km epicentral distance, for five azimuths and at frequencies of 1, 2, 3, and 4 Hz. The seismograms at $\phi = 90^\circ$ are equivalent to those of an isotropic reference medium.

Figure 11: Three-component synthetic seismograms for a layer over half-space at a 50 km epicentral distance, for five azimuths and at frequencies of 1, 2, 3, and 4 Hz. The seismograms at $\phi = 90^\circ$ are equivalent to those of an isotropic reference medium.

Stratified anisotropic media

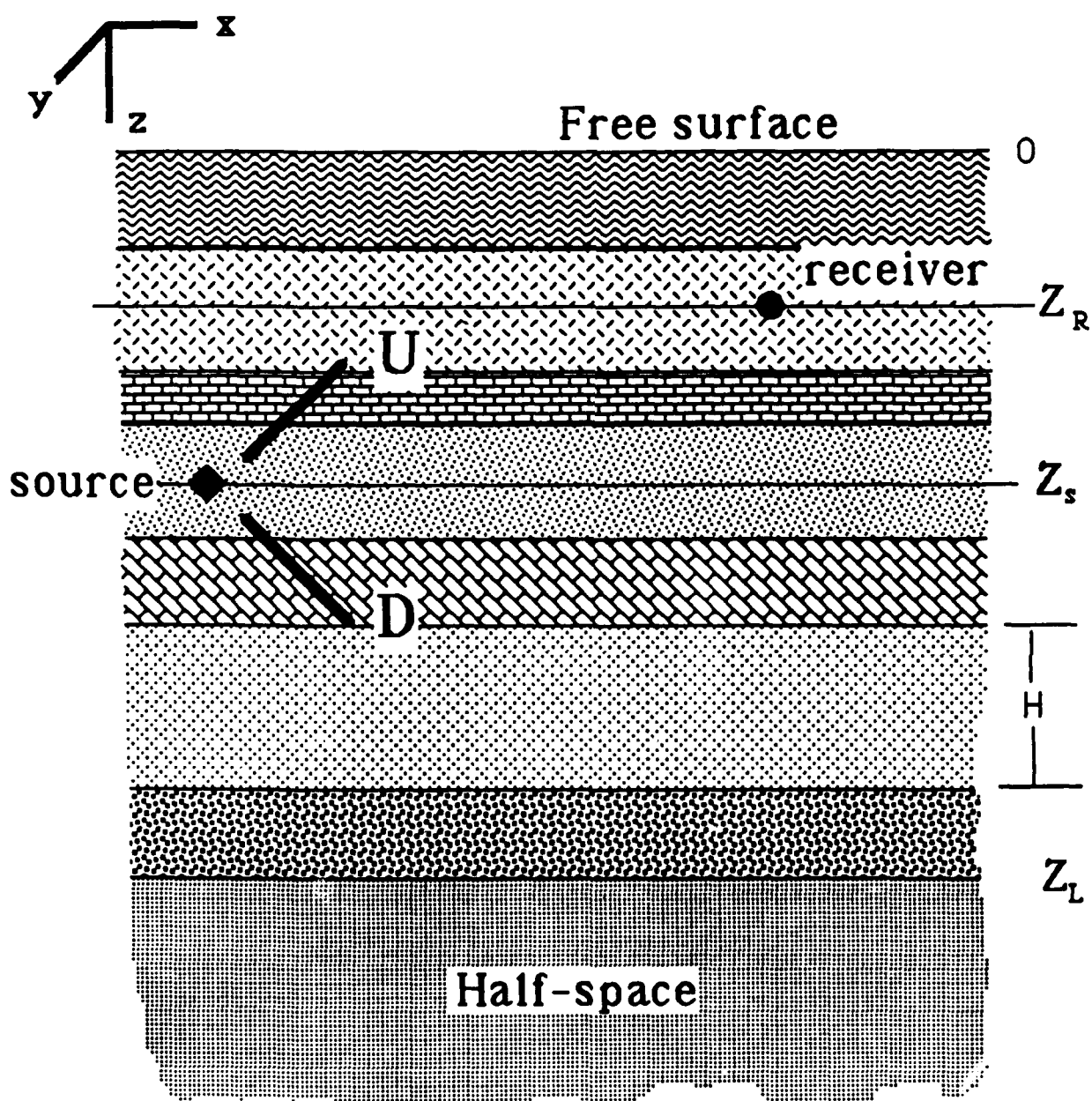


Figure 1: Anisotropic layered model.

FREQUENCY LOOPCompute K_{max} , K_{step} and N_k **K_{step} Loop****Layer Loop**

Compute Eigenvalues and Eigenvectors

Compute M_U , M_D , R_U , R_D , T_U , T_D **If Source Layer**Put: $R_U^{fs} = R_U$, $T_U^{fs} = T_U$ **If Receiver Layer** $M_{UR} = M_U$, $M_{DR} = M_D$ $Z_R < Z_s$ Put: $R_U^{fR} = R_U$, $T_U^{fR} = T_U$ **Source Layer = Receiver Layer**Put: $R_U = 0$, $R_D = 0$, $T_U = I$, $T_D = I$ $Z_R > Z_s$ Put: $R_U^{sR} = R_U$, $R_D^{sR} = R_D$, $T_U^{sR} = T_U$, $T_D^{sR} = T_D$ **Layer Loop End**Put: $R_D^{sL} = R_D$ **Receiver Loop** $Z_R < Z_s$ Compute $u(z_R)$ (33) $Z_R > Z_s$ Compute $u(z_R)$ (34)**Distance Loop**

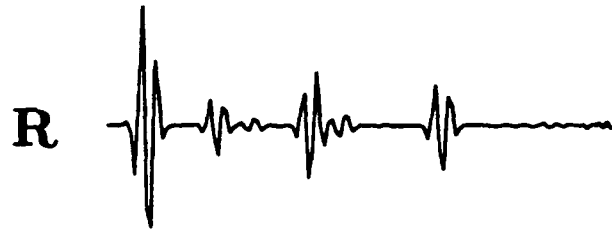
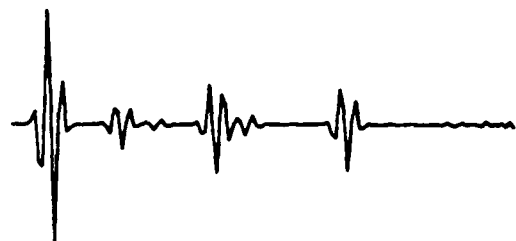
Wavenumber summation

Distance Loop End**Receiver Loop End**

Store Response

 K_{step} Loop End**FREQUENCY LOOP END**

Figure 2: Schematic flowchart of the algorithm.

Isotropic algorithm**Anisotropic algorithm**

11.3

43.05

11.3

43.05

Explosion source depth = 10 km
Receiver dist. = 75 km

Figure 3: Synthetic seismograms at a distance of 75 km, for a source at a depth of 10 km, using the results of Mandal and Mitchell (1986) (left traces) and present anisotropic algorithm (right traces). Both seismograms are computed for the isotropic model given in figure 3.

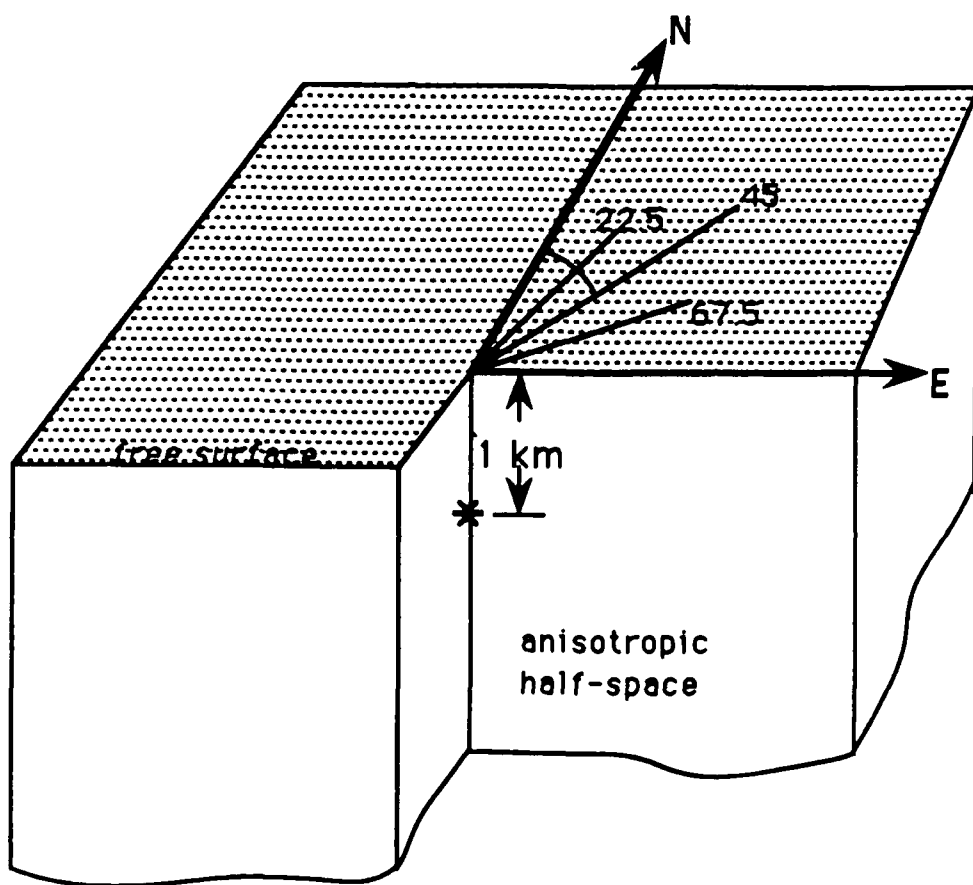
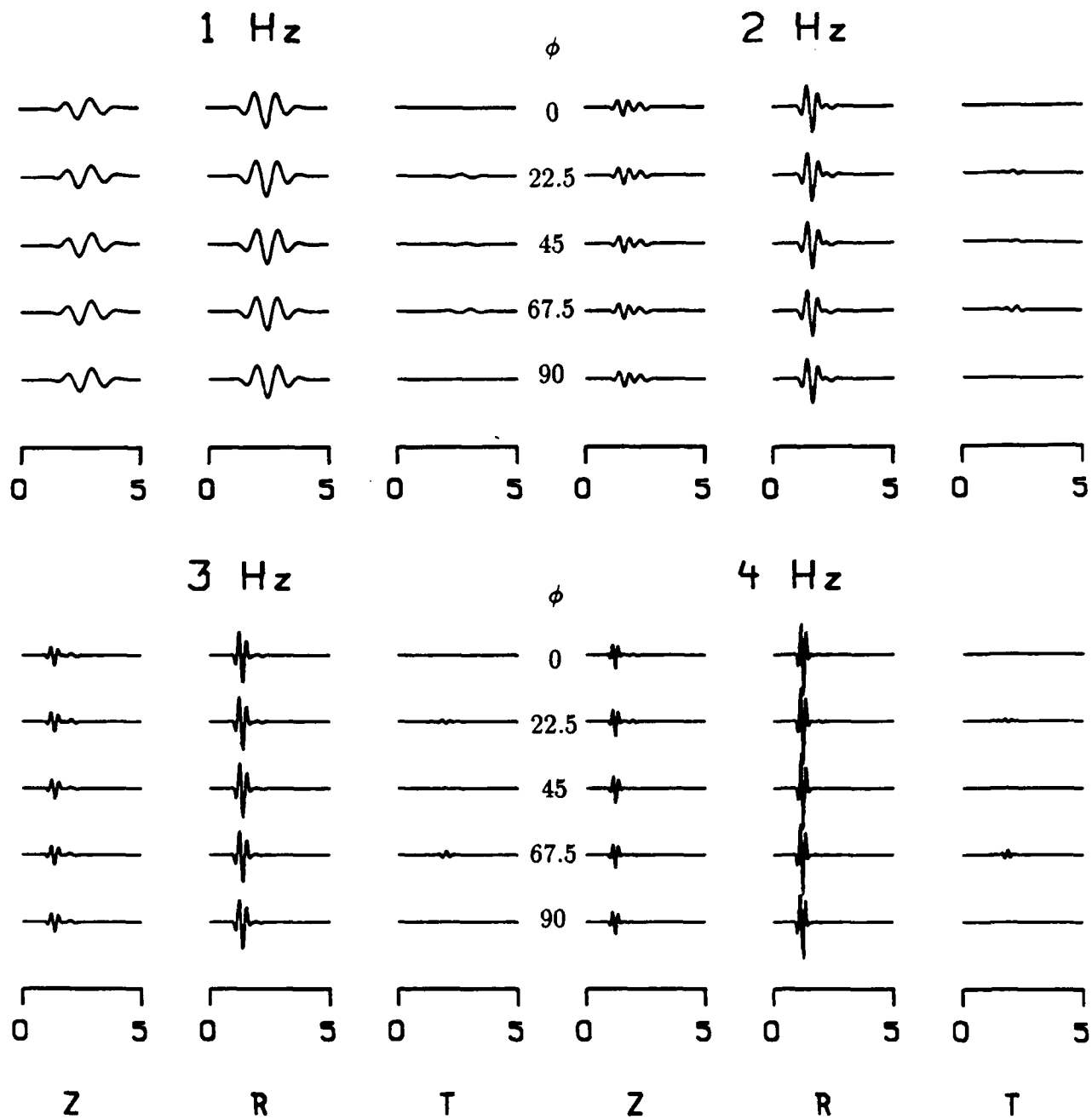
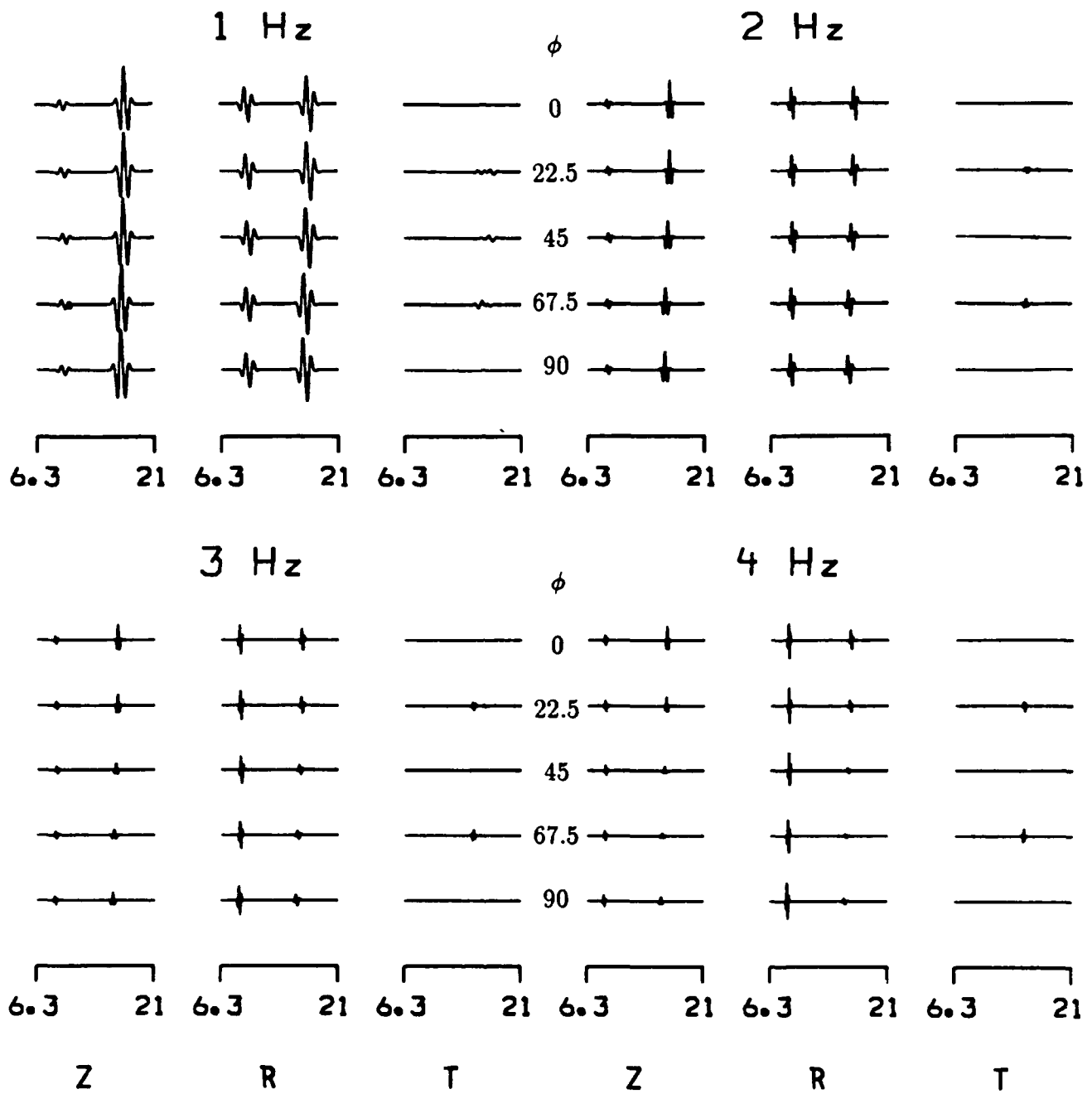


Figure 4: Schematic diagram of an anisotropic half-space model. Dashed lines represent fractures.



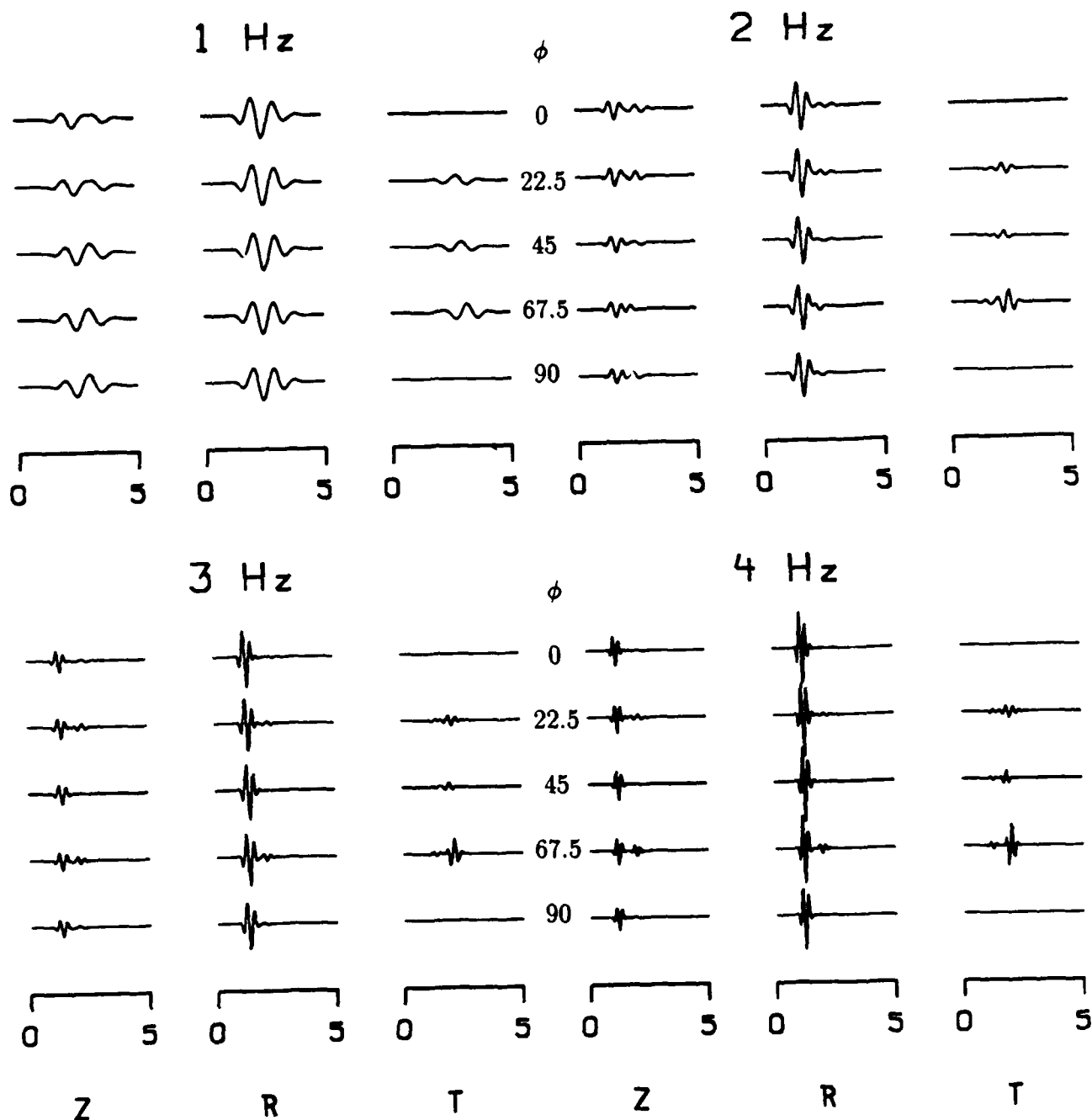
Dist = 5 Km, Half-space, 5% crack density

Figure 5: Three-component synthetic seismograms at a 5 km epicentral distance, for five azimuths and at frequencies of 1, 2, 3, and 4 Hz. The anisotropic model has 5% fracture density. The seismograms at $\phi = 90^\circ$ are equivalent to those of an isotropic reference medium.



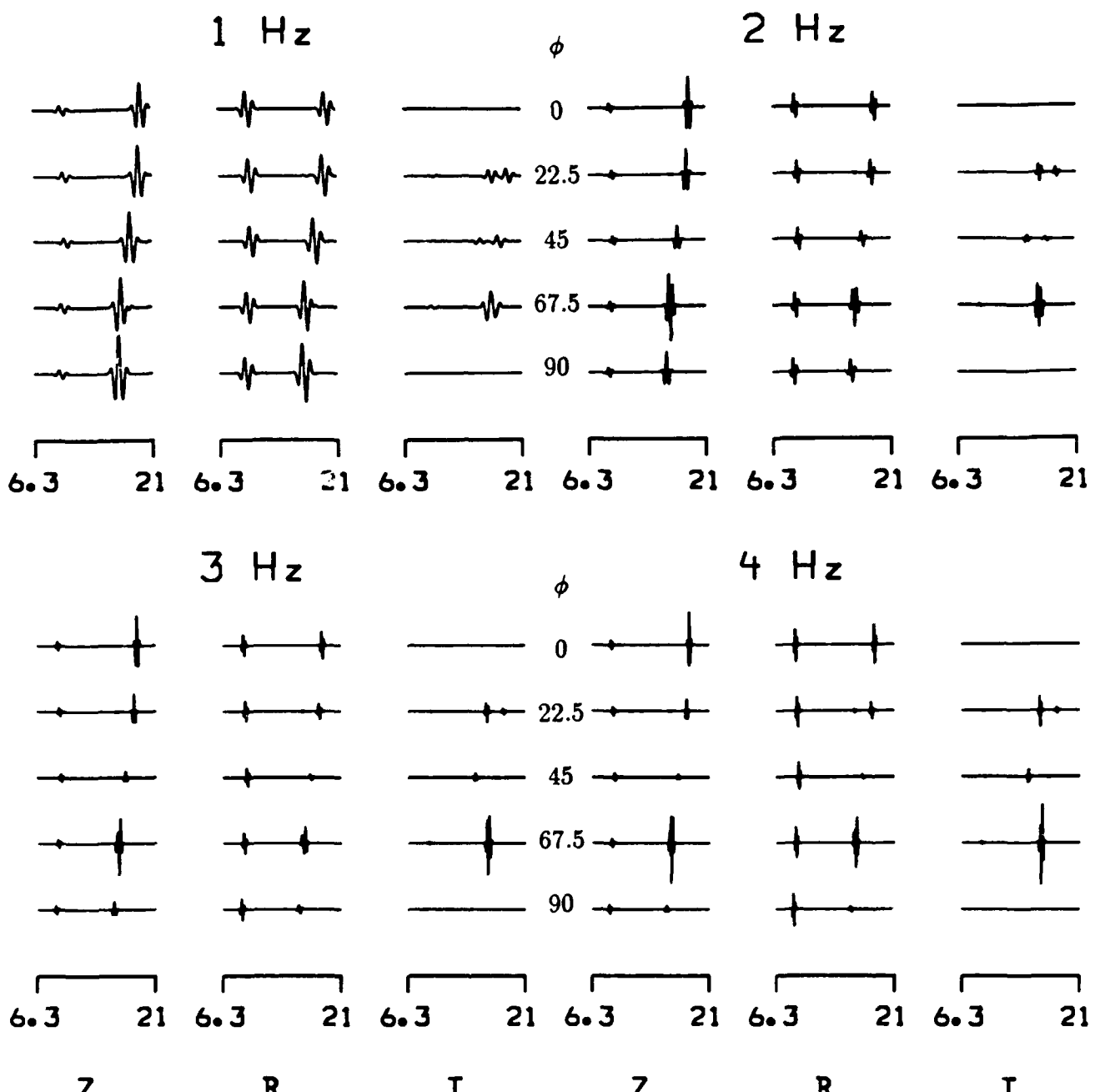
Dist = 50 Km, Half-space, 5% crack density

Figure 6: Three-component synthetic seismograms at a 50 km epicentral distance, for five azimuths and at frequencies of 1, 2, 3, and 4 Hz for 5% fractured model. The seismograms at $\phi = 90^\circ$ are equivalent to those of an isotropic reference medium.



Dist = 5 Km, Half-space, 20% crack density

Figure 7: Three-component synthetic seismograms at a 5 km epicentral distance, for five azimuths and at frequencies of 1, 2, 3, and 4 Hz. The anisotropic medium has 20% fracture density. The seismograms at $\phi = 90^\circ$ are equivalent to those of an isotropic reference medium.



Dist = 50 Km, Half-space, 20% crack density

Figure 8: Three-component synthetic seismograms at a 50 km epicentral distance, for five azimuths and at frequencies of 1, 2, 3, and 4 Hz for 20% fracture density. The seismograms at $\phi = 90^\circ$ are equivalent to those of an isotropic reference medium.

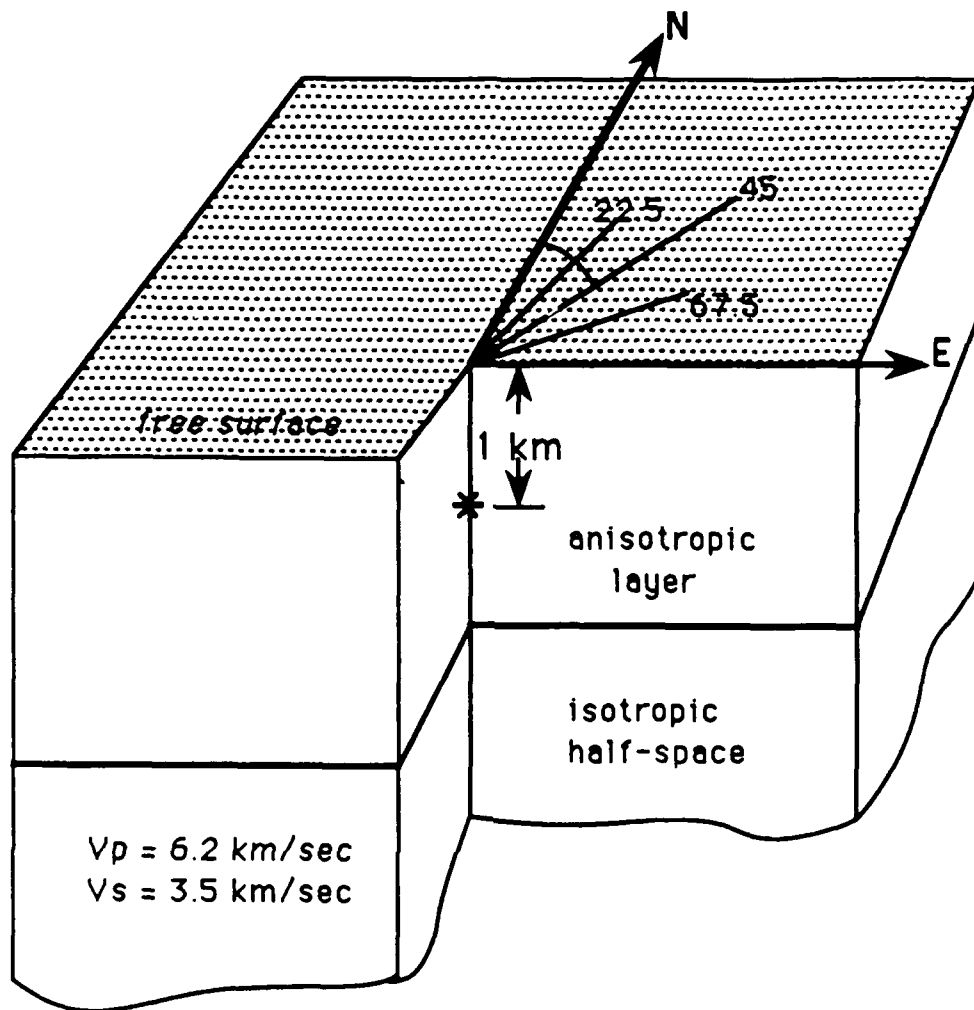
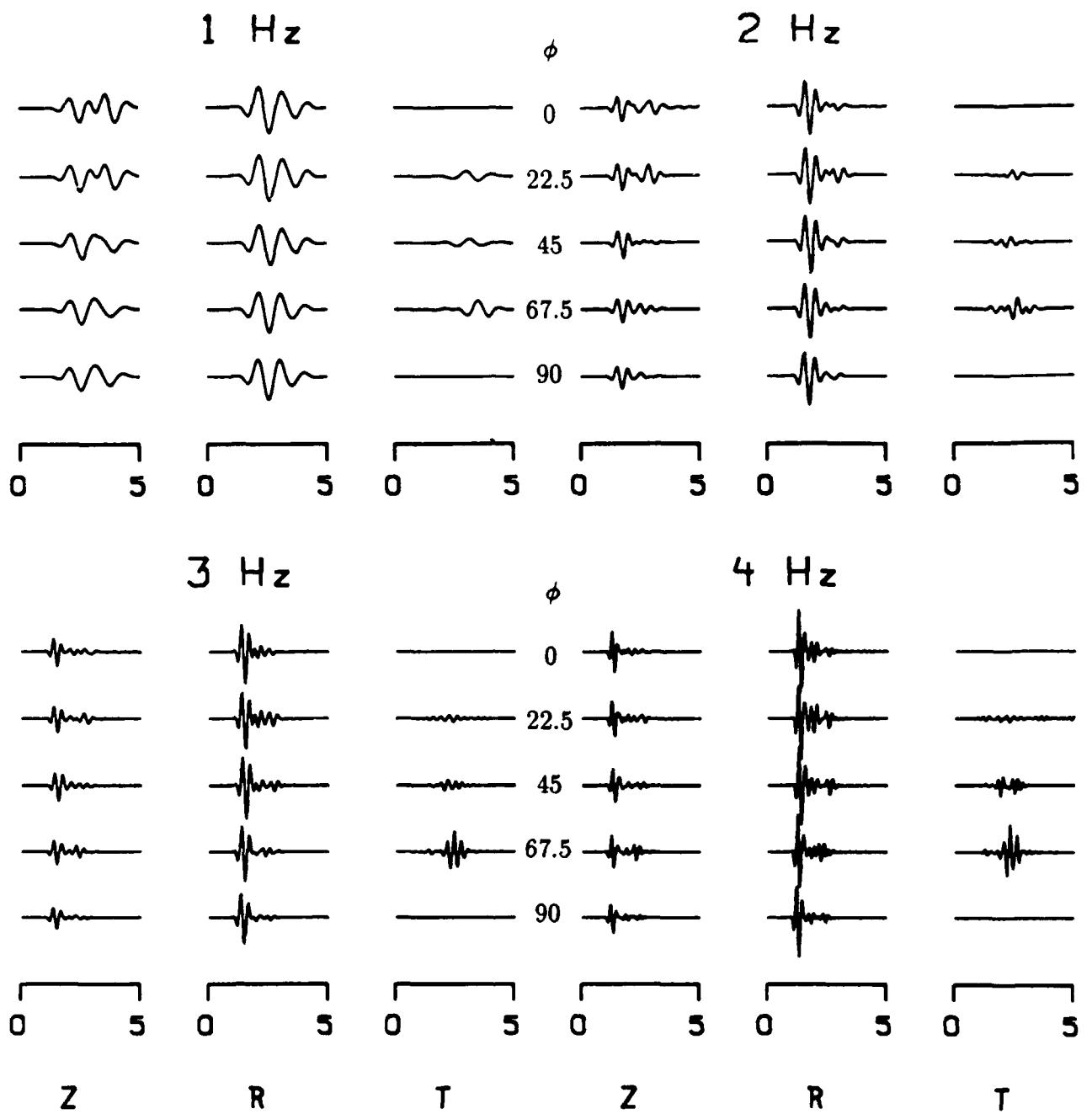
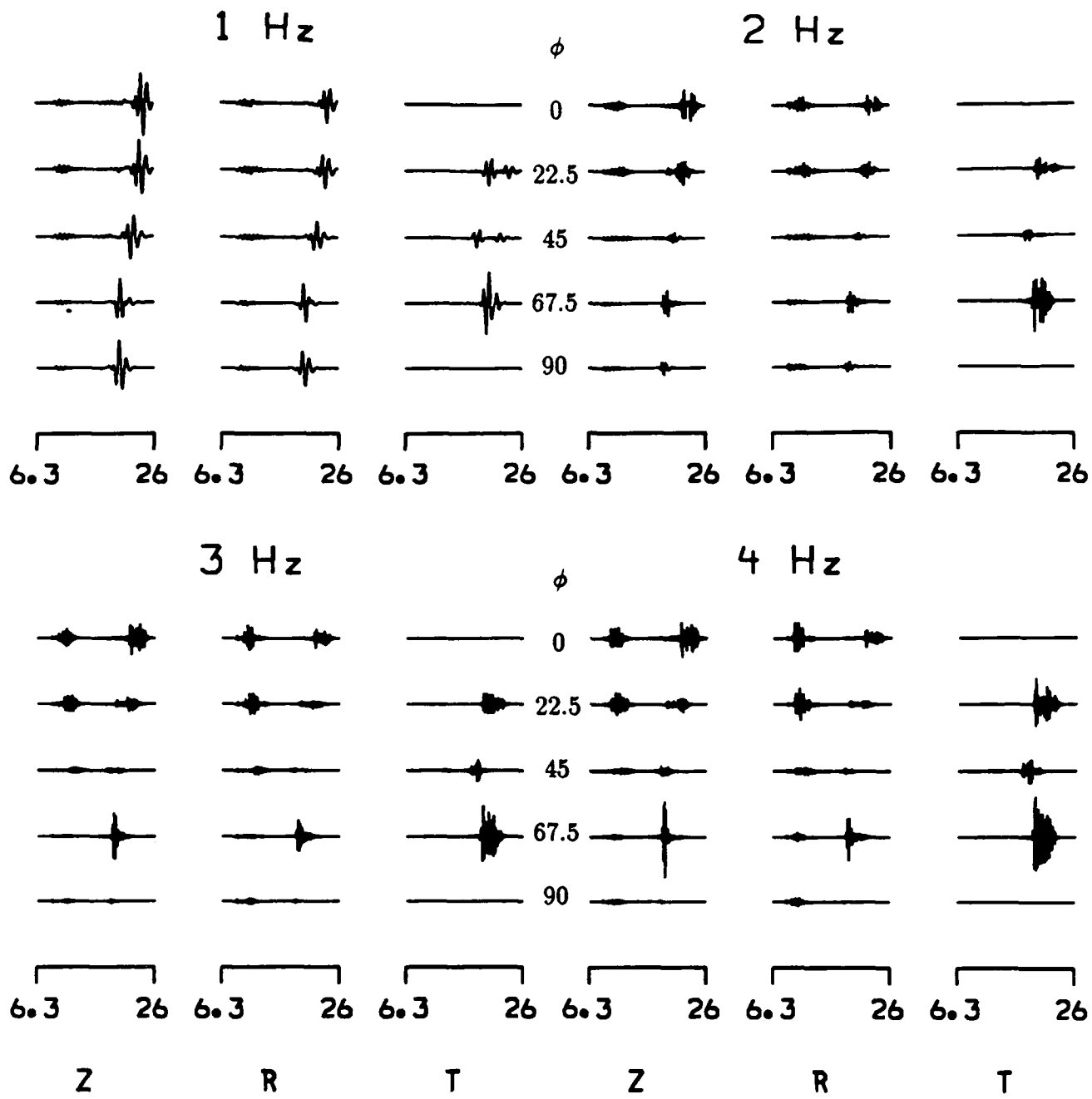


Figure 9: Schematic diagram of an anisotropic layer over isotropic half-space.



Dist = 5 Km. Layer over Half-space, 20% crack density

Figure 10: Three-component synthetic seismograms for a layer over half-space at a 5 km epicentral distance, for five azimuths and at frequencies of 1, 2, 3, and 4 Hz. The seismograms at $\phi = 90^\circ$ are equivalent to those of an isotropic reference medium.



Dist = 50 Km, Layer over Half-space, 20% crack density

Figure 11: Three-component synthetic seismograms for a layer over half-space at a 50 km epicentral distance, for five azimuths and at frequencies of 1, 2, 3, and 4 Hz. The seismograms at $\phi = 90^\circ$ are equivalent to those of an isotropic reference medium.

FREQUENCY-DEPENDENT ATTENUATION IN THE CRUST

M. Nafi Toksöz, Batakrishna Mandal and Anton M. Dainty

Earth Resources Laboratory, Massachusetts Institute of Technology

In Preparation for Geophys. Res. Lett., October, 1989

Abstract. The shear wave attenuation (Q^{-1}) in the crust beneath the northeastern US and Scandinavia is determined as a function of depth and frequency with the aid of data analysis and theoretical modeling of complete wave synthesis. To determine attenuation in the uppermost crust, short period ($0.25 < T < 2$ sec) Rg waves generated by explosive sources and recorded by linear arrays of seismometers are used. These data are combined with longer period ($6 < T < 20$ sec) crustal data and high frequency Lg data to extend the investigation into the deeper crust. The combination of broad-band Rayleigh waves and short period ($T < 1.0$ sec) Lg waves makes it possible to determine attenuation as a function of depth and frequency in the crust, parameterised as $Q = Q_0 f^c$. To match the observations, theoretical models for three mechanisms that contribute to attenuation in the crust—frequency independent anelastic (Q_a^{-1}) and frequency dependent fluid-flow (Q_f^{-1}) and scattering (Q_s^{-1})—are calculated. The best fitting models require low Q ($Q_0 < 100$) in the shallow crust that increases with increasing frequency as $f^{0.5}$ above 1 Hz. In the middle crust between about 2 to 10 km depth Q is moderate ($100 < Q_0 < 500$) with a frequency dependence of f^1 . In the lower crust, the attenuation is very low ($Q \geq 500$) and its frequency dependence is difficult to establish. The low intrinsic Q and the frequency dependence in the uppermost crust can be explained by fluid flow in fractures. In the middle crust the frequency dependence suggests

scattering. The increase of Q in the lower crust is most likely due to annealing of microcracks under pressure and temperature as observed in the laboratory.

Introduction

Seismic attenuation in the crust and lithosphere affects the propagation efficiency of seismic phases at regional distances. The primary objective of this study is to determine shear wave attenuation (Q^{-1}) as a function of *depth* and *frequency* in the crust. The anelastic attenuation of seismic waves is commonly determined by studying the decay of seismic energy with epicentral distances. Different wave types (e.g., Lg, Rg) are used. Several studies have evaluated the attenuation characteristics of seismic waves, especially Lg waves in various parts of the world (e.g. Nuttli, 1973; Mitchell, 1975; Bollinger, 1979; Nicolas *et al.*, 1982; Campillo *et al.*, 1985). This subject has also been studied using theoretical approaches (e.g. Båth and Crampin, 1965; Müller and Mueller, 1979; Bache *et al.*, 1981; Bouchon, 1982; Olsen *et al.*, 1983; Herrmann and Kijko, 1983; Campillo *et al.*, 1984). Mitchell (1980, 1981) has evaluated the frequency dependence of attenuation of Lg waves in the United States for longer periods ($6 < T > 20$ sec).

In this article, we examine the attenuation mechanisms in different regions of the earth's crust by generating complete synthetic seismograms for the best match attenuation model. The complete synthetic seismograms are computed by the reflectivity technique combined with numerical wavenumber integration (Mandal and Mitchell, 1986; Mandal, 1988). The effect of attenuation is introduced through the use of complex velocities (Aki and Richards, 1980, Eq. 5.87, p 182). We assume that the coda and/or Lg attenuation represents the intrinsic attenuation in the crust

(Toksoz *et al.*, 1988). We further assume that three mechanisms contribute to intrinsic attenuation:

(1) Frequency-independent material anelasticity; (2) frequency-dependent fluid flow or relaxation effects; and (3) frequency-dependent scattering. Both mechanisms will depend on depth in the crust. For layer k , we can express intrinsic attenuation as

$$\frac{1}{Q_{t_k}(f)} = \frac{1}{Q_{a_k}} + \frac{1}{Q_{f_k}(f)} + \frac{1}{Q_{s_k}(f)} \quad (1)$$

where $Q_t^{-1}(f)$ is the total attenuation, Q_a^{-1} is frequency-independent anelastic attenuation, $Q_f^{-1}(f)$ is the frequency-dependent attenuation due to fluid flow or relaxation, and $Q_s^{-1}(f)$ is the frequency-dependant attenuation due to scattering. Toksoz and Johnston (1981) summarise results for anelastic attenuation in dry rocks, demonstrating that it is frequency-independent. Toksoz *et al.* (1987) have shown that P and S wave Q_f varies as $f^{0.5}$ due to fluid flow above a critical frequency that may be as low as 1 Hz. Dainty (1981) presents a model of scattering attenuation that predicts Q_s varies as f^1 and suggests that it should apply in the lithosphere for frequencies greater than 1 Hz. An empirical relationship for frequency dependence of Q is

$$Q_{t_k} = Q_{0_k} f^\zeta. \quad (2)$$

In central and northeastern U.S., eastern Canada and European shield areas, values of ζ are found to vary between 0.3 and 0.9 and generally cluster around $\zeta = 0.5$ (e.g., Singh and Herrmann, 1983; Pulli, 1984; Campillo *et al.*, 1985; Dysart and Pulli, 1987). As an initial attempt to fit the data, we use equation (2) and then interpret the value of ζ .

Q Models

Two cases of modelling for different observations are presented. We start with approximate initial velocity and attenuation models, from published results or otherwise. By trial and error, we establish the velocity and attenuation models of the area which match the observed data well. For all the cases we use the short period vertical component. The seismograms are observed at ranges 5–250 km and are in the frequency band 0–10 Hz. The data from the two different regions are:

- (a) USGS refraction experiment in Maine (Doll *et al.*, 1986).
- (b) Leningrad quarry blasts observed in Fennoscandia at the FINESA array.

USGS refraction experiment in Maine:

The seismograms (*left* of Figure 1) from 6 to 29 km were acquired in northeast Maine (the Chain Lakes Massif) during the 1986 USGS seismic refraction and wide-angle reflection experiment (Doll *et al.*, 1986). The Rg phase is well recorded. Figure 1 shows the comparison between the observed seismograms (*left*) and complete wave synthetics (*right*). To model this region we start with an approximate model from surface wave inversion (Reiter *et al.*, 1988). The final velocity and attenuation model are shown in Figure 2. The source is assumed to be a point vertical force at depth 40 m. The observed and synthetics are filtered with a frequency band of 0.5 to 4 Hz for purposes of comparison, although the original synthetics were calculated for 0–10 Hz. The waveforms are at constant scale and are corrected for geometric spreading. Note the synthetics do not generate scattered waves clearly seen in the observations. This suggests that the real earth model is highly

heterogeneous and we would expect some scattering attenuation. In the Q model, we see $\zeta = 0.5$ for depths less than 1 km increasing to $\zeta = 1$ below this. Below 8 km depth there is effectively no constraint on Q .

Leningrad quarries:

Two quarry blasts near Leningrad observed at the Fennoscandian array FINESA are presented here. The distances are 200 and 250 km. The preliminary velocity model was taken from results from the FENNOLORA experiment published by Cassell *et al.* (1983). Observed and complete synthetic seismograms are shown in Figure 3. The velocity and attenuation models used for the synthetic seismograms are given in Figure 4. The quarry blasts are represented by a point vertical force at depth 40 m for synthetic computations. Both observed and synthetic seismograms are bandpass filtered between 0.8 and 4 Hz; the synthetics were originally computed for a 0–8 Hz frequency band. Note that the synthetics are not corrected for instrument response. The complete wave synthetics match the major phases (P, Lg, Rg) of the observed waveforms. Specifically, the synthetic waveforms predict quite accurately the higher (Lg) and fundamental (Rg) modes. Again, the scattered coda is not predicted by the synthetic modelling. There is a large phase at about 17 sec on the 250 km synthetic which is a reflection off the Moho; trial calculations demonstrate that this phase is very sensitive to Moho structure and may be easily suppressed by slight modifications of it. We do not do so here because this is not the main focus of the study. The Q model again shows a thin surface layer with $\zeta = 0.5$ with an increase to $\zeta = 1$ between 2 and 16 km. The deep crust has a high shear wave Q of 500 with $\zeta = 0$.

DISCUSSION

Both of these cases are from non-tectonic regions where crystalline rocks are found at the surface. In both cases the seismic attenuation is high in the upper crust and is frequency dependent. Q_0 increases with depth in the crust from less than 100 in the top 2 km to 100–500 from 2–10 km to greater than 500 in the lower crust. The frequency exponent ζ in the same depth ranges is 0.5 (0–2 km), 1.0 (2–10 km) and 0 (lower crust). The high attenuation and the frequency exponent in the upper 2 km can be explained by the presence of fluid flow in fractures. Between 2 and 10 km the frequency exponent indicates that scattering is the dominant mechanism responsible for attenuation. In the lower crust anelastic attenuation is occurring with the high Q values reflecting closing of fractures and annealing of microfractures due to pressure and temperature effects (Smith and Evans, 1984).

ACKNOWLEDGEMENTS

This work has been supported by the Defense Advanced Research Projects Agency through contract F19628-87-K-0054 administered by the Air Force Geophysical Laboratory.

REFERENCES

Aki, K., and P. G. Richards, 1980, *Quantitative Seismology Theory and Methods*, W. H. Freeman and Co.

Bache, T. C., H. J. Swanger, B. Shkoller, and S. M. Day, 1981, Simulation of short period Lg. expansion of three dimensional source simulation capabilities and simulation of near-field ground

motion from the 1971 San Fernando, California Earthquake, *Final Report*, Systems, Science and Software, La Jolla, California.

Büth, M., and S. Crampin, 1965, Higher modes of seismic surface waves—relations to channel waves, *Geophys. J. R. Astr. Soc.*, 9, 309–321.

Bollinger, G. A., 1979, Attenuation of the Lg phase and the determination of m_b in the southeastern United States, *Bull. Seis. Soc. Am.*, 69, 45–63.

Bouchon, M., 1982, The complete synthesis of seismic crustal phases at regional distances, *J. Geophys. Res.*, 87, 1735–1741.

Campillo, M., M. Bouchon, and B. Massinon, 1984, Theoretical study of the excitation, spectral characteristics and geometrical attenuation of regional seismic phases, *Bull. Seis. Soc. Am.*, 74, 79–90.

Campillo, M., J.-L. Plantet, and M. Bouchon, 1985, Frequency-dependent attenuation in the crust beneath central France from Lg waves: data analysis and numerical modeling, *Bull. Seis. Soc. Am.*, 75, 1395–1411.

Cassell, B. R., S. Mykkeltveit, R. Kanestrøm, and E. S. Husebye, 1983, A North Sea—southern Norway seismic crustal profile, *Geophys. J. R. Astr. Soc.*, 72, 733–753.

Dainty, A. M., 1981, A scattering model to explain seismic Q observations in the lithosphere between 1 and 30 Hz, *Geophys. Res. Lett.*, 8, 1126–1128.

Doll, W. E., J. H. Luetgert, and J. M. Murphy, 1986, Seismic refraction and wide-angle reflection in the northern Appalachians; the Chain Lakes Massif, northwest Maine, *EOS*, 67, 312 (abs.).

Dysart, P. S., and J. J. Pulli, 1987, Spectral study of regional earthquakes and chemical explosions

recorded at the NORESS array, *Technical Report C87-03*, 1/4/87-6/30/87, Center for Seismic Studies, Arlington, Virginia, 3-21-3-44.

Herrmann, R. B., and A. Kijko, 1983, Modeling some empirical vertical component Lg relations, *Bull. Seis. Soc. Am.*, 73, 157-171.

Mandal, B., 1988, *Algorithm for generating complete waveforms for isotropic and transversely isotropic layered media*, Software Package, Reservoir Delineation—Vertical Seismic Profiling Consortium, ERL, MIT, 155p.

Mandal, B., and B. J. Mitchell, 1986, Complete seismogram synthesis in transversely isotropic medium, *J. Geophys.*, 59, 33-40.

Mitchell, B. J., 1975, Regional Rayleigh wave attenuation in North America, *J. Geophys. Res.*, 80, 4904-4916.

Mitchell, B. J., 1980, Frequency dependence of shear wave internal friction in continental crust of eastern North America, *J. Geophys. Res.*, 85, 5212-5218.

Mitchell, B. J., 1981, Regional variation and frequency dependence of Q in the crust of the United States, *Bull. Seis. Soc. Am.*, 71, 1531-1538.

Müller, G., and S. Mueller, 1979, Travel time and amplitude interpretation of crustal phases on the refraction profile DELTA-W, Utah, *Bull. Seis. Soc. Am.*, 71, 1531-1538.

Nicolas, M., B. Massinon, P. Mechler, and M. Bouchon, 1982, Attenuation of regional phases in western Europe, *Bull. Seis. Soc. Am.*, 72, 2089-2106.

Nuttli, O. W., 1973, Seismic wave attenuation and magnitude relations for eastern North America, *J. Geophys. Res.*, 78, 876-885.

Olsen, K. H., L. W. Braile, and J. N. Stewart, 1983, Modeling short-period crustal phases (P-Lg) for long-range refraction profiles, *Phys. Earth Planet. Interiors*, 31, 334-347.

Pulli, J. J., 1984, Attenuation of coda waves in New England, *Bull. Seis. Soc. Am.*, 74, 1149-1166.

Reiter, E., M. N. Toksöz, and A. M. Dainty, 1988, *Influence of Scattering on Seismic Waves: Velocity and Attenuation of the Upper Crust in Southeast Maine*, Report AFGL-TR-88-0094, Air Force Geophysics Laboratory, Hanscom AFB, Massachusetts.

Singh, S., and R. B. Herrmann, 1983, Regionalization of crustal coda Q in the continental United States, *J. Geophys. Res.*, 88, 527-538.

Smith, D. L., and B. Evans, 1984, Diffusional crack healing in quartz, *J. Geophys. Res.*, 89, 4125-4135.

Toksöz, M. N., and D. H. Johnston (eds.), 1981, *Seismic Wave Attenuation*, Geophysics Reprint Series No. 2, Society of Exploration Geophysicists.

Toksöz, M. N., R. S. Wu, and D. P. Schmitt, 1987, Physical mechanisms contributing to seismic attenuation in the crust, *Proc. NATO ASI 'Strong Ground Motion Seismology'*, Ankara, Turkey, 225-247.

Toksöz, M. N., A. M. Dainty, E. Reiter, and R.-S. Wu, 1988, A model for attenuation and scattering in the earth's crust, *PAGEOPH*, 128, 81-100.

Figure 1: Observed and synthetic seismograms as a function of distance; observed from USGS refraction experiment in Maine. Synthetics are computed for a point vertical force of depth 40 m. Receivers are on the surface from 6–29 km offset. Both observed and synthetics are filtered with a frequency band of 0.5–4 Hz.

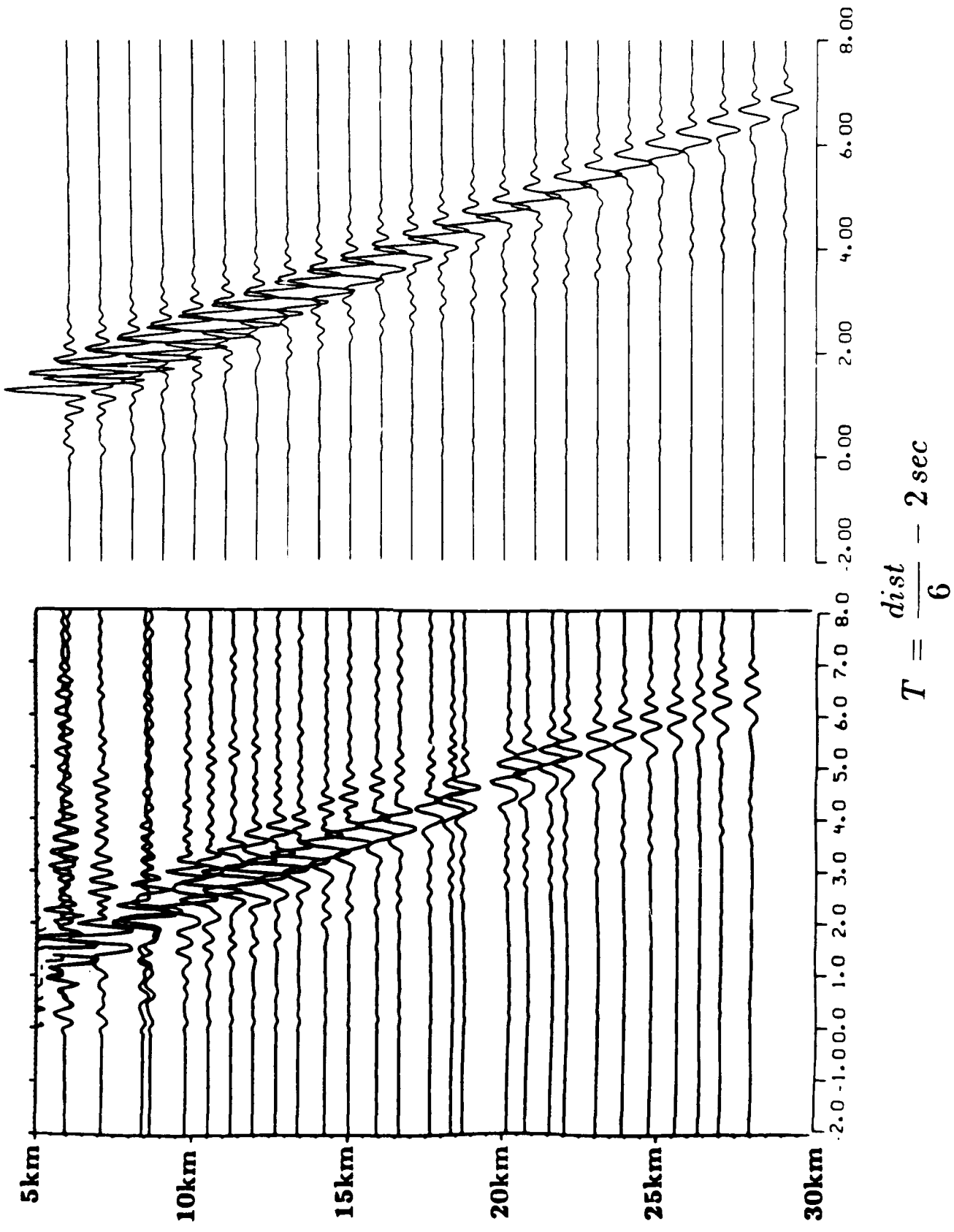
Figure 2: Velocity and attenuation models for synthetic seismograms in Figure 1. Solid lines refer to P wave velocity and Q , dashed or dotted lines to S waves. For Q , $Q_\alpha = 2Q_\beta$ and $Q = Q_0 \times f^\zeta$ for both P and S. It was found that the value of Q_α did not significantly affect the seismograms.

Figure 3: Comparison of observed and synthetic seismograms for two quarry blasts from Leningrad recorded at the FINESA array. Synthetics and observed are filtered with a frequency band of 0.8–4 Hz. See text for discussion.

Figure 4: Velocity and attenuation models for synthetic seismograms in Figure 3. Symbols as for Figure 2.

USGS refraction experiment in Maine

SYNTHETIC



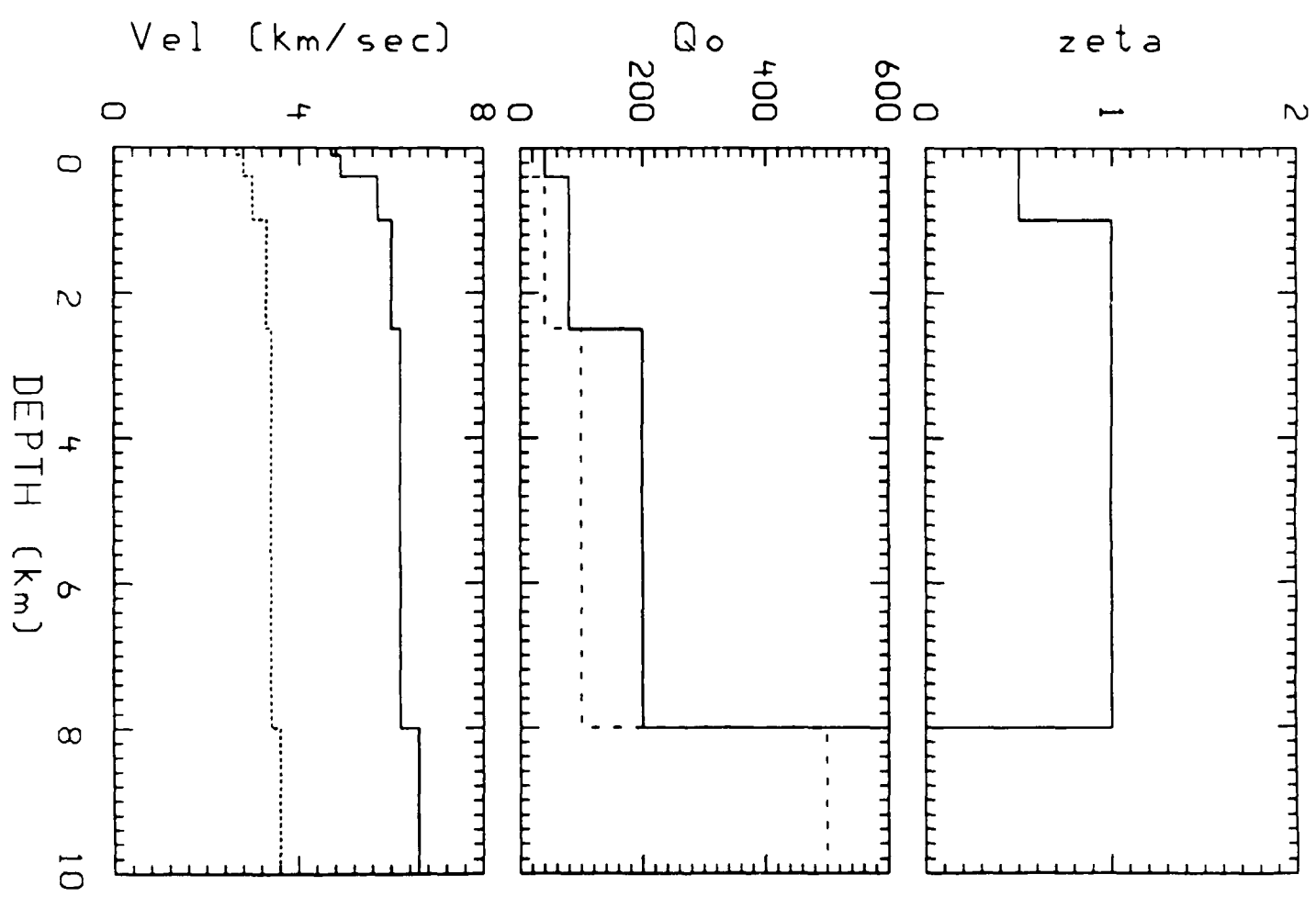
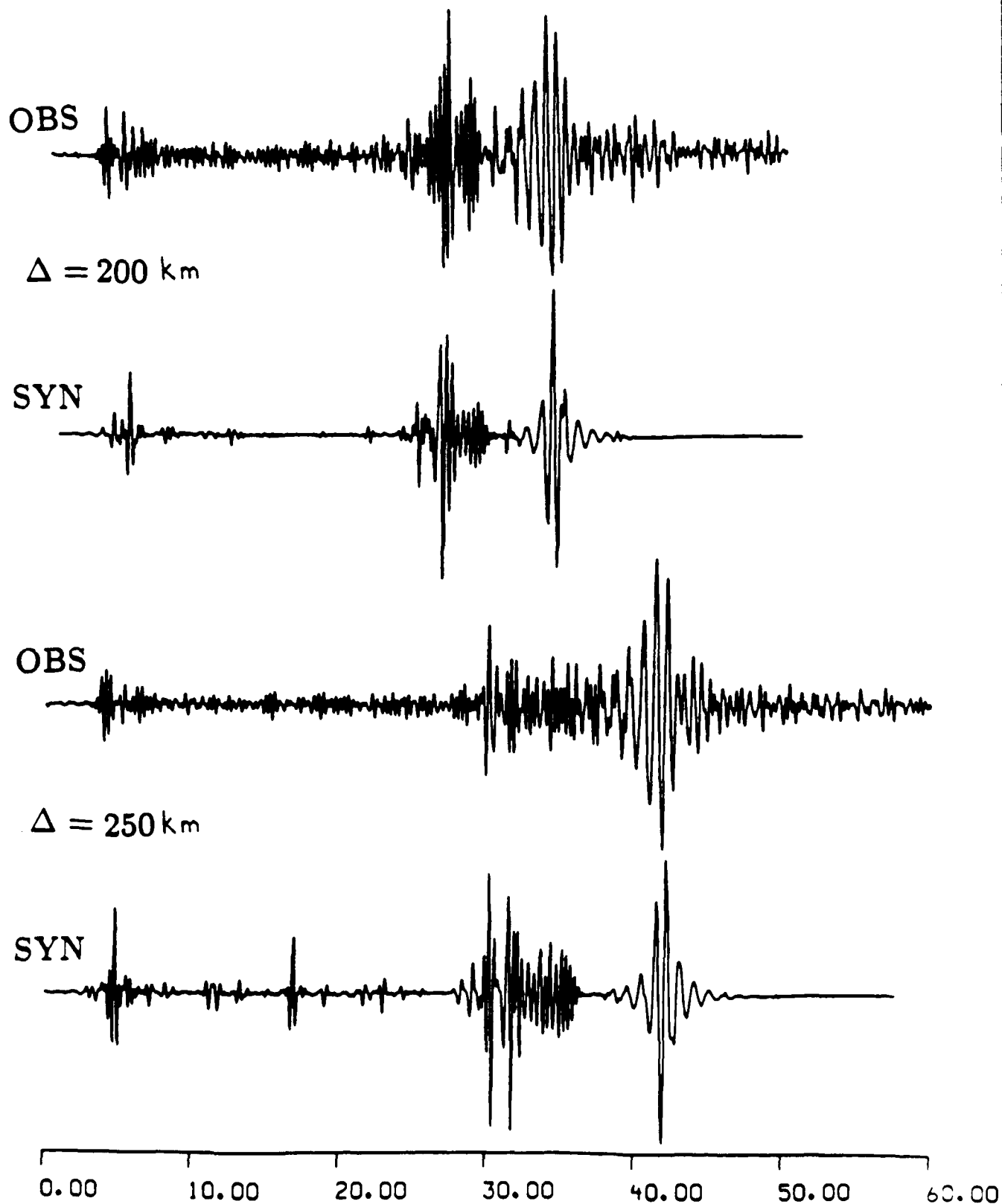


Figure 2.

Leningrad quarry observed at Fennoscandia



$$T = \frac{\text{dist}}{7} \text{ sec}$$

Figure 3.

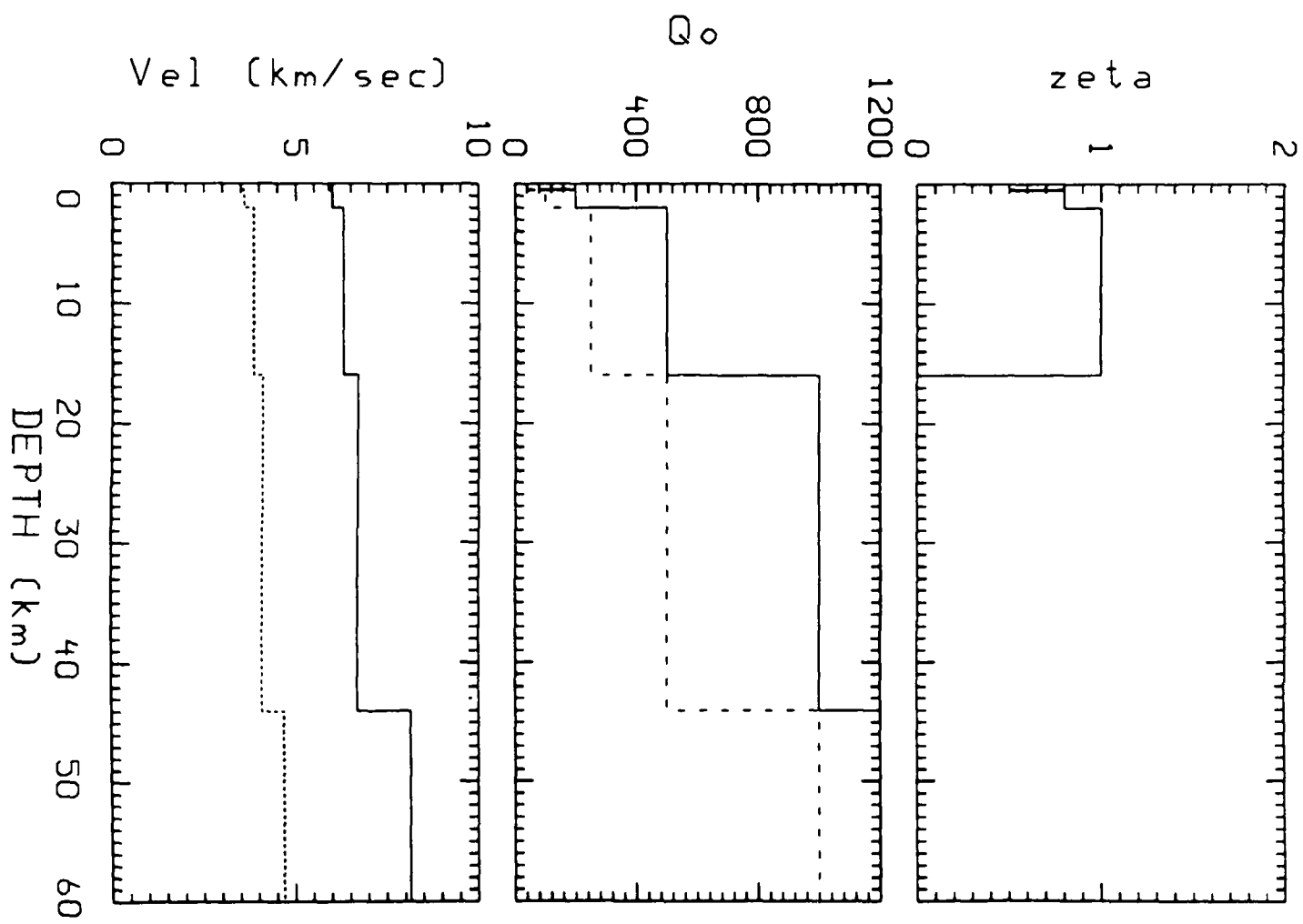


Figure 4.

CONTRACTORS (United States)

Prof. Thomas Ahrens
Seismological Lab, 252-21
Division of Geological & Planetary Sciences
California Institute of Technology
Pasadena, CA 91125

Prof. Charles B. Archambeau
CIRCS
University of Colorado
Boulder, CO 80309

Prof. Muawia Barazangi
Institute for the Study of the Continent
Cornell University
Ithaca, NY 14853

Dr. Douglas R. Baumgardt
ENSCO, Inc
5400 Port Royal Road
Springfield, VA 22151-2388

Prof. Jonathan Berger
IGPP, A-025
Scripps Institution of Oceanography
University of California, San Diego
La Jolla, CA 92093

Dr. Lawrence J. Burdick
Woodward-Clyde Consultants
566 El Dorado Street
Pasadena, CA 91109-3245

Dr. Karl Coyner
New England Research, Inc.
76 Olcott Drive
White River Junction, VT 05001

Prof. Vernon F. Cormier
Department of Geology & Geophysics
U-45, Room 207
The University of Connecticut
Storrs, CT 06268

Prof. Steven Day
Department of Geological Sciences
San Diego State University
San Diego, CA 92182

Dr. Zoltan A. Der
ENSCO, Inc.
5400 Port Royal Road
Springfield, VA 22151-2388

Prof. John Ferguson
Center for Lithospheric Studies
The University of Texas at Dallas
P.O. Box 830688
Richardson, TX 75083-0688

Prof. Stanley Flatte
Applied Sciences Building
University of California
Santa Cruz, CA 95064

Dr. Alexander Florence
SRI International
333 Ravenswood Avenue
Menlo Park, CA 94025-3493

Prof. Henry L. Gray
Vice Provost and Dean
Department of Statistical Sciences
Southern Methodist University
Dallas, TX 75275

Dr. Indra Gupta
Teledyne Geotech
314 Montgomery Street
Alexandria, VA 22314

Prof. David G. Harkrider
Seismological Laboratory
Division of Geological & Planetary Sciences
California Institute of Technology
Pasadena, CA 91125

Prof. Donald V. Helmberger
Seismological Laboratory
Division of Geological & Planetary Sciences
California Institute of Technology
Pasadena, CA 91125

Prof. Eugene Herrin
Institute for the Study of Earth and Man
Geophysical Laboratory
Southern Methodist University
Dallas, TX 75275

Prof. Robert B. Herrmann
Department of Earth & Atmospheric Sciences
St. Louis University
St. Louis, MO 63156

Prof. Bryan Isacks
Cornell University
Department of Geological Sciences
SNEE Hall
Ithaca, NY 14850

Dr. Rong-Song Jih
Teledyne Geotech
314 Montgomery Street
Alexandria, VA 22314

Dr. Gary McCartor
Mission Research Corporation
735 State Street
P.O. Drawer 719
Santa Barbara, CA 93102 (2 copies)

Prof. Lane R. Johnson
Seismographic Station
University of California
Berkeley, CA 94720

Prof. Thomas V. McEvilly
Seismographic Station
University of California
Berkeley, CA 94720

Prof. Alan Kafka
Department of Geology & Geophysics
Boston College
Chestnut Hill, MA 02167

Dr. Keith L. McLaughlin
S-CUBED
A Division of Maxwell Laboratory
P.O. Box 1620
La Jolla, CA 92038-1620

Prof. Fred K. Lamb
University of Illinois at Urbana-Champaign
Department of Physics
1110 West Green Street
Urbana, IL 61801

Prof. William Menke
Lamont-Doherty Geological Observatory
of Columbia University
Palisades, NY 10964

Prof. Charles A. Langston
Geosciences Department
403 Deike Building
The Pennsylvania State University
University Park, PA 16802

Stephen Miller
SRI International
333 Ravenswood Avenue
Box AF 116
Menlo Park, CA 94025-3493

Prof. Thorne Lay
Department of Geological Sciences
1006 C.C. Little Building
University of Michigan
Ann Arbor, MI 48109-1063

Prof. Bernard Minster
IGPP, A-025
Scripps Institute of Oceanography
University of California, San Diego
La Jolla, CA 92093

Prof. Arthur Lerner-Lam
Lamont-Doherty Geological Observatory
of Columbia University
Palisades, NY 10964

Prof. Brian J. Mitchell
Department of Earth & Atmospheric Sciences
St. Louis University
St. Louis, MO 63156

Dr. Christopher Lynnes
Teledyne Geotech
314 Montgomery Street
Alexandria, VA 22314

Mr. Jack Murphy
S-CUBED, A Division of Maxwell Laboratory
11800 Sunrise Valley Drive
Suite 1212
Reston, VA 22091 (2 copies)

Prof. Peter Malin
University of California at Santa Barbara
Institute for Crustal Studies
Santa Barbara, CA 93106

Dr. Bao Nguyen
GL/LWH
Hanscom AFB, MA 01731-5000

Dr. Randolph Martin, III
New England Research, Inc.
76 Olcott Drive
White River Junction, VT 05001

Prof. John A. Orcutt
IGPP, A-025
Scripps Institute of Oceanography
University of California, San Diego
La Jolla, CA 92093

Prof. Keith Priestley
University of Nevada
Mackay School of Mines
Reno, NV 89557

Prof. Paul G. Richards
Lamont-Doherty Geological Observatory
of Columbia University
Palisades, NY 10964

Dr. Wilmer Rivers
Teledyne Geotech
314 Montgomery Street
Alexandria, VA 22314

Dr. Alan S. Ryall, Jr.
Center for Seismic Studies
1300 North 17th Street
Suite 1450
Arlington, VA 22209-2308

Prof. Charles G. Sammis
Center for Earth Sciences
University of Southern California
University Park
Los Angeles, CA 90089-0741

Prof. Christopher H. Scholz
Lamont-Doherty Geological Observatory
of Columbia University
Palisades, NY 10964

Prof. David G. Simpson
Lamont-Doherty Geological Observatory
of Columbia University
Palisades, NY 10964

Dr. Jeffrey Stevens
S-CUBED
A Division of Maxwell Laboratory
P.O. Box 1620
La Jolla, CA 92038-1620

Prof. Brian Stump
Institute for the Study of Earth & Man
Geophysical Laboratory
Southern Methodist University
Dallas, TX 75275

Prof. Jeremiah Sullivan
University of Illinois at Urbana-Champaign
Department of Physics
1110 West Green Street
Urbana, IL 61801

Prof. Clifford Thurber
University of Wisconsin-Madison
Department of Geology & Geophysics
1215 West Dayton Street
Madison, WI 53706

Prof. M. Nafi Toksoz
Earth Resources Lab
Massachusetts Institute of Technology
42 Carleton Street
Cambridge, MA 02142

Prof. John E. Vidale
University of California at Santa Cruz
Seismological Laboratory
Santa Cruz, CA 95064

Prof. Terry C. Wallace
Department of Geosciences
Building #77
University of Arizona
Tucson, AZ 85721

Dr. Raymond Willeman
GL/LWH
Hanscom AFB, MA 01731-5000

Dr. Lorraine Wolf
GL/LWH
Hanscom AFB, MA 01731-5000

Prof. Francis T. Wu
Department of Geological Sciences
State University of New York
at Binghamton
Vestal, NY 13901

OTHERS (United States)

Dr. Monem Abdel-Gawad
Rockwell International Science Center
1049 Camino Dos Rios
Thousand Oaks, CA 91360

Dr. Stephen Bratt
Science Applications Int'l Corp.
10210 Campus Point Drive
San Diego, CA 92121

Prof. Keiiti Aki
Center for Earth Sciences
University of Southern California
University Park
Los Angeles, CA 90089-0741

Michael Browne
Teledyne Geotech
3401 Shiloh Road
Garland, TX 75041

Prof. Shelton S. Alexander
Geosciences Department
403 Deike Building
The Pennsylvania State University
University Park, PA 16802

Mr. Roy Burger
1221 Serry Road
Schenectady, NY 12309

Dr. Ralph Archuleta
Department of Geological Sciences
University of California at Santa Barbara
Santa Barbara, CA 93102

Dr. Robert Burridge
Schlumberger-Doll Research Center
Old Quarry Road
Ridgefield, CT 06877

Dr. Thomas C. Bache, Jr.
Science Applications Int'l Corp.
10210 Campus Point Drive
San Diego, CA 92121 (2 copies)

Dr. Jerry Carter
Rondout Associates
P.O. Box 224
Stone Ridge, NY 12484

J. Barker
Department of Geological Sciences
State University of New York
at Binghamton
Vestal, NY 13901

Dr. W. Winston Chan
Teledyne Geotech
314 Montgomery Street
Alexandria, VA 22314-1581

Dr. T.J. Bennett
S-CUBED
A Division of Maxwell Laboratory
11800 Sunrise Valley Drive, Suite 1212
Reston, VA 22091

Dr. Theodore Cherry
Science Horizons, Inc.
710 Encinitas Blvd., Suite 200
Encinitas, CA 92024 (2 copies)

Mr. William J. Best
907 Westwood Drive
Vienna, VA 22180

Prof. Jon F. Claerbout
Department of Geophysics
Stanford University
Stanford, CA 94305

Dr. N. Biswas
Geophysical Institute
University of Alaska
Fairbanks, AK 99701

Prof. Robert W. Clayton
Seismological Laboratory
Division of Geological & Planetary Sciences
California Institute of Technology
Pasadena, CA 91125

Dr. G.A. Bollinger
Department of Geological Sciences
Virginia Polytechnical Institute
21044 Derring Hall
Blacksburg, VA 24061

Prof. F. A. Dahlen
Geological and Geophysical Sciences
Princeton University
Princeton, NJ 08544-0636

Prof. Anton W. Dainty
Earth Resources Lab
Massachusetts Institute of Technology
42 Carleton Street
Cambridge, MA 02142

Prof. Adam Dziewonski
Hoffman Laboratory
Harvard University
20 Oxford St
Cambridge, MA 02138

Prof. John Ebel
Department of Geology & Geophysics
Boston College
Chestnut Hill, MA 02167

Eric Fielding
SNEE Hall
INSTOC
Cornell University
Ithaca, NY 14853

Prof. Donald Forsyth
Department of Geological Sciences
Brown University
Providence, RI 02912

Prof. Art Frankel
Mail Stop 922
Geological Survey
790 National Center
Reston, VA 22092

Dr. Anthony Gangi
Texas A&M University
Department of Geophysics
College Station, TX 77843

Dr. Freeman Gilbert
Inst. of Geophysics & Planetary Physics
University of California, San Diego
P.O. Box 109
La Jolla, CA 92037

Mr. Edward Giller
Pacific Sierra Research Corp.
1401 Wilson Boulevard
Arlington, VA 22209

Dr. Jeffrey W. Given
Sierra Geophysics
11255 Kirkland Way
Kirkland, WA 98033

Prof. Stephen Grand
University of Texas at Austin
Department of Geological Sciences
Austin, TX 78713-7909

Prof. Roy Greenfield
Geosciences Department
403 Deike Building
The Pennsylvania State University
University Park, PA 16802

Dan N. Hagedorn
Battelle
Pacific Northwest Laboratories
Battelle Boulevard
Richland, WA 99352

Kevin Hutchenson
Department of Earth Sciences
St. Louis University
3507 Laclede
St. Louis, MO 63103

Prof. Thomas H. Jordan
Department of Earth, Atmospheric
and Planetary Sciences
Massachusetts Institute of Technology
Cambridge, MA 02139

Robert C. Kemerait
ENSCO, Inc.
445 Pineda Court
Melbourne, FL 32940

William Kikendall
Teledyne Geotech
3401 Shiloh Road
Garland, TX 75041

Prof. Leon Knopoff
University of California
Institute of Geophysics & Planetary Physics
Los Angeles, CA 90024

Prof. L. Timothy Long
School of Geophysical Sciences
Georgia Institute of Technology
Atlanta, GA 30332

Prof. Art McGarr
Mail Stop 977
Geological Survey
345 Middlefield Rd.
Menlo Park, CA 94025

Dr. George Mellman
Sierra Geophysics
11255 Kirkland Way
Kirkland, WA 98033

Dr. Richard Sailor
TASC Inc.
55 Walkers Brook Drive
Reading, MA 01867

Prof. John Nabelek
College of Oceanography
Oregon State University
Corvallis, OR 97331

Thomas J. Sereno, Jr.
Science Application Int'l Corp.
10210 Campus Point Drive
San Diego, CA 92121

Prof. Geza Nagy
University of California, San Diego
Department of Ames, M.S. B-010
La Jolla, CA 92093

John Sherwin
Teledyne Geotech
3401 Shiloh Road
Garland, TX 75041

Prof. Amos Nur
Department of Geophysics
Stanford University
Stanford, CA 94305

Prof. Robert Smith
Department of Geophysics
University of Utah
1400 East 2nd South
Salt Lake City, UT 84112

Prof. Jack Oliver
Department of Geology
Cornell University
Ithaca, NY 14850

Prof. S. W. Smith
Geophysics Program
University of Washington
Seattle, WA 98195

Prof. Robert Phinney
Geological & Geophysical Sciences
Princeton University
Princeton, NJ 08544-0636

Dr. Stewart Smith
IRIS Inc.
1616 North Fort Myer Drive
Suite 1440
Arlington, VA 22209

Dr. Paul Pomeroy
Rondout Associates
P.O. Box 224
Stone Ridge, NY 12484

Dr. George Sutton
Rondout Associates
P.O. Box 224
Stone Ridge, NY 12484

Dr. Jay Pulli
RADIX System, Inc.
2 Taft Court, Suite 203
Rockville, MD 20850

Prof. L. Sykes
Lamont-Doherty Geological Observatory
of Columbia University
Palisades, NY 10964

Dr. Norton Rimer
S-CUBED
A Division of Maxwell Laboratory
P.O. Box 1620
La Jolla, CA 92038-1620

Prof. Pradeep Talwani
Department of Geological Sciences
University of South Carolina
Columbia, SC 29208

Prof. Larry J. Ruff
Department of Geological Sciences
1006 C.C. Little Building
University of Michigan
Ann Arbor, MI 48109-1063

Prof. Ta-liang Teng
Center for Earth Sciences
University of Southern California
University Park
Los Angeles, CA 90089-0741

Dr. R.B. Tittmann
Rockwell International Science Center
1049 Camino Dos Rios
P.O. Box 1085
Thousand Oaks, CA 91360

Dr. Gregory van der Vink
IRIS, Inc.
1616 North Fort Myer Drive
Suite 1440
Arlington, VA 22209

William R. Walter
Seismological Laboratory
University of Nevada
Reno, NV 89557

Dr. Gregory Wojcik
Weidlinger Associates
4410 El Camino Real
Suite 110
Los Altos, CA 94022

Prof. John H. Woodhouse
Hoffman Laboratory
Harvard University
20 Oxford Street
Cambridge, MA 02138

Dr. Gregory B. Young
ENSCO, Inc.
5400 Port Royal Road
Springfield, VA 22151-2388

GOVERNMENT

Dr. Ralph Alewine III
DARPA/NMRO
1400 Wilson Boulevard
Arlington, VA 01731-5000

Paul Johnson
ESS-4, Mail Stop J979
Los Alamos National Laboratory
Los Alamos, NM 87545

Mr. James C. Battis
GL/LWH
Hanscom AFB, MA 22209-2308

Janet Johnston
GL/LWH
Hanscom AFB, MA 01731-5000

Dr. Robert Blandford
DARPA/NMRO
1400 Wilson Boulevard
Arlington, VA 87185

Dr. Katharine Kadinsky-Cade
GL/LWH
Hanscom AFB, MA 01731-5000

Eric Chael
Division 9241
Sandia Laboratory
Albuquerque, NM 01731-5000

Ms. Ann Kerr
IGPP, A-025
Scripps Institute of Oceanography
University of California, San Diego
La Jolla, CA 92093

Dr. John J. Cipar
GL/LWH
Hanscom AFB, MA 01731-5000

Dr. Max Koontz
US Dept of Energy/DP 5
Forrestal Building
1000 Independence Avenue
Washington, DC 20585

Mr. Jeff Duncan
Office of Congressman Markey
2133 Rayburn House Bldg.
Washington, D.C. 20515

Dr. W.H.K. Lee
Office of Earthquakes, Volcanoes,
& Engineering
345 Middlefield Road
Menlo Park, CA 94025

Dr. Jack Evernden
USGS - Earthquake Studies
345 Middlefield Road
Menlo Park, CA 94025

Dr. William Leith
U.S. Geological Survey
Mail Stop 928
Reston, VA 22092

Art Frankel
USGS
922 National Center
Reston, VA 22092

Dr. Richard Lewis
Director, Earthquake Engineering & Geophysics
U.S. Army Corps of Engineers
Box 631
Vicksburg, MS 39180

Dr. T. Hanks
USGS
Nat'l Earthquake Research Center
345 Middlefield Road
Menlo Park, CA 94025

James F. Lewkowicz
GL/LWH
Hanscom AFB, MA 01731-5000

Dr. James Hannon
Lawrence Livermore Nat'l Laboratory
P.O. Box 808
Livermore, CA 94550

Mr. Alfred Lieberman
ACDA/VI-OA'State Department Bldg
Room 5726
320 - 21st Street, NW
Washington, DC 20451

Stephen Mangino
GL/LWH
Hanscom AFB, MA 01731-5000

Dr. Frank F. Pilote
HQ AFTAC/TT
Patrick AFB, FL 32925-6001

Dr. Robert Massé
Box 25046, Mail Stop 967
Denver Federal Center
Denver, CO 80225

Katie Poley
CIA-OSWR/NED
Washington, DC 20505

Art McGarr
U.S. Geological Survey, MS-977
345 Middlefield Road
Menlo Park, CA 94025

Mr. Jack Rachlin
U.S. Geological Survey
Geology, Rm 3 C136
Mail Stop 928 National Center
Reston, VA 22092

Richard Morrow
ACDA/VI, Room 5741
320 21st Street N.W.
Washington, DC 20451

Dr. Robert Reinke
WL/NTESG
Kirtland AFB, NM 87117-6008

Dr. Keith K. Nakanishi
Lawrence Livermore National Laboratory
P.O. Box 808, L-205
Livermore, CA 94550

Dr. Byron Ristvet
HQ DNA, Nevada Operations Office
Attn: NVCG
P.O. Box 98539
Las Vegas, NV 89193

Dr. Carl Newton
Los Alamos National Laboratory
P.O. Box 1663
Mail Stop C335, Group ESS-3
Los Alamos, NM 87545

Dr. George Rothe
HQ AFTAC/TGR
Patrick AFB, FL 32925-6001

Dr. Kenneth H. Olsen
Los Alamos Scientific Laboratory
P.O. Box 1663
Mail Stop C335, Group ESS-3
Los Alamos, NM 87545

Dr. Michael Shore
Defense Nuclear Agency/SPSS
6801 Telegraph Road
Alexandria, VA 22310

Howard J. Patton
Lawrence Livermore National Laboratory
P.O. Box 808, L-205
Livermore, CA 94550

Donald L. Springer
Lawrence Livermore National Laboratory
P.O. Box 808, L-205
Livermore, CA 94550

Mr. Chris Paine
Office of Senator Kennedy, SR 315

Dr. Lawrence Turnbull
OSWR/NED
Central Intelligence Agency, Room 5G48
Washington, DC 20505

United States Senate
Washington, DC 20510

Colonel Jerry J. Perrizo
AFOSR/NP, Building 410
Bolling AFB
Washington, DC 20332-6448

Dr. Thomas Weaver
Los Alamos National Laboratory
P.O. Box 1663, Mail Stop C335
Los Alamos, NM 87545

J.J. Zucca
Lawrence Livermore National Laboratory
Box 808
Livermore, CA 94550

Defense Technical Information Center
Cameron Station
Alexandria, VA 22314 (5 copies)

GL/SULL
Research Library
Hanscom AFB , MA 01731-5000 (2 copies)

Defense Intelligence Agency
Directorate for Scientific &
Technical Intelligence
Washington, DC 20301

Secretary of the Air Force (SAFRD)
Washington, DC 20330

AFTAC/CA
(STINFO)
Patrick AFB, FL 32925-6001

Office of the Secretary Defense
DDR & E
Washington, DC 20330

TACTEC
Battelle Memorial Institute
505 King Avenue
Columbus, OH 43201 (Final Report Only)

HQ DNA
Attn: Technical Library
Washington, DC 20305

Mr. Charles L. Taylor
GL/LWH
Hanscom AFB, MA 01731-5000

DARPA/RMO/RETRIEVAL
1400 Wilson Boulevard
Arlington, VA 22209

DARPA/RMO/Security Office
1400 Wilson Boulevard
Arlington, VA 22209

Geophysics Laboratory
Attn: XO
Hanscom AFB, MA 01731-5000

Geophysics Laboratory
Attn: LW
Hanscom AFB, MA 01731-5000

DARPA/PM
1400 Wilson Boulevard
Arlington, VA 22209

CONTRACTORS (Foreign)

Dr. Ramon Cabre, S.J.
Observatorio San Calixto
Casilla 5939
La Paz, Bolivia

Prof. Hans-Peter Harjes
Institute for Geophysik
Ruhr University/Bochum
P.O. Box 102148
4630 Bochum 1, FRG

Prof. Eystein Husebye
NTNF/NORSAR
P.O. Box 51
N-2007 Kjeller, NORWAY

Prof. Brian L.N. Kennett
Research School of Earth Sciences
Institute of Advanced Studies
G.P.O. Box 4
Canberra 2601, AUSTRALIA

Dr. Bernard Massinon
Societe Radiomana
27 rue Claude Bernard
75005 Paris, FRANCE (2 Copies)

Dr. Pierre Mecheler
Societe Radiomana
27 rue Claude Bernard
75005 Paris, FRANCE

Dr. Svein Mykkeltveit
NTNF/NORSAR
P.O. Box 51
N-2007 Kjeller, NORWAY

FOREIGN (Others)

Dr. Peter Basham
Earth Physics Branch
Geological Survey of Canada
1 Observatory Crescent
Ottawa, Ontario, CANADA K1A 0Y3

Dr. Fekadu Kebede
Seismological Section
Box 12019
S-750 Uppsala, SWEDEN

Dr. Eduard Berg
Institute of Geophysics
University of Hawaii
Honolulu, HI 96822

Dr. Tormod Kvaerna
NTNF/NORSAR
P.O. Box 51
N-2007 Kjeller, NORWAY

Dr. Michel Bouchon
I.R.I.G.M.-B.P. 68
38402 St. Martin D'Herbes
Cedex, FRANCE

Dr. Peter Marshal
Procurement Executive
Ministry of Defense
Blacknest, Brimpton
Reading RG7-4RS, UNITED KINGDOM

Dr. Hilmar Bungum
NTNF/NORSAR
P.O. Box 51
N-2007 Kjeller, NORWAY

Prof. Ari Ben-Menahem
Department of Applied Mathematics
Weizman Institute of Science
Rehovot, ISRAEL 951729

Dr. Michel Campillo
Observatoire de Grenoble
I.R.I.G.M.-B.P. 53
38041 Grenoble, FRANCE

Dr. Robert North
Geophysics Division
Geological Survey of Canada
1 Observatory Crescent
Ottawa, Ontario, CANADA K1A 0Y3

Dr. Kin Yip Chun
Geophysics Division
Physics Department
University of Toronto
Ontario, CANADA M5S 1A7

Dr. Frode Ringdal
NTNF/NORSAR
P.O. Box 51
N-2007 Kjeller, NORWAY

Dr. Alan Douglas
Ministry of Defense
Blacknest, Brimpton
Reading RG7-4RS, UNITED KINGDOM

Dr. Jorg Schlittenhardt
Federal Institute for Geosciences & Nat'l Res.
Postfach 510153
D-3000 Hannover 51, FEDERAL REPUBLIC OF
GERMANY

Dr. Roger Hansen
NTNF/NORSAR
P.O. Box 51
N-2007 Kjeller, NORWAY

Prof. Daniel Walker
University of Hawaii
Institute of Geophysics
Honolulu, HI 96822

Dr. Manfred Henger
Federal Institute for Geosciences & Nat'l Res.
Postfach 510153
D-3000 Hannover 51, FRG

Ms. Eva Johannsson
Senior Research Officer
National Defense Research Inst.
P.O. Box 27322
S-102 54 Stockholm, SWEDEN

U.S. GOVERNMENT PRINTING OFFICE: 1990-700-000/00045